TRƯỜNG ĐẠI HỌC QUY NHƠN
QUY NHON UNIVERSITY

TẠP CHÍ KHOA HỌC
TRƯỜNG ĐẠI HỌC QUY NHƠN

QUY NHON UNIVERSITY
JOURNAL OF SCIENCE

KHOA HỌC TỰ NHIÊN VÀ KỸ THUẬT
NATURAL SCIENCES AND ENGINEERING

17 (5)

2023

OCTOBER 2023

QUY NHON UNIVERSITY
JOURNAL OF SCIENCE
VOLUME 17, ISSUE 5, OCTOBER 2023
ISSN: 1859-0357 E-ISSN: 2815-6242

CONTENTS

TẠP CHÍ KHOA HỌC
TRƯỜNG ĐẠI HỌC QUY NHƠN

Ứng dụng của công nghệ lắng đọng lớp nguyên tử trong cảm biến khí

Bùi Văn Hào*, Nguyễn Viết Hương

Khoa Khoa học và Kỹ thuật Vật liệu, Trường Đại học Phenikaa, Hà Nội, Việt Nam

Ngày nhận bài: 27/02/2023; Ngày sửa bài: 01/10/2023; Ngày nhận đăng: 11/10/2023; Ngày xuất bản: 28/10/2023

TÓM TẮT

Lắng đọng lớp nguyên tử (ALD) là công nghệ chế tạo vật liệu tiên tiến được ứng dụng rộng rãi trong nhiều lĩnh vực khác nhau. Nhờ vào tính chất tự bão hòa của các phản ứng trên bề mặt đế, ALD cho phép lắng đọng vật liệu với độ đồng đều cao trên mọi bề mặt và khả năng điều khiển chính xác kích thước của vật liệu ở mức độ nguyên tử. Do đó, ALD thường được dùng để lắng đọng các màng siêu mỏng hoặc các hạt nano trên bề mặt của các cấu trúc nano dị thể ứng dụng trong cảm biến khí nhằm làm tăng cường các tính chất điện và tính chất nhạy khí của vật liệu. Đặc biệt, trong thời gian gần đây, một số nghiên cứu cho thấy các vật liệu nhạy khí có độ nhạy và độ lặp lại chưa từng có có thể đạt được bằng cách kết hợp các quy trình ALD của các vật liệu khác nhau. Điều này cho thấy tiềm năng lớn của công nghệ ALD trong lĩnh vực cảm biến khí. Trong bài báo tổng quan này, chúng tôi trình bày tóm tắt những ứng dụng gần đây của ALD trong lĩnh vực cảm biến khí. Trong đó, chúng tôi tập trung vào hai ứng dụng chính của công nghệ ALD là biến tính bề mặt của các cấu trúc nano dị thể và chế tạo các vật liệu cảm biến tiên tiến.

Từ khóa: *Lắng đọng lớp nguyên tử, cảm biến khí, vật liệu màng mỏng, vật liệu hạt nano, vật liệu đơn nguyên tử.*

**Tác giả liên hệ chính.*
Email: hao.buivan@phenikaa-uni.edu.vn

https://doi.org/10.52111/qnjs.2023.17501

QUY NHON UNIVERSITY
JOURNAL OF SCIENCE

Recent advances in atomic layer deposition of nanostructured materials for gas sensors

Hao Van Bui*, Viet Huong Nguyen

Faculty of Materials Science and Engineering, Phenikaa University, Vietnam

Received: 27/02/2023; Revised: 01/10/2023; Accepted: 11/10/2023; Published: 28/10/2023

ABSTRACT

Atomic layer deposition (ALD) has been widely used in the field of gas sensors thanks to the advantages of a non-line-of-sight technique that allows for conformal and uniform coating on virtually any type of substrates, and the capability of depositing various materials in a highly controlled manner. ALD is mainly applied for surface modification using ultrathin films or nanoparticles to fabricate heterostructures, which can drastically change the electronic transport properties and improve the performance of the sensing materials. Recently, ALD has been utilized to fabricate "all-ALD sensing materials", which exhibit unprecedented performance and outstanding reproducibility. This overall review summarizes recent advances in the fabrication of sensing materials for gas sensors by ALD, with focuses on two main applications: ALD for surface modification of sensing materials and ALD for fabrication of sensing materials.

Keywords: *Atomic layer deposition, gas sensors, ultrathin films, nanoparticles, single atoms.*

1. INTRODUCTION

Gas sensors have been popularly used to monitor air pollution. Nowadays, they also appear in most of high buildings, smart homes, and industrial manufacturing processes to detect gas leakage that helps prevent accidents and avoid equipment malfunction. In some emerging areas such as healthcare, gas sensors are used in exhaled breath diagnosis or to provide a correct gas mixture for the sake of safety and health of patients. Hence, it is no doubt that gas sensors have become an indispensable part of our daily life.[1–3]

Gas sensors can be classified into various types based on their sensing materials, such as semiconductor metal oxide (SMO) sensors, polymer sensors, carbon nanotube sensors, or based on their sensing principle, such as resistive sensors, electrochemical sensors, thermal conductivity sensors, acoustic sensors, and optical sensors.[4,5] Among these types, gas sensors using SMOs as sensing materials are most popularly used due to their high stability, low cost, and especially their chemiresistant behavior that represents a change in electrical resistance in response to the change in surrounding chemical environment.[4] Among the SMOs, SnO_2, ZnO, TiO_2, and NiO are most used. During the past decades, various nanostructures of SMOs have been developed, including nanowires, nanorods, nanotubes or 3D architectures (Figure 1), which exhibit superior performance as the sensing materials in chemiresistive sensors to achieve high sensitivity and selectivity.

**Corresponding author.*
Email: hao.buivan@phenikaa-uni.edu.vn

https://doi.org/10.52111/qnjs.2023.17501

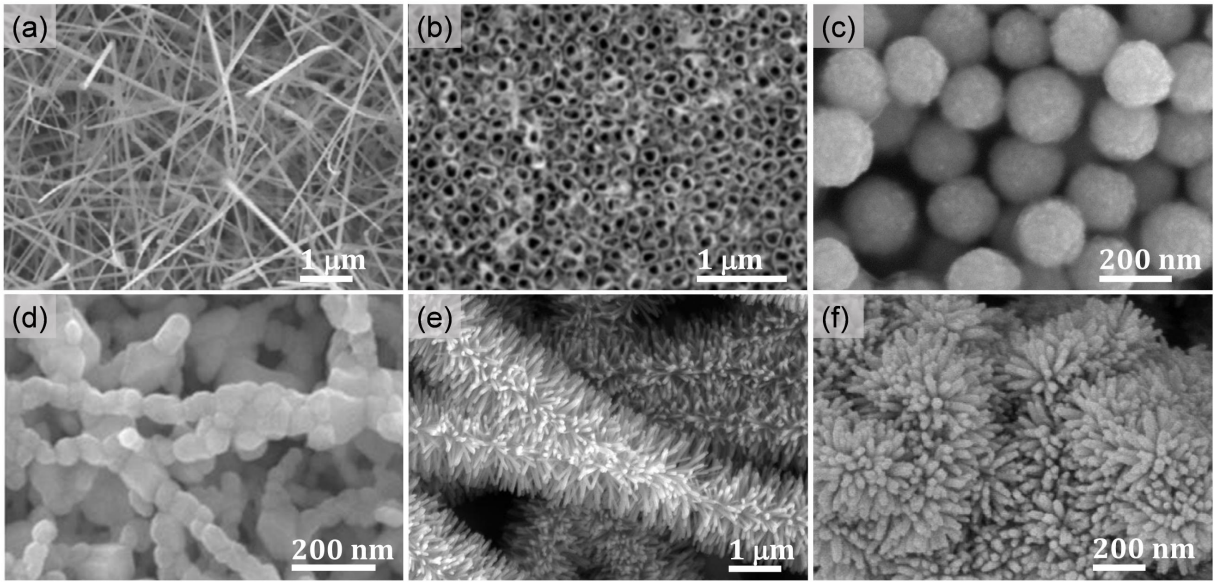

Figure 1. Several typical nanostructured SMOs used as sensing materials for gas sensors: (a) SnO_2 NWs,[6] (b) TiO_2 nanotubes,[7] (c) In_2O_3 nanospheres,[8] (d) WO_3 nanowires,[9] (e) ZnO 3D hierarchical structure,[10] and (f) SnO_2 3D nanoflowers.[11]

The advantages of using nanostructured SMOs as sensing materials rely firstly on their facile synthesis techniques. Most of nanostructures can be achieved by wet-chemistry methods, such as solvothermal and hydrothermal. Chemical vapor deposition is often used to grow high-quality materials (e.g., better crystallinity, lower impurity) due to the higher growth temperatures and the absence of solvent usage. Secondly, nanostructured SMOs allow for tuning the material properties by tailoring their shape and size, which can be obtained by adjusting the synthesis conditions, such as temperature, reaction time, precursor concentration or even pH of the solution. Thirdly, SMO nanostructures provide high specific surface area (SSA) for the adsorption of gaseous species, which is directly proportional to the sensitivity of the sensors. The high SSA of SMO nanostructures also allows for a higher loading of functionalized materials on their surface, with is currently a key technique for improving sensor performance. Hence, nanostructured SMOs have been the most attractive materials for gas sensors. Nevertheless, nanostructured SMOs synthesized by wet-chemistry processes are commonly in form of powders, which are usually transferred onto pre-patterned electrodes by using methods like screen-printing, dip-coating, and drop-coating to realize a sensor device, which is analogous to the process described in Figure 2A. This well-established fabrication process is quite effective and low-cost; however, it suffers from the lack of control in terms of uniformity and reproducibility of the sensing layer. On-chip fabrication of sensing materials, in which the sensing materials are selectively grown on top of the pre-patterned electrodes (Figure 2B), has been developed to replace the dip-/drop-coating methods, which significantly improves the electrical contacts between the sensing materials and the metal electrodes. However, it does not improve much uniformity and reproducibility of the fabrication process. High-precision sensing layer technology is of great significance for the reliable production of sensors and sensor arrays. In this regard, atomic layer deposition (ALD) has emerged as an ideal technology for depositing sensing materials.

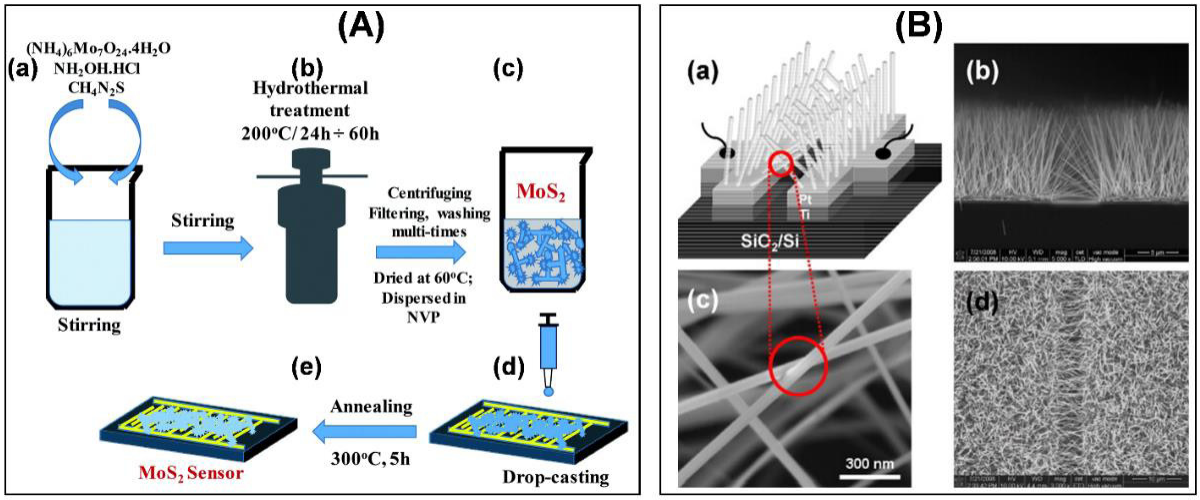

Figure 2. (A) Typical steps in a fabrication process of gas sensors employing sensing materials synthesized by hydrothermal method:[12] (a) mixing precursors and stirring, (b) hydrothermal treatment, (c) collecting and washing the solid product, (d) drop-coating of sensing materials onto pre-patterned electrodes, and (e) thermal annealing; (B) On-chip growth of ZnO nanowires:[13] (a) a schematic drawing describing the selective growth of ZnO, (b)-(d) SEM images of the ZnO nanowires taken in the area between the two Pt electrodes ((b) – cross sectional view and (d) – top view).

2. ATOMIC LAYER DEPOSITION

Atomic layer deposition (ALD) is a gas-phase deposition technique, which is a variant of chemical vapor deposition (CVD).[14] However, ALD can be carried out significantly lower temperatures, which are typically below 400 °C. In CVD, precursors are supplied continuously and co-exist in space and time above the substrate; however, in ALD, precursors are introduced in pulses sequentially and separately, and they are repeated in cycles.[15] A typical ALD cycle consists of 4 sequential pulses: (1) a pulse of the first precursor (i.e., precursor exposure), (2) a pulse of inert gas to evacuate the reaction by-products and unused precursor (i.e., purge), (3) a pulse of the second precursor or co-reactant, and (4) a pulse of inert gas to evacuate the reaction by-products and unused precursor. An animation representing a cycle of Al_2O_3 ALD using trimethylaluminum (TMA – precursor A) and H_2O (precursor B) is given in Figure 3. It is important to note that in ALD, the functional groups on the initial substrate surface are very important, which initiate the chemical reactions (i.e., chemisorption) with the gas molecules of precursor A when they are introduced to the reactor. These functional groups are commonly created by surface pre-treatment prior to the deposition. When TMA molecules are introduced into the reactor (step 1), they react with the functional groups (i.e., −OH) via the ligand-exchange reactions:[14]

$$-OH_{(surface)} + Al(CH_3)_{3(vapor)} \rightarrow -O-Al(CH_3)_{2(surface)} + CH_{4(gas)} \quad (1)$$

After all the −OH groups are consumed, the reactions reach a saturation (self-limiting), resulting in at most 1 monolayer containing Al atoms on the surface. The exceeding (i.e., unused) molecules and the by-products (i.e., CH_4 gas) are then evacuated by a purge of inert gas (step 2). In the next step, when H_2O is introduced into the reactor, the reactions between H_2O molecules and the newly formed ligands on the surface proceed as:

$$-O-Al(CH_3)_{2(surface)} + HOH_{(vapor)} \rightarrow -O-Al(OH)_{2(surface)} + CH_{4(gas)} \quad (2)$$

Similarly, when all the ligands have reacted with H_2O, the reactions stop, forming at most 1 monolayer containing O atoms, and

https://doi.org/10.52111/qnjs.2023.17501

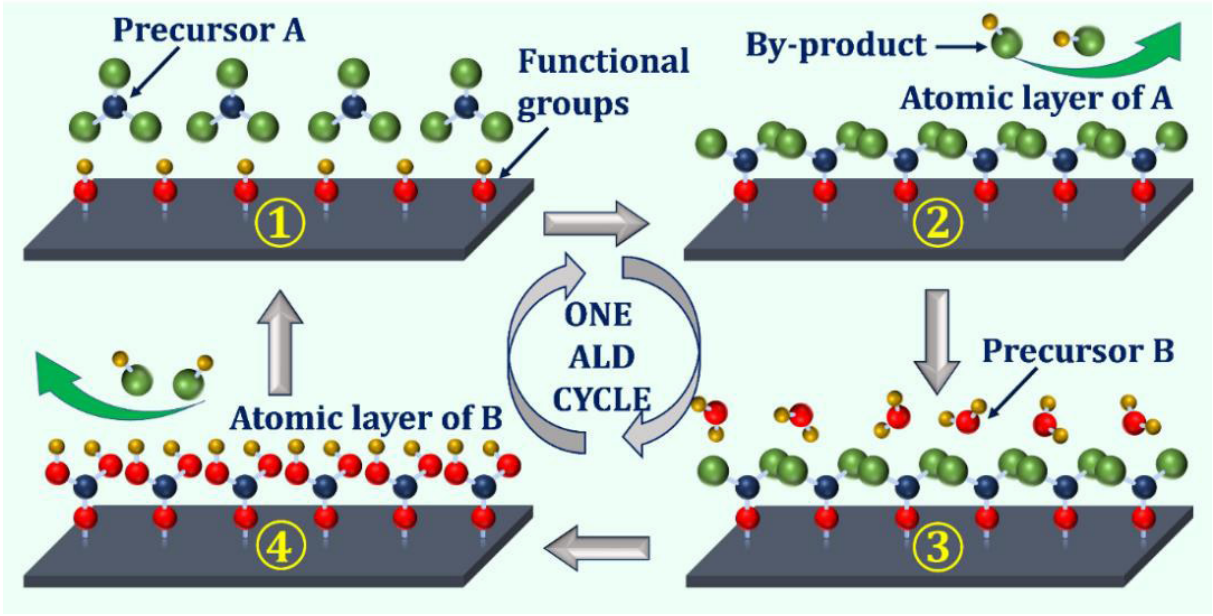

Figure 3. A typical ALD cycle consisting of 4 pulses: (1) precursor A, (2) inert gas, (3) precursor B, and (4) purge.

the surface is now terminated by −OH groups, which are necessary for the reactions with TMA molecules in the next cycles. Reaction (1) and reaction (2) are commonly known as the two "half-reactions" in an ALD cycle. Typically, the growth rate in ALD is in the range of a few angstroms per cycle. Hence, by controlling the number of cycles, the film thickness and the amount of deposited material can be controlled at the atomic level. This is a unique property of ALD, which allows for uniform and conformal coating on various types of substrates with different geometries, such as flat substrates, high aspect ratio structures, 2D materials, porous structures, nanoparticles, and nanowires (Figure 4).

Thanks to the advantages of a solvent-free method with excellent controllability, ALD has been applied in many fields, including electronic and photovoltaic devices,[21,22] catalysis,[23] and energy storage and conversion materials.[24–26] Recently, ALD has been also applied in the field of gas sensors, which is used to deposit ultrathin films of SMOs such as SnO_2, ZnO and TiO_2, as well as nanoclusters of noble metals such as Pt, Pd, and Ni, as presented concisely in a recent review by Marichy and Pinna.[27] The applications of ALD in gas sensors can be divided into two groups: ALD for surface modification of sensing materials and ALD for fabrication of sensing materials.

2.1. ALD for surface modification of sensing materials

Surface modification is a common technique to tailor the properties of materials by coupling them with other materials. Particularly in gas sensors, to improve the selectivity and sensitivity of the sensing layers, they are usually coated with ultrathin films of SMOs or with nanoparticles of noble metals the create various types of heterostructures, such as n−n and p−n heterojunctions.[28] The most investigated heterostructure in gas sensors is the core/shell structure. Due to their different electronic band structure, heterojunctions can drastically change the electronic transport of carriers and improve sensing properties compared to their single components. For example, SnO_2 nanostructures are excellent sensing materials that have been used to detect various types of gases, both reducing and oxidizing gases.[29] However, coating a thin layer of ZnO on SnO_2 nanofibers to form an n-ZnO/n-SnO_2 heterojunction could significantly alter the sensing properties of SnO_2:

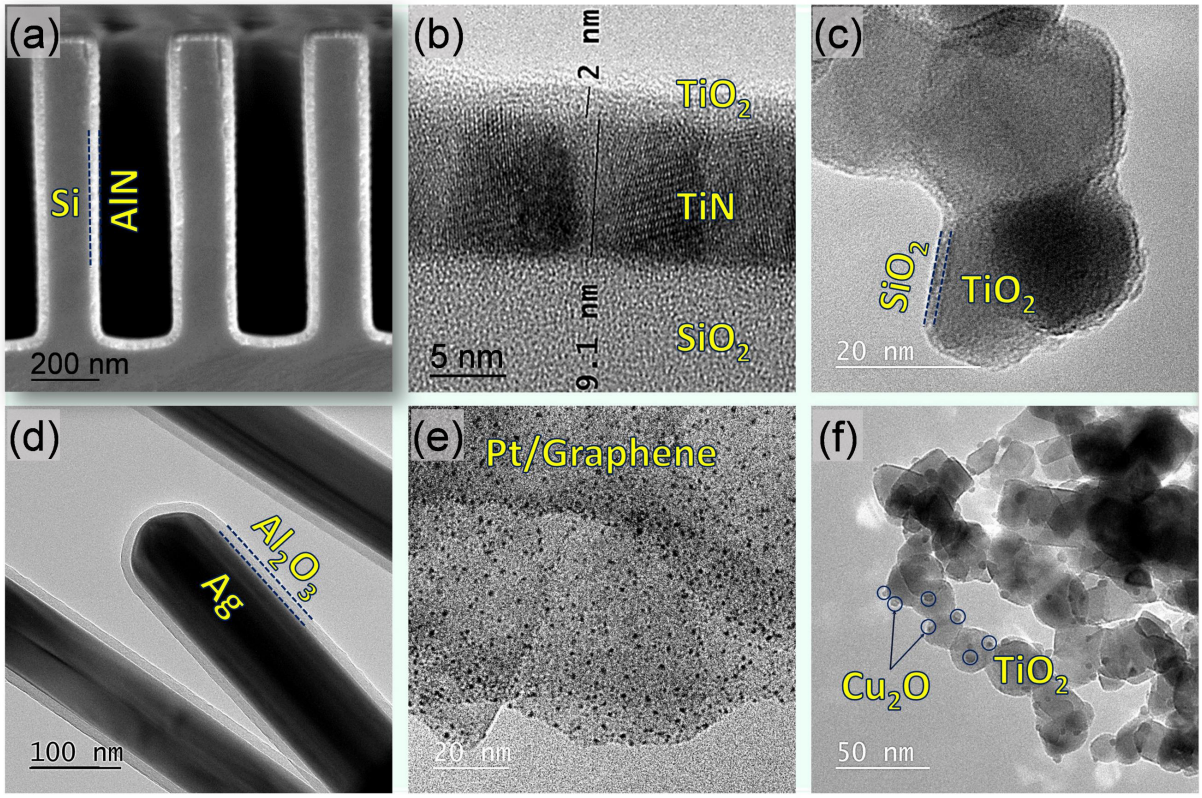

Figure 4. Examples of the uniformity of thin films and nanoclusters deposited by ALD: (a) AlN thin film on Si substrate with trenches,[16] (b) TiN thin film on SiO_2,[17] (c) SiO_2 thin film on TiO_2 nanoparticles,[18] (d) Al_2O_3 thin film on Ag nanorods, (e) Pt nanoclusters on graphene,[19] and (f) Cu_2O nanoclusters on TiO_2 nanoparticles.[20]

the core-shell structure is highly effective in detecting gases only and weakens the sensitivity toward oxidizing gases.[30] A p−n heterostructure based on p-CuO/n-ZnO core/shell nanofibers exhibited superior performance with a prominent enhancement of sensing ability compared to the bare ZnO nanofibers, allowing for detecting reducing gas CO at extremely low concentrations, i.e., down to 0.1 ppm.[31] Many other core/shell structures of MSOs have been utilized in gas sensors, such as MoO_3–TiO_2,[32] CeO_2–TiO_2,[33] In_2O_3–ZnO,[34] Fe_2O_3–ZnO,[35] Ga_2O_3–SnO_2,[36] and Ga_2O_3–ZnO.[37] In all cases, the thickness of the shell layer plays a pivotal role in the performance of sensing layer. Particularly, when the shell thickness is in the range of the Debye length of the shell material, the highest performance is achieved. For example, the n-ZnO/n-SnO_2 core/shell structure exhibited the highest sensitivity for the ZnO thickness of 20 nm (Figure 5A),[30] whereas an optimum shell layer of 16 nm was found for the p-CuO/n-ZnO core/shell structure (Figure 5B),[31] both of which are in the Debye length range of the shell layers. These examples indicate that achieving heterostructured gas sensors with desired properties and optimum performance requires a precise thickness of the shell layer. Hence, ALD has been widely used to deposit various SMO thin films to realize different heterostructures for gas sensors, as presented in Table 1.

The coupling of SMOs with nanoparticles of noble metals and transition metals such as Pt,[38] Pd,[39] Ru,[40] Ag,[41] and Co[42] has been an effective method to improve the sensitivity, selectivity and response of gas sensors. The enhanced performance of the sensors due to the presence of the metal nanoparticles is attributed to two key factors: the catalytic activity of the metals (chemistry aspect) and the formation of Schottky contacts between the metal and the SMO (physics aspect).[10] In the chemistry aspect, the high catalytic activity of the meal nanoparticles

https://doi.org/10.52111/qnjs.2023.17501

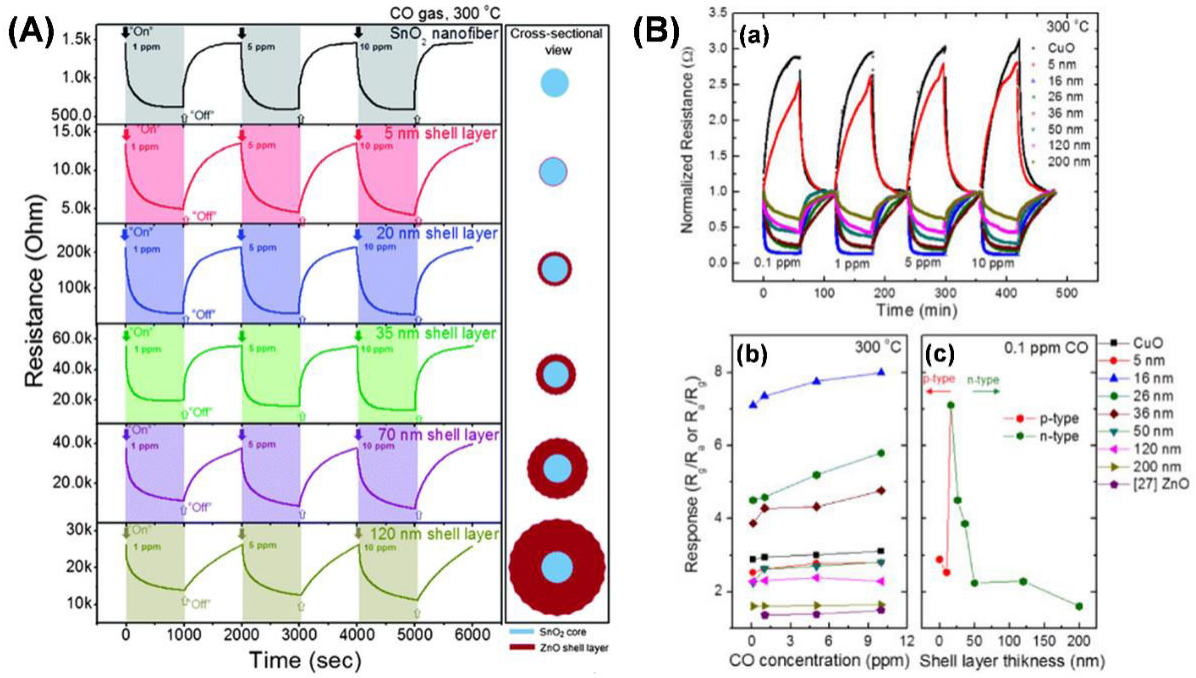

Figure 5. (A) Influence of the shell thickness on the response of sensors based on n-ZnO/n-SnO_2 core/shell structure;[30] (B) for p-CuO/n-ZnO core/shell structure with the shell thickness being varied in the range of 0–200 nm:[31] (a) Dynamic response curves, (b) responses at various CO concentrations, and (c) responses at 0.1 ppm CO.

promotes the adsorption of oxygen on the SMO surface, which enhances the extraction of electrons from the SMO to create ionic oxygen species. The enhanced extraction of electrons can cause a significant change in the SMO resistance, whereas the higher density of ionic oxygen species on the SMO surface provides more active sites for the interaction between the detected gas and the sensing layer. In the physics aspect, the presence of metal nanoparticles create Schottky junctions on the SMO surface in the vicinity of the nanoparticles.[64] This narrows the conducting channel, resulting in the increase in resistance. Both the chemistry and the physics aspects can bring a significant improvement of sensitivity, selectivity, and response of sensors. For example, Rh nanoparticles on SnO_2 nanofibers can act as effective adsorption sites to bind and dissociate oxygen molecules. This increases the adsorbed oxygen content, resulting in a thicker electron depletion layer and an increase resistance. Another example, the surface modification of ZnO hierarchical nanorods by Pt nanoparticles improved the selectivity of the sensor to methanol, increased its response approximately 19500 times and significantly lowered the operating temperature compared to the pristine ZnO.[10] In that case, the Pt nanoparticles not only enhanced the adsorption of O_2, but also promoted the dissociation of methanol molecules and facilitated the electron transfer from Pt to ZnO, which consequently caused an abnormal decrease of resistance of sensing layer when exposed to methanol. These are a few examples among numerous research on the advantages of surface modification of sensing materials by metal nanoparticles that have been reported in the literature. With the advantages of a non-line-of-sight technique that allows for conformal and uniform coating on all kinds of substrates, and the capability of depositing various pure metals in a highly controlled manner, ALD of metal nanoparticles has been recently applied for functionalize nanostructured metal oxides in gas sensors. Due to their high catalytic and sensing activities and well-developed ALD processes, Pt and Pd are most used. A few examples are given in Table 1.

Table 1. SMO thin films and noble metal nanoparticles grown by ALD for surface modification of nanostructured sensing materials.

Material (Shell)	Substrate (Core)	Shell thickness/ Cluster size (nm)	Junction type	Test gas	Ref.
ZnO	Graphene	0.5 – 10	n–n	HCHO, NO_2	43
	SnO_2 nanofibers	22 – 250	n–n	O_2, NO_2, CO	44
	SnO_2 nanorods	3.5 – 9.5	n–n	CO, NO_2; C_7H_8, C_6H_6	45
	TiO_2 nanorods	20	n–n	C_2H_5OH	46
	TiO_2 nanofibers	50 – 250	n–n	O_2	47
	WO_3 nanorods	15	n–n	NO_2	48
	In_2O_3 nanowires	10 – 53	n–n	C_2H_5OH	49
	CuO nanorods	9	n–p	NO_2	50
	CuO nanowires	5 – 110	n–p	C_6H_6	51
	CuO nanofibers	5 – 200	n–p	CO	31
SnO_2	Carbon nanotubes	1.5 – 15	n–p	NO_2	52
	CuO nanowires	0 – 31	n–p	HCHO	53
	TiO_2 nanotubes	4 – 16	n–n	NO_2	54
	Ga_2O_3 nanowires	2 – 15	n–n	C_2H_5OH, NH_3, CO, H_2	36
	WO_3 nanosheets	5 – 30	n–n	NH_3	55
	Nb_2O_5 nanorods	7 – 34	n–n	H_2S	56
TiO_2	ZnO nanorods	10	n–n	RH, NO_2	57
	Carbon nanotubes	1.5 – 15	n–p	O_2, NO_2	58
NiO	SnO_2 nanowires	2 – 82	p–n	H_2	59
	Carbon nanotubes	0.8 – 21.8	p–p	Acetone, C_2H_5OH	60
	Co_3O_4 nanoparticles		p–p	Trimethylamine	61
Cu_2O	SnO_2 nanowires	5 – 80	p–n	NO_2	62
CuO	SnO_2 nanowires	5 – 80	p–n	NO_2, C_7H_8, C_6H_6	51
SiO_2	SnO_2 nanowires	1.8 – 10.5		H_2	63
Pt	SnO_2 nanowires	4 – 8	Schottky	C_2H_5OH	64
	Al_2O_3/ZnO nanorods	3 – 5	Schottky	Acetylene	65
	MoS_2 nanoflakes	< 1	–	H_2	66
Pd	ZnO nanowires	10	Schottky	C_6H_6, C_7H_8, C_2H_5OH, CH_3COCH_3	67
Rh	ZnO nanoflowers	0.4 – 1.6	Schottky	Trimethylamine	68

2.2. ALD of sensing materials

In addition to the application in modifying the surface of SMO nanostructures, ALD has also been used to deposit thin films of SnO_2,[69–71] TiO_2,[72,73] and ZnO[74] as the sensing layers for gas sensors directly on top of substrates without the need of complex nanostructures. The studies on the sensing performance of these thin films also revealed the strong influence of film thickness on the sensitivity and response of the sensors. For example, Rosental et al.[69] investigated the sensing properties of ALD SnO_2 films toward CO gas and observed that the maximum performance was achieved for the layer with a thickness of 10 nm. This thickness is comparable to the Debye length of SnO_2. Du et al.[70] found that the sensor

https://doi.org/10.52111/qnjs.2023.17501

response changed drastically by varying the SnO_2 thickness in a very narrow range, i.e., 1.6–5.9 nm. The use of ALD not only provides precise control of the film thickness, but also tackles the uniformity and reproducibility issues that are commonly encountered in traditional sensor preparation techniques (i.e., drop-/dip-coating of sensing materials on prepatterned electrodes).

Up to date, ALD of shell layers, including SMO thin films and metal nanoparticles, for gas sensors has been widely utilized. However, this approach can only offer an improved performance of sensors, but it cannot solve the problems in the reproducible fabrication gas sensors due to it is still strongly dependent on the fabrication of the nanostructures (e.g., wet chemistry) and transfer them to the sensor electrodes (e.g., drop-/dip-coating). An "all ALD" or "ALD only" process in which all materials are deposited by ALD is highly desirable for taking full advantages of ALD: Precise control, uniform, and reproducible. This has just been realized very recently by Zhang et al,[75] who fabricated the sensors based on SnO_2 ultrathin films and Pt single atoms, both deposited by ALD (Figure 6A), and investigated their sensing performance to triethylamine (TEA) gas. The work is distinctive from existing research in developing sensing materials for advanced gas sensors, both in both fundamental mechanistic and technological aspects. For the first time, Pt single atoms were used to improve the sensing properties of SnO_2 ultrathin films with thicknesses in the range of a few nanometers, resulting in an exceptionally high sensitivity of 8.76 ppm^{-1} and an extremely low detection limit of 7 ppb. The sensors also exhibited excellent selectivity, low operating temperature, very fast response and recovery (Figure 6B), which are

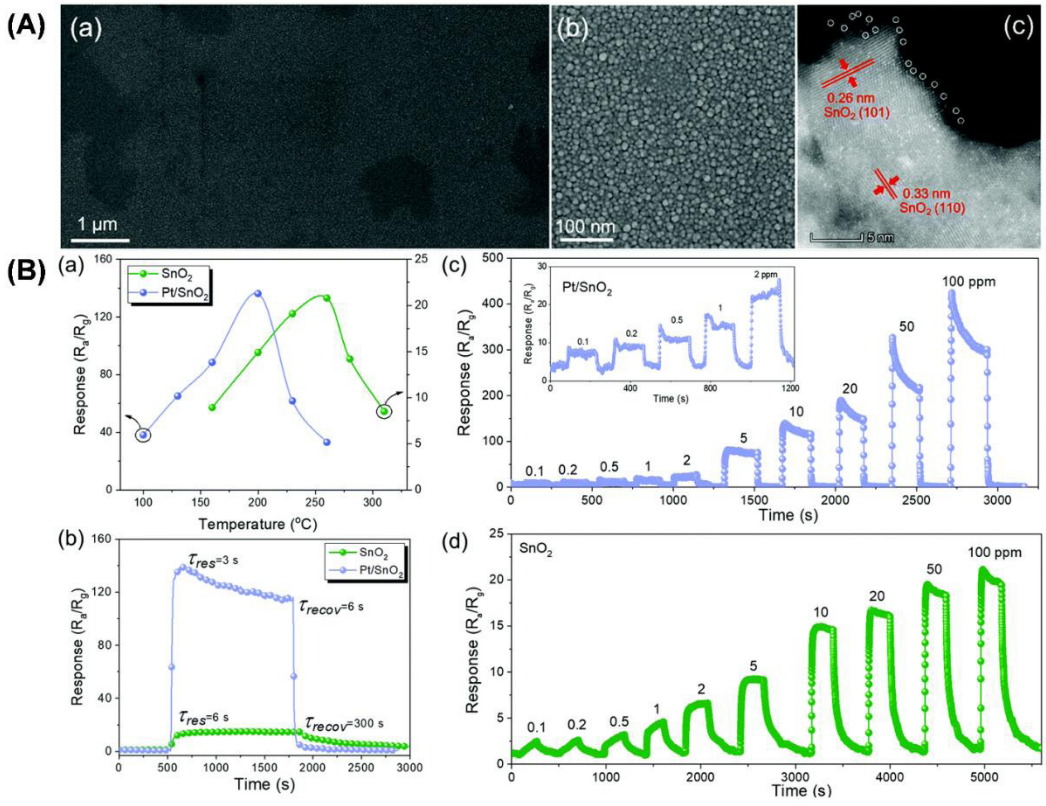

Figure 6. (A) Structural characterization of SnO_2 and Pt/SnO_2 thin films: (a & b) SEM images of a SnO_2 thin film, and (c) HAADF-STEM image showing the presence of Pt single atoms. (B) Sensing performance of the Pt/SnO_2 toward TEA vapor: (a) responses to 10 ppm TEA of SnO_2 and Pt/SnO_2 thin films (9 nm) at different temperatures; (b) dynamic transients of SnO_2 and Pt/SnO_2 thin films to 10 ppm TEA at 200 °C, and dynamic transients of (c) Pt/SnO_2 and (d) SnO_2 thin films to TEA concentrations in the range of 0.1–100 ppm at 200 °C.[75]

far beyond the results reported in the literature.[75] Most recently, an "all ALD" process has also been demonstrated by Zhuiykov et al. for the fabrication of heterostructures based on SnO_2 and In_2O_3 ultrathin films with a total thickness of below 10 nm at wafer scale.[76] Without the use of functionalized metal nanoparticles, the sensors based using SnO_2/In_2O_3 heterostructures also exhibited excellent sensitivity, high rate of gas detection, good selectivity and long-term stability. The sensitivity of S = 53 and limit of detection of ~1.0 ppm towards ethanol achieved by the ALD fabricated SnO_2/In_2O_3 heterostructures are the highest performance of the reported sensors based on SnO_2 and In_2O_3 composites prepared by various methods.[76] Hence, the excellent performance of the sensing materials prepared by an "all ALD" process in combination with the great advantages of ALD (precise control, high reproducibility, high uniformity and well-established large scale production) can pave the way for the scalable production of reliable and high performance thin film sensors.

3. CONCLUSIONS AND OUTLOOK

The versatility and precision offered by this ALD make it an ideal choice when developing novel sensing layers, as well as engineering complex nanostructures that further improve performance levels while providing additional perspectives into development processes related to these types of technologies. Hence, ALD has been widely applied in the fabrication of resistive gas sensor devices, where at least one step involves using this method. On the one hand, an effective surface modification method, ALD has been employed to deposit ultrathin films and nanoparticles of a wide range of materials on virtually any sophisticated nanostructures. This provides a feasible route to realize heterojunctions of sensing materials, which can drastically change the electronic transport properties and improve the sensing performance. On the other hand, ALD can be used to realize all-ALD-fabricated nanostructures. This approach not only allows for the fabrication of novel nanostructures with unprecedented sensing performance in the sensitivity, selectivity, and stability, but also assures the high reproducibility and reliability of the sensors, which are highly important for practical applications. Furthermore, its compatibility with integrated circuits makes it a cost-effective solution compared to other fabrication methods which can lead towards more widespread adoption in various industries such as automotive or medical applications where reliable detection systems are essential.

REFERENCES

1. X. Zhou, Z. Xue, X. Chen, C. Huang, W. Bai, Z. Lu, T. Wang. Nanomaterial-based gas sensors used for breath diagnosis, *Journal of Materials Chemistry B,* **2020**, *8*(16), 3231–3248.

2. G. F. Fine, L. M. Cavanagh, A. Afonja, R. Binions. Metal oxide semi-conductor gas sensors in environmental monitoring, *Sensors,* **2010**, *10*(6), 5469–5502.

3. X. Chen, M. Leishman, D. Bagnall, N. Nasiri. Nanostructured gas sensors: From air quality and environmental monitoring to healthcare and medical applications, *Nanomaterials,* **2021**, *11*(8), 1927.

4. A. Dey. Semiconductor metal oxide gas sensors: A review, *Materials Science and Engineering B,* **2018**, *229*, 206–217.

5. J. B. A. Gomes, J. J. P. C. Rodrigues, R. A. L. Rabêlo, N. Kumar, S. Kozlov. Io T-enabled gas sensors: Technologies, applications, and opportunities, *Journal of Sensor and Actuator Networks,* **2019**, *8*(4), 57.

6. Y.-J. Choi, I.-S. Hwang, J.-G. Park, K. J. Choi, J.-H. Park, J.-H. Lee. Novel fabrication of an SnO_2 nanowire gas sensor with high sensitivity, *Nanotechnology,* **2008**, *19*(9), 095508.

7. S. Lin, D. Li, J. Wu, X. Li, S. A. Akbar. A selective room temperature formaldehyde gas sensor using TiO_2 nanotube arrays, *Sensors and Actuators B: Chemical,* **2011**, *156*(2), 505–509.

8. X. Liu, L. Jiang, X. Jiang, X. Tian, X. Sun, Y. Wang, W. He, P. Hou, X. Deng, X. Xu. Synthesis

of Ce-Doped In_2O_3 nanostructure for gas sensor applications, *Applied Surface Science,* **2018**, *428*, 478–484.

9. N. M. Vuong, D. Kim, H. Kim. Surface Gas Sensing Kinetics of a WO_3 Nanowire Sensor: Part 1-Oxidizing Gases, *Sensors and Actuators B: Chemical,* **2015**, *220*, 932–941.

10. N. M. Vuong, D. D. Duy, H. N. Hieu, V. N. Nguyen, N. N. K. Truong, H. V. Bui, N. V. Hieu. Low-Operating temperature and remarkably responsive methanol sensors using Pt-decorated hierarchical ZnO structure, *Nanotechnology,* **2021**, *33*(6), 065502.

11. Y. Liu, J. Huang, J. Yang, S. Wang. Pt Nanoparticles functionalized 3D SnO_2 nanoflowers for gas sensor application, *Solid-State Electronics,* **2017**, *130*, 20–27.

12. N. T. Thang, L. T. Hong, N. H. Thoan, C. M. Hung, N. V. Duy, N. V. Hieu, N. D. Hoa. Controlled synthesis of ultrathin MoS_2 nanoflowers for highly enhanced NO_2 sensing at room temperature, *RSC Advances,* **2020**, *10*(22), 12759–12771.

13. M.-W. Ahn, K.-S. Park, J.-H. Heo, D.-W. Kim, K. J. Choi, J.-G. Park. On-Chip fabrication of ZnO-Nanowire gas sensor with high gas sensitivity, *Sensors and Actuators B: Chemical,* **2009**, *138*(1), 168–173.

14. S. M. George. Atomic Layer Deposition: An Overview, *Chemical Reviews,* **2010**, *110*(1), 111–131.

15. H. V. Bui, F. Grillo, J. R. van. Ommen. Atomic and molecular layer deposition: Off the beaten track, *Chemical Communications,* **2017**, *53*(1), 45–71.

16. H. V. Bui, F. B. Wiggers, A. Gupta, M. D. Nguyen, A. A. I. Aarnink, M. P. de Jong, A. Y. Kovalgin. Initial growth, refractive index, and crystallinity of thermal and plasma-enhanced atomic layer deposition AlN films, *Journal of Vacuum Science & Technology A,* **2015**, *33*(1), 01A111.

17. H. V. Bui, A. W. Groenland, A. a. I. Aarnink, R. a. M. Wolters, J. Schmitz, A. Y. Kovalgin. Growth kinetics and oxidation mechanism of ALD TiN thin films monitored by in situ spectroscopic ellipsometry, *Journal of the Electrochemical Society,* **2011**, *158*(3), H214.

18. J. Guo, D. Benz, T.-T. D. Nguyen, P.-H. Nguyen, T.-L. T. Le, H.-H. Nguyen, D. L. Zara, B. Liang, H. T. Hintzen (Bert), J. R. V. Ommen, H. V. Bui. Tuning the photocatalytic activity of TiO_2 nanoparticles by ultrathin SiO_2 films grown by low-temperature atmospheric pressure atomic layer deposition, *Applied Surface Science,* **2020**, *530*, 147244.

19. H. V. Bui, F. Grillo, S. S. Kulkarni, R. Bevaart, N. V. Thang, B. van der Linden, J. A. Moulijn, M. Makkee, M. T. Kreutzer, J. R. V. Ommen. Low-temperature atomic layer deposition delivers more active and stable Pt-Based catalysts, *Nanoscale,* **2017**, *9*(30), 10802–10810.

20. D. Benz, Y.-N. T. Nguyen, T.-L. T. Le, T.-H. T. Le, V.-T. Le, J. R. V. Ommen, H. V. Bui. Controlled growth of ultrasmall Cu_2O clusters on TiO_2 nanoparticles by atmospheric-pressure atomic layer deposition for enhanced photocatalytic activity, *Nanotechnology,* **2021**, *32*(42), 425601.

21. A. F. Palmstrom, P. K. Santra, S. F. Bent. Atomic layer deposition in nanostructured photovoltaics: Tuning optical, electronic and surface properties, *Nanoscale,* **2015**, *7*(29), 12266–12283.

22. R. W. Johnson, A. Hultqvist, S. F. Bent. A brief review of atomic layer deposition: From fundamentals to applications, *Materials Today,* **2014**, *17*(5), 236–246.

23. B. J. O'Neill, D. H. K. Jackson, J. Lee, C. Canlas, P. C. Stair, C. L. Marshall, J. W. Elam, T. F. Kuech, J. A. Dumesic, G. W. Huber. Catalyst design with atomic layer deposition, *ACS Catalysis,* **2015**, *5*(3), 1804–1825.

24. M. Mattinen, M. Leskelä, M. Ritala. Atomic layer deposition of 2D Metal dichalcogenides for electronics, catalysis, energy storage, and beyond, *Advanced Materials Interfaces,* **2021**, *8*(6), 2001677.

25. B. Gupta, Md. A. Hossain, A. Riaz, A. Sharma, D. Zhang, H. H. Tan, C. Jagadish, K. Catchpole, B. Hoex, S. Karuturi. Recent advances in materials design using atomic layer deposition

for energy applications, *Advanced Functional Materials,* **2022**, *32*(3), 2109105.

26. Y. Zhao, L. Zhang, J. Liu, K. Adair, F. Zhao, Y. Sun, T. Wu, X. Bi, K. Amine, J. Lu, X. Sun. Atomic/Molecular layer deposition for energy storage and conversion, *Chemical Society Reviews,* **2021**, *50*(6), 3889–3956.

27. C. Marichy, N. Pinna. Atomic layer deposition to materials for gas sensing applications, *Advanced Materials Interfaces,* **2016**, *3*(21), 1600335.

28. D. R. Miller, S. A. Akbar, P. A. Morris. Nanoscale metal Oxide-based heterojunctions for gas sensing: A review, *Sensors and Actuators B: Chemical,* **2014**, *204*, 250–272.

29. S. Das, V. Jayaraman. SnO_2: A comprehensive review on structures and gas sensors, *Progress in Materials Science,* **2014**, *66*, 112–255.

30. A. Katoch, S.-W. Choi, G.-J. Sun, S. S. Kim. An approach to detecting a reducing gas by radial modulation of electron-depleted shells in core–shell nanofibers, *Journal of Materials Chemistry A,* **2013**, *1*(43), 13588–13596.

31. A. Katoch, S.-W. Choi, G.-J. Sun, H. W. Kim, S. S. Kim. Mechanism and prominent enhancement of sensing ability to reducing gases in p/n core–shell nanofiber, *Nanotechnology,* **2014**, *25*(17), 175501.

32. Y.-J. Chen, G. Xiao, T.-S. Wang, F. Zhang, Y. Ma, P. Gao, C.-L. Zhu, E. Zhang, Z. Xu, Q. Li. α-MoO_2/TiO_3 Core/Shell Nanorods: Controlled-synthesis and low-temperature gas sensing properties, *Sensors and Actuators B: Chemical,* **2011**, *155*(1), 270–277.

33. Y.-J. Chen, G. Xiao, T.-S. Wang, F. Zhang, Y. Ma, P. Gao, C.-L. Zhu, E. Zhang, Z. Xu, Q. Li. Synthesis and enhanced gas sensing properties of crystalline CeO_2/TiO_2 Core/Shell nanorods, *Sensors and Actuators B: Chemical,* **2011**, *156*(2), 867–874.

34. N. Singh, A. Ponzoni, R. K. Gupta, P. S. Lee, E. Comini. Synthesis of In_2O_2–ZnO core–shell nanowires and their application in gas sensing, *Sensors and Actuators B: Chemical,* **2011**, *160*(1), 1346–1351.

35. J. Zhang, X. Liu, L. Wang, T. Yang, X. Guo, S. Wu, S. Wang, S. Zhang. Synthesis and Gas Sensing Properties of α-Fe_2O_3@ZnO Core–Shell Nanospindles, *Nanotechnology,* **2011**, *22*(18), 185501.

36. Y.-G. Jang, W.-S. Kim, D.-H. Kim, S.-H. Hong. Fabrication of Ga_2O_3/SnO_2 Core–Shell Nanowires and Their Ethanol Gas Sensing Properties, *Journal of Materials Research,* **2011**, *26*(17), 2322–2327.

37. C. Jin, S. Park, H. Kim, C. Lee. Ultrasensitive multiple networked Ga_2O_3-Core/ZnO-Shell nanorod gas sensors, *Sensors and Actuators B: Chemical,* **2012**, *161*(1), 223–228.

38. Q. Zhou, L. Xu, A. Umar, W. Chen, R. Kumar, Pt nanoparticles decorated SnO_2 nanoneedles for efficient CO gas sensing applications, *Sensors and Actuators B: Chemical,* **2018**, *256*, 656–664.

39. P. Cao, Z. Yang, S. T. Navale, S. Han, X. Liu, W. Liu, Y. Lu, F. J. Stadler, D. Zhu. Ethanol sensing behavior of Pd-Nanoparticles decorated ZnO-Nanorod based chemiresistive gas sensors. *Sensors and Actuators B: Chemical,* **2019**, *298*, 126850.

40. X. Kou, F. Meng, K. Chen, T. Wang, P. Sun, F. Liu, X. Yan, Y. Sun, F.Liu, K. Shimanoe, G. Lu. High-Performance acetone gas sensor based on Ru-Doped SnO_2 nanofibers, *Sensors and Actuators B: Chemical,* **2020**, *320*, 128292.

41. X. Cheng, Y. Xu, S. Gao, H. Zhao, L. Huo. Ag nanoparticles modified TiO_2 spherical heterostructures with enhanced gas-sensing performance, *Sensors and Actuators B: Chemical,* **2011**, *155*(2), 716–721.

42. H. W. Kim, H. G. Na, Y. J. Kwon, H. Y. Cho, C. Lee. Decoration of Co nanoparticles on ZnO-branched SnO_2 nanowires to enhance gas sensing, *Sensors and Actuators B: Chemical,* **2015**, *219*, 22–29.

43. H. Mu, Z. Zhang, X. Zhao, F. Liu, K. Wang, H. Xie. High sensitive formaldehyde graphene gas sensor modified by atomic layer deposition zinc oxide films, *Applied Physics Letters,* **2014**, *105*(3), 033107.

https://doi.org/10.52111/qnjs.2023.17501

44. S.-W. Choi, J. Y. Park, S. S. Kim. Synthesis of SnO_2–ZnO Core–Shell nanofibers via a novel two-step process and their gas sensing properties, *Nanotechnology,* **2009**, *20*(46), 465603.

45. S.-W. Choi, A. Katoch, G.-J. Sun, J.-H. Kim, S.-H. Kim, S. S. Kim. Dual functional sensing mechanism in SnO_2–ZnO core–shell nanowires, *ACS Applied Materials & Interfaces,* **2014**, *6*(11), 8281–8287.

46. S. Park, S. An, H. Ko, S. Lee, H. W. Kim, C. Lee, Enhanced ethanol sensing properties of TiO_2/ZnO Core–Shell nanorod sensors, *Applied Physics A,* **2014**, *115*(4), 1223–1229.

47. J. Y. Park, S.-W. Choi, J.-W. Lee, C. Lee, S. S. Kim. Synthesis and gas sensing properties of TiO_2–ZnO core-shell nanofibers, *Journal of the American Ceramic Society,* **2009**, *92*(11), 2551–2554.

48. S. An, S. Park, H. Ko, C. Lee. Enhanced NO_2 gas sensing properties of WO_3 nanorods encapsulated with ZnO, *Applied Physics A,* **2012**, *108*(1), 53–58.

49. S. Park, H. Ko, S. Kim, C. Lee. Role of the interfaces in multiple networked one-dimensional core–shell nanostructured gas sensors, *ACS Applied Materials & Interfaces,* **2014**, *6*(12), 9595–9600.

50. C. Jin, H. Kim, S. Park, S.-W. Choi, S. S. Kim, C. Lee. NO_2 gas sensing properties of ZnO sheathed CuO nanorods, *Surface and Interface Analysis,* **2012**, *44*(11–12), 1534–1537.

51. J.-H. Kim, A. Katoch, S. S. Kim. Optimum shell thickness and underlying sensing mechanism in p–n CuO–ZnO core–shell nanowires, *Sensors and Actuators B: Chemical,* **2016**, *222*, 249–256.

52. C. Marichy, N. Donato, M.-G. Willinger, M. Latino, D. Karpinsky, S.-H. Yu, G. Neri, N. Pinna. Tin dioxide sensing layer grown on tubular nanostructures by a non-aqueous atomic layer deposition process, *Advanced Functional Materials,* **2011**, *21*(4), 658–666.

53. L.-Y. Zhu, K. Yuan, J.-G. Yang, H.-P. Ma, T. Wang, X.-M. Ji, J.-J. Feng, A. Devi, H.-L. Lu. Fabrication of heterostructured P-CuO/n-SnO_2 core-shell nanowires for enhanced sensitive and selective formaldehyde detection, *Sensors and Actuators B: Chemical,* **2019**, *290*, 233–241.

54. S. Ng, J. Prášek, R. Zazpe, Z. Pytlíček, Z. Spotz, J. R. Pereira, J. Michalička, J. Přikryl, M. Krbal, H. Sopha, J. Hubálek, J. M. Macák. Atomic layer deposition of SnO_2 - Coated anodic one-dimensional TiO_2 nanotube layers for low concentration NO_2 sensing, *ACS Applied Materials & Interfaces,* **2020**, *12*(29), 33386–33396.

55. K.-P. Yuan, L.-Y. Zhu, J.-H. Yang, C.-Z. Hang, J.-J. Tao, H.-P. Ma, A.-Q. Jiang, D. W. Zhang, H.-L. Lu. Precise preparation of WO_3@SnO_2 core shell nanosheets for efficient NH_3 gas sensing, *Journal of Colloid and Interface Science,* **2020**, *568*, 81–88.

56. L.-W. Mao, L.-Y. Zhu, T. T. Wu, L. Xu, X.-H. Jin, H.-L. Lu. Excellent long-term stable H_2S gas sensor based on Nb_2O_5/SnO_2 core-shell heterostructure nanorods, *Applied Surface Science,* **2022**, *602*, 154339.

57. Y.-C. Liang, W.-K. Liao, S.-L. Liu. Performance enhancement of humidity sensors made from oxide heterostructure nanorods via microstructural modifications, *RSC Advances,* **2014**, *4*(92), 50866–50872.

58. C. Marichy, N. Donato, M. Latino, M. G. Willinger, J.-P. Tessonnier, G. Neri, N. Pinna. Gas sensing properties and P-Type response of ALD TiO_2 coated carbon nanotubes, *Nanotechnology,* **2015**, *26*(2), 024004.

59. M. H. Raza, N. Kaur, E. Comini, N. Pinna. Toward optimized radial modulation of the space-charge region in one-dimensional SnO_2–NiO core–shell nanowires for hydrogen sensing, *ACS Applied Materials & Interfaces,* **2020**, *12*(4), 4594–4606.

60. M. H. Raza, K. Movlaee, S. G. Leonardi, N. Barsan, G. Neri, N. Pinna. Gas sensing of NiO-SCCNT core–shell heterostructures: optimization by radial modulation of the hole-accumulation layer, *Advanced Functional Materials,* **2020**, *30*(6), 1906874.

61. C. Lou, H. Pan, H. Mei, G. Lu, X. Liu, J. Zhang. Low coordination states in Co_3O_4/NiOx

heterostructures by atomic layer deposition for enhanced gas detection, *Chemical Engineering Journal,* **2022**, *448*, 137641.

62. J.-H. Kim, A. Katoch, S.-H. Kim, S. S. Kim. Chemiresistive sensing behavior of SnO_2 (n)–Cu_2O (p) core–shell nanowires, *ACS Applied Materials & Interfaces,* **2015**, *7*(28), 15351–15358.

63. M. H. Raza, N. Kaur, E. Comini, N. Pinna. SnO_2/SiO_2 1D core/shell nanowires heterostructures for selective hydrogen sensing, *Advanced Materials Interfaces,* **2021**, *8*(17), 2100939.

64. Y.-H. Lin, Y.-C. Hsueh, P.-S. Lee, C.-C. Wang, J. M. Wu, T.-P. Perng, H. C. Shih. Fabrication of tin dioxide nanowires with ultrahigh gas sensitivity by atomic layer deposition of platinum, *Journal of Materials Chemistry,* **2011**, *21*(28), 10552–10558.

65. V. V. Kondalkar, L. T. Duy, H. Seo, K. Lee. Nanohybrids of Pt-functionalized Al_2O_3/ZnO core–shell nanorods for high-performance MEMS-Based acetylene gas sensor, *ACS Applied Materials & Interfaces,* **2019**, *11*(29), 25891–25900.

66. S. Lee, Y. Kang, J. Lee, J. Kim, J. W. Shin, S. Sim, D. Go, E. Jo, S. Kye, J. Kim, J. An. Atomic layer deposited Pt nanoparticles on functionalized MoS_2 as highly sensitive H_2 sensor, *Applied Surface Science,* **2022**, *571*, 151256.

67. M. Weber, J.-Y. Kim, J.-H. Lee, J.-H. Kim, I. Iatsunskyi, E. Coy, P. Miele, M. Bechelany, S. S. Kim. Highly efficient hydrogen sensors based on Pd nanoparticles supported on boron nitride coated ZnO nanowires, *Journal of Materials Chemistry A,* **2019**, *7*(14), 8107–8116.

68. Z. Li, C. Lou, G. Lei, G. Lu, H. Pan, X. Liu, J. Zhang, Atomic layer deposition of Rh/ZnO nanostructures for anti-humidity detection of trimethylamine, *Sensors and Actuators B: Chemical,* **2022**, *355*, 131347.

69. A. Rosental, A. Tarre, A. Gerst, J. Sundqvist, A. Hårsta, A. Aidla, J. Aarik, V. Sammelselg, T. Uustare. Gas sensing properties of epitaxial SnO_2 Thin films prepared by atomic layer deposition, *Sensors and Actuators B: Chemical,* **2003**, *93*(1–3), 552–555.

70. X. Du, S. M. George. Thickness dependence of sensor response for co gas sensing by tin oxide films grown using atomic layer deposition, *Sensors and Actuators B: Chemical,* **2008**, *135*(1), 152–160.

71. A. J. Niskanen, A. Varpula, M. Utriainen, G. Natarajan, D. C. Cameron, S. Novikov, V. M. Airaksinen, J. Sinkkonen, S. Franssila. Atomic layer deposition of tin dioxide sensing film in microhotplate gas sensors, *Sensors and Actuators B: Chemical,* **2010**, *148*(1), 227–232.

72. S. Boyadjiev, V. Georgieva, L. Vergov, Z. Baji, F. Gáber, I. M. Szilágyi. Gas sensing properties of very thin TiO_2 films prepared by atomic layer deposition (ALD), *Journal of Physics: Conference Series,* **2014**, *559*, 012013.

73. O. Lupan, V. Postica, N. Ababii, T. Reimer, S. Shree, M. Hoppe, O. Polonskyi, V. Sontea, S. Chemnitz, F. Faupel, R. Adelung. Ultra-Thin TiO_2 films by atomic layer deposition and surface functionalization with au nanodots for sensing applications, *Materials Science in Semiconductor Processing,* **2018**, *87*, 44–53.

74. S. I. Boyadjiev, V. Georgieva, R. Yordanov, Z. Raicheva, I. M. Szilágyi. Preparation and characterization of ALD deposited ZnO Thin films studied for gas sensors, *Applied Surface Science,* **2016**, *387*, 1230–1235.

75. Y. Xu, W. Zheng, X. Liu, L. Zhang, L. Zheng, C. Yang, N. Pinna, J. Zhang. Platinum single atoms on tin oxide ultrathin films for extremely sensitive gas detection, *Materials Horizons,* **2020**, *7*(6), 1519–1527.

76. H. Xu, M. K. Akbari, Z. Wei, J. Hu, F. Verpoort, S. Zhuiykov. Plasma-induced Sub-10 Nm Au-SnO_2-In_2O_3 heterostructures fabricated by atomic layer deposition for highly sensitive ethanol detection on ppm level, *Applied Surface Science,* **2021**, *563*, 150400.

https://doi.org/10.52111/qnjs.2023.17501

TẠP CHÍ KHOA HỌC
TRƯỜNG ĐẠI HỌC QUY NHƠN

Máy phát điện ma sát nano: giải pháp tiềm năng cho năng lượng hiện đại

Phan Hải[1,2,*], Nguyễn Hữu Đức[3], Phạm Đức Thắng[4]

[1]Trường Đại học Công nghệ, Đại học Quốc gia Hà Nội, Việt Nam
[2]Phòng thí nghiệm trọng điểm công nghệ Micro/nano, Đại học Quốc gia Hà Nội, Việt Nam
[3] Đại học Quốc gia Hà Nội, Việt Nam
[4]Trường Đại học Phenikaa, Việt Nam

Ngày nhận bài: 07/03/2023; Ngày sửa bài: 26/08/2023; Ngày nhận đăng: 28/08/2023; Ngày xuất bản: 28/10/2023

TÓM TẮT

Cuộc khủng hoảng năng lượng toàn cầu kéo theo sự quan tâm lâu dài tới sự đổi mới khoa học và công nghệ. Ở bình diện toàn cầu, các nhiên liệu hóa thạch truyền thống như than đá, dầu và khí đang dần bị kiệt quệ do sự công nghiệp hóa và đô thị hóa nhanh chóng. Vì những đặc tính này, việc tìm kiếm các nguồn năng lượng nhân tạo sạch và tái tạo luôn là một ưu tiên hàng đầu của các nhà khoa học để hướng đến sự phát triển bền vững của xã hội. Máy phát điện ma sát nano (TENG) đã được giới thiệu vào năm 2012 bởi nhóm nghiên cứu của Wang. Kể từ đó, một loạt các thiết kế máy phát điện nano đã chứng minh tiềm năng ứng dụng và những lợi thế độc đáo. TENG cũng đã chứng minh tiềm năng trong việc chuyển đổi năng lượng cơ học thành năng lượng điện bằng cách thu thập nhiều dạng năng lượng cơ học xung quanh. Hoạt động của TENG phụ thuộc vào hiệu ứng ma sát điện, gây ra tĩnh điện giữa hai bề mặt vật liệu khi tiếp xúc. Do đó, TENG được coi là một loại "máy phát điện nano" do sự phụ thuộc vào ma sát điện nano và dòng dịch chuyển do tĩnh điện gây ra trong quá trình hoạt động. Trong bài báo này, lý thuyết cơ bản, các thí nghiệm và ứng dụng của TENG được nêu rõ như một nền tảng cho năng lượng của thời đại mới.

Từ khóa: *Máy phát điện, ma sát điện, chuyển đổi năng lượng.*

**Tác giả liên hệ chính.*
Email: phanhaik53v@gmail.com

QUY NHON UNIVERSITY
JOURNAL OF SCIENCE

Triboelectric nanogenerator: the promising solution for modern energy

Phan Hai[1,2,*], Nguyen Huu Duc[3], Pham Duc Thang[4]

[1]VNU University of Engineering and Technology, Vietnam
[2]Key laboratory for micro and nano technology, Vietnam National University, Hanoi, Vietnam
[3]Vietnam National University, Hanoi, Vietnam
[4]Phenikaa University, Vietnam

Received: 07/03/2023; Revised: 26/08/2023; Accepted: 28/08/2023; Published: 28/10/2023

ABSTRACT

The global energy crisis is accompanied by the long-term interest of scientific and technological innovation. At the macro level, traditional fossil fuels such as coal, oil and gas are gradually being exhausted due to rapid industrialization and urbanization. Because of these characteristics, the search for clean and renewable sources of artificial energy is always a top priority of scientists to aim at sustainable development of the society. Since the introduction of triboelectric nanogenerators (TENG) by Z. L. Wang group in 2012, a wide range of nanogenerator designs have proven application potentials and unique advantages. TENG have also demonstrated potentials in mechanical energy to electrical energy conversion by capturing many forms of ambient mechanical energy. The operation of TENG depends on the effect of electric friction, which induces static electricity between two material surfaces when being in contact. Therefore, TENG are considered as a kind of "nanogenerators" due to their dependence on electrostatically induced nano-electrical friction and displacement currents during operation. In this paper, the fundamental theory, experiments, and applications of TENG are reviewed as a foundation of the energy for the new era.

Keywords: *Generator, triboelectric, energy conversion.*

1. INTRODUCTION

Mechanical energy is the most common source of energy existing around us. It can be in the form of human movement, breathing, heartbeat or vehicle movement, the shaking of things such as leaves or waves. In essence, these mechanical energies are the result of the conversion of energy from one form to another. For example, the energy that exists internally in fuels such as gasoline is converted into the mechanical energy that drives the vehicle when it is burned in the fuel chamber. The motion of the car just mentioned is one of the examples showing that mechanical energies around us can be generated from simple small parts of life with specific purposes. In the process of producing these energies, there are many techniques that can be developed to capture and use them for necessary human activities or convert them directly into electricity.

Electromagnetic induction is the scientific basis for most electric generators. The

**Corresponding author.*
Email: phanhaik53v@gmail.com

https://doi.org/10.52111/qnjs.2023.17502

operating principle of the generator is based on the phenomenon of electromagnetic induction namely Faraday's law. That law states that when the magnetic flux through a coil and changes due to the external mechanical forces, an induced current will be introduced inside. This principle is widely used in devices that capture energy from the surrounding environment. The traditional electromagnetic generator structure consists of the following parts:

The generator has the function of generating electromagnetic energy from the raw material supplied to the machine. The generator is composed of two main parts, the inductor (roto) and the armature (stator). These two small parts work in harmony with each other to create motion between electromagnetic and electrical.

- Stator - armature: consists of coils of the same shape and size, the number of turns is also the same.

- Roto - inductor: consists of an electromagnet (powered by 1-way oscillations) rotating around a fixed axis. The rotor's job is to generate a variable magnetic field.

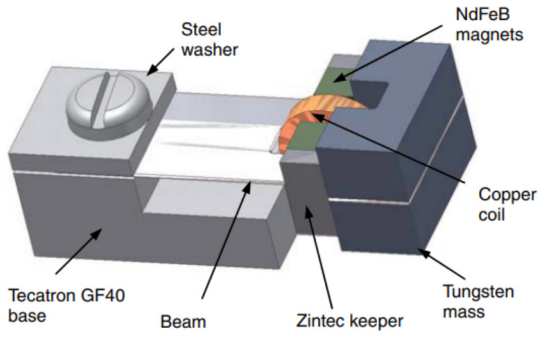

Figure 1. Micro generator structure based on electromagnetic induction.[1]

Most studies on small/tiny power generators based on electromagnetic induction are also conducted. A good example of a generator based on electromagnetic induction is the generator developed by Beeby's research group with the structure shown in Figure 1. The structure of this device consists of four magnets attached to the tip of the vibrating blade. When the unit is in operation, the generator generates a maximum power of 46 μW from 60 mg of acceleration at an external load of 4000 Ω. The power density can be calculated as approximately 307 W/m^3. Energy conversion efficiency is about 30%.

The drawback of generators based on electromagnetic induction effect is the need for large magnets, resulting in large size and unsuitable for mobile applications.

Piezoelectric generator

The piezoelectric effect is one of the most popular and widely studied effects in the field of energy conversion. Devices that collect energy based on the piezoelectric effect operate on the piezoelectric properties of the materials they use. The piezoelectric effect in each material is described as the phenomenon in which a material generates an electrical charge (or potential difference) when acted upon by a mechanical stress. Some popular piezoelectric materials are studied and used such as quartz, Lead Zirconate Titanate (PZT), Zinc oxide (ZnO) or Polyvinylidene Fluoride (PVDF). These materials have been widely used to fabricate MEMS microelectromechanical systems and large piezoelectric energy collectors. In the last few years, along with the concept of micro/nano effect generator, piezoelectric materials have also been used to fabricate power converters based on the micro/nano piezoelectric effect.[2-6]

Electrostastic Induction generator

Electrostatic induction-based generators were one of the first human electromechanical energy conversion technologies in which a differential voltage was generated between two sheets of material leading to induced electrification static electricity.[7-10] The best example of electrostatic induction-based generators are those that use Electret, which is a polymer that can hold electrostatic charges on their surfaces almost permanently. Before operating the device, a surface charge process is

carried out to create electrostatic charges on the surface of the electret. As the electret material moves, the electrostatic effect directs the electrons to move between the two electrodes under short-circuit conditions.

2. GENERATOR BASED ON TRIBOELECTRIC EFFECT

In recent years, a new electromechanical energy conversion mechanism named triboelectric generation has been developed as a new method for electromechanical energy conversion.[11]

2.1. Triboelectric effect and Triboelectric nanogenerator

The Triboelectric effect (TE) is a classic physical phenomenon in which two dissimilar materials become electrically charged after rubbing against each other under the action of an external force. In human life, the electric friction effect occurs everywhere in the form of Contact Electrification (CE), on many kinds of things and manifests itself in the electrostatic phenomenon.[12]

The electric friction effect is one of the classic physical phenomena that has been explored for thousands of years. Although triboelectric effect is encountered every day, the mechanism of electric friction is still being studied. In general, scientists think that when two different materials physically rub together, a chemical bond is formed between some parts of the two planes and is collectively known as adhesion.[13] Then, the charges will move from one material to another to balance their electrochemical potential. Those displaced charges can be electrons, ions, or material molecules. When the two materials are no longer rubbing against each other, some of the chemical bond atoms tend to retain electrons and a few other bonded atoms tend to give away electrons, thereby generating electric friction charges on the surface of materials.

The electric friction charge density is the most important value that determines the output signal of the nano friction generator. However, the origin of the electric friction charges or in other words the origin of the electric friction mechanism is not really clear, especially when the structure of TENG always contains at least one insulating material or polymer. Controversy surrounds the electric charge due to friction as a result of ion-electron transfer. The phenomenon of electrification due to friction is a very common one that can occur with a variety of materials, such as solid - solid, solid - liquid, solid – gas, etc. Therefore, the in-depth study of the phenomenon of electric charge due to friction will make a great contribution to the development of physics - chemistry - biology.

Wang and co-workers found that the mechanism of CE between two solids is ion exchange.[14] Considering specifically for the case of a pair of triboelectric materials, a conductive and an insulator, surface state and Fermi level models were used to verify the above conclusion. If the distance between two materials is greater than the bond length (BE), the two atoms tend to attract each other. Experimental studies indicate that CE can only occur when the atomic distance is shorter than the bond length. To account for the exchange of electrons between two substances, electron cloud cover is used as shown in Figure 2. Figure 2a simulates the electron cloud of two materials before rubbing together. When two atoms of different matter come closer and rub against each other, a more electron cloud will cover the junction of the two electrons under the action of a force leading to a lowering of the potential barrier and allowing electrons move between the two atoms (Figure 2b). Mechanical force is essential to close the intraatomic gap and maximize electron cloud cover (Figures 2c and 2d).

https://doi.org/10.52111/qnjs.2023.17502

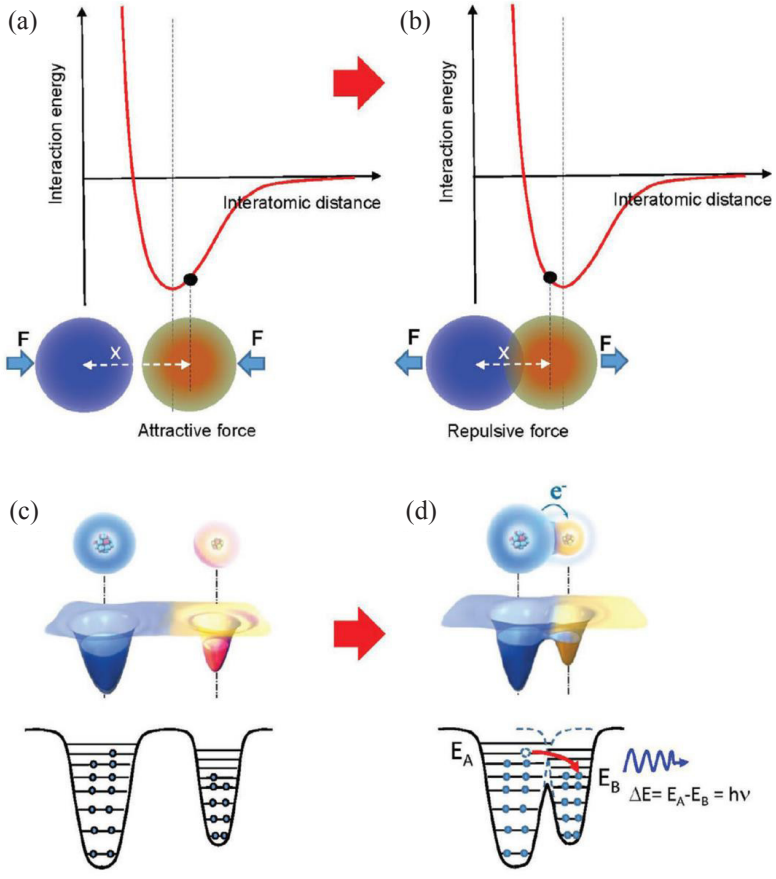

Figure 2. The process of electrification due to the friction of a pair of triboelectric materials.[14]

Besides, photon emission is also believed to exist during CE and is being investigated for clarification. CE between solid and liquid materials has been studied and is thought to include two steps. The first step is the exchange of electrons between the solid and liquid material. The second step is the interaction between the different ions in the liquid. In research practice, ion absorption and electron exchange occur and exist at the liquid and solid interface.

2.2. The popular electrical friction materials

All materials known to man have tribological properties, including metals and polymers, fabrics, wood, etc. Therefore, all such materials can be suitable material objects for TENG studies in specific cases and also confirm the material choice for ghost generator application. nanoscale is extremely abundant.

However, whether that electric friction property is strong or weak depends greatly on the charge polarity of each material. Materials with strong tribological properties are usually low conductivity or dielectric. As a result, these materials tend to retain charges that travel between two material surfaces and retain those charges for long periods of time, resulting in the generation of electrostatic charges, which are causes of negative effects in daily life and the development of technology. The most obvious is the electric shock when touching the winter doorknob or sucking hair into nylon fabrics, etc. The positive/negative character of the charge generated by friction on materials depends on the intrinsic electrical polarity of the material relative to the material that is rubbing against it.

Table 1. Comparison chart of electric friction properties of common materials.[15]

Materials	Abbr.	Average TECD ($\mu C\ m^{-2}$)
Chemical-Resistant Viton® Fluoroelastomer Rubber		−148.20
Acetal		−143.33
Flame-retardant garolite		−142.76
Garolite G-10		−139.89
Clear cellulose		−133.30
Clear polyvinyl chloride	PVC	−117.53
Polytetrafluoroethylene	PTFE	−113.06
Abrasion-resistant polyurethane rubber		−109.22
Acrylonitrile butadiene styrene	ABS	−108.07
Clear polycarbonate (Glossy)	PC	−104.63
Polystyrene	PS	−103.48
Ultem polyetherimide	PEI	−102.91
Polydimethylsiloxane*	PDMS	−102.05
Polyester fabric (Plain)		−101.48
Easy-to-machine electrical-insulating garolite		−100.33
Food-grade high-temperature silicone rubber		−94.03
Polyimide film	Kapton	−92.88
DuraLar polyester film	PET	−89.44
Polyvinylidene fluoride	PVDF	−87.35
Polyetheretherketone	PEEK	−76.25
Polyethylene	PE	−71.20
High-temperature silicone rubber		−69.95
Wear-resistant garolite		−68.51
Low-density polyethylene	LDPE	−67.94
High impact polystyrene		−67.37
High-density polyethylene	HDPE	−59.91
Weather-resistant EPDM rubber		−53.61
Leather strip (Smooth)		−52.75
Oil-filled cast nylon 6		−49.59
Clear cast acrylic	PMMA	−48.73
Silicone		−47.30
Abrasion-resistant SBR rubber		−40.13
Flexible leather strip (Smooth)		−34.40
Noryl polyphenyl ether		−31.82
Poly(phenylene Sulfide)	PPS	−31.82
Pigskin (Smooth)		−30.10
Polypropylene	PP	−27.23
Slippery nylon 66		−26.09
Weather- and chemical-resistant santoprene rubber		−25.23
Chemical- and steam-resistant aflas rubber		−22.65
Polysulfone		−18.92
Cast nylon 6		−18.35
Copy paper		−18.35
Chemical-resistant and low-temperature fluorosilicone rubber		−18.06
Delrin® Acetal Resin		−14.91
Wood (marine-grade plywood)		−14.05
Wear-resistant slippery garolite		−11.47
Super-stretchable and abrasion-resistant natural rubber		−10.61
Oil-resistant buna-N rubber		2.49
Food-grade oil-resistant buna-N/vinyl rubber		2.95

2.3. Capacitance characteristics of TENG

The working principle of TENG is a combination of the effect of electric friction and electrostatic induction. While electrical friction induces electrostatic charge polarization, electrostatic induction is the main mechanism for converting mechanical energy into electrical energy based on the existence of electrostatic charge that has

formed under the action of magnetism close to electricity. Studies on devices that operate on the electrostatic principle have shown that the formation of capacitors is the nature of the device, therefore, TENG also has inherent capacitive behavior/characteristics of current. electrostatic phenomena in matter.[15]

In order to clarify the inherent capacitive behavior of TENG, a simple structure of TENG consisting of a pair of electric friction (two different materials) is used for the analysis. Let the distance between two opposite surfaces of the materials be x, and suppose the charge passing through the two electrodes at the moment of consideration is Q and –Q, the potential difference between the two electrodes is contributed from two parts. The first part is the polarization of the charge generated by the electric friction process $V_{OC}(x)$. Besides, the displaced charge Q also contributes to the formation of this potential difference. If assuming that the charges caused by electric friction do not exist, then the electric friction pair structure is a mere capacitor, then the contribution of Q is calculated as –Q/C(x) where C is capacitance of the capacitor between two electrodes. Based on the principle of electric field superposition, the total potential difference between the two electrodes is:

$$V = -1/C(x)\ Q + V_{OC}(x) \quad (1)$$

The above equation is the basic equation for all TENGs and shows the capacitive nature of this type of device. During the operation of the TENG, the separation of the electric friction charges will form the potential difference between the two electrodes. If an external circuit is connected between the two electrodes, this potential difference will cause electrons to move from one electrode to another in order to balance the potential difference between the two electrodes. Under short circuit conditions (Short Circuit (SC), QSC balances the potential difference created by the electric friction charge polarization. From there, the QSC calculated from formula (1) is:

$$Q_{SC}(x) = C(x).V_{OC}(x) \quad (2)$$

The equivalent circuit of TENG is described as follows

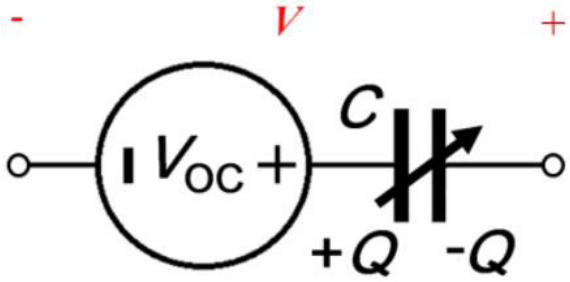

Figure 3. Analog circuit showing the intrinsic characteristics of TENG.[16]

The impedance of the TENG is mostly the capacitance of the internal capacitor. With TENG designs, the intrinsic resistance of the device is almost immeasurable because of the mandatory insulation between the two electrodes. Therefore, in the equivalent circuit structure of TENG, this part of the resistance is ignored.

3. THE BASIC MECHANISM OF TENG

The basic model of TENG was first built with the structure shown in Figure 4. This structure uses two material sheets, Kapton and Polymethyl Methacrylate (PMMA) placed opposite each other, and metal electrodes coated on the other side of them. Figures 4a and 4b show how TENG operates under open circuit (OC) and short circuit (SC) conditions.

As shown in Figure 4a, in the initial state, no charge is generated or applied, and there is no potential difference between the two electrodes (Figure 4a-I). With a displacement by an external force, the two polymers are brought into contact. The charge moves across the surface at the contact area due to the effect of electric friction. The magnetic charge is injected (PMMA) into the Kapton, resulting in a negative charge at the Kapton surface and a positive charge at the PMMA surface. It is remarkable that the insulating properties of the polymers allow the retention of high charges for long periods of time for hours or even days. As confined to the surface, opposite charges are almost in the same plane, practically producing no potential difference between the two electrodes (Figure 4a-II).

When the generator starts working, the Kapton pad tends to return to its original position due to its own resilience. When the two polymers separate, a potential difference is established between the two electrodes under open circuit conditions due to the charges separating during friction (Figure 4 a-III).

When the generator is active, Voc continues to increase until it reaches the maximum value when the Kapton membrane returns to its original state (Figure 4a-IV, V). Such a signal will be constant provided that the input impedance of the galvanometer is infinitely large. Once pressed immediately, the potential difference starts to decrease as the two polymer layers get closer together. As a result, the V_{OC} decreased from the maximum value to zero when the two polymers were in full contact again (Figure 4a-V, VI).

If in the short-circuited state, a voltage difference is established as the two polymer sheets separate electrons from the upper electrode to the lower electrode (Figure 4b-III), resulting in an instantaneous current during the dissolution process. zoom (Figure 4b-IV). When we press the transmitter again, reducing the distance between the layers will cause the upper electrode to have a higher potential than the lower electrode. As a result, electrons are directed from the lower electrode back to the upper electrode, reducing the number of induced charges (Figure 4b-VI). This process corresponds to an instantaneous reverse current (Figure 4b-V). When the two polymers are in contact again, all induced charges are neutralized (Figure 4b-II). By explaining the above operating principle, it can be seen that the signal of TENGs has the form of alternating pulses.

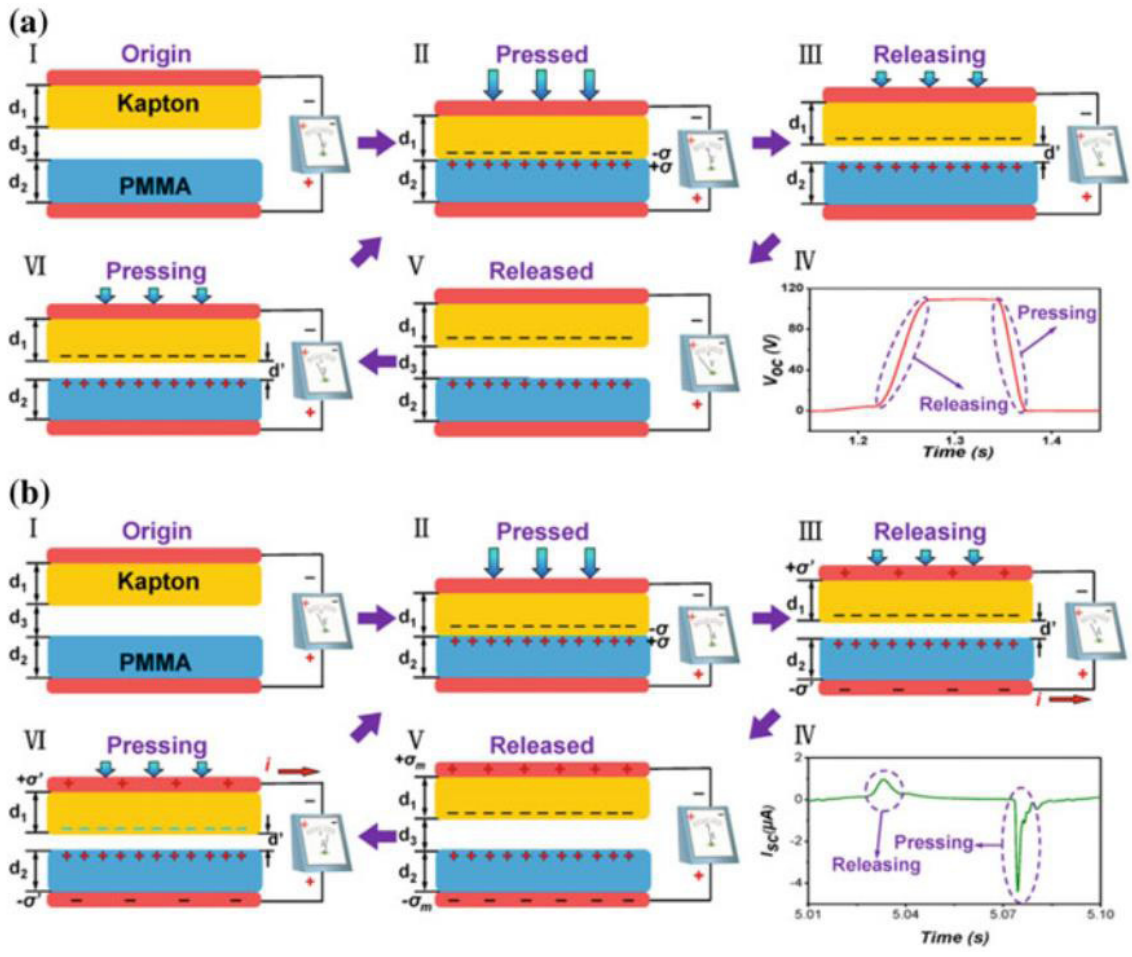

Figure 4. Working mechanism of TENG in (a) circuit conditions and (b) short circuit conditions.[16]

https://doi.org/10.52111/qnjs.2023.17502

Based on the basic principle, scientists have divided into four different TENG modes as follows:

3.1. Vertical contact mode

The simplest design model of TENG is detailed in Figure 5. In this structure, two different insulating materials (or an insulator and a conductive material) are placed opposite (collectively, the triboelectric material). Each layer of insulation is covered with a metal electrode on the other side. When two layers of materials come to rub together in a perpendicular direction under the action of an external force, an electric friction charge will be generated at the surface of those two layers of material. Once the external force is removed, the two layers of material tend to separate and the distance between them gradually increases. Then, a potential difference between the two surfaces of the material will be generated, and, if the two electrodes are connected through an electrical circuit, the free charges generated in each electrode will move through the circuit to balance, which is equal to the electric friction potential mentioned above. When the distance between the two rods returns to zero, the electric friction potential disappears and the electrons move in the opposite direction again.[17]

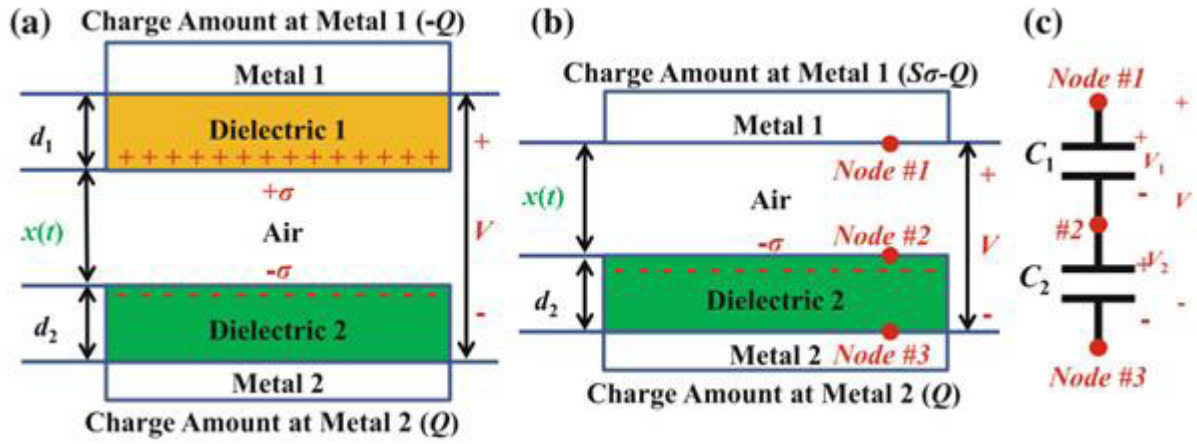

Figure 5. Detailed structure of TENG (a) using pairs of insulating materials and (b) using pairs of insulating and conductive materials. (c) Equivalent circuit of TENG using an insulating-conductive pair.[17]

Based on the types of electric friction materials shown in Figure 1.6, the vertical contact mechanism nano friction generators are divided into two main types: TENG using a pair of insulating materials (Figure 5a) and TENG using a pair of insulating and conductive materials (Figure 5b).

3.2. Horizontal sliding mode

Similar to the vertical contact mode, the horizontal slide mode also starts with two rods of different electro-frictional material coated with electrodes on opposite sides. Figure 6 describes the structure of STENG in detail according to the types of pairs of electric friction materials used. Initially, two rods of material are placed exactly on top of each other. When the external force causes them to slide relative to each other's surface and generate electric friction charges and charge polarization in the sliding direction, it generates electron flow in the external circuit to balance the generated electric field by electric friction charge. These sliding movements can be sliding in a horizontal plane or sliding in a curved surface.

Different from the vertical friction direction discussed in depth above, this mechanism of the nano friction generator operates in the form of the relative sliding friction of the two materials in the horizontal direction.

The nano friction generator works based on the charge distribution mechanism. In this model, STENG is also divided into two types based on the pair of materials used.

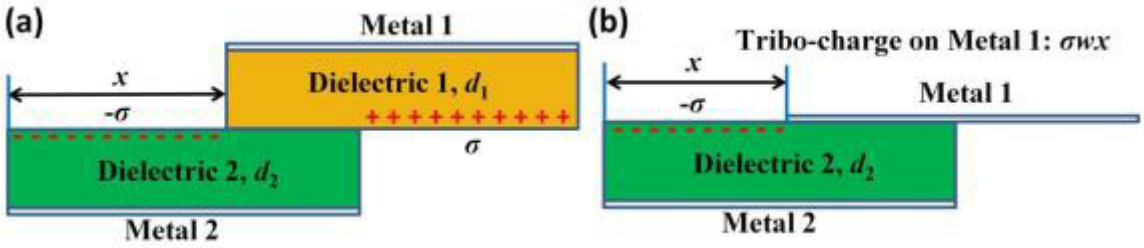

Figure 6. Detailed structure of STENGs (a) using pairs of insulating materials and (b) using pairs of insulating and conductive materials.[17]

Structural analysis uses two types of insulating materials as electrical friction materials, assuming the width w of the material layers is much larger than their respective thicknesses as shown in the figure. The length dimensions of the two insulating layers are l and their respective thicknesses are d1 and d2. Two metal electrodes are made on their remaining surfaces. If considered in the initial state, the two layers of material almost coincide, then when they start to move to rub horizontally, the rubbing distance is called x. At that time, the contact surface of the two materials will be charged oppositely at the non-contact surface due to the effect of electric friction. Assuming that the electric friction charges are evenly distributed at these two surfaces, let the electric friction charge density at the surface of material 1 and - is the electric friction charge density at the surface of the object. The electric friction charge density in the overlapping area can be considered as o because the distance between them is close to each other.

3.3. Single electrode mode

The vertical contact and sliding mode TENG discussed above always require insulating materials with respective electrodes coated on the opposite surface. To overcome this weakness, several structures of TENG have been studied and completely ignored the relative motion of the electrodes. One of these two models is called single-electrode-mode nano-friction generators (Single Electrode TENG – SETENGs). In this section, the basic working mechanism of SETENGs will be discussed in detail.

Many studies have been conducted to demonstrate the usability of SETENGs. In this structure, only one electrode is coated on the surface of a triboelectric material (primary electrode). Another electrode called the reference electrode is placed in any position or grounded. The two electrodes mentioned above have different roles. Similar to the two TENGs above, SETENGs have two modes of vertical contact and sliding mode with almost the same characteristics. Here, our research focuses mainly on the vertical exposure mode SETENGs.

The figure below shows the structure of SETENGs using a pair of conductive and insulating materials. In it, an insulator and a conductive sheet of length l and width w are placed opposite each other with a distance x to form an electric friction pair. The insulating layer has a thickness of d1 and the conductive layer has a thickness of dm. The reference electrode is about the same size as the primary electrode and is separated by a distance of g from the primary electrode.

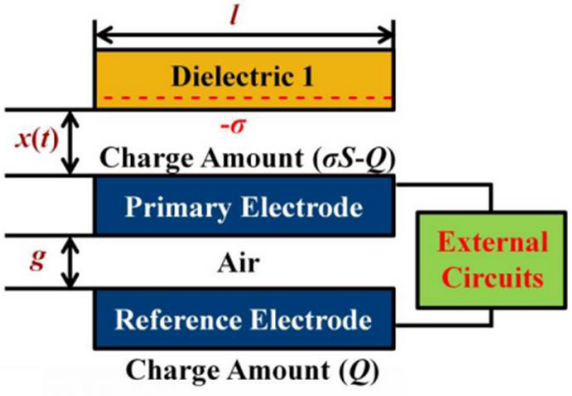

Figure 7. Basic theoretical model of SETENG.[18]

https://doi.org/10.52111/qnjs.2023.17502

The two electrodes are fixed in position while the insulator plate can be easily moved vertically under external force. As an inevitable result of the process of electrification due to friction, when two layers of triboelectric materials rub together, the surface of the insulating sheet becomes negatively charged with a surface charge density of –σ. Assuming that the electric friction charge is evenly distributed over the surface on a large scale, then the charge charged on the surface of the insulator is σwl. Let Q be the charge that moves from the primary charge to the counter charge, the charges at those two electrodes are σwl-Q and Q, respectively.

3.4. Freestanding electrode mode

In reality, a moving object cannot avoid becoming electrified by rubbing against other potential bodies or air. These charges remain on the surface for hours. If a pair of symmetric electrodes are placed underneath and of a size-distance equivalent to that of the insulating rod, the relative near- and far-away movements of the insulating material cause the induced charges at the difference between the two electrodes leads to an electric current flowing between the two electrodes to balance the difference.

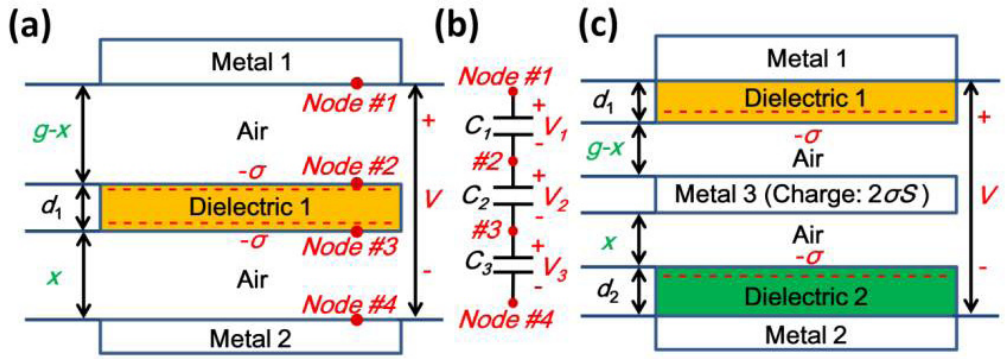

Figure 8. Basic theoretical model of FETENG.[19]

Vertical contact suspension electrode mode of TENG (Freestading TENG – FSTENG) suspension electrode model is described as shown in Figure 8. An insulating sheet of thickness d1 with an insulation constant of εr1 and two metal plates are placed opposite each other and form pairs of electric friction materials. These two metal plates also serve as two electrodes. The space between the two electrodes is called g. When an insulating sheet is subjected to an external force and comes into contact with two metal plates, both sides of it will be charged due to the phenomenon of electric friction. Assuming this surface charge density is –σ on both sides, at the same time the two metal plates will have the same amount of positive charge.

4. Performance enhancement methods

Experimental and theoretical studies on TENG have shown that the electric friction charge density is the main factor that directly affects the performance of the TENG. In order to increase the density of electric friction charge, the commonly used methods are: treatment of material composition, increase of local contact area and change of environmental conditions.

Material composition handling

Surface chemical functional group treatment is a method which changes the functional groups coated on the friction surface to enhance the ability of the material surface to capture the charge during the electric friction process.[20] Zhong Lin Wang's group employed this method when using functional groups (–NH_2) introduced into the surface of Au. In this way, the output signal of TENG greatly increased. If the group (-NH_2) is replaced by the group (–Cl), the performance of TENG is much worse.

Increase the contact area by surface modification

The local contact area between two layers of materials can be significantly increased with surface modification by creating micro-nanostructures on their surface. The two layers of materials can then come into deeper, more frictional contact because the surface structure allows for such a higher level of contact. Surface structures exploited include nanowires, cubic, pyramidal, and nanofiber surface structures. Surface treatment technologies are used such as chemical etching,[21] plasma-electron-ray etching,[22,23] lithography - lithography,[24] fusion molding,[25] or femtolaser,[26] etc. All the methods mentioned significantly increase the efficiency of TENG from 3 to 21 times.

Changing environmental conditions

This method deals with influencing factors in the operating environment of TENG such as temperature or pressure, humidity, etc. Studies[26-29] have shown the effect of temperature on the performance of TENG using teflon, showing that the TENG in this study can perform well and stably in the temperature range from 20 ^{o}C to 100 ^{o}C. The temperature dependence of the performance is related to the dielectric coefficient and to the surface deterioration of the material under high temperature such as oxidation of the surface matter or the reduction of fluorine radicals.

According to studies, the main application directions of TENGs can be divided into four different areas including: micro-nano-scale energy sources for self-powered devices system; active sensors for biomedical, human-machine, human-machine interaction applications; low frequency mechanical energy harvesting equipment system; and power supplies for high voltage applications.[30]

5. POTENTIAL APPLICATION MICRO/ NANO ENERGY SOURCE

With the advantages such as light weight, low cost, plenty structural and material choices, TENG possess wide applications as micro power source for self-powered systems by harvest ambient energy, such as human movement, vibration, wind energy or water motion. Because of the outstanding performance at low frequencies, biomechanical energy harvesting using TENG is of great importance and has been explored since the early stages of TENG development.

Active sensing and self-powered sensors

Since TENG can directly convert a mechanical trigger into an electrical signal, it has been extensively studied for use as self-powered sensors, such as touch sensors, acoustic sensors, sensors, motion and acceleration, and even chemical sensors. With the rapid development of technology, the challenges of interaction and power/energy will be limitations for its further advancement.

Blue energy

Among the application of TENG in harvesting natural mechanical energy from wind, raindrop, and ultrasonic, the wave energy in ocean as blue energy is especially important, owing to the higher efficiency of TENG for harvesting low-frequency vibration energy compared with an electromagnetic generator. Compared to other prototypes of TENGs reported for the blue energy, the fully enclosed rolling spherical structure has been identified as the most promising method.

6. CONCLUSION

TENG has become a promising energy conversion technology due to its advantage in fabrication, low-cost, wide choice of materials and high efficiency. TENG operates by the combination of electrostatic induction effects and contact electrification. The ambient mechanical energy are in various forms such as rotation, motion, vibration, impact, etc. The devices structures can be considered in four models: vertical contact mode, sliding mode, freestanding mode and single electrode mode. TENG has many features such as light weight,

https://doi.org/10.52111/qnjs.2023.17502

high output strength and small volume, which makes it very interesting in the field of energy extraction. TENG can be a more efficient good solution for self-powered devices and systems fabrication. Moreover, TENG is expected to be the key technology leading to solution for energy crisis.

REFERENCES

1. S. P. Beeby, R. N. Torah, M. J. Tudor, P. Glynne-Jones, T. O'Donnell, C. R. Saha, S. Roy. A micro electromagnetic generator for vibration energy harvesting, *Journal of Micromechanics Microengineering*, **2007**, *17*(7), 1257-1265.
2. X. Niu, W. Jia, S. Qian, J. Zhu, J. Zhang, X. Hou, J. Mu, W. Geng, J. Cho, J. He, X. Chou. High-performance PZT-based stretchable piezoelectric nanogenerator, *ACS Sustainable Chemical Engineering,* **2019**, *7*(1), 979-985.
3. M. P. Lu, J. Song, M. Y. Lu, M. T. Chen, Y. Gao, L. J. Chen, Z. L. Wang. Piezoelectric nanogenerator using p-type ZnO nanowire arrays, *Nano Letter,* **2009**, *9*(3), 1223-1227.
4. A. Arnau, D. Soares. Fundamentals of piezoelectricity, *Piezoelectric Transducers and Applications,* **2008**, 1-38.
5. Z. L. Wang, J. Song. Piezoelectric nanogenerators based on zinc oxide nanowire arrays, *Science*, **2006**, *312*(5771), 242-246.
6. C. Chang, V. H. Tran, J. Wang, Y. K. Fuh, L. Lin. Direct-write piezoelectric polymeric nanogenerator with high energy conversion efficiency, *Nano Letter,* **2010**, *10*(2), 726-731.
7. R. Tashiro, N. Kabei, K. Katayama, F. Tsuboi, K. Tsuchiya. Development of an electrostatic generator for a cardiac pacemaker that harnesses the ventricular wall motion, *Journal of Artificial Organs,* **2002**, 0239-0245.
8. Y. Xie, D. Bos, L. J. D. Vreede, H. L. D. Boer, M. J. V. D. Meulen, M. Versluis, A. J. Sprenkels, A. V. D. Berg, J. C. T. Eijkel. High-efficiency ballistic electrostatic generator using microdroplets, *Nature Communication*, **2014**, 1-5.
9. G. Zhu, Y. S. Zhou, P. Bai, X. S. Meng, Q. Jing, J. Chen, Z. L. Wang. A shape-adaptive thin-film-based approach for 50% high-efficiency energy generation through micro-grating sliding electrification, *Advanced Materials*, **2014**, *26*(23), 3788-3796.
10. F. R. Fan, Z. Q. Tian, Z. Lin Wang. Flexible triboelectric generator, *Nano Energy*, **2012**, *1*, 328–334.
11. S. Pan, Z. Zhang. Fundamental theories and basic principles of triboelectric effect: A review, *Friction*, **2019**, *7*, 2-17.
12. J. J. Shao, T. Jiang, Z. L. Wang. Theoretical foundations of triboelectric nanogenerators (TENGs), *Science China Technological Sciences,* **2020**, *63*, 1087-1109.
13. Z. L. Wang, A. C. Wang. On the origin of contact-electrification, *Materials Today*, **2019**, *30*, 34-51.
14. Z. L. Wang. On Maxwell's displacement current for energy and sensors: The origin of nanogenerators, *Materials Today*, **2017**, *20*(2), 74-82.
15. Z. L. Wang, L. Lin, J. Chen, S. Niu, Y. Zi. Triboelectric nanogenerator: Vertical contact-separation mode, scientific report, *Triboelectric Nanogenerator,* Springer, 2016, 23-47.
16. S. Wang, L. Lin, Y. Xie, Q. Jing, S. Niu, Z. L. Wang. Sliding-triboelectric nanogenerators based on in-plane charge-separation mechanism, *Nano Letter,* **2013**, *13*(5), 2226-2233.
17. S. Niu, Y. Liu, S. Wang, L. Lin, Y. S. Zhou, Y. Hu, Z. L. Wang. Theoretical investigation and structural optimization of single-electrode triboelectric nanogenerators, *Advanced Functional Materials,* **2014**, *24*(22), 3332-3340.
18. V. -T. Bui, J. -H. Oh, J. -N. Kim, Q. Zhou, D. P. Huynh, I. -K. Oh. Nest-inspired nanosponge-Cu woven mesh hybrid for ultrastable and high-power triboelectric nanogenerator, *Nano Energy*, **2020**, *71*, 104561.
19. H. Phan, D. -M. Shin, S. H. Jeon, T. Y. Kang, P. Han, G. H. Kim, H. K. Kim, K. Kim, Y. H. Hwang, S. W. Hong. Aerodynamic

and aeroelastic flutters driven triboelectric nanogenerators for harvesting broadband airflow energy, *Nano Energy*, **2017**, *33*, 476-484.

20. S. Wang, Y. Zi, Y. S. Zhou, S. Li, F. Fan, L. Lin, Z. L. Wang. Molecular surface functionalization to enhance the power output of triboelectric nanogenerators, *Journal of Materials Chemistry A,* **2016**, *4*(10), 3728-3734.
21. W. Kim, T. Okada, H. W. Park, J. Kim, S. Kim, S. W. Kim, S. Samukawa, D. Choi. Surface modification of triboelectric materials by neutral beams, *Journal of Materials Chemistry A*, **2019**, *7*(43), 25066–25077.
22. C. X. Lu, C. B. Han, G. Q. Gu, J. Chen, Z. W. Yang, T. Jiang, C. He, Z. L. Wang. Temperature effect on performance of triboelectric nanogenerator, *Advanced Engineering Materials,* **2017**, *19*(12), 1700275.
23. C. Wu, A. C. Wang, W. Ding, H. Guo, Z. L. Wang. Triboelectric nanogenerator: A Foundation of the Energy for the New Era, *Advanced Energy Materials*, **2019**, *9*(1), 1802906.
24. S. Wang, L. Lin, Z. L. Wang. Nanoscale triboelectric-effect-enabled energy conversion for sustainably powering portable electronics, *Nano Letter,* **2012***, 12*(12), 6339-6346.
25. J. Huang, X. Fu, G. Liu, S. Xu, X. Li, C. Zhang, L. Jiang. Micro/nano-structures-enhanced triboelectric nanogenerators by femtosecond laser direct writing, *Nano Energy*, **2019**, *62*, 638–644.
26. V. Nguyen, R. Zhu, R. Yang. Environmental effects on nanogenerators, *Nano Energy*, **2014**, *14*, 49-61.
27. V. Nguyen, R. Yang. Effect of humidity and pressure on the triboelectric nanogenerator, *Nano Energy*, **2013**, *2*(5), 604-608.
28. Z. Lin, J. Chen, X. Li, Z. Zhou, K. Meng, W. Wei, J. Yang, Z. L. Wang. Triboelectric nanogenerator enabled body sensor network for self-powered human heart-rate monitoring, *ACS Nano*, **2017**, *11*(9), 8830–8837.
29. S. Y. Chou, P. R. Krauss, P. J. Renstrom. Nanoimprint lithography, *Journal of Vacuum Science & Technology B*, **1996**, *14*, 4129–4133.
30. J. Huang, X. Fu, G. Liu, S. Xu, X. Li, C. Zhang, L. Jiang. Micro/nano-structures-enhanced triboelectric nanogenerators by femtosecond laser direct writing, *Nano Energy*, **2019**, *62*, 638–644.

https://doi.org/10.52111/qnjs.2023.17502

TẠP CHÍ KHOA HỌC
TRƯỜNG ĐẠI HỌC QUY NHƠN

Phát hiện tin giả dựa trên nội dung và ngữ cảnh xã hội sử dụng học máy

Lê Thị Xinh[1,*], Lê Quang Hùng[2], Nguyễn Thị Ngọc Bích[3], Nguyễn Thị Kim Phượng[2], Phạm Trần Thiện[2]

[1]Khoa Sư phạm, Trường Đại học Quy Nhơn, Việt Nam
[2]Khoa Công nghệ thông tin, Trường Đại học Quy Nhơn, Việt Nam
[3]Công ty Fujinet, Bình Định, Việt Nam

Ngày nhận bài: 07/04/2023; Ngày sửa bài: 18/06/2023; Ngày nhận đăng: 06/09/2023; Ngày xuất bản: 28/10/2023

TÓM TẮT

Bài báo này trình bày nghiên cứu về phát hiện tin giả dựa trên nội dung tin và ngữ cảnh xã hội sử dụng học máy. Đầu tiên, chúng tôi phân tích các khái niệm liên quan, các phương pháp phát hiện tin giả. Tiếp theo, chúng tôi mô hình hóa nhiệm vụ này như một bài toán phân lớp nhị phân, biểu diễn nội dung tin và ngữ cảnh xã hội dưới dạng véc-tơ đặc trưng. Sau đó, chúng tôi sử dụng một số thuật toán học máy để xây dựng mô hình phân lớp. Kết quả thực nghiệm với ba thuật toán học máy: Support Vector Machine, Naive Bayes và *k*-Nearest Neighbors trên bộ dữ liệu FakeNewsNet cho thấy hiệu quả của phương pháp đề xuất.

Từ khóa: *Phát hiện tin giả, nội dung tin, ngữ cảnh xã hội, phân lớp, học máy.*

**Tác giả liên hệ chính.*
Email: lethixinh@qnu.edu.vn

https://doi.org/10.52111/qnjs.2023.17503

QUY NHON UNIVERSITY
JOURNAL OF SCIENCE

Fake news detection based on news content and social contexts using machine learning

Le Thi Xinh[1,*], Le Quang Hung[2], Nguyen Thi Ngoc Bich[3], Nguyen Thi Kim Phuong[2], Pham Tran Thien[2]

[1]Faculty of Education, Quy Nhon University, Vietnam
[2]Faculty of Information Technology, Quy Nhon University, Vietnam
[3]Fujinet Company, Binh Dinh, Vietnam

Received: 07/04/2023; Revised:18/06/2023; Accepted: 06/09/2023; Published: 28/10/2023

ABSTRACT

This paper presents research on detecting fake news based on news content and social context approach using machine learning. First of all, we analyze related concepts, methods of detecting fake news. Next, we model this task as a binary classification problem, representing news content and social context as feature vectors. Then we use machine learning algorithms to build the classification model. Experimental results with three machine learning algorithms: Support Vector Machine, Naive Bayes and *k*-Nearest Neighbors on the FakeNewsNet dataset show the effectiveness of the proposed method.

Keywords: *Fake news detection, news content, social context, classify, machine learning.*

1. INTRODUCTION

The development of online social media platforms (e.g. Facebook, Twitter, Instagram, etc.) brought about a significant increase in the accessibility of information on the one hand, and accelerated the propagation of fake news on the other hand. As a result, the influence of fake news is growing and threatening the safety of the community.[1] The scope of fake news was most marked during the 2016 US presidential election campaign. The top 20 election fake news received 8,711,000 shares and comments on Facebook, larger than the total of 7,367,000 shares and comments on top 20 election stories from 19 major media outlets.[2]

Distinguishing true news from fake news is one of the difficult tasks for humans. Psychosocial and media studies show that people's ability to detect deception ranges from 55% –58%.[3]

There have been several expert-based manual fake news detection tools, platforms and websites (e.g. PolitiFact, Snopes) and community-based (e.g. Fiskkit, VAFC) so far. However, manual fake news detection is not suitable for the large amount of information generated, especially on social media.[4] Therefore, the research direction fake news detection [automatic] has become a "hot" topic recently.[5-9] In which, fake news detection can be classified

**Corresponding author.*
Email: lethixinh@qnu.edu.vn

https://doi.org/10.52111/qnjs.2023.17503

into two approaches namely (i) content-based and (ii) propagation-based.[10-13]

Content-based fake news can be detected by analyzing the news content. Meanwhile, propagation-based fake news detection exploits how news spread on social networks. The "life-cycle" of fake news has three basic stages: (1) content creation, (2) publication, and (3) propagation as illustrated in Figure 1. Propagation-based approach using social context information is difficult to apply in predicting fake news before the third stage (before fake news is spread on social media). Therefore, it is necessary to detect fake news early to prevent its spread (i.e., when fake news is at the publication stage and it has not yet spread widely).

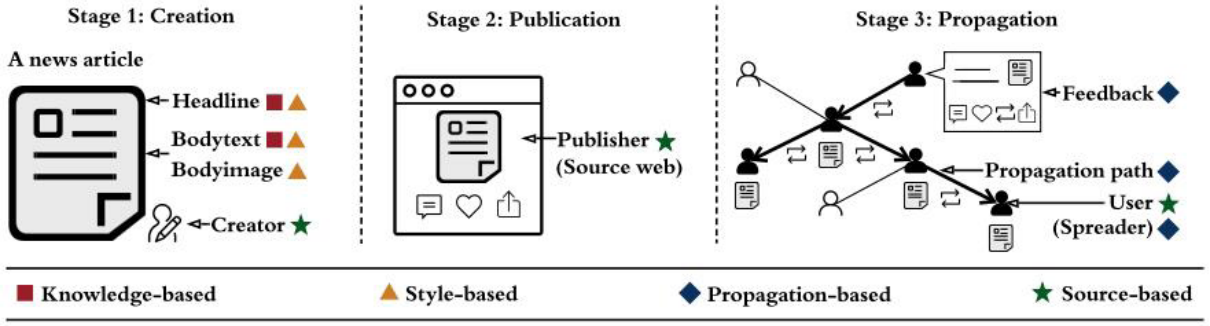

Figure 1. Fake news life cycle and detection methods.[2]

In this paper, we present a research on detecting fake news according to content-based and social context approach using machine learning. The main contributions of the paper are:

1) Analysis of related concepts, methods of detecting fake news.

2) Proposal of a method to detect fake news based on news content and social context using machine learning, including: (i) modeling this task as a binary classification problem; (ii) representing content at the lexical and social context level in the form of feature vectors; and (iii) using machine learning algorithms to build classification models.

3) Experiment to evaluate the effectiveness of classification models on the FakeNewsNet dataset.

The rest of the paper is organized as follows: Section 2 presents an overview of fake news and fake news detection. Section 3 then presents news content and social context-based fake news detection method using machine learning followed by Section 4 describing experiments. Section 5 wraps up the article with the conclusion.

2. OVERVIEW OF FAKE NEWS AND FAKE NEWS DETECTION

2.1. Definition of fake news

Current studies about fake news detection often involves the following concepts: fake news, false news, satire news, disinformation, misinformation, and rumor. These concepts can be distinguished based on three characteristics: (i) authenticity, (ii) intention, and (iii) whether information is news. Table 1 summarizes related concepts based on these characteristics.[1] For example, disinformation has false authenticity [news or not news] with bad intentions.[2]

Table 1. Compare related concepts.

Concepts	Authenticity	Intention	News or not news?
Fake news	False	Bad	News
False news	False	-	News
Satire news	-	Not bad	News
Disinformation	False	Bad	-
Misinformation	False	-	-
Rumor	-	-	-

According to Zhou,[2] "*fake news is intentionally false news published by a news outlet"*. Typically, news agencies publish news in the form of articles with the following components: title, content, author (including user's feedback) as illustrated in Figure 1.

2.2. Fake news detection methods

2.2.1. Content-based

Content-based approaches include (i) knowledge-based and (ii) style-based/writing-style. Knowledge-based fake news detection evaluates the veracity of news by comparing knowledge drawn from verified news content with known facts (i.e. true knowledge). Similar to knowledge-based methods, style-based fake news detection also focuses on news content analysis. This process includes two steps called style representation (using language features) and style classification (using machine learning models). While the knowledge-based method mainly evaluates the authenticity of the news, the style-based method can assess the intention of the news.[2,14-15]

2.2.2. Propagation-based

Propagation-based approach uses social context information to detect fake news, for example, how fake news spreads on social networks, who spreads it, and how spreaders connect with each other.

The news ecosystem on social media provides social contextual information regarding three basic entities: publishers, news [pieces], and users.

Figure 2 and Figure 3 illustrate the spread of news. In Figure 3, p_1, p_2 and p_3 are the publisher of the news a_1, ..., a_4 and u_1, ..., u_6 are the users sharing these news. In addition, users tend to form social links with people with similar interests.[16-17]

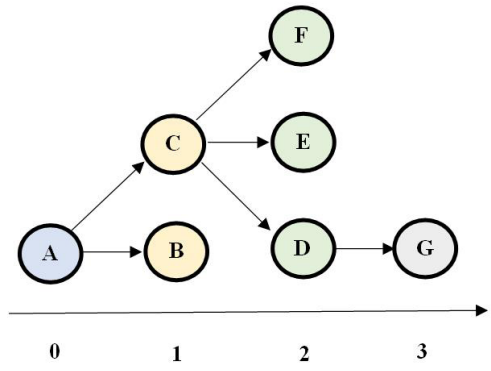

Figure 2. Tree structure-based news propagation.

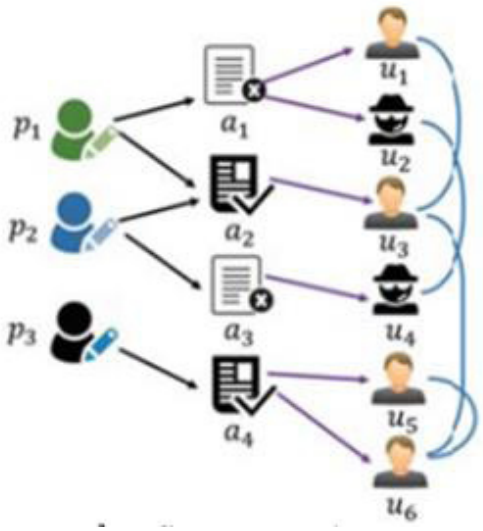

Figure 3. The relationship between publisher and user.

In general, the input to a propagation-based method can be (i) news cascades or (ii) self-defined propagation graphs.

A news layer is a tree structure that represents the direct spread of news on social network (example in Figure 2).[2] The root node corresponds to the user who first shared the news (i.e. the initiator); other nodes in the layer correspond to users who then forwarded the post after it was posted by the parent node. In a news propagation network (subgraph of a social network), each network corresponds to news, each node in the network represents a user, and an edge between two nodes represents the relationship of the two users. For example, in Figure 3, edge ($p \rightarrow a$) represents publisher p publishing news a, edge ($a \rightarrow u$) represents new a sspread by user u and edge ($u_1 \rightarrow u_2$) is social relationship between u_1 and u_2.[16]

https://doi.org/10.52111/qnjs.2023.17503

Thus, propagation-based fake news detection focuses on categorizing (i) news layers or (ii) self-defined graphs.

3. PROPOSED METHODS

In this section, we present a news content and social context-based fake news detection method using machine learning. First, we model this task as a binary classification problem. Next, we represent the news content at the lexical level according to the BoW model (Bag of Words) as a feature vector and connect to the social context vector. Then we use machine learning algorithms to build the classification model.

3.1. Problem definition

We consider the problem of detecting fake news based on content (part of text), where A = $\{a_1, a_2,..., a_n\}$ is the set of n news. Suppose the news to be verified a can be represented as a feature vector $v \in R^k$. The task of verifying the content-based is defined a function f, such that:

$$f : v \xrightarrow{D} y \quad (1)$$

Where $y \in \{0,1\}$ (0 – true news, 1- fake news) is the predicted label of the news and $D = \{(v_i, y_i) | v_i \in R^k, y_i \in \{0,1\}, i = 1..n\}$ is the training dataset. The training dataset D consists of n news, each news $a_i \in D$ is represented by the feature vector v_i with the label y_i.

And news content and social context based fake news detection problem is defined as follows: Let $N = \{n_1, n_2,\ldots, n_{|N|}\}$ is a set of news, each of which is labeled as $y_i\{0,1\}$, $y = 1$ is the fake news and $y_i = 0$ is the true news. The news n_i is represented by the news content (news body) and side information such as (title, source, author, ...). When n_i is posted on a social network, it is usually interacted with by social network users $U = \{u_1, u_2,\ldots, u_{|U|}\}$. Social context includes user interactions such as comments, posts, likes/shares, etc.

$$SC(n_i) = \left((u_1, sc_1, t_1), (u_2, sc_2, t_2), \ldots, (u_{sc}, sc_{sc}, t_{sc})\right) \quad (2)$$

Each tuple (u, sc, t) refer to user u's context sc for news n_i in timet . Here, a user can interact with a post multiple times.

Task of this problem is to find a model M to predict the label $y(n_i) \in \{0,1\}$ for each news based on the news content and social context. Therefore, this task is defined by Equation (3):

$$y(n_i) = M(C(n_i), SC(n_i)) \quad (3)$$

Where $C(n_i)$ is news content and $SC(n_i)$ is the social context of the news. Figure 4 describes the problem of detecting fake news through news content and social context.

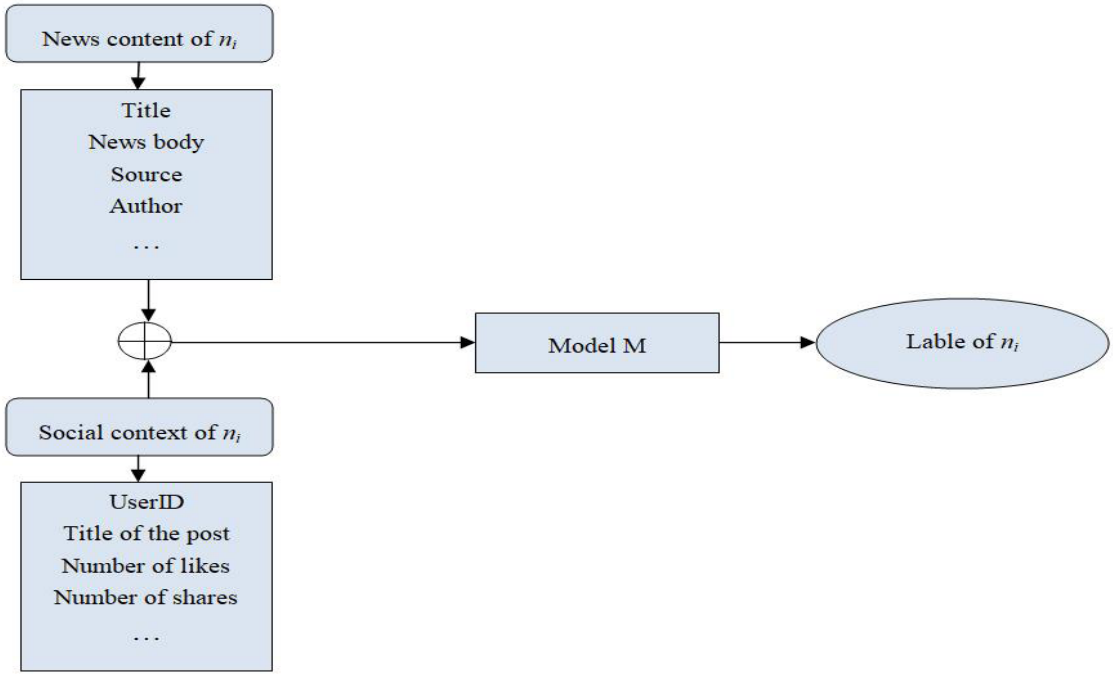

Figure 4. Description of problem.

3.2. News content and social context

3.2.1. News content

News content is the main component that makes up the story/event (news body) and includes the following auxiliary information:

- Source (e.g. https://dantri.com.vn, https://saobiz.vn).
- Headline is the title that describes the main topic of the news. The title is often named so that it attracts the reader's attention.
- Author
- Publication time

3.2.2. Social context

The social context of a news can be posts, likes, shares, replies, etc. When the features relevant to the news content are insufficient or unavailable, the social context is useful information for authenticating the news. Ancillary information related to the social context is as follows:

- Social network users (user)
- Title is the title or short caption of the post. This title is closely related to the title of the news.
- Score is the rating for a post given by other users, which determines the acceptance or disapproval of the post by other users.
- Number of comments is the number of comments on a post, this characteristic shows the popularity of the post.
- The upvote/downvote ratio estimates the approval/disapproval of other user's posts.
- User credibility: This is a feature that helps determine if users are prone to spreading fake news. For example, if the user's other posts are not trusted, it is likely that the next post will also be unreliable.

3.2.3. Representation of news content and social context

News content description features have four [language] levels: (i) lexicon, (ii) syntax, (iii) discourse and (iv) semantic. In this step, we represent the content at the lexical level according to the BoW model. Suppose the dataset contains n news $N = \{n_1, n_2, ..., n_{|N|}\}$ with a total of t words $W=\{w_1, w_1, \ldots, w_t\}$. Let x_j^i is the number of words w_j appearing in n_i. Then, the normalized frequency of w_j for the news n_i is calculated according to Equation (4).

$$w_j = \frac{x_j^i}{\sum_{j=1}^{t} x_j^i} \quad (4)$$

Thus, the new n_i is represented as a feature vector $v_i = \{w_1, w_1, \ldots, w_t\}$.

3.3. Classification model

Figure 5 shows an overview of the model that we propose to use.

- First, from the raw dataset (as shown in Figure 6), the data is preprocessed and extracted featuring news content and social context, respectively. The input is news content (identifier of news, publishing source, title of news, main content) and social context features (number of likes, number of shares, user identifier), the output is a vector representation of news content and social context. For each news $n_i \in A$ (set of news), we represent it as a feature vector $v_i \in R^k$. This representation is tailored to each machine learning algorithm. The vector representations are combined to produce a single representation that is passed as input at the next stage. The final output is passed to the classifier.
- Next, we use machine learning algorithms to train the classification model (traditional machine learning algorithms such as Support Vector Machine (SVM), Naive Bayes (NB), k-Nearest Neighbor (k-NN)).
- Finally, we use the classification model to predict whether the input data is true or fake news. The model's prediction results are compared with actual (labeled) data to evaluate the model's effectiveness.

https://doi.org/10.52111/qnjs.2023.17503

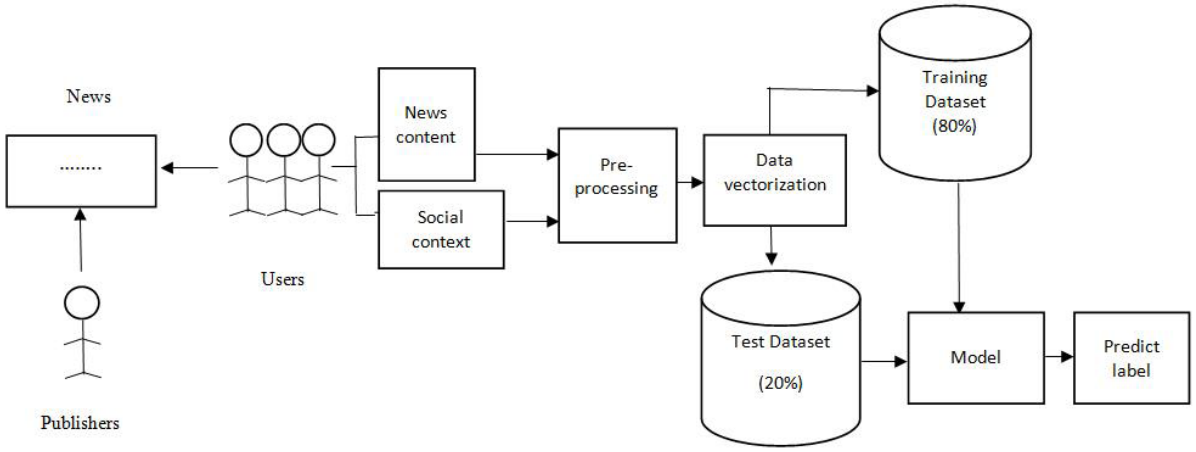

Figure 5. Proposed model.

3.3.1. Naive Bayes

Naive Bayes algorithm uses conditional probability between attributes and class label to determine the class of a data sample to be classified.[18]

Let D is the training dataset: $D = \{X_1, X_2,\ldots, X_n\}$. Where, each X_1 is represented by a vector containing m attributes $X_1 = \{x_{i1}, x_{i2},\ldots, x_{im}\}$. Let C be a set of labels consisting of p classes: $C = \{C_1, C_2, ..., C_p\}$.

Given the data sample $X = \{X_1, X_2,\ldots, X_m\}$, the Naive Bayes classifier will predict X belong to class C_i if: $P(C_i|X) > P(C_j|X)$, $(1 \le i, j \le p, i \ne j)$. The process of classifying data sample X according to Naive Bayes algorithm is described in Algorithm 1.

Algorithm 1 Naive Bayes classifier algorithm

Input: D: Training dataset; C: Label set; X: New data samples.
Output: Label of X

1: for $i = 1$ to p do
2: $P(C_i) = |X_i|/|D|$ //Calculate the probability of occurrence of the class C_i, where $|X_i|$ is the number of data samples belonging to the class C_i.
3: $P(C_i|X) = P(x_1|C_i) \times P(x_2|C_i) \times ... \times P(x_n|C_i) \times P(C_i)$ //Calculate the classification probability C_i is the label of the data sample X.
4: $label(X) \longleftarrow C_i$ if $P(C_i|X)$ is the biggest.

3.3.2. Support Vector Machine

The main idea of the SVM algorithm is that given a training set represented in vector space, where each data sample is a point, this method finds a decision hyperplane h that can best divide the points on this space into separate classes. The quality of this hyperplane is determined by the distance of the nearest data point of each class to this plane. The larger the boundary distance, the better the decision plane, and the more accurate the classification. The purpose of the SVM algorithm is to find the maximum boundary distance to give the best classification result.[19]

Suppose we need to classify a data sample X into one of two classes $C_1 = -1$ and $C_2 = 1$. The SVM classification algorithm is detailed in Algorithm 2.

Algorithm 2 SVM classifier algorithm

Input: D: Training dataset; C: Label set; X: New data samples; T: bias coefficient; $W = \{w_1, w_2, ..., w_n\}$: The set of hyperplane coefficients (*vector* weights).
Output: Label of X

1: for $i = 1$ to n do
2: $f(X) \longleftarrow sign(T + \sum w_i \times x_i)$
3: $z = T + \sum w_i \times x_i$
4: if $(z \geq 0)$ then
5: $sign(z) \longleftarrow 1$
6: else $sign(z) \longleftarrow -1$
7: $label(X) \longleftarrow sign(z)$

The SVM classification algorithm depends on the weight vector parameters W and the bias coefficient T. The goal of SVM is to estimate W and T to maximize the margin between the data classes.

3.3.3. k-Nearest Neighbor

k-NN is one of the simplest supervised learning algorithms. k-NN algorithm classifies new data points based on k nearest data points (k - neighbors). The measure used to calculate the distance between two data points can be Euclidean, Manhattan, Minkowski, Cosine.[20] Algorithm 3 describes the steps to classify a data point according to the k-NN algorithm.

Algorithm 3 k-NN classifier algorithm

Input: D: Training dataset; C: Label set; X: New data samples; K: Number of neighbors.

Output: Label of X

1: for $i = 1$ to n do
2: $d(X_i, X)$ //Calculate the distance between X and the data points in the training set.
3: end for
4: Create a set $I = \{X_i\}$, $|I| = K$ //I contains K data point closest to X.
5: for $i = 1$ to p do
6: Count the number of classes C_i that appear in I
7: $label(X) \longleftarrow C_i$, if C_i is the most appear class.

4. EXPERIMENT

4.1. Dataset

A significant challenge for automated fake news detection is the availability and quality of datasets. In the experiment, we use two datasets PolitiFact and GossipCop.[21]

Table 2 describes the news type, size and number of label 1 (fake news) statistics of the datasets. PolitiFact dataset has news of the type of article, and it includes 1,056 news, in which 432 news is fake news.

Table 2. Description of experimental data.

Dataset	Type	Size	Number of label 1
PolitiFact	article	1,056	432
GossipCop	article	22,140	5,323

Figure 6 is a snapshot of the data in the GossipCop dataset. The data includes news content and social context. In which, the content features include id (identifier of news), news_url (publishing source), title (title of news), news_body (main content), count_like (number of likes), count_share (number of shares), user_ids (user identifier, each with 18 numbers). For example, the first data line in Figure 6 has the following features:

	A	B	C	D	E	F	G	H
1	id	news_url	title	news_body	count_like	count_share	user_ids	label
2	gossipcop-2493749932	www.daily	Did Miley Cyr	Congratulations mig	12096	5421	2843290759029	fake
3	gossipcop-4580247171	hollywooc	Paris Jackson & Cara Delevingne E		746	1167	9928955082671	fake
4	gossipcop-941805037	variety.co	Celebrities Joi	Elaine L. Chao, a vet	1269	529	8533593535328	fake
5	gossipcop-2547891536	www.daily	Cindy Crawfo	In a move that left r	870	577	9888219051961	fake
6	gossipcop-5476631226	variety.co	Full List of 201	Good morning. (Wa	756	921	9557927936324	fake
7	gossipcop-5189580095	www.tow	Here's What F	Federal prosecutors	2932	147	8902530052993	fake
8	gossipcop-9588339534	www.foxn	Biggest celebr	As he prepared last	4564	125	6832263807425	fake
9	gossipcop-8753274298	www.eonl	Caitlyn Jenne	Taiwan scrambled	4511	1000	1026891446081	fake
10	gossipcop-8105333868	www.inqu	Taylor Swift R	President Xi Jinping	1966	2476	8189285335694	fake
11	gossipcop-2803748870	www.huff	For The Love	First it was the icy sr	629	1185	8160302481900	fake
12	gossipcop-7312096991	www.msn	Miley Cyrus, L	Abdul Ali Shamsi ha	11188	917	9301835055138	fake
13	gossipcop-5328748354	yournews	Miley Cyrus C	SEOUL, South Korea	8573	93	9142087416078	fake
14	gossipcop-9878194459	www.mar	Selena Gome	Photographs recent	4529	1741	1016502265060	fake
15	gossipcop-9521617242	www.eonl	Critics' Choice	President Obama de	538	500	9386812614086	fake

Figure 6. Part of the data in the GossipCop dataset.

news_body	count_like	count_share	user_ids	label

Congratulations might be in order for Miley Cyrus and Liam Hemsworth, according to new reports. Insiders told Life & Style magazine the pair secretly web in a 'hippie-style' ceremony at their Malibu, California mansion. 'They've actually done the deed for real this time! Miley and Liam recently had a secret wedding at her Malibu mansion,' the source said. 'Neighbors had no clue it was a wedding. Kids were running around everywhere. It was a hippie-style wedding.' The source continued: 'She wore a white, flowey dress and all her animals were roaming around, it was crazy! The food was vegetarian and organic.' As for their vows, the anonymous informant said: 'They expressed their love, how they're each other's best friend and want to grow old together. 'There wasn't a dry eye in the house.' Life & Style reported that, rather than invite someone to perform at their wedding, Miley did the honors herself. She sang a rendition of godmother Dolly Parton's song, Islands in the Stream. Wayne Coyne of the Flaming Lips also performed a few songs. Miley's mother and father, Billy Ray and Trish Cyrus, were both present along with siblings Noah, Trace, Brandi, Braison and Christopher. Liam's famous family attended as well. According to the report, both Chris and Luke Hemsworth looked on as Miley and Liam said their 'I Dos'. Neither Miley nor Liam have shared photos from their rumoured wedding day, but this won't be their last opportunity. According to the outlet, the couple plan to have another wedding ceremony in Australia so that more of Liam's family can be involved. As for their post wedding plans, the source said Miley and her alleged hubby have their sights set on a baby. 'It's been Miley's dream to have a baby,' they said. Here's what you need to know.

Figure 7. Main content of the news.

user_ids	label

2843290759029268 4828433274455996825628433541259029708928435991879288012828438538515133235328445638883345203228464487826731827328465655896356454528470539196579430428470539195740160128476242555372339228476608982772121728476976680625766428476976949062041628476977544233779228476977298030182428476977865518694428476977707391795228477191375304294428490294320183705628491893997530316928559226671688499328563542187297996928563551692430131328573132410128793729595453355579392029663963271045939229665127662682521670013715214369996870050164241256038470059945776789094470092521303114137675759898037304524875761401780843724875781020444874342575785545488629350481845487229916364981853220899037184181862238252499763281862364473787187282432805933569229084023792664253644984027798806743040084030555673687244884031264104210432084032038343787724884032137815067033684032544938960076884034679267169894584035911575499981084035914011969945784036645967506227484039688158698291284041337065005056084044084752711680084044429973291008084046255013536563384184926864633856084967804105588736092585119156055654492742672865323008092753101221245747392758887557652889792758887555136307292758912119076044992760651040602931492844201952916275292853261305635225692865342475275878495320193757434265895333640865099366495369219206488473795399944538488832195430767034491699210100397788914524161010184150970654720101018441015727361101019144461775257610102290139089920001010262428670709766101033476770156134410103938091447992321010418444016259072101112776426139648110137235788340142081013723601571340291101372381368566988910160005628931235841016431705132093440103644429634866380810605947074478530581060595446488358912106067950224043622410606833976499527701060708573590773761106072222723731865610608121262002

Figure 8. User identifier.

- id: gossipcop-2493749932

- news_url:

www.dailymail.co.uk/tvshowbiz/article-5874213/Did-Miley-CyrusLiam-Hemsworth-secretly-married.html

- title: Did Miley Cyrus and Liam Hemsworth secretly get married?

- news_body: (Figure 7)

- count_like: 12096

- count_share: 5421

- user_ids: (Figure 8)

4.2. Experimental setup

We use three machine learning algorithms, including: SVM, NB, and *k*-NN to train classification models on two different datasets. From the input datasets, we preprocess the data by removing stop word and special symbols, then vectorize the data matching each algorithm at the lexical level.

The training data and the test data were split in a ratio of 8:2, using a 5-fold cross-validation method.

To evaluate the classification models, we use the confusion matrix as shown in Table 3, where:

- TP (true positive): Number of news predicted to be fake news and actually fake news;
- FN (false negative): Number of news that are predicted to be fake news when in fact they are true;

● FP (false positive): Number of news that are predicted to be true when they are actually fake;

● TN (true negative): Number of news predicted to be true and in fact true.

Table 3. Confusion matrix performance.

Actual ↓ Prediction →	Fake news	True news
Fake news	TP	FP
True news	FN	TN

P (Precision), R (Recall) and F_1 is calculated as follows:

$$P = \frac{TP}{TP + FP} \quad (5)$$

$$\mathrm{R} = \frac{TP}{TP + FN} \quad (6)$$

$$\mathrm{F_1} = 2 \times \frac{P \times R}{P + R} \quad (7)$$

We implement machine learning algorithms and evaluate classification models based on the open source tool Scikit-learn.[22] We use the following classification models:

● SVM classification model: *SVC (kernel = linear)*

● Naive Bayes classification model: *GaussianNB()*

● *k*-NN classification model: *KNeighborsClassifier()*

4.3. Results and discussion

Table 4, Table 5 and Table 6 present the experimental results of the classification models on the datasets that are news content only (PolitiFact (C) and GossipCop (C)) and social context only, respectively (PolitiFact (SC) and GossipCop (SC)), and combine both news content and social context (PolitiFact (C+SC) and GossipCop (C+SC)). Experimental data show that all three classification models (SVM, NB and *k*-NN) achieve the measure of F_1 above 75%. It can be seen from the experimental results that when using a dataset combining news content and social context, almost all three models give better classification results. Specifically, when applying the *k*-NN algorithm on the PolitiFact (C+SC), the F_1 measure is 7.4% higher when running on the PolitiFact (C) and 7.7% higher when running on the PolitiFact (SC). In another case, when applying the SVM algorithm on the GossipCop (C+SC) dataset, the F_1 measure is 2.8% higher when running on the GossipCop (C) dataset and 2.6% higher when running on the GossipCop(SC) dataset.

Figure 9 and Figure 10 show the comparison of the F_1 measure between the classifiers on PolitiFact(C), PolitiFact(SC) and PolitiFact(C+SC) datasets; and between classifiers on GossipCop(C), GossipCop(SC) and GossipCop (C+SC) datasets. Experimental results show that most algorithms applied to datasets that combine news content and social context give better results of measuring F_1 when applied on datasets with only news content or social only social context.

Table 4. Experimental results on datasets with only news content.

Dataset→	PolitiFact (C)			GossipCop (C)		
Metric→	**P**	**R**	**F_1**	**P**	**R**	**F_1**
***k*-NN**	0.609	0.995	0.755	0.827	0.879	0.852
NB	0.821	0.862	0.841	0.87	0.655	0.751
SVM	0.795	0.922	0.853	0.876	0.904	0.890

https://doi.org/10.52111/qnjs.2023.17503

Table 5. Experimental results on datasets with only social context.

Dataset→	PolitiFact (SC)			GossipCop (SC)		
Metric→	P	R	F_1	P	R	F_1
***k*-NN**	0.603	1.0	0.752	0.831	0.894	0.861
NB	0.831	0.817	0.824	0.875	0.645	0.743
SVM	0.793	0.849	0.820	0.876	0.910	0.892

Table 6. Experimental results on datasets combining news content and social context.

Dataset→	PolitiFact (C+SC)			GossipCop (C+SC)		
Metric→	P	R	F_1	P	R	F_1
***k*-NN**	0.887	0.779	0.829	0.798	0.856	0.826
NB	0.874	0.832	0.852	0.831	0.868	0.849
SVM	0.815	0.917	0.863	0.883	0.956	0.918

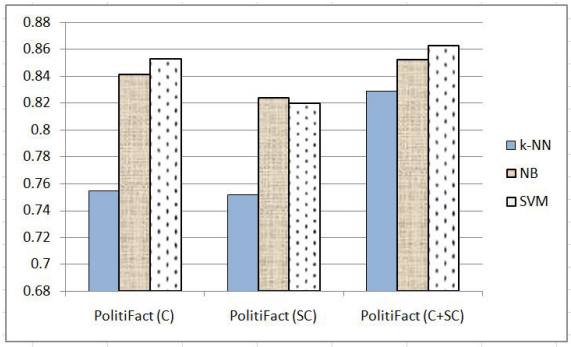

Figure 9. Compare the F_1 measure on the PolitiFact(C), PolitiFact(SC) and PolitiFact(C+SC) datasets.

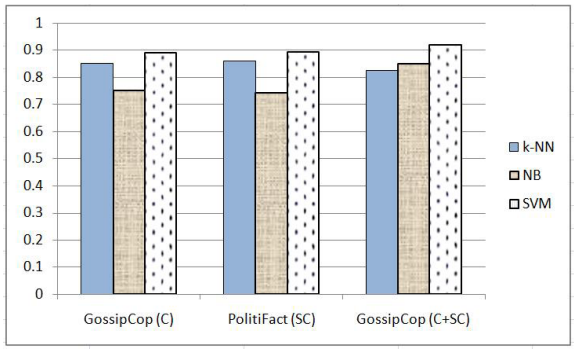

Figure 10. Compare the F_1 measure on the GossipCop(C), GossipCop(SC) and GossipCop(C+SC) datasets.

5. CONCLUSION

In this paper, we have presented a research on detecting fake news based on news content and social context approach using machine learning. We have analyzed related concepts, methods of detecting fake news. We have modeled this task as a binary classification problem, representing content and social contexts as feature vectors. Then we used machine learning algorithms to build the classification model. Experimental results with three machine learning algorithms (SVM, NB and *k*-NN) on two different datasets show the effectiveness of the proposed method.

In the future, we plan to extend this study towards content analysis in terms of natural language processing at the syntactic and semantic levels, and build a Vietnamese dataset for research on fake news detection problem.

Acknowledgement

This research is conducted within the framework of science and technology projects at institutional level of Quy Nhon University under the project code T2022.762.18.

REFERENCE

1. R. Oshikawa, J. Qian, and W. Y. Wang. *Asurvey on natural language processing for fakenews detection*, Proceedings of the 12th Language Resources and Evaluation Conference, May 2020.
2. X. Zhou and R. Zafarani. A survey of fakenews: Fundamental theories, detection methods,

and opportunities, *ACM Computing Surveys (CSUR),* **2020**, 1–40.

3. V. L. Rubin. *On deception and deception detection: Content analysis of computermediated stated beliefs,* Proceedings of the American Society for Information Science and Technology, 2010, 1–10.

4. R. Zafarani, M. A. Abbasi, and H. Liu. *Socialmedia mining: An introduction*, Cambridge University Press, 2014.

5. A. Choudhary and A. Arora. Linguistic feature based learning model for fake news detection and classification, *Expert Systems with Applications*, **2021**, 114-171.

6. Y. Bang, E. Ishii, S. Cahyawijaya, Z. Ji, and P. Fung. Model generalization on covid-19 fake news detection, *Communications in Computer and Information Science*, **2021**, 128-140.

7. C. Song, K. Shu, and B. Wu. Temporally evolving graph neural network for fake news detection, *Information Processing & Management*, **2021**, 102-712.

8. J. A. Nasir, O. S. Khan, and I. Varlamis. Fake news detection: A hybrid cnn-rnn baseddeep learning approach, *International Journal of Information Management Data Insights*, **2021**, 100007.

9. R. K. Kaliyar, A. Goswami, and P. Narang. Deepfake: Improving fake news detection using tensor decomposition-based deep neuralnetwork, *The Journal of Supercomputing*, **2021**, 1015–1037.

10. V. Pérez-Rosas, B. Kleinberg, A. Lefevre, R. Mihalcea. *Automatic detection of fake news*, Proceedings of the 27th International Conference on Computational Linguistics, August 2018.

11. A. Jain, and A. Kasbe. *Fake news detection*, 2018 IEEE International Students' Conference on Electrical, Electronics and Computer Science (SCEECS), Bhopal, India, 2018.

12. J. C. S. Reis, A. Correia, F. Murai, A. Veloso, and F. Benevenuto. Supervised learning for fake news detection, *IEEE Intelligent Systems*, **2019**, 76-81.

13. N. K. Conroy, V. L. Rubin, and Y. Chen. *Automatic deception detection: Methods for finding fake news,* Proceedings of the Association for Information Science and Technology, 2015, 1-4.

14. O. Ngada, and B. Haskins. *Fake news detection using content-based features and machine learning*, 2020 IEEE Asia-Pacific Conference on Computer Science and Data Engineering (CSDE), Gold Coast, Australia, 2020.

15. H. E. Wynne, and Z. Z. Wint. *Content based fake news detection using n-gram models*, Proceedings of the 21st International Conference on Information Integration and Web-based Applications & Services, December 2019.

16. K. Shu, S. Wang, and H. Liu. *Beyond news contents: The role of social context for fake news detection*, Proceedings of the twelfth ACM international conference on web searchand data mining, 2019.

17. P. K. Verma, and P. Agrawal. *PropFND: Propagation based fake news detection*, Applications of Artificial Intelligence and Machine Learning: Select Proceedings of ICAAAIML 2021, 2022.

18. J. Han, J. Pei, and M. Kamber. *Data mining: concepts and techniques*, Elsevier, 2011.

19. V. Vapnik, I. Guyon, and T. Hastie. Supportvector machines, *Machine Learning*, **1995**, 273–297.

20. T. Hastie and R. Tibshirani. Discriminant adaptive nearest neighbor classification, *IEEE Transactions on Pattern Analysis Andmachine Intelligence*, **1996**, 607–616.

21. K. Shu, D. Mahudeswaran, S. Wang, D. Lee and H. Liu. Fake news net: A data repository with news content, social context, and spatio temporal information for studying fakenews on social media, *Big Data,* **2020,** 171–188.

22. F. Pedregosa, G. Varoquaux, A. Gramfort,V. Michel, B. Thirion, O. Grisel, M. Blondel, P. Prettenhofer, R. Weiss, V. Dubourg, J. Vanderplas, A. Passos, D. Cournapeau. Scikit-learn: Machine learning in python, *The Journal of Machine Learning Research,* **2011**, 2825–2830.

https://doi.org/10.52111/qnjs.2023.17503

TẠP CHÍ KHOA HỌC
TRƯỜNG ĐẠI HỌC QUY NHƠN

Xác định hàm lượng Aflatoxin B1 trong sản phẩm ngũ cốc dinh dưỡng cho trẻ em bằng phương pháp sắc ký lỏng siêu hiệu năng đầu dò khối phổ hai lần (UPLC-MS/MS) làm sạch bằng cột ái lực miễn nhiễm

Nguyễn Thị Hồng[1,2,*], Nguyễn Trương Nhật Ni[1], Đặng Tấn Hiệp[2,*], Phạm Cẩm Nam[3,*]

[1] Công ty TNHH Dịch vụ Khoa học Công nghệ Khuê Nam, TP. Hồ Chí Minh, Việt Nam
[2] Trường Đại học Công nghiệp Thực phẩm Thành phố Hồ Chí Minh, TP. Hồ Chí Minh, Việt Nam
[3] Khoa Hóa, Trường Đại học Bách Khoa - Đại học Đà Nẵng, Đà Nẵng, Việt Nam

Ngày nhận bài: 09/05/2023; Ngày sửa bài: 09/08/2023; Ngày nhận đăng: 24/08/2023; Ngày xuất bản: 28/10/2023

TÓM TẮT

Kết quả nghiên cứu quy trình phân tích độc tố Aflatoxin B1 (AFB1) với kỹ thuật sắc ký lỏng siêu hiệu năng đầu dò khối phổ (MS) hai lần (UPLC-MS/MS) trong nền mẫu sản phẩm ngũ cốc dinh dưỡng cho trẻ em được thể hiện trong nghiên cứu này. Theo kết quả nghiên cứu, phương pháp UPLC-MS/MS xác định Aflatoxin B1 với thời gian lưu 4,07 phút bằng cách sử dụng cột BEH C18 1,7 µm (2,1×150 mm), pha động ở chế độ ingredient 2 dung môi với tỷ lệ: 5 mM Amonium acetate/H_2O và 0,1% HCOOH/MeOH, dung môi chiết mẫu là hỗn hợp của metanol/nước tỷ lệ 70:30 (v/v). Điều kiện phân mảnh để định lượng AFB1: cặp ion định lượng m/z: 313,05 > 285 và cặp ion định tính (m/z) 313,05 > 241. Kết quả nghiên cứu cho thấy, hệ số xác định (R^2) của đường chuẩn đạt giá trị trên 0,9993; độ lặp lại (nồng độ ≤ 1 µg/kg) trong khoảng (6,72 - 9,00)%; độ tái lặp đạt trong khoảng (7,89 - 10,4)%; giới hạn phát hiện (LOD) là 0,03 µg/kg; giới hạn định lượng (LOQ) 0,10 µg/kg và độ không đảm bảo đo (U, Uncertainty) là ±17,1%.

Từ khóa: *Aflatoxin B1, UPLC-MS/MS (IAC), bột ngũ cốc cho trẻ nhỏ.*

**Tác giả liên hệ chính.*
Email: hongedc@gmail.com, hiepdt@hufi.edu.vn, pcnam@dut.udn.vn

QUY NHON UNIVERSITY
JOURNAL OF SCIENCE

Determination of Aflatoxin B1 in cereal for infants using ultra-performance liquid chromatography to triple quadrupole mass (UPLC-MS/MS) cleaning up by an immunoaffinity column

Nguyen Thi Hong[1,2,*], Nguyen Truong Nhat Ni[1], Dang Tan Hiep[2,*], Pham Cam Nam[3,*]

[1] Khue Nam Technology Science Service, Ho Chi Minh city, Vietnam
[2] Ho Chi Minh City University of Food Industry, Ho Chi Minh city, Vietnam
[3] Faculty of Chemical Engineering, the University of Danang – University of Science and Technology, Da Nang, Vietnam

Received: 09/05/2023; Revised: 09/08/2023; Accepted: 24/08/2023; Published: 28/10/2023

ABSTRACT

This work studied on developing the analytical procedure for determination of Aflatoxin B1 (AFB1) in cereal for infants by using ultra-performance liquid chromatography triple quadrupole mass spectrometry detector (UPLC-MS/MS). Under optimal conditions, the retention time of AFB1 is identified at 4.07 minutes as using BEH C18 1.7 µm (2.1×150 mm) column and mobile phase with two solutions gradient: 5 mM Ammonium acetate/H_2O and 0.1% HCOOH/MeOH, and ratio methanol/water is 70/30 for extraction. The mass-to-charge ratio (m/z) of AFB1 for quantitative and qualitative analyses are 313.05 > 285 and 313.05 > 241, respectively. Furthermore, the obtained results are validated. Typically, the statistical parameters are significant such as linear correlation coefficient of determination (R^2) ≥ 0.9993, repeatability (concentration ≤ 1 µg/kg) in range of (6.72 - 9.00)%, (7.89 - 10.4)% of reproducibility and uncertainty is ±17.1%, while the limit of detection (LOD) and the limit of quantitation (LOQ) are 0.03 µg/kg and 0.10 µg/kg, respectively.

Keywords: *Aflatoxin B1, UPLC-MS/MS (IAC), cereal for infants.*

1. INTRODUCTION

Currently, food safety has become the most important issue in protecting the health of consumers in Vietnam as well as in the world. Foods that contain viruses, bacteria, biological toxins and toxic chemicals (such as synthetic dyes, antibiotic residues and pesticides, etc.) are considered unsafe and can cause diseases from diarrhea to cancer.[1] They can be present in agricultural and food products such as peanuts, corn, wheat, and coffee, as well as in products that are made from these ingredients. *Aspergillus, Fusarium, and Penicillium* are the main fungi causing mycotoxins in agricultural products and foods. Up to now, more than 300 types of mycotoxins have been identified and documented. However, the groups of mycotoxins that frequently contaminate food and animal feed are aflatoxins, ochratoxins, fumonisin, patulin,

**Corresponding authors.*
Email: hongedc@gmail.com, hiepdt@hufi.edu.vn, pcnam@dut.udn.vn

https://doi.org/10.52111/qnjs.2023.17504

zearalenone, deoxynivalenol, and T2-toxin.[2] Among them, the most influential and most concerned is aflatoxin (AF) which needs to be controlled. In high concentrations, aflatoxin can lead to acute poisoning (aflatoxicosis) and can be life-threatening, usually through liver damage. They can cause genetic changes, damage genes (DNA) and cause liver cancer in animals and humans.[3]

Until now, about 17 different types of aflatoxin have been recorded and studied. Of these, the four most common *bis*-furanocoumarin compounds are named B1, B2, G1, and G2, respectively. In terms of prevalence, aflatoxin B1 (AFB1) is the most abundantly found in nature and culture, followed by aflatoxin G1 (AFG1), aflatoxin B2 (AFB2), and then aflatoxin G2 (AFG2) and other substances have a rather low ratio.[4]

Cereals are important in providing primary nutrients for the growth and development of infants and children. Therefore, the identification and analysis of food contaminants have become a crucial concern due to the presence of mycotoxins and other common contaminants in cereals.[5] In Vietnam, the Ministry of Health has set the maximum allowable limit for aflatoxin (B1) at 0.1 µg/kg.[6]

Most of the AFB1 analytical methods used fluorescence detector high performance liquid chromatography (HPLC/FLD) using trifluoroacetic acid (TFA) derivatives to achieve sensitivity, meeting the allowable limit for AFB1 in food analysis.

However, in the case of nutritional foods for children, only TCVN 9522:2012[12] has a declared level of LOD = 0.05 µg/kg, which is lower than the regulation. However, theoretically, it is not easy to get the LOQ to 0.1 µg/kg when the LOD is 0.05 µg/kg. In the Annex to the standard, AFB1 concentrations at a quantitative threshold of LOQ = 0.05 µg/kg can be analyzed by increasing the HPLC/FLD injection volume to 1000µL. However, this injection volume is difficult to implement and is not suitable for practice. If injected at this volume, it will clog the column, cross-contaminate, waste solvent chemicals, take time to perform and clean.

Recent work by Nguyen Thanh Duy et al.[7] has presented a procedure for aflatoxin B1, B2, G1 and G2 analysis by UPLC-FLD fluorescence detector super-performance liquid chromatography for shows that the method is selective, the standard curve is linear in the range of 0.5 - 7.5 µg/L, the recovery ranges from 80.7 to 98.8% with the relative standard deviation (RSD) below 5% was obtained for each aflatoxin. The method detection limit (MDL) and method quantification limit (MQL) were 0.025 - 0.1 and 0.075-0.3 µg/kg, respectively. In which the MDL of aflatoxin B1 is 0.1 µg/kg, therefore the MQL will not meet the maximum allowable limit of 0.1 µg/kg.

In addition, compared with other analytical methods, the UPLC-MS/MS method applied to analyze AFB1 in nutritional cereals for children is evaluated to have the advantage of increasing selectivity and meeting current regulatory levels, operating more environmentally friendly, reducing analysis time, reducing operating pressure, reducing solvent costs, reducing environmental pollution.[8] Several papers reported that this method is sensitive, rapid, and durable enough for multiple mycotoxin determinations that fulfill international testing criteria.[9]

As an analytical method, this study has focused on the development and validation of a ultra-performance liquid chromatography with triple quadrupole mass spectrometer (UPLC-MS/MS) method for the determination of AFB1 toxin in the sample matrix namely cereal for infants.

2. APPARATUS, MATERIALS, AND METHODS

2.1. Apparatus

- The experiments were carried out at Khue Nam Science and Technology Service Co., Ltd – *address*: 2/17 Pham Van Bach, Ward 15, Tan Binh District, Ho Chi Minh City, Vietnam (https://khuenam.vn/nang-luc.php).

- The equipment used is the Acquity UPLC- MS/MS Xevo TQD by Waters supplier, and the analytical column is BEH C18 1.7 µm (2.1 × 150 mm).

- Other instruments and supporting equipment are required (solid phase extractor, centrifuge, ultrasonic machine, vortex...).

2.2. Chemicals

2.2.1. Reagents and standards

The chemicals in this study are methanol (MeOH), formic acid (HCOOH) of HPLC grade, NaCl with a purity of ≥ 99%, and phosphate buffer solution pH 7.4 (PBS), water of HPLC grade. The immunoaffinity column used is Aflatoxin with a column volume of 3 mL (IAC- AflaTest of Romer Lab). The stock solution of aflatoxin standard mixture consists of B1 (10 µg/mL), B2 (3 µg/mL), G1 (10 µg/mL), G2 (3 µg/mL) diluted in acetonitrile solvent.

2.2.2. Standard preparation

Intermediate mixed standard of 260 µg/L, 26 µg/L was prepared from a stock standard of 2600 µg/mL of acetonitrile (ACN) solvent, in which concentration of AFB1 standard is 1000 µg/L.

Working solutions were used to make a standard calibration curve of five points in AFB1 concentration of 0.2, 0.4, 0.8, 1.6, 3.2 µg/L. MeOH is solvent in preparing the calibration curve.

2.2.3. Solution preparation

MeOH/H_2O extraction solution (70/30) by volume: 150 mL of water was mixed with 350 mL of MeOH.

Phosphate buffer salt (PBS): Dissolve 8.0 g of sodium chloride, 1.2 g of anhydrous disodium hydrogen phosphate or 2.9 g of $Na_2HPO_4.12H_2O$, 0.2 g of potassium dihydrogen phosphate, and 0.2 g of potassium chloride in 900 mL of DI water. After dissolving, adjust the pH to 7.4 using hydrochloric acid or sodium hydroxide solution appropriately 5 mM ammonium acetate solution: Dissolve 0.385 g amonium acetate in 1.0 L of water in HPLC grade.

0.1% HCOOH/MeOH solution: Transfer 1.0 mL of formic acid into a 1.0 L volumetric flask and make up to the mark with MeOH.

2.2.4. Cereal sample preparation

The cereal powder sample was homogenized using a dry grinder. 10g of weighed powder was transferred to a centrifuge tube and 40 mL of MeOH/H_2O = 70/30 (v/v) was added. The mixture was vortexed for 1.0 minute and shaken for 30 minutes. It was sonicated for 30 minutes to extract the sample, then centrifuged at 3000 rpm for 5 minutes. The solution was filtered through a ∅110 mm diameter filter paper. 10 mL of the filtrate was collected and mixed with 20 mL of PBS buffer. The solution was gently mixed and passed through an IAC column. The column was washed twice with 20 mL of distilled water. The column was dried and eluted with 1.0 mL of MeOH. The eluate was filtered through a 0.22 µm PTFE membrane and analyzed using UPLC-MS/MS.[9]

2.3. Chromatographic conditions

To develop an analytical procedure for testing AFB1 in cereal powder using ultra-high performance liquid chromatography-tandem mass spectrometry (UPLC-MS/MS) without using derivatives, the chromatographic conditions, including the mobile phase and fragmentation conditions, are listed in Tables 1 and 2.

Table 1. Mobile phase condition.

Time	Flow rate (mL/min)	%A	%B
Initial	0.30	90	10
4.00	0.30	0	100
5.00	0.30	0	100
6.00	0.30	90	10
7.00	0.30	90	10
Solution A (5 mM Ammonium acetate/H_2O); Solution B (0,1% HCOOH in MeOH)			

https://doi.org/10.52111/qnjs.2023.17504

Table 2. Fragmentation condition.

Analytes	Precursor ion (m/z)	Product ion (m/z)	Cone Volt (V)	Collision energy (eV)
Aflatoxin B1	313.05	241.00	50	30
Aflatoxin B1	313.05	285.00 (*)	50	37
(*) Quantitative ion				

3. RESULTS AND DISCUSSION

3.1. Determination of the linearity of the standard curve

Calibration curve for AFB1 was constructed based on AFB1 standard solution in MeOH with five specific standards of 0.2; 0.4; 0.8; 1.6; 3.2 µg/L, the results of the calibration curve are presented in Figure 1.

The statistical analysis was performed using the least-squares method, and the resulting linear equation was AUC = 1028.75×Conc. - 29.36 with a coefficient of determination, (R^2) ≥ 0.9993. Here, AUC represents the peak area and Conc. stands for the concentration of AFB1.

3.2. Method evaluation

To evaluate the analysis method for determining AFB1 content, the method parameters were analyzed and evaluated. The evaluated parameters include repeatability, reproducibility, recovery efficiency, measurement uncertainty, limit of detection, and limit of quantification, which are specifically presented in Table 3.

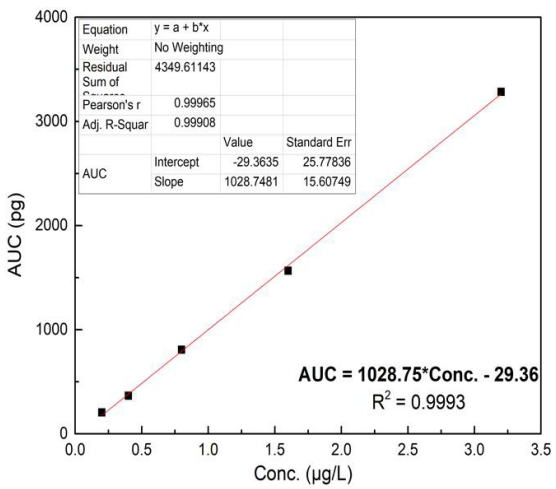

Figure 1. The calibration curve for determination of AFB1.

From this evaluation result, we certainly confirm that the UPLC-MS/MS method developed in this study can be used to determine the AFB1 content in the actual sample. That is the basis for studying and analyzing AFB1 on a sample of nutritious cereal powder for children in Ho Chi Minh City market.

3.3 Analysis of nutritional cereal powder samples for children in the Ho Chi Minh city market

To evaluate the AFB1 content on the actual sample, conduct an assessment of the AFB1 content of the sample "Supplementary Food Supplements Vanilla Organic Milk Powder with Vitamin B1 Babybio/Infant Cereals Vanilla/Babybio Céréales Vanille". Samples of weaning powder including cereals and milk for children over six months old, batch number: 3288131500102. According to the analytical procedure UPLC-MS/MS has been developed and evaluated as described in Section 3.1. and 3.2. The analysis results obtained for the specific sample are shown in Figure 4.

From the analytical results obtained on the chromatogram (Figure 2C), we can conclude that the proposed and validated method is UPLC-MS/MS, which is a highly accurate and sensitive analytical technique. The method's limit of quantitation (LOQ) is 0.10 µg/kg, which means that it is capable of detecting very low levels of AFB1 in a sample of Babybio/Infant Cereals Vanilla/Babybio Céréales Vanille.

Table 3. The results of the evaluation of the analytical method through the parameters.

No	Parameters	Criteria [11]	Result	Evaluation
1	Linearity of the standard curve	$R^2 \geq 0.99$	$R^2 \geq 0.9993$	Qualified
2	Repeatability (C ≤ 1µg/kg)	RSDr ≤ 30%	6.72 - 9.00	Qualified
3	Reproducibility (C ≤ 1µg/kg)	$RSD_R \leq 45\%$	7.89 - 10.4	Qualified
4	Recovery efficiency	40 -120%	73.6 - 110	Qualified
5	Limit of detection (LOD), µg/kg	0.03	0.03	Qualified
6	Limit of quantitation (LOQ), µg/kg	0.10	0.10	Qualified
7	Uncertainty of measurement (%)	-	± 17.1	-

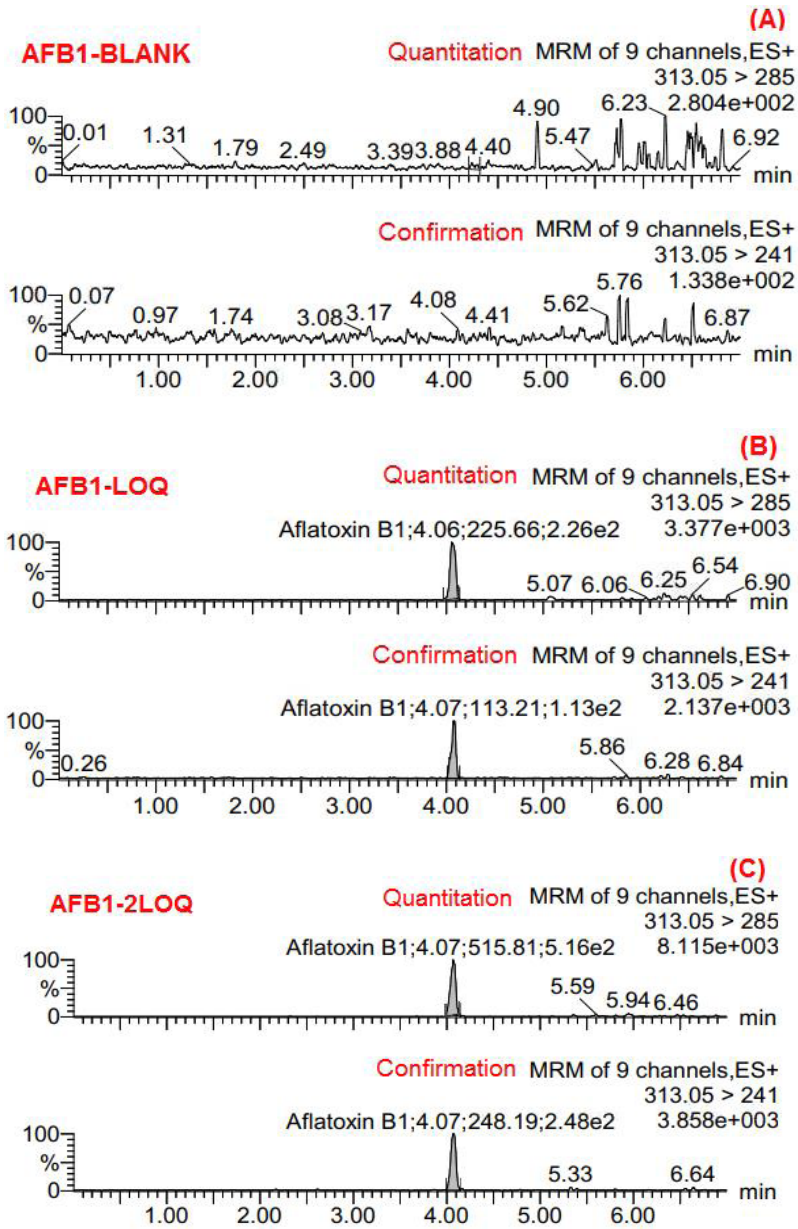

Figure 2. UPLC-MS/MS chromatograms of aflatoxins: (A) standard AFB1 blank sample (B) concentration control sample (< 0.1 g/kg) (C) supplemental food sample powdered organic milk powder with added vanilla flavor vitamin B1 Babybio/Infant Cereals Vanilla/Babybio Céréales Vanille.

https://doi.org/10.52111/qnjs.2023.17504

3.4 Quality assurance of test results by interlaboratory comparison

In order to verify the reliability of the analysis process, it is recommended to send an interlaboratory comparison sample to the Ho Chi Minh City Center for Laboratory Analysis Service (CASE), under the Department of Science and Technology in Ho Chi Minh City. The following steps should be followed: i) Take a sample of Babybio cereal powder that has not been analyzed for AFB1, spike the AFB1 concentration at 0.2 µg/kg and divide into three equal parts of 10g each in a centrifuge tube. ii) One tube sends to CASE, 1 tube to be made at the laboratory, 1 tube to store samples (Figure 3).

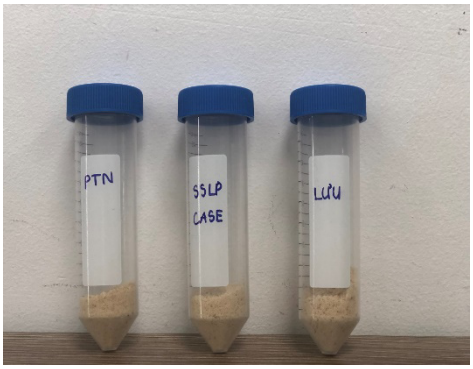

Figure 3. Samples of cereal powder after adding standards for quality assurance of test results.

Table 4. Results of analysis of AFB1 content in control laboratories.

Place of testing	Methods	AFB1 (µg/kg)	Recovery efficiency (%)	RSD_R (%)
In this work	AOAC 2005.08*	0.19	95%	2.1%
CASE	CASE.SK.0018**	0.22	110%	2.1%

* Validated method
** The method published by "Khue Nam" analytical center

Based on the analysis results presented in Table 4, it can be inferred that the method used for interlaboratory comparison was found to be satisfactory with a reproducibility of 2.1% and a recovery efficiency of 95 - 110%. Therefore, the method described in this work has been validated.

4. CONCLUSIONS

The analytical procedure for determining the content of Aflatoxin B1 by UPLC-MS/MS method has been developed in samples of nutritious cereal powder for children. The method of determining the content of Aflatoxin B1 by UPLC-MS/MS method has been validated in samples of nutritious cereal powder for children.

This method has the advantage of a simple sample processing technique, and the results of the verification of the analytical parameters are in line with the standards allowed by AOAC. Parameters such as selectivity, calibration curve, residual solvent, repeatability, reproducibility, recovery efficiency, measurement uncertainty, sample stability on UPLC-MS/MS with collection efficiency recovery ranged from 73.6 to 110% with a relative standard deviation of less than 15%, detection limit of 0.03 µg/kg and limit of quantification 0.1 µg/kg meeting the strict regulation of AFB1 in powders Weaning food for children from 6 months to 36 months according to QCVN 8:1:2011/BYT.

We have applied this developed analysis and appraisal process to analyze AFB1 in a sample of baby food powder. The product is a supplement that contains organic vanilla-flavored milk mixed with vitamin B1, meant for infants and is called Babybio/Infant Cereals Vanilla/Babybio Céréales Vanille. The result of the analysis is that AFB1 was not detected in the sample.

REFERENCES

1. E.-Sayed, A. Raghda, A. B. Jebur, W. Kang, M. A. El-Esawi, and F. M. El-Demerdash. An overview on the major mycotoxins in food products: Characteristics, toxicity, and analysis, *Journal of Future Foods 2*, **2022**, *2*, 91-102.

2. S. Marin, A. J. Ramos, G. Cano-Sancho, and V. Sanchis. Mycotoxins: Occurrence, toxicology, and exposure assessment, *Food and Chemical Toxicology*, **2013**, *60*, 218-237.

3. R. Krska, P. S. Ullrich, A. Molineli, M. Sulyok, S. MacDonald, Colin Crew. Mycotoxin Analysis: An update*, Food Addtives & Contaminants: Part A*, **2008**, *25*, 152-163.

4. M. A. Klich. Aspergillus flavus: the major producer of aflatoxin, *Molecular Plant Pathology 8*, **2007**, *6*, 713-722.

5. C. Pereira, S. C. Cunha, and J. O. Fernandes. Mycotoxins of concern in children and infant cereal food at European level: Incidence and bioaccessibility, *Toxins*, **2022**, *14*(7), 488.

6. A. M. Khaneghah, M. Elmi, M. Amirahmadi, S. Shoeibi. Simultaneous analysis of mycotoxins in corn flour using LC/MS-MS combined with a modified QuEChERS procedure, *Toxin Reviews*, **2017**, *37*(2), 187-195.

7. N. T. Duy, N. T. N. Ha, D. T. K. Hang, N. L. K. Diem, C. V. Hai, and N. Q. Trung. Building and validating a process for analyzing aflatoxin B1, B2, G1, G2 in weaning powder by super-performance liquid chromatography with fluorescence detector UPLC-FLD, *Journal of Analytical Sciences*, **2022**, *27*(1), 77-81.

8. B. Thomas, M. Claudia, M. Pascal and D. Aurelien. Multiple mycotoxins determination in food by LC-MS/MS: An international collaborative study, *Toxins*, **2019**, *11*(11), 658.

9. X. Hu, R. Hu, Z. Zhang, P. Li, Q. Zhang & M. Wang. Development of a multiple immunoaffinity column for simultaneous determination of multiple mycotoxins in feeds using UPLC-MS/MS, *Analytical and Bioanalytical Chemistry*, **2016**, *408*(22), 6027-6036.

10. E. T. James, R. L. David, R. Kathleen, C. G. Richard. Extraction, cleanup, and quantitative determination of aflatoxins in corn, *Journal of AOAC International*, **2020**, *63*(3), 631-633.

11. H. Manuel, C. T. Harold, M. C. Willie, L. H. Marvin. SPE extraction of aflatoxins (B1, B2, G1 and G2) form corn and analysis by HPLC, *The Journal of Supercritical Fluids*, **1996**, *9*(2), 118-121.

12. M. Vahl & Kevin. Determination of aflatoxins in food using LC/MS/MS, *European Food Research & Technology*, **1998**, *206*(4), 243-245.

https://doi.org/10.52111/qnjs.2023.17504

TẠP CHÍ KHOA HỌC
TRƯỜNG ĐẠI HỌC QUY NHƠN

Nghiên cứu tổng hợp $CoFe_2O_4$/rGO và ứng dụng làm vật liệu điện cực phân tích dư lượng kháng sinh ciprofloxacin trong nước thải nuôi trồng thủy sản

Nguyễn Thị Liễu*, Nguyễn Văn Lượng

Khoa Khoa học Tự nhiên, Trường Đại học Quy Nhơn, Việt Nam

Ngày nhận bài: 15/06/2023; Ngày sửa bài: 27/08/2023; Ngày nhận đăng: 29/08/2023; Ngày xuất bản: 28/10/2023

TÓM TẮT

Trong nghiên cứu này, $CoFe_2O_4$/rGO đã được tổng hợp. Hình thái và cấu trúc của $CoFe_2O_4$/rGO được đặc trưng bởi giản đồ nhiễu xạ tia X (XRD), phổ tán xạ năng lượng tia X (EDX), hiển vi điện tử quét (SEM) và quang phổ hồng ngoại biến đổi Fourier (FT-IR). Điện cực dán than chì biến tính bởi $CoFe_2O_4$/rGO (GPE-$CoFe_2O_4$/rGO) đã được chuẩn bị và sử dụng để phát hiện dư lượng kháng sinh ciprofloxacin (Cip). Một phương pháp phân tích Cip đã được xây dựng trong các điều kiện tối ưu với khoảng tuyến tính là 0,5 - 100 µM (R^2 = 0,991). Giới hạn phát hiện và giới hạn định lượng của phương pháp phân tích được xác định lần lượt là 0,094 µM và 0,314 µM. Nồng độ Cip trong các mẫu nước thải nuôi trồng thủy hải sản ở Bình Định được xác định bằng phương pháp đề xuất với độ thu hồi đạt từ 93,7–101,0%.

Từ khóa: *$CoFe_2O_4$, graphene oxide bị khử, graphite paste electrode, Von – Ampe hòa tan anot sóng vuông, ciprofloxacin.*

**Tác giả liên hệ chính.*
Email: nguyenthilieu@qnu.edu.vn

QUY NHON UNIVERSITY
JOURNAL OF SCIENCE

Research on the synthesis of $CoFe_2O_4$/rGO and its application as electrode materials to analyze ciprofloxacin antibiotic residues in aquaculture wastewater

Nguyen Thi Lieu*, Nguyen Van Luong

Faculty of Natural Sciences, Quy Nhon University, Vietnam

Received: 15/06/2023; Revised: 27/08/2023; Accepted: 29/08/2023; Published: 28/10/2023

ABSTRACT

In the present study, $CoFe_2O_4$/reduced graphene oxide ($CoFe_2O_4$/rGO) has been synthesized. The morphology and structure of nanocomposites $CoFe_2O_4$/rGO were characterized by X-ray diffraction (XRD), Energy Dispersive X-Ray spectrometer (EDX), scanning electron microscopy (SEM), and Fourier Transform infrared spectroscopy (FTIR). The $CoFe_2O_4$/rGO modified graphite paste electrode (GPE-$CoFe_2O_4$/rGO) was prepared and used for the electrochemical detection of ciprofloxacin (Cip) antibiotic residues. A Cip analytical method formed under the optimal conditions had a good linear relationship between the Cip signal with its concentration range from 0.5 to 100 µM (R^2 = 0.991). The limit of detection and quantity was observed as 0.094 µM and 0.314 µM, respectively. Finally, Cip concentration in aquaculture wastewater samples was determined by the proposed method with recovery = 93.7–101.0%.

Keywords: *$CoFe_2O_4$, reduced graphene oxide, graphite paste electrode, square wave anodic stripping voltammetry, ciprofloxacin.*

1. INTRODUCTION

Reduced graphene oxide (rGO) has electrical conductivity, high surface area, and electrochemical stability that can be used to manufacture electrodes. Recently, rGO-supported composites have indicated fascinating advantages as a sensing platform in electrochemical sensors.[1] Among them are composites of rGO and spinel ferrites nanoparticles with the chemical formula $CoFe_2O_4$ which is a very important magnetic material,[2] and can appreciate the optical, magnetic, and electrochemical properties of rGO.[3] $CoFe_2O_4$ nanoparticles have attracted increasing interest in the construction of sensors because of their low toxicity, strong superparamagnetic properties, easy preparation, and high adsorption ability. Its composite with rGO can improve rGO characteristics. Accordingly, a combination of $CoFe_2O_4$ with rGO is hoped to result in a composite with electrical conductivity, high surface area, and a possibility of application in electrochemistry.

The use of antibiotics and other chemicals is common in aquaculture. More than 20 antibiotics have been used to prevent and treat diseases in shrimp and fish farming, including banned antibiotics. Interestingly, the most used antibiotic in shrimp farming is Ciprofloxacin (CIP), which has been banned

**Corresponding author.*
Email: nguyenthilieu@qnu.edu.vn

https://doi.org/10.52111/qnjs.2023.17505

for a long time. The antibiotic Ciprofloxacin has the IUPAC name: 1-cyclopropyl-6-fluoro-4-oxo-7-(piperazin-1-yl) quinoline-3-carboxylic acid. Ciprofloxacin belongs to the quinolone antibiotic class. A wide range of techniques have been used for the determination of CIP, such as spectrophotometry,[4,5] capillary electrophoresis,[6] spectrofluorometry,[7,8] high-performance liquid chromatography (HPLC),[9,10] and electrochemical analysis.[11,12,13] Among all the above, the electrochemical technique may be the most widely applied owing to its advantages of low cost, relatively short analysis time compared to other analytical techniques, simple instruction, high sensitivity, and facile miniaturization.

The use of $CoFe_2O_4$/rGO composite materials as electrode materials in analyzing Cip antibiotics by electrochemical method has not been of interest in the country and the world. The electrodes modified by $CoFe_2O_4$/rGO nanocomposite materials have the advantage of increasing selectivity and increasing the sensitivity of the analysis, and the limit of detecting antibiotics on these electrodes is reduced. This research reported the synthesis of $CoFe_2O_4$/rGO and its application as electrode materials to analyze ciprofloxacin antibiotic residues in aquaculture wastewater.

2. MATERIALS AND METHODS

2.1. Reagents and apparatus

Chemicals: Ciprofloxacin hydrochloride ($C_{17}H_{18}FN_3O_3 \cdot HCl.H_2O$ (Cip), 98.0%) was purchased from TCI company Japan. Graphite powder and paraffin oil were received from Sigma-Aldrich. $Fe(NO_3)_3.9H_2O$; $CoCl_2.6H_2O$ were purchased from Macklin (China), absolute ethanol (C_2H_5OH), ammonia (NH_4OH), KH_2PO_4, K_2HPO_4 were purchased from Guangdong – Guanghua Sci-Techn Co. Ltd (China).

2.2. Preparation of $CoFe_2O_4$/rGO material

At first, prepare a mixture containing 50 mL of distilled water, 30 mL of ethanol, and 0.10 g rGO and stir for 10 minutes. Ultrasonic vibration for 1 hour is mixed 1. Subsequently, add 3.232 g $Fe(NO_3)_3.9H_2O$ and 0.952 g $CoCl_2.6H_2O$ to the above mixture, and stir for 60 minutes. Afterwards, add another 15 mL solution NH_3 and stir for another 120 minutes. Then transfer the entire solution to the Teflon flask, and conduct hydrothermal at 180 ^oC for 12 hours (in the drying oven). Finally, filter and wash the precipitate several times with distilled water and ethanol (until pH = 7). Dried under at 60 ^oC for 24 hours. Heating the solid at 500 ^oC for 5 hours.[14,15] $CoFe_2O_4$/rGO was obtained.

2.3. Preparation of $CoFe_2O_4$/rGO-GPE modified electrode

The $CoFe_2O_4$/rGO-GPE modified electrode was prepared by thoroughly mixing 40 mg of graphite powder and 10 mg $CoFe_2O_4$/rGO powder with 15 µL of paraffin oil. The obtained paste was put into the cavity of a Teflon holder. The obtained electrode surface was smoothed using paper. Next, using an in pin, stuff the resulting paste into an inlet tube 52 mm long, inner diameter (3.0 ± 0.1 mm), the upper part has a metal pin that can be connected to the electrochemical machine as an electric current.

2.4. Electrochemical measurements

Electrochemical measurements (cyclic voltammetric (CV) and square wave voltammetry (SWV) were performed on a system Autolab Electrochemical CPA-HH5 (Hanoi, Vietnam), with a three-electrode configuration (GPE-$CoFe_2O_4$/rGO modified electrode or GPE unmodified electrode as a working electrode, Ag/AgCl reference electrode, and platinum wire as an auxiliary electrode.

All experiments described in this section were performed at room temperature (25 ± 1 ^oC).

3. RESULTS AND DISCUSSION

3.1. Morpho-structural characterization of $CoFe_2O_4$/rGO material

3.1.1. XRD and TEM study

Figure 1 shows the XRD patterns of the $CoFe_2O_4$/rGO composite. The peaks at 2θ values

of 30.5; 35.7; 43.3; 57.1, and 62.9 correspond to respective (220), (311), (400), (511), and (440) are consistent with the spinel ferrite structure of $CoFe_2O_4$ (JCPDS 75 – 0033).[16] Apart from the characteristic lines for the spinel cubic crystal structure of the oxide compound, no other peaks can be observed indicating the high purity of $CoFe_2O_4$/rGO. This result is completely consistent with previous publications.[16,17]

The TEM image of the $CoFe_2O_4$/rGO shows the appearance of sharp $CoFe_2O_4$ particles with size about 50 nm on the surface of rGO thin sheets (Figure 2).

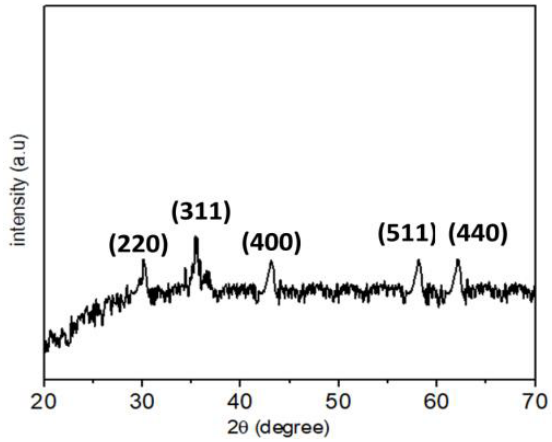

Figure 1. XRD pattern of $CoFe_2O_4$/rGO.

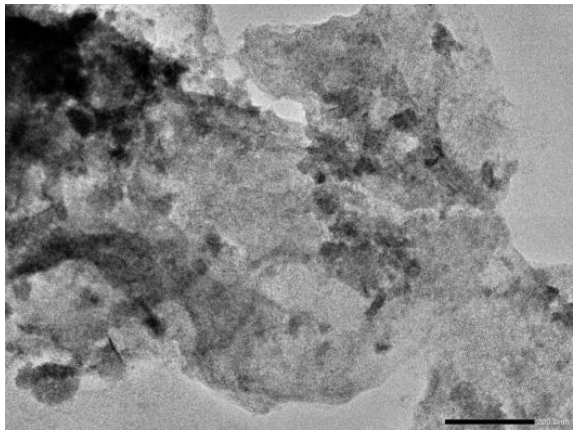

Figure 2. TEM images of $CoFe_2O_4$/rGO.

3.1.2. FTIR study

The FTIR spectrum of the $CoFe_2O_4$/rGO nanocomposites is shown in Figure 3. The O–H stretching vibration of absorbed water molecules and structural O−H groups is shown as a typical peak at 3448 cm^{-1} with an observed peak at 1720 cm^{-1} assigned for the carboxylic (C=O) functional groups. The O–H bending vibration can be observed as a peak at 1536 cm^{-1}. The presence of an absorption peak at wave number 592 cm^{-1} is believed to be the strain oscillation of the Fe (Co)- O bond in cobalt ferrite shown in the FTIR spectrum of $CoFe_2O_4$/rGO. Fe (Co)- O bonds are formed due to electrostatic attraction between functional groups (COOH, COH) on the rGO surface with Co^{2+} and Fe^{3+}.[18] This evidence confirms the cobalt ferrite precursor in the obtained rGO.

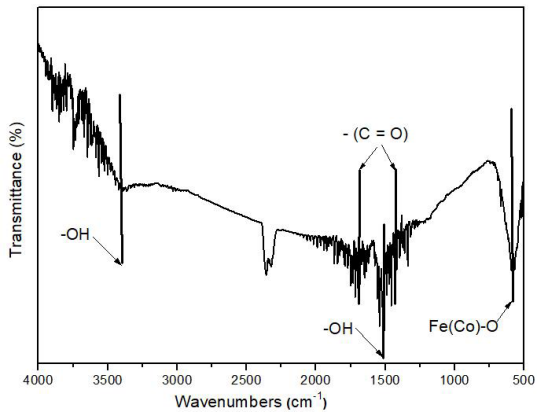

Figure 3. FTIR pattern of $CoFe_2O_4$/rGO.

3.1.3. SEM Analysis

The surface morphology of the $CoFe_2O_4$/rGO is investigated by SEM with different scales.

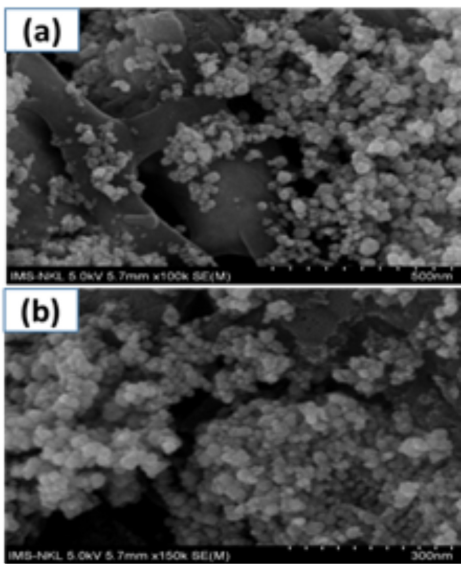

Figure 4. SEM images of $CoFe_2O_4$/rGO with different scales.

https://doi.org/10.52111/qnjs.2023.17505

The surface morphology of $CoFe_2O_4$/rGO with different scales shown in Figure 4a-b is the $CoFe_2O_4$ particles with a particle size of about 30-50 nm dispersed on rGO sheets according to an ordered structure conducive to the diffusion process and analyte adsorption.

3.1.4. EDX study

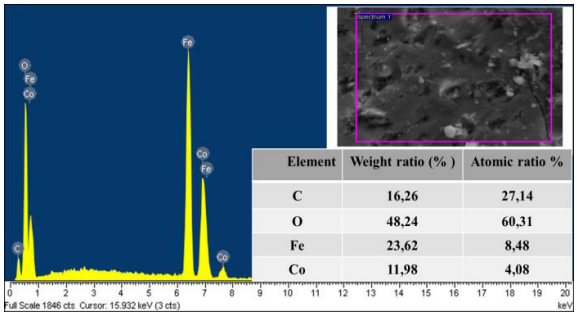

Figure 5. EDX spectra of $CoFe_2O_4$/rGO.

The analysis of the Energy Dispersive X-Ray spectrometer pattern in Figure 5 confirms the existence of C, O, Fe, and Co elements in the composites. The results show the presence of 4 elements C, O, Fe, and Co with the respective mass ratios of 12.53%; 39.02%; 32.13%, and 16.32%. The ratio of Fe/Co atoms was found to be 2:1, confirming the successful formation of the $CoFe_2O_4$/rGO structure. This result is completely consistent with the results of the previous studies.

3.2. Electrochemical results analysis

3.2.1. Electrochemical behavior of GPE and GPE modified $CoFe_2O_4$/rGO

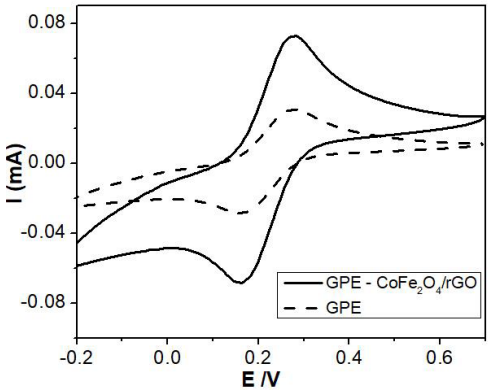

Figure 6. Cyclic voltammograms were obtained at a bare GPE and GPE-$CoFe_2O_4$/rGO in 0.2 M phosphate buffer solution (PBS), pH, 7.0 containing 5 mM $K_3Fe(CN)_6$ at a scan rate of 0.1 $V.s^{-1}$.

The cyclic voltammograms of a GPE and GPE modified $CoFe_2O_4$/rGO (GPE-$CoFe_2O_4$/rGO) in 5 mM $K_3Fe(CN)_6$ dissolved in 0.2 M phosphate buffer solution (PBS), pH, 7.0 showed the electrochemical behavior of the electrode. The electrochemical peaks of the bare GPE in the PBS are low. Their electrochemical peaks could also be observed at the GPE-$CoFe_2O_4$/rGO, with the intensity increased significantly. Based on the Randles-Sevcik equation, the electrochemically active surface areas of the GPE-$CoFe_2O_4$/rGO modified electrode were calculated as 0.2182 cm^2 larger than the bare GPE (0.0501 cm^2). The surface area calculated according to the BET model of the GPE-$CoFe_2O_4$/rGO modified electrode is 54.903 m^2/g, which is nearly 4 times higher than that of the bare GPE. This result is completely consistent with the calculation results based on the Randles-Sevcik equation.

3.2.2. Analytical performance of the $CoFe_2O_4$/rGO modified graphite paste electrode (GPE-$CoFe_2O_4$/rGO)

Linear range: To investigate the ciprofloxacin analytical performance on the proposed electrode, SWV was carried out in Cip solutions with concentrations ranging from 0.5 ÷ 150 µM under optimal conditions (0.2 M phosphate buffer solution (pH = 2.0) with 240 s accumulation time, 50 mV pulse amplitude, and 0.25 $V.s^{-1}$ scan rate). The wide linearity range was good in the range of 0.5 – 100.0 µM. The corresponding calibration plot is I(µA) = 0.7064 + 0.0995 × C (µM). The SWASVs and linear regression lines/ equations for the Cip are shown in Figure 7a and 7b, respectively.

Limit of detection (LOD): The limit of detection (LOD) was calculated as 3σ. The LOD was found as 0.094 µM and LOQ = 3× LOD = 0.314 µM. Table 1 presents the performance of various modified sensors in Cip analysis for comparison.

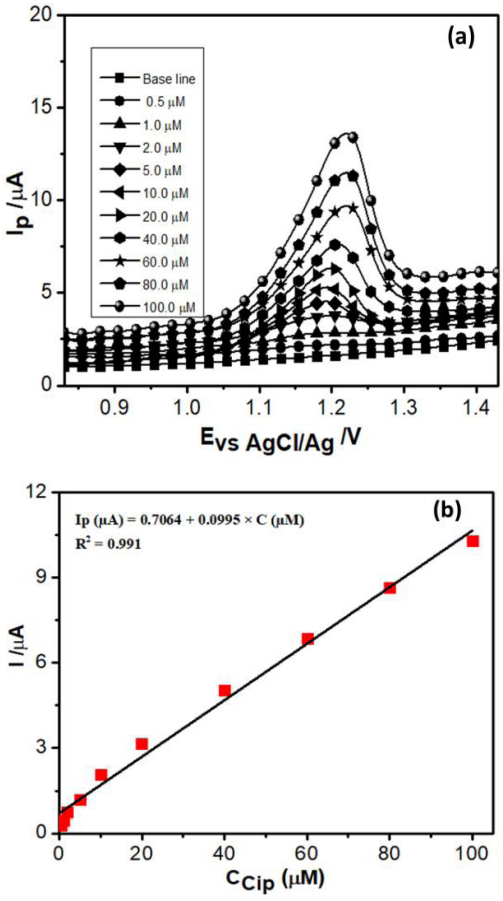

Figure 7. SWVs of Cip samples ranging in concentration from 0.5 to 100.0 µM (a) and the relationship between Cip concentrations with corresponding peak current (b).

3.3. Real sample analysis

A real sample tested by the proposed method is four samples of shrimp farming wastewater in Binh Dinh province, Vietnam.

Measurement results are in Table 2. The trueness is evaluated through the recovery of the experimental results measured in the real sample with three individual measurements. Table 2 exhibits the obtained analytical results in four samples of shrimp farming wastewater in Binh Dinh with recovery values in the range of 93.7% to 101.0%, proving that the measurement has good precision.

The results of the analysis of farmed shrimp samples showed that the Cip antibiotic index exceeded the allowable threshold from 1.8 to 3.0 times. Thus, it can be concluded that wastewater from shrimp ponds is a source of pollution. If this water source is discharged directly into the environment, the risk of environmental pollution and disease spread is very high. It also facilitates the growth of antibiotic-resistant bacteria.

Table 1. Comparison of the data obtained using various electrodes for the determination of Cip.

Electrode	Method	LOD (µM)	Range (µM)	Ref.
Graphene SPCE	SWV	0.1	0.1-100	[19]
Ch-AuMIP/GCE	DPV	0.21	1-100	[20]
PANI – β–CD/fMWCNT		0.05	10-80	[21]
MgFe2O4-MWCNTs/GCE	CV	0.01	0.1-1000	[13]
MWCNT/GCE	CV	6	40-1000	[22]
GPE-$CoFe_2O_4$/rGO	**SWV**	**0.094**	**0.5-100**	**This work**

SWV: Square Wave Voltammetry, DPV: Differential Pulse Voltammetry, CV: Cyclic Voltammetry, SPCE: Screen printed carbon electrode, MIP: Molecularly Imprinted Polymer, GCE: glassy carbon electrode, PANI: PolyAniline, β-CD: β – cyclodextrin, MWCNT: Multi-Walled Carbon Nanotube, GPE: graphite paste electrode.

https://doi.org/10.52111/qnjs.2023.17505

Table 2. Analytical results for the Cip determination using GPE-$CoFe_2O_4$/rGO in aquaculture wastewater samples in Binh Dinh province, Vietnam.

Sample	Cip (μM)				
	Sample location		Added	Found	Recovery(%)
Samples of wastewater 1	Tuy Phuoc, Binh Dinh	13°50'03.3"N 109°11'40.8"E	0	0.53 ± 0.26	100.1
			10	10.54 ± 0.22	
Samples of wastewater 2	Tuy Phuoc, Binh Dinh	13°49'47.0"N 109°11'18.7"E	0	0.92 ± 0.25	99.4
			10	10.86 ± 0.28	
Samples of wastewater 3	Phu My, Binh Dinh	14°22'10.7"N 109°07'17.3"E	0	0.66 ± 0.33	101.0
			10	10.76 ± 0.27	
Samples of wastewater 4	Phu My, Binh Dinh	14°22'10.8"N 109°07'17.0"E	0	0.85 ± 0.19	93.7
			10	10.22 ± 0.26	

4. CONCLUSIONS

$CoFe_2O_4$/reduced graphene oxide nanocomposite material was successfully synthesized by a simple easy hydrothermal method. Successful application of modified graphite paste $CoFe_2O_4$/rGO to determine ciprofloxacin in aquaculture wastewater. The signal of Cip on the modified electrode is 4.41 times higher than on the graphite paste electrode. The sensor provided satisfied LOD (0.094 μM) and LOQ (0.314 μM). The Cip concentration in aquaculture wastewater in Binh Dinh province, Vietnam was determined with good recovery (93.7–101.0%).

Acknowledgments

This research is conducted within the framework of science and technology projects at the institutional level of Quy Nhon University under the project code T2023.795.05.

REFERENCES

1. S. Cheemalapati, S. Palanisamy, V. Mani, and S. M. Chen. Simultaneous electrochemical determination of dopamine and paracetamol on multiwalled carbon nanotubes/graphene oxide nanocomposite-modified glassy carbon electrode, *Talanta,* **2013***, 117*, 297-304.
2. H. Bagheri, A. Afkhami, M. S. Tehrani, and H. Khoshsafar. Preparation and characterization of magnetic nanocomposite of Schiff base/silica/magnetite as a preconcentration phase for the trace determination of heavy metal ions in water, food and biological samples using atomic absorption spectrometry, *Talanta*, **2012,** *97,* 87–95.
3. S. Li, B. Wang, J. Liu, and M. Yu. In situ one-step synthesis of $CoFe_2O_4$/graphene nanocomposites as high-performance anode for lithium-ion batteries, *Electrochimica Acta*, **2014**, *129*, 33–39.
4. M. I. Pascual-Reguera, G. P. Parras, and A. M. Diaz. Solid-phase UV spectrophotometric method for determination of ciprofloxacin, *Microchemical Journal*, **2004**, *77*(1)*,* 79–84.
5. B. S. Nagaralli, J. Seetharamappa, and M. B. Melwanki. Sensitive spectrophotometric methods for the determination of amoxycillin, ciprofloxacin and piroxicam in pure and pharmaceutical formulations, *Journal of Pharmaceutical and Biomedical Analysis,* **2002**, *29*(5)*,* 859–864.
6. M. Hernandez, C. Aguilar, F. Borrull, and M. Calull. Determination of ciprofloxacin, enrofloxacin and flumequine in pig plasma samples by capillary isotachophoresis-capillary zone electrophoresis, *Journal of Chromatography B: Analytical Technologies in the Biomedical and Life Sciences*, **2002**, *772*(1), 163–172.
7. J. L. Vilchez, O. Ballesteros, J. Taoufiki, G. S. Palencia, and A. Navalon. Determination of the

antibacterial norfloxacin in human urine and serum samples by solid-phase spectrofluorimetry, *Analytica Chimica Acta*, **2001**, *444*(2), 279–286.

8. L. M. Du, Y. Q. Yang, and Q. M. Wang. Spectrofluorometric determination of certain quinolone through charge transfer complex formation, *Analytica Chimica Acta,* **2004,** *516* (1–2), 237–243.
9. G. H. Wan, H. Cui, Y. L. Pan, P. Zheng, and L. J. Liu. Determination of quinolones residues in prawn using high-performance liquid chromatography with Ce(IV)-Ru(bpy)$_3^{2+}$-HNO_3 chemiluminescence detection, *Journal of Chromatography B*, **2006**, *843*(1), 1–9.
10. O. R. Idowu and J. O. Peggins. Simple, rapid determination of enrofloxacin and ciprofloxacin in bovine milk and plasma by high-performance liquid chromatography with fluorescence detection, *Journal of Pharmaceutical and Biomedical Analysis*, **2004**, *35*(1), 143–153.
11. L. Fotouhi and M. Alahyari. Electrochemical behavior and analytical application of ciprofloxacin using a multi-walled nanotube composite film-glassy carbon electrode, *Colloids Surfaces B Biointerfaces*, **2010**, *81*(1), 110–114.
12. F. Zhang, S. Gu, Y. Ding, Z. Zhang, and L. Li. A novel sensor based on electropolymerization of β-cyclodextrin and l-arginine on carbon paste electrode for determination of fluoroquinolones, *Analytica Chimica Acta,* **2013**, *770*, 53-61.
13. A. A. Ensafi, A. R. Allafchian, and R. Mohammadzade. Characterization of $MgFe_2O_4$ nanoparticles as a novel electrochemical sensor of ciprofloxacin, *Analytical Sciences*, **2012**, *28*, 705–710.
14. N. T. V. Hoan, N. N Minh, N. T. H. Trang, L. T. T. Thuy, C. V. Hoang, T. X. Mau, H. X. A. Vu, P. T. K. Thu, N. H. Phong and D. Q. Khieu. Simultaneous voltammetric determination of uric acid, xanthine, and hypoxanthine using $CoFe_2O_4$/Reduced graphene oxide-modified electrode, *Journal of Nanomaterials*, **2020**, 9797509.
15. P. T. K. Thu, N. D. Trinh, N. T. V. Hoan, D. X. Du, T. X. Mau, V. H. Trung, N. H. Phong, T. T. T. Toan, D. Q. Khieu. Synthesis of cobalt ferrite and simultaneous determination of ascorbic acid, acetaminophen and caffeine by voltammetric method using cobalt ferrite modified electrode, *Journal Materials Science: Materials in Electronics,* **2019**, *30*(18), 17245–17261.
16. M. Zong, Y. Huang, and N. Zhang. Reduced graphene oxide-$CoFe_2O_4$ composite: Synthesis and electromagnetic absorption properties, *Applied Surface Science*, **2015**, *345*, 272–278.
17. Z. Liu, G. Xu, M. Zhang, K. Xiong, and P. Meng. Synthesis of $CoFe_2O_4$/RGO nanocomposites by click chemistry and electromagnetic wave absorption properties, *Journal Materials Science: Materials in Electronics*, **2016**, *27*(9), 9278–9285.
18. F. Sakhaei, E. Salahi, M. E. Olya, and I. Mobasherpour. Synthesis, characterization and application of pH-sensitive $CoFe_2O_4$/reduced graphene oxide (RGO) nanocomposite in a circulated photocatalytic reactor for Reactive Red 141 removal of wastewaters, *Research on Chemical Intermediates*, **2017**, *43*(7), 4063–4078.
19. S. A. Lim and M. U. Ahmed. A simple DNA-based electrochemical biosensor for highly sensitive detection of ciprofloxacin using disposable graphene, *Analytical Sciences*, **2016**, *32*(6), 687–693.
20. S. G. Surya, S. Khatoon, A. A. Lahcen, A. T. H. Nguyen, B. B. Dzantiev, N. Tarannum, K. N. Salama. A chitosan gold nanoparticles molecularly imprinted polymer based ciprofloxacin sensor, *RSC Advances*, **2020**, *10*(22), 12823–12832.
21. J. M. P. J. Garrido, M. Melle-Franco, K. Strutyński, F. Borges, C. M. A. Brett, and E. M. P. J. Garrido. β–Cyclodextrin carbon nanotube-enhanced sensor for ciprofloxacin detection, *Journal of Environmental Science and Health*, **2017**, *52*(4), 313–319.
22. A. Depeursinge, D. Racoceanu, J. Iavindrasana, G. Cohen, A. Platon, P.-A. Poletti, H. Müller. Fusing visual and clinical information for lung tissue classification in high-resolution computed tomography, *Artificial Intelligence in Medicine*, **2010**, *50*(1), 13-21.

https://doi.org/10.52111/qnjs.2023.17505

TẠP CHÍ KHOA HỌC
TRƯỜNG ĐẠI HỌC QUY NHƠN

Biến động theo mùa, trọng lượng và giới tính của độc tố tetrodotoxin trong cua móng ngựa *Carcinoscorpius rotundicauda* thu từ biển Cần Giờ, thành phố Hồ Chí Minh, Việt Nam

Đinh Thị Cúc[1], Đặng Thị Mai[1], Đỗ Thị Cẩm Vân[2], Trần Hữu Quang[1], Trần Đăng Thuần[1,*]

[1]Viện Hóa học, Viện Hàn lâm Khoa học và Công nghệ Việt Nam, Hà Nội, Việt Nam
[2]Viện Công nghệ HaUI, Trường Đại học Công nghiệp Hà Nội, Hà Nội, Việt Nam

Ngày nhận bài: 23/07/2023; Ngày sửa bài: 18/08/2023; Ngày nhận đăng: 24/08/2023; Ngày xuất bản: 28/10/2023

TÓM TẮT

Biến động của hàm lượng tetrodotoxin (TTX) trong cua móng ngựa *Carcinoscorpius rotundicauda* được thu thập từ bờ biển Cần Giờ, Thành phố Hồ Chí Minh, Việt Nam từ tháng 5/2021 đến tháng 5/2022 theo mùa, trọng lượng cơ thể và giới tính được xác định bởi phương pháp sắc ký lỏng kết hợp khối phổ (LC-MS/MS). Dữ liệu cho thấy có sự thay đổi đáng kể về hàm lượng TTX theo tháng với độc tính TTX tối đa được xác định là 197,6 ± 134,5 MU/g đối với các mẫu được thu thập vào tháng 5 năm 2021, trong khi *C. rotundicauda* được thu thập vào tháng 1 năm 2021 chỉ đạt hàm lượng TTX trung bình 7,8 ± 8,4 MU/g. Điều thú vị là sự khác biệt về hàm lượng TTX ở các nhóm *C. rotundicauda* trọng lượng cơ thể khác nhau cũng có khác biệt về mặt thống kê, với độc tính TTX tối đa là 230,3 ± 116,3 MU/g được xác định cho các mẫu vật có trọng lượng cơ thể lớn hơn 300g, trong khi mức TTX thấp nhất (9,8 ± 12,3 MU/g) được đo cho nhóm *C. rotundicauda* có trọng lượng cơ thể dưới 150g. Hơn nữa, có sự khác biệt đáng kể về hàm lượng TTX giữa các nhóm *C. rotundicauda* cái và đực, với độc tính TTX cao hơn đáng kể được xác định cho mẫu cua móng ngựa cái (123,9 ± 45,8 MU/g) so với *C. rotundicauda* đực (68,7 ± 45,8 MU/g). Đặc biệt, hàm lượng TTX trung bình trong các mẫu cua móng ngựa thu ở biển Cần Giờ đạt 96,3 ± 94,2 MU/g là khá cao, cho thấy chúng không an toàn cho con người sử dụng làm nguồn thức ăn. Tuy nhiên, cua móng ngựa từ vùng biển Cần Giờ, thành phố Hồ Chí Minh, Việt Nam là nguồn tiềm năng để phân lập và tinh sạch tetrodotoxin cho các ứng dụng khác nhau (ví dụ làm thuốc).

Từ khóa: *Carcinoscorpius rotundicauda, Tetrodotoxin (TTX), LC-MS/MS.*

**Tác giả liên hệ chính.*
Email: tdangthuan@ich.vast.vn

QUY NHON UNIVERSITY
JOURNAL OF SCIENCE

Seasonal, body weight and gender variation of tetrodotoxin in horseshoe crab *Carcinoscorpius rotundicauda* collected from Can Gio coast, Ho Chi Minh city, Vietnam

Dinh Thi Cuc[1], Dang Thi Mai[1], Do Thi Cam Van[2], Tran Huu Quang,[1] Tran Dang Thuan[1,*]

[1]Institute of Chemistry, Vietnam Academy of Science and Technology (VAST), Hanoi, Vietnam
[2]HaUI Institute of Technology, Hanoi University of Industry (HaUI), Hanoi, Vietnam

Received: 23/07/2023; Revised: 18/08/2023; Accepted: 24/08/2023; Published: 28/10/2023

ABSTRACT

Liquid chromatography-mass spectrometry (LC-MS/MS) was used for measurement of the variation of tetrodotoxin (TTX) in a horseshoe crab *Carcinoscorpius rotundicauda* collected from Can Gio coast, Ho Chi Minh City, Vietnam from May 2021 to May 2022 over the seasons, body weight and gender. The data revealed that there was significant variation of TTXs level over the months with maximal TTXs toxicity determined of 197.6 ± 134.5 MU/g for specimens collected in May 2021, whereas the *C. rotundicauda* collected in January 2021 was found to yield minimum TTXs level of 7.8 ± 8.4 MU/g. Interestingly, the difference of TTXs level in different body-weight *C. rotundicauda* groups was also statistically significant, with maximal TTXs toxicity of 230.3 ± 116.3 MU/g determined for specimens having body weight of greater than 300g, while the lowest level of TTXs (9.8 ± 12.3 MU/g) was assayed for *C. rotundicauda* group of body weight less than 150g. Moreover, there was a significant difference in TTXs levels among female and male *C. rotundicauda* groups, with notable higher TTXs toxicity determined for female specimens (123.9 ± 45.8 MU/g) than that of male *C. rotundicauda* (68.7 ± 45.8 MU/g). In particular, the average level of TTXs of 96.3 ± 94.2 MU/g measured in all studied crabs indicated that they are unsafe for human consumption. Fortunately, horseshoe crab collected from Can Gio coast, Ho Chi Minh City, Vietnam is a promising source for isolation and purification of tetrodotoxin for other applications (e.g., drug).

Keywords: *Carcinoscorpius rotundicauda, Tetrodotoxin (TTX), LC-MS/MS.*

1. INTRODUCTION

Among four horseshoe crab species often found in Asia region,[1,2] *Cacinoscopius rotundicauda* is reported as poisonous, and intoxication due to its intake. Previous studies have been reported that *C. rotundicauda* generally contains majority of tetrodotoxin (TTX) and minor amount of paralytic poisoning (PSP) toxins.[1-3] These toxins have caused widespread of food poisoning due to consumption of horseshoe crabs in Thailand,[4-8] Malaysia,[9] China,[10,11] and Vietnam.[1] It was evaluated that the mortality caused by consumption of *C. rotundicauda* in Thailand was about 1.75%, which was considerable high.[12] Consequently, identification and determination of toxin and toxicity in *C. rotundicauda* in Asian countries is critically important for examining potential hazard of this creature when they are

**Corresponding author.*
Email: tdangthuan@ich.vast.vn

https://doi.org/10.52111/qnjs.2023.17506

often consumed as one of seafood. Although several studies have been carried out to determine toxin and toxicity of *C. rotundicauda* collected from China, Thailand, Cambodia, Malaysia and Vietnam, these studies were case-by-case investigation with specimens collected in one time only. Remarkably, it has generally stated that Thai people can be poisoned by *C. rotundicauda* at certain seasons of the year, with peaked number of poisoning cases between December and March.[6,7] However, the authors did not determine variation of toxins and toxicity of *C. rotundicauda* collected over the months of year. Moreover, Ngy et al.[13] only investigated variation of TTXs in *C. rotundicauda* collected from Cambodia within two successive months during rainy (April-May) and dry (December-January) season. In mouse-based experiments, Liao and Li summarized that the toxicity of adult horseshoe crabs was much higher than that of young group without quantification of toxin and toxicity. Furthermore, majority of studies discussed that toxicity dominantly accumulated in eggs of female horseshoe crabs.[3,13,14] Nevertheless, statistical evaluation of the variation of toxin and toxicity levels in *C. rotundicauda* collected over different collection times, body weight and gender was not reported in the literature.

In this work, *C. rotundicauda* collected from Can Gio coast, Ho Chi Minh city, Vietnam from May 2021 to March 2022 with the total of six collections (60 specimens) analyzed for examining the variation of toxicity and toxin over seasonal variation climate in Vietnam. Extensively, the sixty specimens were divided into five groups based on body weight of *C. rotundicauda* and two groups of male *C. rotundicauda* and female *C. rotundicauda* for statistical analysis of toxin composition and toxicity level. The data obtained in this work will alert Vietnamese citizens about potential hazards when using *C. rotundicauda* as a seafood. More importantly, the results reported in this study will point out that *C. rotundicauda* is a promising source for isolation and purification of tetrodotoxin which is currently applied as a bioactive compound for drug formulation (e.g., cancer treatment, pain treatment, etc.).

2. MATERIALS AND METHODS

2.1. Chemicals

Tetrodotoxin (TTX, 4-epiTTX, Anh-TTX), formic acid and acetic were obtained from Wako pure chemicals (Osaka, Japan). Saxitoxin (C1/2, GTX1-5, dcGTX2/3, NEO, dcSTX) was a gift from Dr. Oshima, Tohoku University, Japan. Ammonium hydroxide 25% for liquid chromatography-mass spectrometry (LC-MS) was purchased from Sigma-Aldrich (Tokyo, Japan). Acetonitrile was purchased from Kanto Chemicals (Tokyo, Japan).

2.2. Specimen collection

Horseshoe crabs *C. rotundicauda* were collected from Can Gio coast, Ho Chi Minh City, Vietnam from May 2021 to May 2022. The specimens were classified by referencing relevant literature.[1,3] After transferred to the Laboratory of Technology of Bioactive Compounds, Institute of Chemistry, Vietnam Academy of Science and Technology, specimens were immediately frozen and kept frozen at −20°C for sample preparation and toxin extraction.

2.3. Extraction and analyzing of tetrodotoxin and saxitoxins

Specimens were dissected to collect all soft tissues, which were then homogenized with acetic acid 1% (2:1 w/v). The homogenized samples were boiled for 5 min, followed by cooling down at room temperature and centrifugation at 9,000 rpm, 20 ^{o}C for 10 min to collect supernatant. The supernatant was treated using an ENVI-Carb SPE cartridge 250 mg/3 ml (Sigma Aldrich Japan, Tokyo, Japan), eluted by four-fold diluted acetonitrile (MeCN) with 1% acetic acid. The TTXs-rich eluate was analyzed by a Hydrophilic interaction liquid

Chromatography-Mass spectrometer (HILIC/MS-MS) coupled to a Shimadzu system triple-quadrupole mass spectrometer (LCMS−8040; Shimadzu Corporation, Kyoto, Japan). The HILIC separation was performed using a Waters Xbrige (HILIC) Amide column (4.6 mm I.D ×150 mm, 3.5 µm) at 60°C with 5 µl sample volume injected. Mobile phases were water/formic acid/ammonium hydroxide (500:0.075:0.3 v/v/v) (A); acetonitrile/water/formic acid (700:300:0.1 v/v/v) (B) with flow rate of 0.6 mL/min.

The chromatographic conditions consist of initial conditions 100% B, held for 20 min, then a linear gradient 50:50 A and B within 15 min, held for 9.90 min. Ion source parameters of MS spectrometer were as follows: Entrance Potential (EP): 10 V; Curtain gas (CUR): 30 psi; Ion Spray Voltage (IS): 4500 V; Source desolvation temperature (TEM): 250 ºC; Source ion block temperature: 400 °C; Desolvation gas flow: 1000 L/h, Nebulizer gas flow: 2L/min; Collision gas flow rate: 0.15 mL/min. Multiple reaction monitoring (MRM) was performed in positive electrospray ionization (ESI^+). A minimum of two transitions were used for each TTX and STX analogues. For each target ion, an MRM ion channels were selected for specific product ions generated from the selected precursor ion.[15] To confirm TTXs in the extract of horsecrabs, MS/MS spectra were obtained at -25 eV of collision energy with m/z 320.1 > 302.1 for TTX and 4epi-TTX, m/z 302.0 > 284.1 for Anh- TTX in the 1st transition; and -40 eV with m/z 320.1 > 162.1 for TTX and 4epi-TTX, m/z 302.0 > 162.0 for Anh-TTX in the 2nd transition. STXs were scanned in the same mode with mass ranging from m/z 50-m/z 350.[16] Toxicities were calculated from HILIC-MS/MS data and expressed in mouse unit (MU/g) according to Nakamura and Yasumoto (1985),[17] in which 1 mg TTX corresponding to 4500 MU, 4-epiTTX to 710 MU and 4,9-anhydroTTX to 92 MU. One MU is the dose of toxin that will kill a 20 g male mouse (ddY) in 30 min.

2.4. Statistical analysis

Experiment was carried out in triplicate and data was reported as mean ± standard error (SE). Statistical analysis was done using one-way ANOVA followed by post hoc Tukey's test and a *p*-value of < 0.05 was declared as significant. The statistical analysis was conducted using software package IBM SPSS statistics (SPSS 22, SPSS Inc., IBM, New York, USA).

3. RESULT AND DISCUSSION

3.1. Seasonal variation of tetrodotoxin

Horseshoe crab specimens were all identified as *Carcinoscorpius rotundicauda*.[1,3] The toxicities of all the specimens were calculated based on the specific toxicity of each toxin component and expressed in mouse units (MU) (Table 1).[18]

Table 1. TTX toxicity (MU/g) of *Carcinoscorpius rotundicauda* specimens collected from Can Gio coast, Ho Chi Minh city, Vietnam in 2021 - 2022.

Specimen No.	Body size			Toxicity (MU/g)			Total toxicity (MU/g)
	Weight (g)	Length (cm)	Width (cm)	4epi-TTX	TTX	Anh-TTX	TTXs
May 2021							
f1	300.1	34.1	18.3	11.7±0.13	56.2±2.72	49.8±2.73	117.6±5.09
f2	210.3	24.5	12.5	7.9±0.09	58.5±3.04	10.7±0.72	77.1±3.78
f3	305.2	33.0	18.0	18.9±1.21	304.1±9.23	4.8±0.11	327.8±13.36
f4	307.1	33.5	17.2	1.4±0.04	331.4±10.32	3.7±0.06	336.5±11.14
f5	319.4	35.2	19.5	17.4±1.04	424.1±12.27	39.1±1.33	480.6±19.34

https://doi.org/10.52111/qnjs.2023.17506

Specimen No.	Body size			Toxicity (MU/g)			Total toxicity (MU/g)
	Weight (g)	Length (cm)	Width (cm)	4epi-TTX	TTX	Anh-TTX	TTXs
m1	290.5	32.5	16.7	105.4±3.72	28.9±0.55	2.2±0.05	136.5±5.81
m2	230.1	29.5	12.5	68.6±2.88	41.3±1.17	4.0±0.62	113.9±9.63
m3	251.6	25.5	15.2	56.8±1.23	49.2±2.16	5.8±0.22	111.7±8.77
m4	261.2	24.5	18.5	6.9±0.03	109.1±5.22	12.5±0.72	128.5±7.82
m5	215.4	26.6	11.2	45.3±1.82	98.5±4.06	1.8±0.04	145.5±10.77
October 2021							
f6	278.1	27.5	11.8	67.1±2.08	56.4±1.26	33.3±0.52	156.8±13.16
f7	311.2	34.5	17.5	40.0±1.13	39.8±2.67	42.0±1.88	121.8±10.66
f8	315.0	34.5	19.5	16.3±0.71	48.0±3.11	52.0±2.89	116.4±7.62
f9	227.1	28.5	15.2	27.0±1.52	39.5±0.97	47.0±2.89	113.5±7.25
f10	177.3	23.6	14.4	13.1±0.24	48.8±2.72	2.0±0.04	63.8±2.81
m6	195.5	25.5	16.6	7.1±0.11	40.9±1.22	28.0±2.90	76.0±3.78
m7	159.1	27.6	15.7	6.6±0.08	31.2±0.97	19.9±0.62	57.6±1.98
m8	197.6	28.0	12.0	17.0±1.26	47.7±3.10	10.7±0.47	75.5±3.38
m9	267.1	32.5	17.5	18.7±1.02	42.8±3.67	32.1±1.88	93.6±2.09
m10	295.3	33.5	18.5	28.9±1.08	40.2±1.89	21.6±0.71	90.6±4.78
November 2021							
f11	100.3	21.0	11.0	1.7±0.05	1.2±0.04	0.3±0.01	3.1±0.09
f12	210.1	29.0	13.0	5.6±0.17	86.8±2.60	1.2±0.05	93.6±3.81
f13	104.6	25.6	15.5	1.2±0.04	3.0±0.05	1.0±0.03	5.2±0.16
f14	182.0	26.6	12.1	7.6±0.23	2.0±0.06	0.1±0.01	9.7±0.29
f15	115.1	25.2	15.3	4.0±0.12	2.0±0.09	0.7±0.02	6.8±0.22
m11	250.3	29.5	15.4	51.3±2.54	37.0±1.13	11.1±0.33	99.4±2.78
m12	104.5	22.4	15.4	1.6±0.03	3.0±0.07	0.4±0.01	5.0±0.13
m13	259.2	30.6	17.5	12.8±0.37	22.7±0.68	1.2±0.04	36.7±1.12
m14	272.3	31.6	18.5	14.9±0.45	48.6±1.46	1.3±0.05	64.8±1.94
m15	165.1	23.5	14.3	9.4±0.28	35.9±1.08	29.6±0.78	75.0±2.56
January 2022							
f16	104.0	25.0	11.0	0.0±0.00	0.0±0.00	2.1±0.06	2.1±0.02
f17	110.4	25.7	13.0	0.6±0.02	4.1±0.11	0.1±0.00	4.8±0.11
f18	109.2	26.1	15.4	2.1±0.06	2.9±0.08	0.1±0.00	5.1±0.15
f19	112.1	24.9	11.5	0.9±0.02	3.0±0.08	1.1±0.03	5.1±0.17
f20	168.3	22.5	11.0	15.7±0.42	11.7±0.32	3.6±0.10	31.0±0.04

Specimen No.	Body size			Toxicity (MU/g)			Total toxicity (MU/g)
	Weight (g)	Length (cm)	Width (cm)	4epi-TTX	TTX	Anh-TTX	TTXs
m16	101.1	25.2	12.1	0.9±0.02	2.3±0.06	1.0±0.03	4.2±0.11
m17	213.3	32.0	13.5	6.0±0.16	1.9±0.05	1.1±0.02	8.9±0.24
m18	109.5	23.0	10.0	1.0±0.03	3.2±0.09	0.1±0.00	4.3±0.12
m19	248.1	30.0	15.0	1.2±0.03	2.8±0.08	3.7±0.10	7.7±0.18
m20	210.2	29.0	13.0	1.5±0.04	2.3±0.06	1.3±0.04	5.1±0.21
February 2022							
f21	289.2	34.1	20.1	11.1±0.39	129.4±4.22	35.3±1.24	175.8±6.12
f22	399.1	31.7	17.5	0.0±0.0	87.1±3.05	30.8±1.08	117.9±4.13
f23	312.2	35.1	19.5	125.6±4.1	2.1±0.07	1.9±0.07	129.6±3.89
f24	156.3	27.2	17.3	15.5±0.54	11.7±0.41	2.0±0.03	29.1±1.07
f25	178.6	29.1	16.5	56.3±1.97	20.5±0.72	2.6±0.07	79.4±2.89
m21	135.5	27.4	17.1	6.0±0.21	31.1±1.09	2.2±0.02	39.3±1.39
m22	259.2	32.8	12.5	21.5±0.75	37.8±1.32	2.1±0.01	61.4±2.15
m23	176.6	31.5	17.5	9.4±0.33	33.7±1.18	10.7±0.13	53.8±1.88
m24	178.2	28.8	13.0	10.0±0.35	24.3±0.85	3.7±0.02	38.0±2.88
m25	145.5	29.1	12.2	0.6±0.02	31.5±1.10	0.3±0.01	32.4±1.43
March 2022							
f26	305.0	34.5	21.0	11.3±0.09	138.4±4.17	3.2±0.03	152.9±4.43
f27	298.3	31.0	18.8	5.7±0.23	117.0±3.39	8.1±0.17	130.8±3.71
f28	316.2	34.5	19.8	83.4±0.49	193.9±5.62	16.8±2.11	294.2±7.22
f29	308.1	32.7	18.5	15.0±1.63	243.6±7.05	18.2±0.71	276.8±8.89
f30	306.5	32.2	19.0	154.8±1.75	76.1±2.21	19.8±0.87	250.6±2.17
m26	318.6	35.0	19.5	56.3±0.16	91.3±2.65	10.8±0.24	158.4±4.59
m27	276.1	31.0	15.0	60.4±0.17	32.0±0.93	10.8±0.51	103.3±3.19
m28	204.0	33.3	15.0	5.6±0.75	40.4±1.17	3.2±0.06	49.2±1.42
m29	151.2	28.5	15.0	6.0±0.17	52.3±1.52	4.7±0.17	63.1±2.19
m30	256.4	29.6	14.0	60.5±2.78	49.9±1.45	10.9±0.26	121.3±1.89

MU: mouse unit; f: female; m: male

The data collected showed that ten specimens collected in May 2021 were toxic with toxicity varied from 77.1 to 480.6 MU/g. In October 2021, ten specimens accounting for 100% of *C. rotundicauda* specimens were toxic with TTXs toxicity ranging between 57.6 and 156.8 MU/g. For specimens collected in November 2021, five out of ten specimens were determined for toxicity range of 31.1 – 99.4 MU/g, indicating 50% of specimens were toxic. By January 2022, there were 90% non-toxic and 10% toxic specimens identified from ten

https://doi.org/10.52111/qnjs.2023.17506

specimens collected with TTXs toxicity of 21 – 31 MU/g. The specimens collected in February 2022 were assayed and yielded ten out of ten, accounting for 100% of toxic specimens (29.1 – 175.8 MU/g). The collection in March 2022 also resulted in 100% toxic specimens (49.2 – 294.2 MU/g). In sum, the frequency of occurrence of toxic specimens is very high (46 out of 60 specimens; 76.7%). The present data strongly suggest that the frequency of toxic specimens of *C. rotundicauda* in Vietnam is extremely high. This result was in line with the data reported by Dao et al. showing that 83% of *C. rotundicauda* specimens collected in Tan Hai village, Vung Tau province, Vietnam were toxic.[1] The average toxicity determined for all specimens was 96.3 ± 94.2 MU/g, which is considerably higher than 10 MU/g recommended as the safe consumption level of TTX in Japan.[19]

The maximal toxicity of specimens collected in May21, Oct21, Nov21, Jan22, Feb22 and Mar22 were 480.6, 156.8, 99.4, 31.0, 175.8 and 294.2 MU/g, respectively. These toxicity levels were about 2 – 28 fold-time higher than 17.0 MU/g reported for *C. rotundicauda* collected in China by Zheng et al.,[3] 2 – 30 fold-time higher than 16 MU/g reported for Thailand *C. rotundicauda*,[2] and 4 – 65 fold-time higher than 7.4 MU/g determined for Bangladeshi *C. rotundicauda*.[14] However, the toxicity of Vietnamese *C. rotundicauda* collected from Can Gio coast were comparable among the toxicity level reported for Cambodia *C. rotundicauda* (315 MU/g).[13]

It was remarkably noted that 4epi-TTX, TTX and Anh-TTX were three major compounds identified in the specimen's extract (Figure 1) without detection of STXs (Figure 2), making 100% of the total toxicity contributed by TTXs. Consistently, *C. rotundicauda* collected from Cambodia was assayed by LC/MS yielding TTX and its analogues of anhydro-TTX ($[M+H]^+$=302) and deooxy-TTX ($[M+H]^+$ = 304) with no PSPs were detected. Contrastingly, Zheng el al. (2019) reported that *C. rotundicauda* collected from China contained TTX, 11-oxoTTX, 4.9-anhydro-11-oxoTTX, 4.9-anhydroTTX, 5-deoxyTTX, 5.11-dideoxyTTX, 5.6.11-trideoxyTTX and 4.9-anhydro-5.6.11- trideoxyTTX in which 5-deoxy TTX in which 4.9-anhydro-11-oxoTTX were found as the major TTX analogues in all specimens. Furthermore, dcGTX2 and dcSTX were also determined with small amount in Chinese *C. rotundicauda* extract.[3] Dao et al. examined *C. rotundicauda* collected from Tan Hai village, Vung Tau province, Vietnam and reported that all specimens contained 4epi-TTX, TTX, Anh-TTX and a certain amount of PSPs (e.g., neoSTX, dcSTX, STX, GTX4, GTX1, GTX3, GTX2, C1, C2) with their composition varied individually.

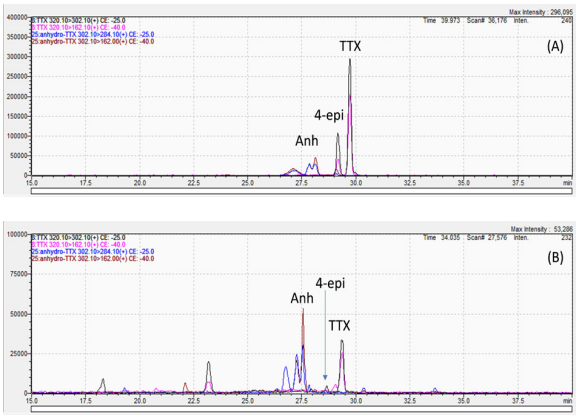

Figure 1. HPLC chromatograms of TTXs standards (A) and in an extract *Carcinoscorpius rotundicauda* specimens (B) collected from Can Gio coast, Ho Chi Minh city, Vietnam.

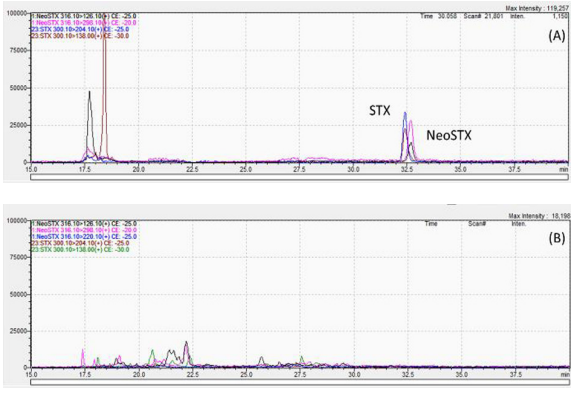

Figure 2. HPLC chromatograms of STXs standards (A) and in an extract *Carcinoscorpius rotundicauda* specimens (B) collected from Can Gio coast, Vietnam.

Statistical analysis of variation of 4epi-TTX, TTX, Anh-TTX and TTXs of *C. rotundicauda* is illustrated in Figure 3A, Figure 3B, Figure 3C and Figure 3D, respectively. Sixty specimens were collected over the study period. For 4epi-TTX, the variation of its toxicity was significant over the months (ANOVA, $F = 2.583$, $p = 0.036$, $n = 10$, Figure 3A). Particularly, the maximal toxicity of 4epi-TTX recorded for ten specimens collected in Mar22 and May21 were 45.9 ± 48.0 and 34.0 ± 34.0 MU/g, respectively, which were significantly higher than those determined of 11.1 ± 14.9 MU/g in Nov21 ($p = 0.039$) and 3.0 ± 4.8 MU/g in Jan22 ($p = 0.013$). Pair comparisons also revealed that 4epi-TTX toxicity determined for specimens collected in Oct21 of 24.2 ± 18.2 MU/g was significantly higher than 3.0 MU/g determined for specimens in Jan22. However, there was no statistically significant difference of 4epi-TTX toxicity of specimens collected in Mar22 and May21 ($p = 0.512$), Mar22 and Feb22 ($p = 0.151$), Mar22 and Oct21 (0.271), May21 and Feb22 ($p = 0.649$), May21 and Oct21 ($p = 0.518$), Feb22 and Oct21 ($p = 0.926$), Feb22 and Nov22 ($p = 0.339$), Feb22 and Jan22 ($p = 0.088$), Oct21 and Nov21 ($p = 0.164$) and Nov21 and Jan22 ($p = 0.164$).

TTX toxicity for specimens collected in May21, Oct21, Nov21, Jan22, Feb22 and Mar22 were 150.1 ± 145, 43.4 ± 6.9, 24.2 ± 28.3, 3.4 ± 3.1, 40.9 ± 38.4, and 103.5 ± 70.5 MU/g, respectively, indicating greater variation among the months (ANOVA, $F = 6.392$, $p = 9.9\times10^{-5}$, n = 10, Figure 3B). Among these pairs, TTX toxicity measured for specimens collected in May21 and Oct21 ($p = 0.044$), May21 and Feb22 ($p = 0.04$), May21 and Nov21 ($p = 0.035$), May21 and Jan22 ($p = 0.010$), Mar22 and Oct22 ($p = 0.023$), Mar22 and Feb22 ($p = 0.039$), Mar22 and Nov21 ($p = 0.014$), Mar22 and Jan22 ($p = 0.002$), Oct21 and Jan22 ($p = 0.000$), Feb22 and Jan22 ($p = 0.015$) and Nov21 and Jan22 ($p = 0.048$) were significantly statistical difference. The remaining pairs including May21 and Mar21 ($p = 0.0266$), Oct21 and Feb22 ($p = 0.826$), Oct21 and Nov21 ($p = 0.080$) and Feb22 and Jan22 ($p = 0.243$) were identified as no statistical difference in TTX toxicity (Figure 3B). Anh-TTX toxicity was also varied significantly over the months (ANOVA, $F = 6.647$, $p = 6.88\times10^{-5}$, $n = 10$, Figure 3C) with maximum and minimum levels of 28.9 ± 15.8 and 1.4 ± 1.3 MU/g determined for specimens collected in Oct21 and Jan22, respectively. The specimens collected in May21, Nov21 Feb22 and Mar22 yielded Anh-TTX toxicity of 13.4 ± 16.9, 4.7 ± 9.3, 9.2 ± 12.9 and 10.7 ± 6.1 MU/g, respectively. Statistical analysis of Anh-TTX toxicity revealed that the pairs e.g., Oct21 and Mar22 ($p = 0.007$), Oct21 and Feb22 ($p = 0.008$), Oct 21 and Nov21 ($p = 0.004$), Oct21 and Jan22 ($p = 0.000$), May21 and Jan22 ($p = 0.043$) and Mar22 and Jan22 ($p = 0.001$) were significantly different. Overall, TTXs toxicity of *C. rotundicauda* collected over the studied months displayed a considerable variation (ANOVA, $F = 10.1$, $p = 7.28\times10^{-7}$, Figure 3D). The mean TTXs toxicity of specimens collected in May21, Oct21, Nov21, Jan21, Feb21 and Mar21 were 197.6 ± 134.5, 96.6 ± 30.6, 39.9 ± 39.5, 7.8 ± 8.4, 75.7 ± 49.7, 160.1 ± 86.4 MU/g, respectively. Typically, measurements of TTXs toxicity in May21 and Oct21 ($p = 0.021$), May21 and Feb22 ($p = 0.026$), May21 and Nov21 ($p = 0.012$), May 21 and Jan22 ($p = 0.001$), Mar22 and Oct 22 ($p = 0.042$), Mar22 and Feb22 ($p = 0.015$), Mar22 and Nov21 ($p = 0.007$), Mar22 and Jan22 ($p = 0.000$), Oct21 and Nov21 ($p = 0.008$), Oct21 and Jan22 ($p = 0.000$), Feb22 and Jan22 ($p = 0.002$) and Nov21 and Jan22 ($p = 0.042$) were exhibited significant differences. Ngy et al.[13] also reported that the toxicity level of TTXs in Cambodia were varied notably between dry (December – January) and rainy seasons (April – May) with generally higher TTXs level observed in rainy months.

https://doi.org/10.52111/qnjs.2023.17506

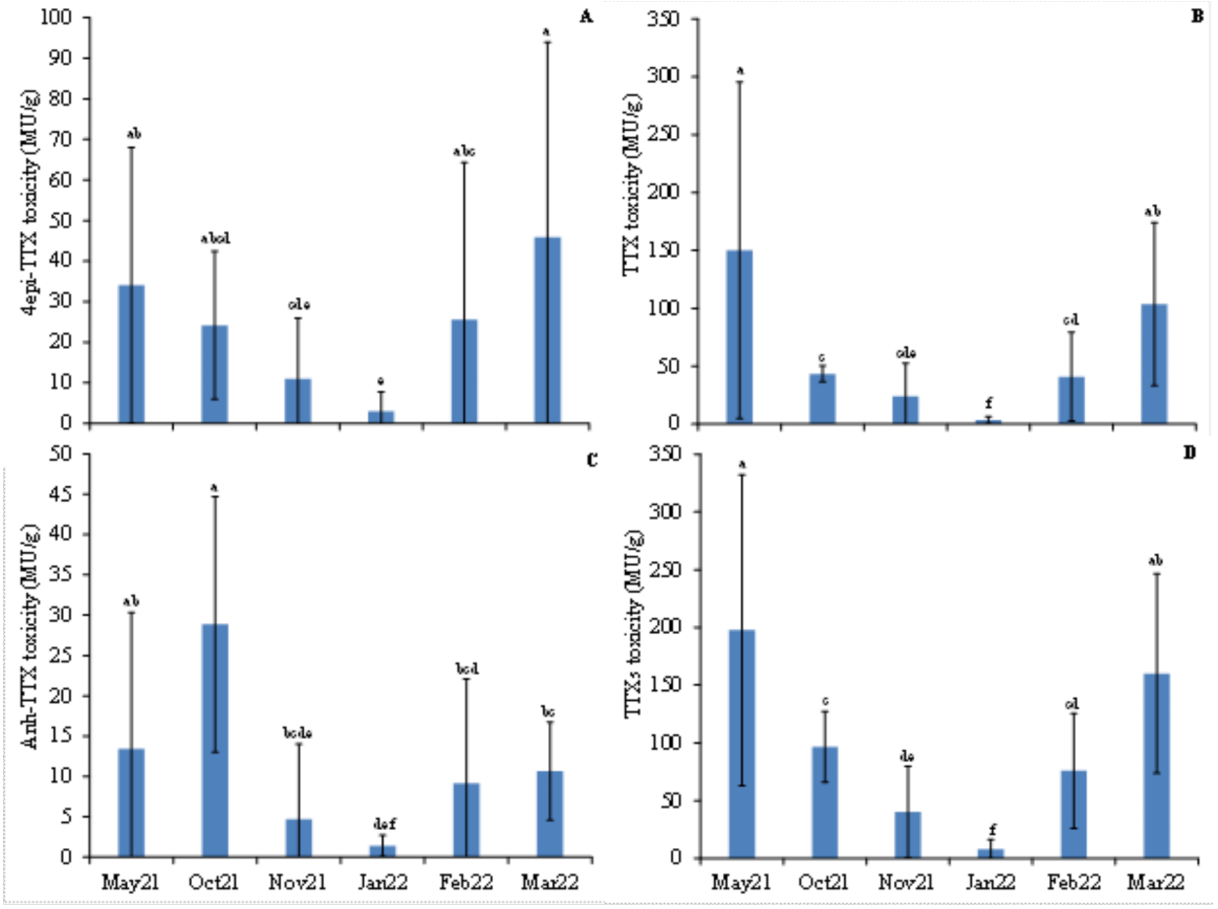

Figure 3. Seasonal variation of 4epi-TTX (A), TTX (B), Anh-TTX (C) and TTXs (D) in *Carcinoscorpius rotundicauda* collected from Can Gio coast, Vietnam in 2021 - 2022. Data is expressed as mean ± SD (n = 10). a, c, e, f are denoted as significant ($p < 0.05$).

Since horseshoe crab mainly feeds on Mollusca, arthropoda and detritus.[20] Consequently, bacteria or other microorganism inhabiting the decayed organic mattes might be the primary origin of TTX.[21] Therefore, the seasonal variation of TTXs in *C. rotundicauda* can be originated from TTX-bearing organisms which are consumed as their food through several steps of food web,[22] due to seasonal and spatial variation in TTX-producing bacteria community in the aquatic environment.[23] Among these food, TTX-producing bacteria such as *Vibrio* sp. was mentioned elsewhere.[24] On the other hand, toxins in *C. rotundicauda* may originate directly from defense mechanism, in which *C. rotundicauda* use these toxins for their defense to fight with enemy in the environment.[2]

3.2. Tetrodotoxin variation with body weight of C. rotundicauda

In this analysis, total sixty specimens were divided into five different groups. Each group contained 12 specimens with body weight categorized between 100 and 150g (100W150), 150 and 200g (150W200), 200 and 250g (200W250), 250 and 300g (250W300) and heavier than 300g (300W). The data shown in Figure 4 indicates that TTX and its analogues are generally higher levels in *C. rotundicauda* having larger body weight. Particularly, the variation of toxicity of 4epi-TTX (ANOVA, F= 4.049, p = 0.006, n = 12, Figure 4A), TTX (ANOVA, F= 10.062, $p = 3.4\times10^{-6}$, n = 12, Figure 4B), Anh-TTX (ANOVA, F= 4.596, p = 0.003, n = 12, Figure 4C) and TTXs (ANOVA, F = 22.589, $p = 4.47\times10^{-11}$,

n = 12, Figure 4D) among *C. rotundicauda* groups of 100W150, 150W200, 200W250, 250W300 and 300W are very significant. The maximal 4epi-TTX, TTX, Anh-TTX and TTXs toxicity were determined for 300W groups of 46.0 ± 50.0, 162.4 ± 135.8, 21.9 ± 18.9 and 230.3 ± 116.3 MU/g, respectively, whereas, the minimum levels of 4epi-TTX, TTX, Anh-TTX and TTXs toxicity of 1.7 ± 1.7, 7.3 ± 11.3, 0.8 ± 0.7 and 9.8 ± 12.3 MU/g, respectively, were quantified for 100W150 specimens. Toxicity of 4epi-TTX, TTX, Anh-TTX and TTXs determined for 150W200, 200W250 and 250W300 groups were 14.5 – 33.9 (Figure 4A), 30.1 – 57.7 (Figure 4B), 9.8 – 15.8 (Figure 4C) and 54.3 – 107.5 MU/g (Figure 4D), respectively. This interesting data resonate results obtained from moussed-based experiments conducted by Liao & Li who claimed that adult *C. rotundicauda* was more toxic than young *C. rotundicauda*.[25]

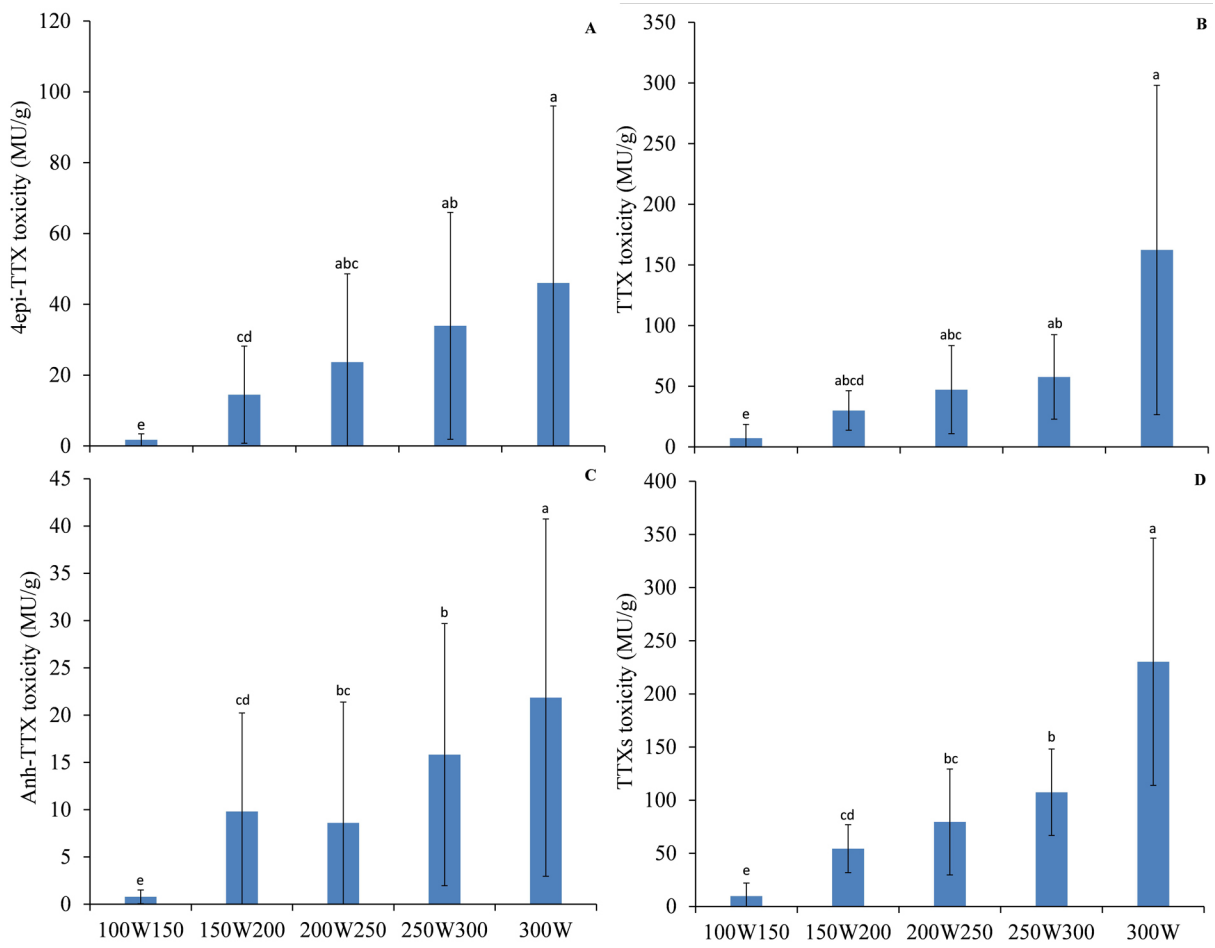

Figure 4. Toxicity variation of 4epi-TTX (A), TTX (B), Anh-TTX (C) and TTXs (D) in five different body-weight groups of *Carcinoscorpius rotundicauda* collected from Can Gio coast, Vietnam in 2021 - 2022. Data is presented as mean ± SD (n = 12). a, b, e are denoted as significant ($p < 0.05$).

3.3. Tetrodotoxin variation with gender of C. rotundicauda

The total of sixty specimens were divided into two groups of thirty female and thirty male *C. rotundicauda*. The data shown in Figure 5A illustrates that the toxicity levels of 4epi-TTX determined for female and male specimens were 24.6 ± 37.6 and 23.3 ± 26.8 MU/g, respectively, revealing the insignificant difference in variation of 4epi-TTX levels between two *C. rotundicauda* groups (ANOVA, $F = 0.025$, $p = 0.873$, $n = 30$, Figure 5A). Similarity, there was no significant difference of the Anh-TTX levels among female and male *C. rotundicauda* with respective

https://doi.org/10.52111/qnjs.2023.17506

toxicities determined of 14.5 ± 17.6 and 8.3 ± 9.3 MU/g (ANOVA, F = 2.870, p = 0.096, n = 30, Figure 5C). Contrastingly, there was a great variation of toxicity of TTX (ANOVA, F = 5.298, p = 0.025, n = 30, Figure 5B) and TTXs (ANOVA, F = 5.431, p = 0.023, n = 30, Figure 5D) among two groups of *C. rotundicauda.* Basically, female *C. rotundicauda* contained the significantly higher levels of TTX (84.8 ± 110.2 MU/g) and TTX (123.9 ± 121.3 MU/g) than those in male *C. rotundicauda* (TTX, 37.1 ± 26.6 MU/g; TTXs, 68.7 ± 45.8 MU/g). This data is attributed to eggs of female *C. rotundicauda* which generally contain high level of TTXs when compared to those of all soft tissue of male *C. rotundicauda*.[3,13,14]

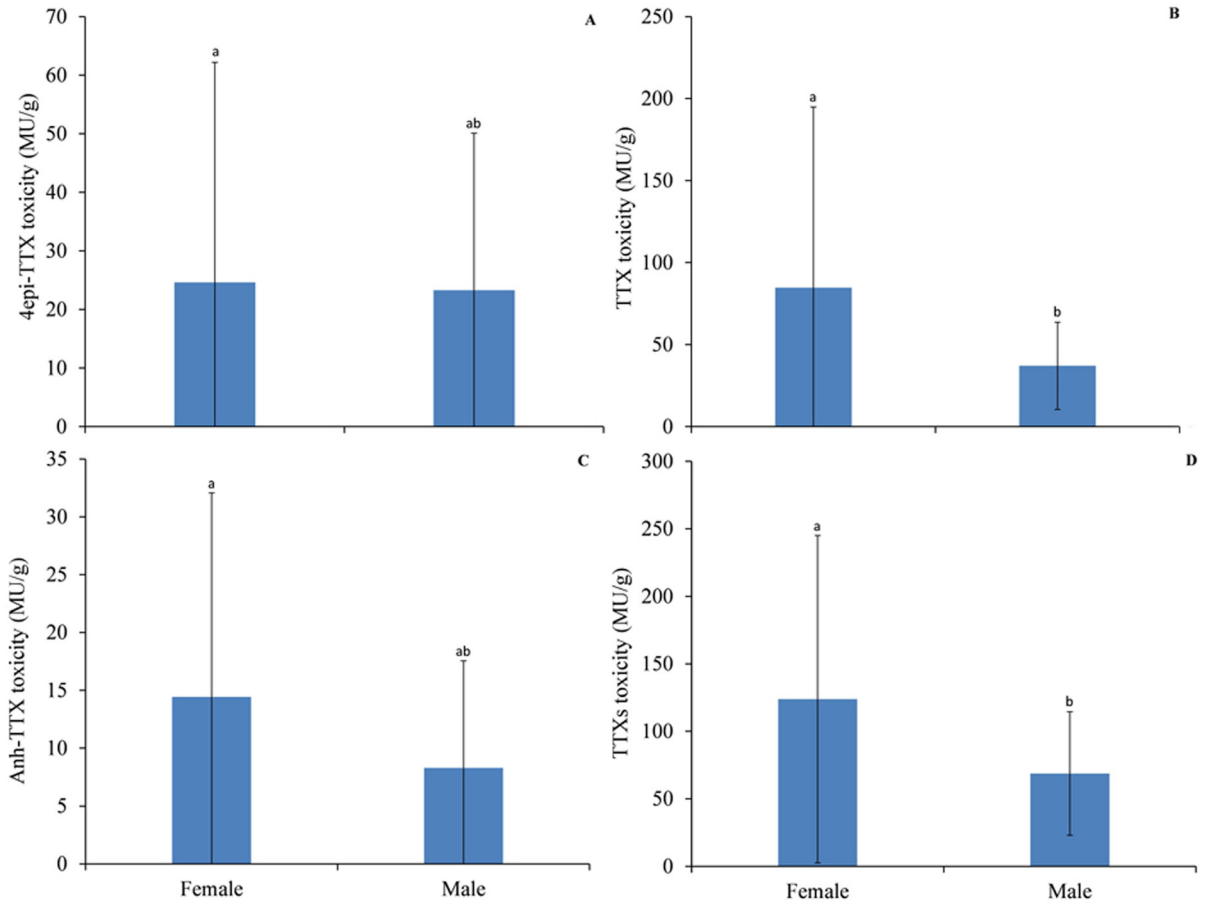

Figure 5. Toxicity variation of 4epi-TTX (A), TTX (B), Anh-TTX (C) and TTXs (D) in two different *Carcinoscorpius rotundicauda* female and male groups collected from Can Gio coast, Vietnam in 2021 - 2022. Data is presented as mean ± SD (n = 30), a, b are denoted as significant ($p < 0.05$).

Overall, toxicity and toxin composition of *C. rotundicauda* are principally varied depending on regional and individual variations.[1,3,13,14] Moreover, results obtained in this study further demonstrated that toxicity and toxin composition of *C. rotundicauda* are also season, gender as well as age variation. Despite considerable variation in TTXs composition and toxicity in Vietnamese *C. rotundicauda* over the months, the majority of specimens were toxic with the mean TTXs toxicity level of 96.3 ± 94.2 MU/g, suggesting that *C. rotundicauda* collected from Vietnam is not suitable for human consumption. Nevertheless, this is a promising source for isolation and purification of TTXs for research and development applications.

4. CONCLUSIONS

TTXs contributed 100% toxicity of *C. rotundicauda* collected from Can Gio coast, Ho Chi Minh City, Vietnam in May 2021 to March 2022. There were

significant variations of TTXs level over the months with maximal TTXs toxicity determined of 197.6 ± 134.5 MU/g for specimens collected in May 2021, whereas the *C. rotundicauda* collected in January 2021 was found to yield minimum TTXs level of 7.8 ± 8.4 MU/g. Interestingly, the difference of TTXs level in different body-weight *C. rotundicauda* groups was also statistically significant, with maximal TTXs toxicity of 230.3 ± 116.3 MU/g determined for specimens having body weight of greater than 300g, while the lowest level of TTXs (9.8 ± 12.3 MU/g) was assayed for *C. rotundicauda* group of body weight less than 150g. Moreover, there was a significant difference in TTXs levels among female and male *C. rotundicauda* groups, with notable higher TTXs toxicity determined for female specimens (123.9 ± 45.8 MU/g) than that of male *C. rotundicauda* (68.7 ± 45.8 MU/g). The data obtained in this study further confirmed that this is a promising source for isolation and purification of TTXs for research and development applications.

Acknowledgement

This research was financially funded by Vietnam Academy of Science and Technology (VAST) under the grant code of TĐĐTB0.06/21-23.

REFERENCES

1. H. V. Dao, Y. Takata, S. Sato, Y. Fukuyo, M. Kodama. Frequent occurrence of the tetrodotoxin-bearing horseshoe crab *Carcinoscorpius rotundicauda* in Vietnam, *Fisheries Science,* **2009**, 75, 435-438.
2. A. Kungsuwan, Y. Nagashima, T. Noguchi, Y. Shida, S. Suvapeepan, P. Suwansakornkul, K. Hashimoto. Tetrodotoxin in the Horseshoe crab *Carcinoscorpius rotundicauda* inhabiting Thailand, *Nippon Suisan Gakkaishi,* **1987**, *53*, 261-266.
3. R. Zheng, Q. Guan, M. Zheng, Z. Huang, H. Huang, W. Fu, S. Lin, Y. Yang. Toxin and toxicity identification of mangrove horseshoe crab *Carcinoscorpius rotundicauda* collected from South China, *Toxicon,* **2019**, *161*, 23-27.
4. N. Fusetani, H. Endo, K. Hashimoto, K. Takahashi. Occurrence of potent toxins in the horseshoe crab *Carcinoscorpius rotundicauda*, *Toxicon,* **1982**, *20,* 662-664.
5. S. Konosu, A. Inoue, T. Noguchi, and Y. Hashimoto. Comparison of crab toxin with saxitoxin and tetrodotoxin, *Toxicon*, **1968**, *6*, 113-117.
6. J. Kanchanapongkul, A. Kungsuwan, V. Tantisiriwan, C. Punthawangkun, P. Krittayapoositpot. An outbreak of horseshoe crab poisoning in Chon Buri, Thailand: clinical, toxicologic and therapeutic considerations, *The Southeast Asian Journal of Tropical Medicine and Public Health,* **1996**, *27*, 806-809.
7. J. Kanchanapongkul. Tetrodotoxin poisoning following ingestion of the toxic eggs of the horseshoe crab *Carcinoscorpius rotundicauda*, a case series from 1994 through 2006, *The Southeast Asian Journal of Tropical Medicine and Public Health,* **2008**, *39*, 303-306.
8. J. Kanchanapongkul, P. Krittayapoositpot. An epidemic of tetrodotoxin poisoning following ingestion of the horseshoe crab *Carcinoscorpius rotundicauda*, *The Southeast Asian Journal of Tropical Medicine and Public Health,* **1995**, *26*, 364-367.
9. M. Suleiman, J. Muhammad, J. Jelip, T. William, T. H. Chua. An outbreak of tetrodotoxin poisoning from consuming Horseshoe crabs in sabah, *The Southeast Asian Journal of Tropical Medicine and Public Health,* **2017**, *48*, 197-203.
10. H. N. Huang, R. J. Zheng, L. L. Liu, M. Zheng, Z. J. Li. Determination of tetrodotoxin in *Carcinoscorpius rotundicauda* (Horseshoe Crab) by high-performance liquid chromatography-tandem mass spectrometry, *Analytical Letters,* **2016**, *49*, 2377-2383.
11. Y. Liao, X. Li. Poisoning from eating horseshoe crab and its prevention and treatment, *Wei Sheng Yan Jiu,* **2001**, *30*, 122-124.

12. B. Joob, V. Wiwanitkit. Death rate due to horseshoe crab poisoning: summarization on Thai reports, *Journal of Coastal Life Medicine,* **2015**, *3*.

13. L. Ngy, C.-F. Yu, T. Takatani, O. Arakawa. Toxicity assessment for the horseshoe crab *Carcinoscorpius rotundicauda* collected from Cambodia, *Toxicon,* **2007**, *49*, 843-847.

14. M. B. Tanu. Tetrodotoxin as a toxic principle in the horseshoe crab *Carcinoscorpius rotundicauda* collected from Bangladesh, *Food Hygiene and Safety Science,* **1999**, *40*, 426-430.

15. S. Brillantes, W. Samosorn, S. Faknoi, Y. Oshima. Toxicity of puffers landed and marketed in Thailand, *Fisheries Science,* **2003**, *69*, 1224-1230.

16. M. J. Boundy, A. I. Selwood, D. T. Harwood, P. S. McNabb, A. D. Turner. Development of a sensitive and selective liquid chromatography-mass spectrometry method for high throughput analysis of paralytic shellfish toxins using graphitised carbon solid phase extraction, *Journal of Chromatography A,* **2015**, *1387*, 1-12.

17. M. Nakamura, T. Yasumoto. Tetrodotoxin derivatives in puffer fish, *Toxicon,* **1985**, *23*, 271-276.

18. M. Nakamura, T. Yasumoto. Tetrodotoxin derivatives in puffer fish, *Toxicon: Official Journal of the International Society on Toxinology,* **1985**, *23*, 271-276.

19. P. Katikou, C. Gokbulut, A. R. Kosker, M. Campàs, and F. Ozogul. An updated review of tetrodotoxin and its peculiarities, *Marine Drugs*, **2022**, *20*, 47.

20. A. Chatterji, J. K. Mishra, A. H. Parulekar. Feeding behaviour and food selection in the horseshoe crab, *Tachypleus gigas* (Müller), *Hydrobiologia,* **1992**, *246*, 41-48.

21. U. Simidu, T. Noguchi, D. F. Hwang, Y. Shida, K. Hashimoto. Marine bacteria which produce tetrodotoxin, *Applied and Environmental Microbiology,* **1987**, *53*, 1714-1715.

22. A. Kungsuwan, T. Noguchi, O. Arakawa, U. Simidu, K. Tsukamoto, Y. Shida, K. Hashimoto. Tetrodotoxin-producing bacteria from the horseshoe crab *Carcinoscorpius rotundicauda*, *Nippon Suisan Gakkaishi,* **1988**, *54*, 1799-1802.

23. L. Biessy, J. K. Pearman, K. F. Smith, I. Hawes, S. A. Wood. Seasonal and spatial variations in bacterial communities from tetrodotoxin-bearing and non-tetrodotoxin-bearing clams, *Frontiers in Microbiology,* **2020**, *11*.

24. T. Y. Magarlamov, D. I. Melnikova, A. V. Chernyshev. Tetrodotoxin-producing bacteria: detection, distribution and migration of the toxin in aquatic systems, *Toxins,* **2017**, *9*, 166.

25. Y. Liao, X. Li. Study on the toxicity of horseshoe crabs in mice, *Journal of Hygiene Research,* **2000**, *29*, 184-185.

TẠP CHÍ KHOA HỌC
TRƯỜNG ĐẠI HỌC QUY NHƠN

Sử dụng mô hình tensor để mở rộng bài toán ước lượng kênh LS cho các hệ thống MIMO có hỗ trợ bề mặt phản xạ thông minh

Đào Minh Hưng*, Nguyễn Đỗ Dũng

Khoa Kỹ thuật và Công nghệ, Trường Đại học Quy Nhơn

Ngày nhận bài: 25/07/2023; Ngày sửa bài: 06/09/2023; Ngày nhận đăng: 18/09/2023; Ngày xuất bản: 28/10/2023

TÓM TẮT

Bài báo đề xuất mở rộng hai thuật toán ước lượng kênh LS dựa trên mô hình tín hiệu tensor cho các hệ thống MIMO được hỗ trợ bởi bề mặt phản xạ thông minh (IRS). Hai thuật toán này khai thác cấu trúc tensor của tín hiệu hoa tiêu để thiết lập bài toán ước lượng kênh ghép tầng. Thuật toán thứ nhất mở rộng ước lượng LS dựa trên việc khai thác cấu trúc Khatri-Rao Factorization (KRF) của kênh MIMO ghép tầng, bằng cách giải các bài toán con xấp xỉ ma trận hạng 1. Bài toán ước lượng thứ hai dựa trên thuật toán BALS (Bilinear Alternating Least Squares), đây là phiên bản đơn giản hóa của thuật toán TALS (Trilinear Alternating Least Squares). Ngoài ra, bài báo này cũng trình bày mối quan hệ giữa các tham số kênh MIMO để các thuật toán ước lượng trên có tính khả thi. Kết quả mô phỏng cho thấy các phương pháp ước lượng LS mở rộng dựa trên mô hình tín hiệu tensor đã cải thiện hiệu suất so với ước lượng LS truyền thống.

Từ khóa: *Ước lượng kênh, bề mặt phản xạ thông minh, thuật toán dựa trên tensor, Khatri-Rao factorization*.

**Tác giả liên hệ chính.*
Email: daominhhung@qnu.edu.vn

QUY NHON UNIVERSITY
JOURNAL OF SCIENCE

Using tensor model to extend least squares channel estimation problem for the intelligent reflecting surface assisted MIMO systems

Dao Minh Hung*, Nguyen Do Dung

Faculty of Engineering and Technology, Quy Nhon University, Vietnam

Received: 25/07/2023; Revised: 06/09/2023; Accepted: 18/09/2023; Published: 28/10/2023

ABSTRACT

This paper proposes to extend two Least Squares (LS) channel estimation algorithms based on tensor signal model to MIMO systems supported by Intelligent Reflective Surfaces (IRS). These two algorithms exploit the tensor structure of the pilot signal to establish the cascaded channel estimation problem. The first algorithm extends the LS estimation based on exploiting the Khatri-Rao Factorization (KRF) structure of the cascaded MIMO channel, by solving subproblems approximating the 1-rank matrix. The second estimator is based on the Bilinear Alternating Least Squares (BALS) algorithm, which is a simplified version of the Trilinear Alternating Least Squares (TALS) algorithm. In addition, this paper also presents the relationship between the MIMO channel parameters for the above estimation algorithms to be feasible. The simulation results show that the extended LS estimation methods based on the tensor signal model have improved performance compared with the conventional LS estimation.

Keyword: *Channel estimation, intelligent reflecting surfaces, tensor-based algorithm, Khatri-Rao factorization*.

1. INTRODUCTION

Over the past decade, Multiple Input Multiple Output (MIMO) communication systems have been extensively studied and considered a key technology for enhanced mobile broadband communications in fifth generation networks (5G), the future beyond-5G (B5G) and sixth generation (6G). Several works have thoroughly investigated both theoretical and practical solutions on spectral efficiency analysis, data rate increase, reliability improvement and interference reduction, etc.[1-4] MIMO systems can be classified into different types, such as Single-User MIMO (SU-MIMO), Multi-User MIMO (MU-MIMO), massive MIMO and millimeter wave MIMO, depending on the number of user, the number of antennas and the operating frequency bands. MIMO systems can be applied in wireless communication systems, such as cellular networks, wireless Local Area Networks (WLANs), vehicle networks, satellite communications, and radar systems. Some trends in the application of MIMO systems include: Internet of Things (IoT) device systems, MIMO for Unmanned Aerial Vehicles (UAVs) and MIMO for cognitive radio networks.

The above mentioned advantages of MIMO systems are achieved by the outstanding

**Corresponding author.*
Email: daominhhung@qnu.edu.vn

https://doi.org/10.52111/qnjs.2023.17507

characteristic of channel hardening, i.e. the characteristic of user channels that do not fading over time and the favorable propagation over multipath channel. However, for MIMO systems, including massive MIMO, there is an open problem to ensure the performance of users in service dead zones, for example, indoor users with thick walls between them and the Base Station (BS) or outdoor users surrounded by many tall buildings, where gain is difficult to compensate for severe channel loss.

In the last few years, a number of studies have discussed the potentials and challenges of wireless communications assisted by Intelligent Reflective Surfaces (IRS).[5-7] Much research has been done on both the theory and implementation of IRS application in MIMO communication systems to maintain performance and increase user coverage in service dead zones. With the assistance of the IRS, MIMO systems can suppress Co-Channel Interference (CCI) when the user is at the edge of the cell,[8,9] or to improve physical layer security.[10,11] Besides, IRS can be used for information and power transfer in a IoT networks.[8] IRS also known as reconfigurable smart surface or software controlled hypersurface consisting of a 2D array with a large number of passive or semi-passive elements can control the electromagnetic characteristics of radio frequency waves so that the reflected signal adds coherently at the receiver or cancels it out to reduce CCI.[5-9] Each element can operate independently and can be reconfigured in a software-defined manner using an external controller. The IRS does not require dedicated Radio Frequency (RF) strings and is powered wirelessly by an external RF source. This is in contrast to relay systems that need amplify-and-forward or decode-and-forward, and require specialized power sources.[6]

In MIMO systems, the availability of Channel State Information (CSI) is a topic of intense research. Accurate and timely CSI knowledge plays an important role in wireless communication systems. For IRS-assisted MIMO systems, there are often a large number of IRS elements, which poses a significant challenge to solving the channel estimation problem in collecting CSI. In these systems, there are two basic methods for performing channel estimation. First, use the IRS with a semi-passive structure in which several active elements connected to receive the RF string. In this case, the parts that actively perform baseband processing at the IRS facilitate the collection of CSI.[12]

In the second method, the IRS has a full passive structure, where the IRS works by reflecting the impinging waves according some phase shift pattern. This is a more difficult case, where at the receiver based on the pilot signals sent by the transmitter and reflected by the IRS performs a cascade estimation between the transmitter to the IRS and the IRS to the receiver. In this case, the IRS uses a phase shift model in which the training phases play an important role. This is the method used in this paper.

A number of published works refer to different solutions to the channel estimation problem for the case of passive IRS. T. L. Jensen et al. have proposed an unbiased estimation method with minimal variance and an optimal calculation of the IRS phase shift matrix, in which the IRS elements are completely passive.[13] The authors in the reference,[14] propose a two-stage algorithm by exploiting the sparse code characteristics of multipath channels with low rank channel matrices. The cooperative channel estimation through the training beam of IRS-assisted massive MIMO systems on the terahertz channel is presented[15]. IRS was proposed as a solution to reduce the congestion problem and also presented the method of channel estimation on millimeter wave channel.[16] The IRS-assisted MIMO system is considered and channel estimation is performed by the two-stage

method and the IRS-supported transmission route is estimated by the approximate message transmission method.[17] In the study,[18] established the channel estimation based on sparse matrix factorization of the Internet of Things (IoT) system supported by the IRS. The latest research works,[19-21] successfully applied tensor models in many signal processing problems, especially for wireless communication systems. Semi-blind channel estimation methods for MIMO systems have also considered,[22,23] channel estimation methods for cooperative communication,[24,25] and more recently, estimation methods compressed channel in massive MIMO systems.[26,27]

In most of these works, signal processing is very efficient thanks to the uniqueness of tensor decomposition to exploit the multidimensional nature of transmitted/received signals and communication channels. The parallel factor (PARAFAC) structure of the tensor model is very convenient for the estimation problem of time varying multipath channel parameters by using pilot signal pattern and IRS phase shift signals in time domain.[28]

In this paper, the tensor model is used to extend the least squares channel estimation problem. Instead of solving the cascaded MIMO channel estimation problem, we propose the separate MIMO channel estimation problem between the base station transmitter to the IRS (BS-IRS) and between the IRS to the User Terminal (IRS-UT) by exploiting the PARAFAC structure. Accordingly, we set up two algorithms. The first algorithm is a closed-form solution based on the Khatri-Rao factorization (KRF) of the combination of BS-IRS and IRS-UT channels. The second algorithm performs an iterative Bilinear Alternating Least Squares (BALS). The first algorithm is a closed-form algebraic and less complex solution, the second one can operate under less restrictive conditions on the system parameters.

The contributions of this article are summarized as follows.

• Using tensor model to set up two LS channel estimation algorithms based on Khatri-Rao Factorization (KRF) and the Bilinear Alternating Least Squares (BALS).

• Consider the relationship between the IRS-assisted MIMO system parameters for the estimated matrix rank to make the problems feasible.

Notation and operator: Matrices are represented with boldface capital letters (**A**; **B**;…), and vectors are denoted by boldface lowercase letters (**a**; **b**;...). Tensors are symbolized by calligraphic letters. Transpose and pseudo-inverse of a matrix $\mathbf{A}$ are denoted as $\mathbf{A}^T$ and $\mathbf{A}^\dagger$. $\|\mathbf{A}\|_F$ denote the Frobenius norm of $\mathbf{A}$. The operator diag(**a**) forms a diagonal matrix out of its vector argument, while $*, \circ, \lozenge, \odot, \otimes$ denote the conjugate, outer product, Khatri Rao, Hadamard and Kronecker products, respectively. $\mathbf{I}_N$ denotes the $N \times N$ identity matrix. The operator vec(·) vectorizes an $I \times J$ matrix argument, while $\text{unvec}_{I\times J}(\cdot)$ does the opposite operation. Moreover, vecd(·) forms a vector out of the diagonal of its matrix argument. The n-mode product between a tensor $\Upsilon \in \mathbb{C}^{I\times J\ldots K}$ and a matrix $\mathbf{A} \in \mathbb{C}^{I\times R}$ is denoted $\Upsilon \times_n \mathbf{A}$, for $1 \le n \le N$. The operator $D_i(\mathbf{A})$ forms a diagonal matrix from the i-th row of its matrix argument $\mathbf{A}$. Moreover, $\mathbf{A}_i$ denotes the i-th row of the matrix $\mathbf{A}$.

2. SIGNAL MODEL AND SYSTEM

In this article review the MIMO communication systems assisted by an IRS. The transmitter side is a Base Station (BS) equipped with an array of M_B antennas and the receiver side is a User Terminal (UT) with M_U antennas. The IRS consists of L passive elements, capable of individually adjusting their reflectances (i.e. phase shift control). The system model is illustrated in Figure 1.

https://doi.org/10.52111/qnjs.2023.17507

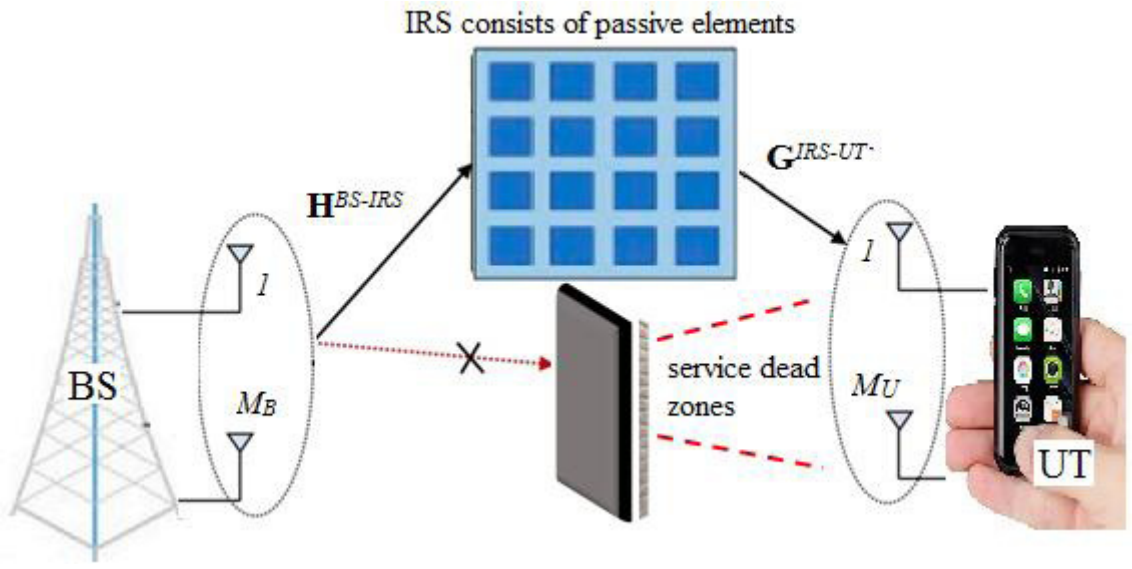

Figure 1. Model of the IRS-assisted MIMO system.

The signal at the device input can be represented by,[14,15]

$$\mathbf{y}[t] = \mathbf{G}^{IRS-UT}(\mathbf{s}[t] \odot \mathbf{H}^{BS-IRS}\mathbf{x}[t]) + \mathbf{n}[t], \quad 1 \le t \le T, \tag{1}$$

or in a different way,

$$\mathbf{y}[t] = \mathbf{G}^{IRS-UT}\text{diag}(\mathbf{s}[t])\mathbf{H}^{BS-IRS}\mathbf{x}[t]) + \mathbf{n}[t], \tag{2}$$

where, $\mathbf{x}[t] \in \mathbb{C}^{M_B \times 1}$ is a vector whose elements are transmitted pilot signals at time t, $\mathbf{s}[t]=\left[s_{1,t}e^{j\phi_1},...,s_{L,t}e^{j\phi_L}\right]^T \in \mathbb{C}^{L\times 1}$ is the vector that models the phase shifts and activation pattern of the IRS, where $\phi_n \in (0, 2\pi]$ is phase shift and $s_{n,t} \in \{0,1\}$ is the magnitude that controls the on-off state of the IRS elements at time t, respectively. $\mathbf{H}^{BS-IRS} \in \mathbb{C}^{L\times M_B}$ is the MIMO channel matrix from base station BS to IRS and $\mathbf{G}^{IRS-UT} \in \mathbb{C}^{M_U \times L}$ denote the MIMO channel between the IRS and the user terminal UT, and $\mathbf{n}[t] \in \mathbb{C}^{M_U \times 1}$ is the Additive White Gaussian Noise (AWGN) vector.

The training signal is modeled as shown in Figure 2. The training signal length T_s is divided into Q blocks, where each block is called a time slot of length T, i.e. $T_s = QT$. In expression (2), $\mathbf{y}[q,t] \triangleq y[(q-1)T+t]$ as the received signal at the t-th time slot of the q-th block, $t = 1,..., T$, $q = 1,..., Q$. Suppose, the time slot transmission, IRS adjusts its phase shifts as a function of time $t = 1,..., T$ and a block-fading channel, which means that the BS-IRS and IRS-UT channels are constant during T time slots.

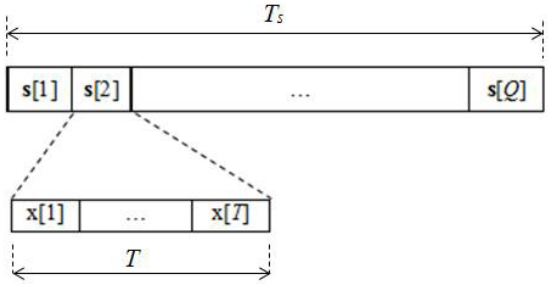

Figure 2. The time frame structure of the pilot signal pattern.

According to the signal frame structure in Figure 2, the IRS phase shift vector $\{\mathbf{s}[1],...,\mathbf{s}[Q]\}$ is constant during the T time slots of the q-th block and varies from block to block and the pilot signals $\{\mathbf{x}[1],...,\mathbf{x}[T]\}$ are repeated over the Q blocks. Mathematical representation in,[14]

$$\mathbf{s}[q,t] = \mathbf{s}[q], \ 1 \le t \le T \tag{3}$$

$$\mathbf{x}[q,t] = \mathbf{x}[q], \ 1 \le q \le Q \tag{4}$$

Accordingly, the signal in expression (2) is rewritten as

$$\mathbf{y}[q,t]=\mathbf{G}^{IRS-UT}\text{diag}(\mathbf{s}[q]\mathbf{H}^{BS-IRS}\mathbf{x}[t] + \mathbf{n}[q,t]. \tag{5}$$

All signals received in the time slot T of the q-th block, represented by the vector,

$\mathbf{Y}[q]=\left[\mathbf{y}[q,1]...\mathbf{y}[q,T]\right]\in\mathbf{C}^{M_U\times T}$ so we can perform,[14]

$$\mathbf{Y}[q]=\mathbf{G}^{IRS-UT}\text{diag}(\mathbf{s}[q])\mathbf{H}^{BS-IRS}\mathbf{X}^T+\mathbf{N}[q], \quad (6)$$

where, $\mathbf{X}\triangleq\left[\mathbf{x}[1],...,\mathbf{x}[T]\right]^T\in\mathbb{C}^{T\times M_B}$, and $\mathbf{N}\triangleq\left[\mathbf{n}[1],...,\mathbf{n}[T]\right]\in\mathbb{C}^{M_U\times T}$.

3. LEAST SQUARES (LS) CHANNEL ESTIMATION WITH TENSOR SIGNAL MODELING

Least Squares (LS) channel estimation is the most commonly used basic linear estimation method for channel estimation. LS channel estimation performs the minimum squared distance between the received signal and the transmitted signal.

To derive the LS estimate in the case in question, apply the property $\text{vec}(\mathbf{ABC})=\left(\mathbf{C}^T\lozenge\mathbf{A}\right)\text{vec}(\mathbf{B})$ and transform the expressions from (1) to (6), we have:

$$\begin{aligned}\mathbf{y}[q]&=\left\{\mathbf{X}(\mathbf{H}^{BS-IRS})^T\lozenge\mathbf{G}^{\mathbf{IRS\text{-}UT}}\right\}\mathbf{s}_q\\&=\left(\mathbf{X}\otimes\mathbf{I}_{M_U}\right)\left\{(\mathbf{H}^{BS-IRS})^T\lozenge\mathbf{G}^{\mathbf{IRS\text{-}UT}}\right\}\mathbf{s}[q]+\mathbf{n}[q],\end{aligned} \quad (7)$$

where,

$\mathbf{y}[q]\triangleq\text{vec}(\mathbf{Y}[q])\in\mathbb{C}^{M_UT}$,

$\mathbf{n}[q]\triangleq\text{vec}(\mathbf{N}[q])\in\mathbb{C}^{M_UT}$ and we have used property $(\mathbf{A}\otimes\mathbf{B})(\mathbf{C}\lozenge\mathbf{D})=(\mathbf{AC})\lozenge(\mathbf{BD})$.[28,29]

Defining $\mathbf{Y}\triangleq\left[\mathbf{y}[1]...\mathbf{y}[Q]\right]\in\mathbb{C}^{M_UT\times Q}$ and $\tilde{\mathbf{X}}\triangleq(\mathbf{X}\otimes\mathbf{I}_{M_U})\in\mathbb{C}^{TM_U\times M_BM_U}$, we have

$$\tilde{\mathbf{Y}}=\tilde{\mathbf{X}}\left\{(\mathbf{H}^{BS-IRS})^T\lozenge\mathbf{G}^{IRS\text{-}UT}\right\}\mathbf{S}^T+\mathbf{N}, \quad (8)$$

where, $\mathbf{S}\triangleq\left[\mathbf{s}[1],...,\mathbf{s}[Q]\right]^T\in\mathbb{C}^{Q\times L}$, and $\mathbf{N}\in\mathbb{C}^{M_UT\times Q}$ is the noise matrix set up in the same way as $\mathbf{Y}$. Finally, defined $\mathbf{y}\triangleq\text{vec}\left(\tilde{\mathbf{Y}}\right)\in\mathbb{C}^{M_UTQ}$, and apply the property $vec(\mathbf{ABC})=\left(\mathbf{C}^T\otimes\mathbf{A}\right)vec(\mathbf{B})$ to expression (8), we have

$$\mathbf{y}=\left(\mathbf{S}\otimes\tilde{\mathbf{X}}\right)\text{vec}\left\{(\mathbf{H}^{BS-IRS})^T\lozenge\mathbf{G}^{\mathbf{IRS\text{-}UT}}\right\}+\mathbf{n} \quad (9)$$

or simply write in $\mathbf{y}=\mathbf{U}\boldsymbol{\theta}+\mathbf{n}$, (10)

where, $\mathbf{U}\triangleq\mathbf{S}\otimes\tilde{\mathbf{X}}\in\mathbb{C}^{QTM_U\times LM_BM_U}$, and $\boldsymbol{\theta}\triangleq\text{vec}\left\{(\mathbf{H}^{BS-IRS})^T\lozenge\mathbf{G}^{\mathbf{IRS\text{-}UT}}\right\}\in\mathbb{C}^{M_BM_UL}$ is the composite channel parameter, combining the BS-IRS and IRS-UT channels. Estimating the LS channel applied to the composite channel in our case is the minimum of the problem,[6]

$$\hat{\boldsymbol{\theta}}=\arg\min_{\boldsymbol{\theta}}\left\|\mathbf{y}-\mathbf{U}\boldsymbol{\theta}\right\|^2, \quad (11)$$

the solution (11) results found $\boldsymbol{\theta}=\mathbf{U}^{\dagger}\mathbf{y}$. Applying the Kronecker product of $\mathbf{U}$, this solution can be simply rewritten $\boldsymbol{\theta}=(\mathbf{S}^{\dagger}\otimes\tilde{\mathbf{X}}^{\dagger})\mathbf{y}$.

In the conventional LS estimation problems just presented, the composite channel linear parameter vector $\boldsymbol{\theta}$ does not use the Katri-Rao structure. This is unfortunate, because the signal expression (6), or its equivalent (8) can be written as a parallel factor (PARAFAC) tensor model. The application of tensor model allows to improve the accuracy of channel estimation compared to traditional LS methods. This can compute a separate estimate for the $\mathbf{H}^{BS-IRS}$ and $\mathbf{G}^{IRS-UT}$ channels instead of the composite channel estimate $\boldsymbol{\theta}$.

To simplify the signal modeling by tensor operation, we first ignore the noise component in expression (6), leaving only the signal component, so we can rewrite as

$$\hat{\mathbf{P}}[q]=\mathbf{G}^{IRS-UT}\mathbf{D}_q(\mathbf{S})\mathbf{Z}^T,\ \mathbf{Z}\triangleq\mathbf{X}\left(\mathbf{H}^{BS-IRS}\right)^T\in\mathbb{C}^{T\times L}, \quad (12)$$

where, $\mathbf{D}_q(\mathbf{S})\triangleq\text{diag}(\mathbf{s}[q])$ denotes diagonal matrix of the q-th row of the IRS phase shift matrix $\mathbf{S}$ on its main diagonal. The matrix $\hat{\mathbf{P}}[q]$ can be viewed as the q-th front matrix slice of the 3-dimensional tensor $\overline{\Upsilon}\in\mathbb{C}^{M_U\times T\times Q}$; according to the PARAFAC decomposition. This operation is also the Canonical Polyadic Decomposition (CPD). Each (m, t, q)-th element of the received signal tensor, regardless of noise, is written in,[28-31]

$$\hat{p}_{m,t,q}=\sum_{n=1}^{L}g_{m,n}z_{t,n}s_{q,n}, \quad (13)$$

where, $g_{l,n}\triangleq[\mathbf{G}^{IRS-UT}]_{m,n}$, $z_{t,n}\triangleq[\mathbf{Z}]_{t,n}$, $s_{q,n}\triangleq[\mathbf{S}]_{q,n}$.

The abbreviation for PARAFAC decomposition (13) is written as $\overline{\Upsilon}=\left[\mathbf{G}^{IRS-UT},\mathbf{Z},\mathbf{S}\right]$. Using n-mode product notation, the PARAFAC decomposition

https://doi.org/10.52111/qnjs.2023.17507

of the zero-noise received signal tensor can be represented by,[28,29]

$$\bar{\Upsilon} = \Gamma_{3,L} \times_1 \mathbf{G}^{IRS-UT} \times_2 \mathbf{Z} \times_3 \mathbf{S}. \quad (14)$$

Exploiting the linear triple of the PARAFAC decomposition, we can expand the received signal tensor $\bar{\Upsilon}$ in the form of three matrices as follows,[28,29]

$$\hat{\mathbf{P}}_1 = \mathbf{G}^{IRS-UT}(\mathbf{S} \lozenge \mathbf{Z})^T \in \mathbb{C}^{M_U \times TQ}, \quad (15)$$

$$\hat{\mathbf{P}}_2 = \mathbf{Z}(\mathbf{S} \lozenge \mathbf{G}^{IRS-UT})^T \in \mathbb{C}^{M_U \times TQ}, \quad (16)$$

$$\hat{\mathbf{P}}_3 = \mathbf{S}(\mathbf{Z} \lozenge \mathbf{G}^{IRS-UT})^T \in \mathbb{C}^{Q \times M_U T}, \quad (17)$$

where, $\hat{\mathbf{P}}_1 \triangleq \left[\hat{\mathbf{P}}[1],...,\hat{\mathbf{P}}[K]\right]$, $\hat{\mathbf{P}}_2 \triangleq \left[\hat{\mathbf{P}}^T[1],...,\hat{\mathbf{P}}^T[Q]\right]$ $\hat{\mathbf{P}}_3 \triangleq \left[\text{vec}(\hat{\mathbf{P}}[1]),...,\text{vec}(\hat{\mathbf{P}}[Q])\right]^T$.

Next, the algebraic structure of the PARAFAC (13) model is exploited to establish two methods of channel estimation. The PARAFAC model is very usable thanks to its essential factor identification uniqueness property, which is derived from the concept of Kruskal rank (*k*-rank).

4. PROPOSAL TO EXTEND LS CHANNEL ESTIMATION UNDER TENSOR SIGNAL MODEL

In this section, we extend the estimating $\mathbf{H}^{BS-IRS}$ and và $\mathbf{G}^{IRS-UT}$ channel matrices from the Tensor signal modeling is presented as shown in (13). First, we define, $\Upsilon \triangleq \bar{\Upsilon} + \mathbb{N}$ as the noise-corrupted received signal tensor, where $\mathbb{N} \in \mathbb{C}^{M_U \times T \times Q}$ is the additive noise tensor. Similarly, $\mathbf{P}_i \triangleq \hat{\mathbf{P}}_i + \mathbf{N}_i$, $i = 1,2,3$ are the 1-mode, 2-mode, and 3-mode extended matrix noise versions respectively in the tensor expressions of the received signal (15-17), và $\mathbf{N}_{i=1,2,3}$ corresponds to the extended matrices of the noise tensor.

In this study, the pilot signal matrix $\mathbf{X}$ calculated using semi-unitary matrices satisfying $\mathbf{X}^H\mathbf{X} = T\mathbf{I}_{M_B}$, same for the phase shifts matrix IRS $\mathbf{S}$ is $\mathbf{S}^H\mathbf{S} = Q\mathbf{I}_L$. A best option for computing $\mathbf{X}$ and $\mathbf{S}$ matrices is to use truncated Discrete Fourier transform (DFT) matrices.

4.1. LS channel estimation based on Khatri-Rao Factorization

We can first rewrite the noise expansion matrix (17) as

$$\begin{aligned}\mathbf{P}_3 &= \mathbf{S}(\mathbf{Z} \lozenge \mathbf{G}^{IRS-UT})^T + \mathbf{N}_3 \\ &= \mathbf{S}\left[(\mathbf{H}^{BS-IRS})^T \lozenge \mathbf{G}^{IRS-UT}\right]^T \left[(\mathbf{H}^{BS-IRS})^T \lozenge \mathbf{G}^{IRS-UT}\right]^T + \mathbf{N}_3,\end{aligned} \quad (18)$$

in the transformations of the above expression, we used the property, $\mathbf{A} \otimes \mathbf{B}\ \ \mathbf{C} \lozenge \mathbf{D} = \mathbf{AC} \lozenge \mathbf{BD}$

Applying a bilinear filter on the time domain at the receiver by exploiting the knowledge of the IRS matrix and the pilot signal matrix, as follows

$$\mathbf{X}^\dagger \otimes \mathbf{I}_{M_U}\ \mathbf{P}_3^T\ \mathbf{S}^{T\ \dagger} = \mathbf{H}^{BS-IRS\ T} \lozenge \mathbf{G}^{IRS-UT} + \tilde{\mathbf{N}}_3 \triangleq \mathbf{\Omega}, \quad (19)$$

where, $\tilde{\mathbf{N}}_3 = \mathbf{X}^\dagger \otimes \mathbf{I}_{M_U}\ \mathbf{N}_3^T\ \mathbf{S}^{T\ \dagger}$ is the noise component after filtering. Note, $\mathbf{\Omega} \in \mathbb{C}^{M_B M_U \times L}$ is the Khatri-Rao structured noise version of the virtual MIMO channel in an IRS-assisted MIMO systems. Based on the semi-unitary structure of the $\mathbf{S}$ and $\mathbf{X}$ matrices, the correlation properties of the additive noise are not affected by the bilinear filter step.

From expression (19), we deduce the estimation of the $\mathbf{H}^{BS-IRS}$ and $\mathbf{G}^{IRS-UT}$ matrices by the Khatri-Rao least squares approximation problem,

$$\min_{\mathbf{H},\mathbf{G}} \left\| \mathbf{\Omega} - (\mathbf{H}^{BS-IRS})^T \lozenge \mathbf{G}^{IRS-UT} \right\|_F^2. \quad (20)$$

The efficiency of this problem is thanks to the application of the KRF (Khatri-Rao factorization) algorithm. Expression (20) can be understood as finding the $\mathbf{H}^{BS-IRS}$ and $\mathbf{G}^{IRS-UT}$ matrix estimators to minimize the set rank 1 matrix approximations, [28,32,33]

$$\hat{\mathbf{H}}^{BS-IRS}, \hat{\mathbf{G}}^{IRS-UT} = \arg\min_{\mathbf{h}_n,\ \mathbf{g}_n} \sum_{n=1}^{L} \left\| \tilde{\mathbf{\Omega}}_n - \mathbf{g}_n \mathbf{h}_n^T \right\|_F^2, \quad (21)$$

where,

$\tilde{\mathbf{\Omega}}_n \triangleq \text{unvec}_{M_U \times M_B}\ \mathbf{\omega}_n\ \in \mathbf{C}^{M_U \times M_B}$, $\mathbf{g}_n \in \mathbf{C}^{M_U \times 1}$, and

https://doi.org/10.52111/qnjs.2023.17507

$\mathbf{h}_n^T \in \mathbf{C}^{1\times M_B}$ are the n-th column of $\mathbf{G}^{IRS\text{-}UT}$ matrix, and n-th row of $\mathbf{H}^{BS\text{-}IRS}$ matrix, respectively. The estimates of $\mathbf{g}_n$ and $\mathbf{h}_n$ in (21) can be obtained from the left and right dominant singular vectors $\tilde{\mathbf{\Omega}}_n$, respectively, with $1 \le n \le L$, respectively. Thus, the estimation problem under consideration is transformed into L approximation submatrix problems of rank 1. Once we find $\hat{\mathbf{H}}^{BS-IRS}$ and $\hat{\mathbf{G}}^{IRS-UT}$ from (21), we can set up a composite channel $\boldsymbol{\theta}$.

4.2. BALS channel estimation

From the noise versions of the expansion matrix in expressions (15) and (16), we can derive an iterative solution based on the Bilinear Alternating Least Squares algorithm. This algorithm is a simplified version of the Trilinear Alternating Least Squares algorithm for estimating the factor matrices of the PARAFAC model.[34] In this case, since the matrix $\mathbf{S}$ is known at the receiver, the $\mathbf{G}^{IRS\text{-}UT}$ and $\mathbf{H}^{BS\text{-}IRS}$ matrices are estimated by the method of interleaving by optimizing in the iterative process of the following two cost functions,[34]

$$\hat{\mathbf{G}}^{IRS-UT} = \arg\min_{\mathbf{G}^{IRS-UT}} \left\| \mathbf{P}_1 - \mathbf{G}^{IRS-UT} \left[\mathbf{S} \lozenge \mathbf{X}(\mathbf{H}^{BS-IRS})^T \right]^T \right\|_F^2, \tag{22}$$

$$\hat{\mathbf{H}}^{BS-IRS} = \arg\min_{\mathbf{H}^{BS-IRS}} \left\| \mathbf{P}_2 - \mathbf{X}(\mathbf{H}^{BS-IRS})^T \left[\mathbf{S} \lozenge \ \mathbf{G}^{IRS-UT\ T} \right]^T \right\|_F^2, \tag{23}$$

the results of the solutions are:

$$\hat{\mathbf{G}}^{IRS-UT} = \mathbf{P}_1 \left[\left[\mathbf{S} \lozenge \mathbf{X} \ \mathbf{H}^{BS-IRS\ T} \right]^T \right]^{\dagger}, \tag{24}$$

$$\hat{\mathbf{H}}^{BS\text{-}IRS\ T} = \mathbf{X}^{\dagger}\mathbf{P}_2 \left[\ \mathbf{S} \lozenge \mathbf{G}^{IRS-UT\ T} \right]^{\dagger}, \tag{25}$$

The convergence is declared when $\left\| e_{(i)} - e_{(i-1)} \right\| \le \delta$, with $e_{(i)} = \left\| \Upsilon - \hat{\Upsilon}_{(i)} \right\|_F^2$ is the the the reconstruction erro calculated at the i-th iteration, δ a threshold parameter, and $\hat{\Upsilon}_{(i)} = \left[\hat{\mathbf{G}}^{IRS-UT}, \mathbf{X}\left(\hat{\mathbf{H}}^{BS-IRS}\right)_{(i)}^T, \hat{\mathbf{S}} \right]$ is the reconstructed PARAFAC model (c.f (6), (13)) from the estimated channel matrices $\hat{\mathbf{G}}_{(i)}^{IRS-UT}$ and $\hat{\mathbf{H}}_{(i)}^{BS-IRS}$ at the end of the i-th iteration.

If the matrices $\mathbf{X}$ and $\mathbf{S}$ have orthogonal columns (requires $Q \ge L$ and $T \ge M_U$ are required), the right pseudo-inverse in (24) and (25) can be repeated by matrix products. This results in a low complexity BALS algorithm with simple estimation steps.

The common feature of the two algorithms is that the cascaded channel estimation is achieved by separating the estimates of the two $\mathbf{G}^{IRS\text{-}UT}$ and $\mathbf{H}^{BS\text{-}IRS}$ channel matrices, which improves the performance compared to the direct estimation of the cascaded channel using the conventional least squares algorithm. By focusing on pilot-assisted channel estimation methods, we improve the algorithm in,[39] to have a more comprehensive formulation of IRS-assisted channel estimation methods. Based on the tensor model, thereby giving necessary notes useful for the design of training parameters.

4.3. Feasibility conditions of extended estimation algorithms

The KRF method with a bilinear filter step as in (19) requires an IRS phase shift matrix $\mathbf{S}$ and the pilot symbol matrix $\mathbf{X}$ have full column rank, subject to the following conditions:

$$Q \ge L \text{ and } T \ge M_B \tag{26}$$

As mentioned earlier, it is best to choose the $\mathbf{X}$ and $\mathbf{S}$ matrices as semi-unitary (or column-orthogonal) matrices. It is explained that instead of inverting the matrices in (19) we use semi-unitary single matrix products to simplify processing at the receiver. In addition, the correlation properties of the noise component after filtering in (19) are preserved.

The BALS method requires two Khatri-Rao products $\mathbf{\Lambda}_1 = \mathbf{S} \lozenge \mathbf{X} \ \mathbf{H}^{BS-IRS\ T} \in \mathbb{C}^{QT\times L}$ and $\mathbf{\Lambda}_2 = \mathbf{S} \lozenge \mathbf{G}^{IRS-UT} \in \mathbb{C}^{QM_U\times L}$ have full column rank, such that (24) and (25) admit unique solutions. This means that the conditions $QT \ge L$ and $QM_U \ge L$ must be satisfied. Combining these two inequalities results in $\min(QT, QM_U) \ge L$, or equivalently, $Q\min(T, M_U) \ge L$. Also notice that the condition $T \ge M_B$ in (23) is required,

https://doi.org/10.52111/qnjs.2023.17507

since $\mathbf{X}$ must have the full column rank to be left inverse. Therefore, the following conditions are necessary

$$Q\min(T,\ M_U) \geq L \text{ và } T \geq M_B. \quad (27)$$

Comparing conditions (26) and (27), we can see that the BALS estimation method has less constraints on the minimum number of time blocks Q for the training channel than the KRF method. In the special case $M_U = 1$ (MISO or SISO systems, respectively), the inequalities (26) and (27) equal signs occur, meaning that BALS and KRF are subject to the same training requirements. Obviously BALS algorithm has advantages over KRF when applied in MIMO system, because BALS can work with $Q < L$, while KRF requires $Q \geq L$. Note that, if $Q = 1$, KRF estimation method is equivalent to conventional LS estimator. However, in this case we cannot solve/separate the estimation problem of two channel matrices through solving problem (20). On the other hand, the KRF algorithm has lower computational complexity than BALS, which will be presented later in the results section and discussed in the following section.

In addition, it should be noted that (27) is a necessary but not guaranteed condition for the uniqueness of BALS estimates. The sufficient condition can be derived from the rank characteristics of the matrices $\mathbf{S} \lozenge \mathbf{X}\ \mathbf{H}^{BS-IRS\ T} \in \mathbb{C}^{QT \times L}$ and $\mathbf{S} \lozenge \mathbf{G}^{IRS-UT} \in \mathbb{C}^{QM_U \times L}$.

To ensure the uniqueness of the channel estimates in solving problems (22) and (23) for matrices in Khatri-Rao form, applying the lemmas in,[35,36] the result is

$$\text{rank}(\mathbf{S}) + \text{rank}\left[\mathbf{X}\left(\mathbf{H}^{BS-IRS}\right)^T\right] \geq L+1 \quad (28)$$

$$\text{rank}(\mathbf{S}) + \text{rank}(\mathbf{G}^{IRS-UT}) \geq L+1 \quad (29)$$

We are considering the channel training parameters, specifically calculating such that the IRS phase shift matrix $\mathbf{S}$ and the pilot symbols matrix $\mathbf{X}$ have full rank. These conditions are useful for system design when using the BALS estimation method.

4.3.1. Full rank of channel matrix $\boldsymbol{H}^{BS-IRS}$ and $\boldsymbol{G}^{IRS-UT}$

Assuming that both $\mathbf{H}^{BS-IRS}$ and $\mathbf{G}^{IRS-UT}$ channel matrices have full rank (in case of Rayleigh fading channel), the condition (28)-(29) can be rewritten as

$$\min(Q, L) + \min(M_B, L) \geq L + 1 \quad (30)$$

$$\min(Q, L) + \min(M_U, L) \geq L + 1 \quad (31)$$

We can distinguish two cases as follows.

• $L \geq T \geq M_B$ and $L \geq M_U$: In this case, the base station BS and user equipment UT have small antenna array size, the number of BS and UT antennas is smaller than the number of IRS elements. Condition (28)-(29) becomes

$$M_B + \min(Q, L) \geq L + 1 \quad (32)$$

$$M_U + \min(Q, L) \geq L + 1 \quad (33)$$

• $T \geq M_B \geq L$: In this case, the base station BS is assumed to be equipped with a large antenna array. The minimum number of BS antennas is equal to the number of IRS elements (massive MIMO system setup). Since condition (28) is always satisfied for all values of Q, the uniqueness of the channel estimate depends only on (29), that is

$$\min(Q, L) + \min(M_U, L) \geq L + 1 \quad (34)$$

Conditions (32) and (33) establish a trade-off between the time dimension (the number of IRS training blocks Q) and the two spatial dimensions (the number of transmitting antennas M_B and the number of receiving antennas M_U) for the case channel restore. For example, if $Q < L$, this condition implies $M_B + Q \geq L + 1$ and $M_U + Q \geq L + 1$, which is equivalent to $\min(M_B + Q, M_U + Q) \geq L + 1$. That is, the number of transmitting (or receiving) antennas can be reduced while ensuring that the unique characteristic of the BALS channel estimation method is compensated by increasing the number of time blocks Q.

4.3.2. The $\boldsymbol{H}^{BS-IRS}$ and $\boldsymbol{G}^{IRS-UT}$ channel matrices lack rank

In millimeter wave MIMO systems, a large number of transmit/receive antennas coupled

https://doi.org/10.52111/qnjs.2023.17507

with a poorly scattered propagation medium can result in low-rank $\mathbf{H}^{BS\text{-}IRS}$ and $\mathbf{G}^{IRS\text{-}UT}$ channel matrices. Assume that the signal propagating between the BS base station and the IRS via C_1 clusters, while the signal propagating between the IRS and the user terminal UT through the C_2 cluster. Also, suppose that each cluster contributes a ray of complex amplitude and forms the angle of incidence or angle of departure. We can represent the $\mathbf{H}^{BS\text{-}IRS}$ and $\mathbf{G}^{IRS\text{-}UT}$ channel matrices as follows,[37]

$$\mathbf{H}^{BS-IRS} = \mathbf{A}_{IRS}\text{diag}(\boldsymbol{\alpha})\mathbf{A}_{BS}^{H}, \quad (35)$$

$$\mathbf{G}^{IRS-UT} = \mathbf{B}_{UT}\text{diag}(\boldsymbol{\beta})\mathbf{B}_{IRS}^{H}, \quad (36)$$

where, $\mathbf{A}_{\text{BS}} \in \mathbb{C}^{M_B \times C_1}$, $\mathbf{A}_{\text{IRS}} \in \mathbb{C}^{L \times C_1}$, $\mathbf{B}_{UT} \in \mathbb{C}^{M_U \times C_2}$, $\mathbf{B}_{\text{IRS}} \in \mathbb{C}^{L \times C_2}$ are array response matrices, and the vectors $\boldsymbol{\alpha}$, $\boldsymbol{\beta}$ are the complex amplitude coefficients of the BS-IRS and IRS-UT channels. In case of lack of rank, then rank($\mathbf{H}^{BS\text{-}IRS}$) = C_1 and rank($\mathbf{G}^{IRS\text{-}UT}$) = C_2, with $C_1 \leq \min(M_B, L)$ and $C_2 \leq \min(M_U, L)$.

Considering condition (26), the lack of rank of the channel matrix does not affect the solution of the channel estimation problem for the KRF algorithm. However, for the case of BALS estimation, since the uniqueness of the LS estimate of the $\mathbf{G}^{IRS\text{-}UT}$ and $\mathbf{H}^{BS\text{-}IRS}$ matrices depends on the rank of these matrices, as shown in conditions (28) and (29). For the BALS estimate, we can derive the following useful results.

• Case $T \geq M_B$: Conditions (28) and (29) become

$$\min(Q, L) + \text{C}_1 \geq L + 1 \quad (37)$$

$$\min(Q, L) + \text{C}_2 \geq L + 1 \quad (38)$$

The following scenarios are possible. If $Q \geq L$, we conclude that these conditions are always satisfied, for every ranks of the channel matrices. If $Q < L$, these conditions become $Q + \text{C}_1 \geq L + 1$ and $Q + \text{C}_2 \geq L + 1$, which is useful for choosing a block number Q that ensures the uniqueness of the channel estimates in the case lack of rank.

• Case $Q \geq L$: In this case, conditions (28) and (29) are always satisfied, for all ranks of the $\mathbf{G}^{IRS\text{-}UT}$ and $\mathbf{H}^{BS\text{-}IRS}$ matrices.

5. SIMULATION RESULTS AND DISCUSSION

In this section, some simulation results are presented to evaluate the performance of the channel estimation methods in this article and compare them with similar methods. The channel estimates are evaluated in terms of the Normalized Mean Square Error NMSE given by,[6]

$$\text{NMSE}\left(\hat{\mathbf{H}}^{BS-IRS}\right) = \frac{1}{C}\sum_{r=1}^{C}\frac{\left\|\left(\mathbf{H}^{BS-IRS}\right)^{(l)} - \left(\hat{\mathbf{H}}^{BS-IRS}\right)^{(l)}\right\|_F^2}{\left\|\left(\mathbf{H}^{BS-IRS}\right)^{(l)}\right\|_F^2}, \quad (39)$$

where, $\left(\hat{\mathbf{H}}^{BS-IRS}\right)^{(l)}$ is the estimated BS-IRS channel at the l-th run, C represents the number of Monte Carlo runs. Similar definitions apply to the $\left(\hat{\mathbf{G}}^{IRS-UT}\right)^{(l)}$ channel estimation.

The SNR(dB) ratio is defined as

$$\text{SNR(dB)} = 10\log_{10}\left(\frac{\left\|\bar{\Upsilon}\right\|_F^2}{\left\|\mathbb{N}\right\|_F^2}\right), \quad (40)$$

where, $\bar{\Upsilon}$ is the generated noiseless received signal tensor corresponding to the expression (13), $\mathbb{N}$ is the additive noise tensor.

In the simulation calculations, assuming the elements of the channel matrices $\mathbf{H}^{BS\text{-}IRS}$ and $\mathbf{G}^{IRS\text{-}UT}$ are independent and identically distributed (i.i.d) zero-mean circularly-symmetric complex Gaussian random variables. Note that the estimated channel matrix elements $\hat{\mathbf{H}}^{BS\text{-}IRS}$ and $\hat{\mathbf{G}}^{IRS\text{-}UT}$ in expression (21) of the KRF algorithm found using the SVD (Singular Value Decomposition) tensor operation $t-\text{SVD}(\tilde{\boldsymbol{\Omega}}_n)$.[32,33] In order to facilitate the evaluation of the quality of the algorithms, we choose the same system parameters as the reference articles, depending on each case.

Figure 3 depicts the NMSE performance curves in terms of SNR (dB) for the KRF and BALS algorithms. This is the result of system parameters $T = 4$, $M_B = 4$, $M_U = 2$, $Q = 50$ and the

https://doi.org/10.52111/qnjs.2023.17507

number of IRS elements with different values L = 10, 50. In this article, the BALS estimation calculations, we choose $e = 10^{-5}$. Although the number of iterations of the BALS algorithm is natural, only a few iterations can be converged (usually less than 10 iterations) thanks to the information that the IRS matrix **S** remains constant across the iterations.

Observing the results of Figure 3, we see that both algorithms give the desired performance. With the same number of IRS elements L, the estimated performance of the two algorithms KPF and BALS is similar. In terms of complexity, the KRF algorithm has a lower complexity but more restrictive requirements for the training parameter Q. While the iterative BALS method, although computationally more complex, can operate under more flexible choices of system parameters and with lower training costs. The system parameter constraints we discussed in section 4.3. On the other hand, the NMSE performance decreases as the number of IRS elements increases L, which is the expected result since the number of channel coefficients in the matries $\mathbf{G}^{IRS\text{-}UT}$ và $\mathbf{H}^{BS\text{-}IRS}$ to be estimated also increases with L. This means that it is possible to increase the system estimation performance while reducing the structural complexity of the IRS.

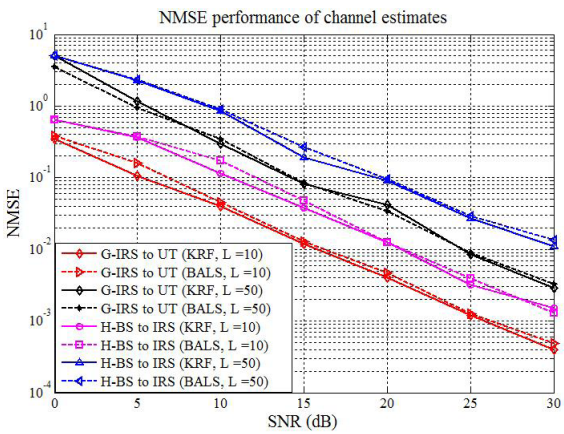

Figure 3. NMSE performance of channel estimates $\hat{\mathbf{H}}^{BS\text{-}IRS}$ và $\hat{\mathbf{G}}^{IRS\text{-}UT}$.

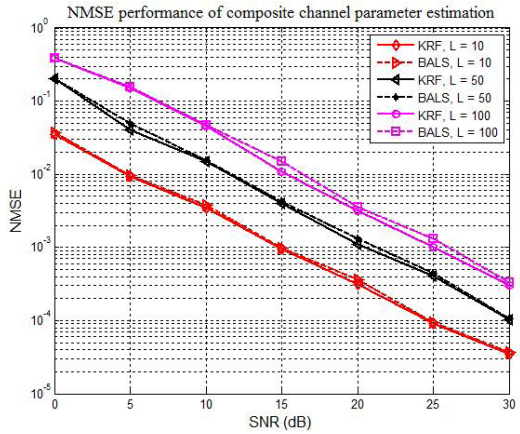

Figure 4. NMSE performance of composite channel parameter estimation $\hat{\boldsymbol{\theta}}$.

Figure 4 is the result of calculating the NMSE performance of estimating the composite parameter vector $\boldsymbol{\theta}$ according to the parameters Q = 100, T = 4, M_B = 3, M_U = 20, and L has the values 10, 50, 100. This result is consistent with the results of Figure 3, the estimated efficiency decreases as the number of IRS elements L increases. Another method to overcome the performance degradation presented in,[40] is to divide the IRS elements into groups of activation/deactivation in a time-domain sequential manner. However, this method will increase the total training time by a factor proportional to the number of element groups.

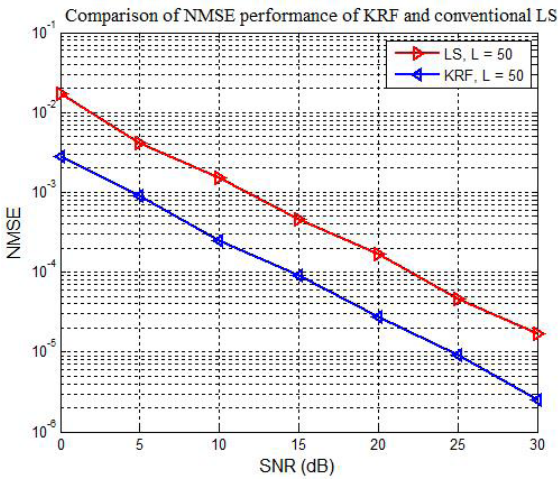

Figure 5. Comparison of NMSE performance of KRF estimator and conventional LS estimator.

In Figure 5, we compare the estimation results of the KRF algorithm with the conventional LS method. In this result, we choose

$Q=L=50$, $T=M_B=20$, $M_U=8$. The conventional LS method plotted on the graph is to estimate the composite channel parameter vector, ignoring the Khatri-Rao structure that is attenuated during the signal model vectorization. In contrast, the KRF algorithm in this paper exploits the Khatri-Rao channel structure and establishes from channel estimation matrices the $\hat{\mathbf{H}}^{BS\text{-}IRS}$ và $\hat{\mathbf{G}}^{IRS\text{-}UT}$.

In Figure 6 is the NMSE performance estimate of the lacking rank $\hat{\mathbf{H}}^{BS\text{-}IRS}$ và $\hat{\mathbf{G}}^{IRS\text{-}UT}$ channel matrices. In this result, the channel matrices are created according to the model (35)-(36), the channel parameters are selected, $Q = L = 64$, $M_U = 4$ and $T = M_B = 4$; 20, where $C_1 = C_2 = 1$. For comparison, we use the NMSE results of the LS channel estimation method proposed in.[38]

Observing the results of Figure 6, we see that the KRF algorithm has superior performance compared to the conventional LS algorithm. The gain in terms of SNR is about 7dB. This result is explained by the fact that KRF effectively exploits the Khatri-Rao structure present in the equivalence channel model.

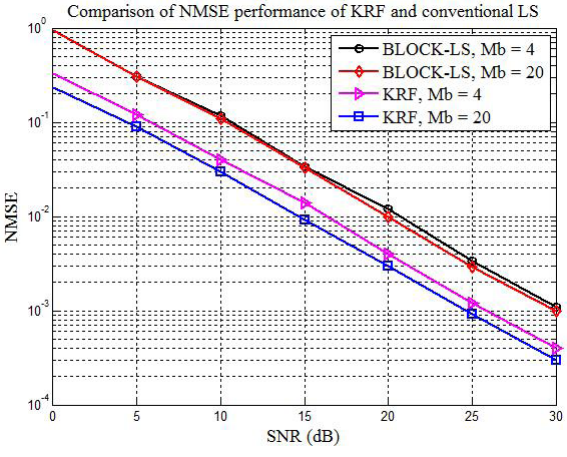

Figure 6. NMSE estimation results of composite channel parameter vector $\hat{\boldsymbol{\theta}}$ in the case of matrices $\hat{\mathbf{H}}^{BS\text{-}IRS}$ và $\hat{\mathbf{G}}^{IRS\text{-}UT}$ lacking rank.

Note that the KRF algorithm solves the problem by reshaping $M_B M_U \times L$ Khatri-Rao channels as L IRS subchannels of size $M_B \times M_U$, increasing noise rejection by rank-1 approximation steps. As M_B and M_U increase in large numbers (corresponding to a masive MIMO systems), the larger the noise spread over the noise subspace and, therefore, the higher the level of noise rejection achieved. This is a special feature of the KRF channel estimation algorithm that the conventional LS channel estimation algorithm cannot exploit.

In study,[38] the pilot signal time frame was the same as in this study, consisting of dividing the total training time into Q blocks and an IRS phase shift pattern that varied from block to block. In,[38] the LS estimation method is used by dividing the training signal frame T into blocks, referred to as the "block-LS" method for short. In this result, we compare the KRF estimation algorithm in this paper with the block-LS estimation method in.[38] We can see that the KRF estimation algorithm outperforms the block-LS estimation method in.[38] The authors in,[38] showed that the performance of the block-LS method was not affected as the number of M_B transmitting antennas and the pilot sequence length T increased. This is in contrast to the KRF method which provides more accurate channel estimation as the antenna arrays are larger. Specifically, the SNR gain of the KRF algorithm compared to the block-LS method is nearly 4.5 dB for $M_B = 4$ and increased to 5.5 dB for $M_B = 20$. This can be explained as follows. For the KRF algorithm, through exploiting the Khatri-Rao structure of the cascaded channel, the level of noise cancellation is higher when the number of M_B transmitting antennas or M_U receiving antennas is increased. However, this advantage comes at the expense of increased computational complexity, as well as increased length of pilot sequences.

6. CONCLUSION AND DEVELOPMENT DIRECTION

In this paper, we have extended the LS channel estimation algorithm for MIMO information system assisted by IRS based on tensor model. The KRF and BALS channel estimation algorithms are established by efficiently

https://doi.org/10.52111/qnjs.2023.17507

exploiting the tensor structure of the received signal. Both algorithms perform separate estimation of the transmission channels between the BS to the IRS and from the IRS to the UT with the passive elements of the IRS. The closed-form KRF algorithm has lower complexity but more restrictive requirements for training parameter Q. While BALS iterative method, although computationally more complex, can operate on more flexible choices for training parameter Q with lower training cost. In this article, we also consider the relationship between the system parameters to ensure the uniqueness of the channel estimates. These constraints are useful when designing system channel estimates. Some simulation and discussion calculation results, we have demonstrated the superior performance of KRF and BALS compared with the conventional LS estimator, ignoring the Khatri-Rao structure of the combined channel matrix. In the proposal of this paper, in section 4.3, we give useful recommendations for the selection of system parameters to ensure the uniqueness of channel estimation.

The KRF and BALS channel estimation algorithms mentioned in this paper can improve the performance by exploiting the knowledge of the rank of the estimation matrices, or, using compression sensing methods to take advantage of the sparse representation of the $\mathbf{H}^{BS\text{-}IRS}$ and $\mathbf{G}^{IRS\text{-}UT}$ channel matrices. This could be the next research direction of interest.

Acknowledgments

The authors would like to thank the editor(s) and anonymous reviewers for their constructive comments and suggestions that have helped to improve the present paper.

REFERENCES

1. M. D. Renzo, H. Haas, A. Ghrayeb, S. Sugiura, and L. Hanzo. Spatial modulation for generalized MIMO: Challenges, opportunities, and implementation, *Proceedings of the IEEE*, **2014**, *102*(1), 56103.
2. F. Boccardi, R. W. Heath, A. Lozano, T. L. Marzetta, and P. Popovski. Five disruptive technology directions for 5G, *IEEE Communications Magazine*, **2014**, *52*(2), 74-80.
3. P. Yang, M. Di Renzo, Y. Xiao, S. Li, and L. Hanzo. Design guidelines for spatial modulation, *IEEE Communications Surveys & Tutorials*, **2015**, *17*(1), 6-26.
4. S. Rangan, T. S. Rappaport, and E. Erkip. MillimeterWave cellular wireless networks: Potentials and challenges, *Proceedings of the IEEE*, **2014**, *102*(3), 366-385.
5. S. Gong, X. Lu, D. T. Hoang, D. Niyato, L. Shu, D. I. Kim, and Y.-C. Liang. Toward smart wireless communications via intelligent reflecting surfaces: A contemporary survey, *IEEE Communications Surveys & Tutorials*, **2020**, *22*(4), 2283-2314.
6. C. Pan, G. Zhou, K. Zhi, S. Hong, T. Wu, Y. Pan, H. Ren, M. D. Renzo, A. L. Swindlehurst, R. Zhang, A. Y. Zhang. An overview of signal processing techniques for RIS/IRS-aided wireless systems, *IEEE Journal of Selected Topics Signal Processing*, **2022**, *16*(5), 883-917.
7. B. Zheng, C. You, W. Mei, and R. Zhang. A survey on channel estimation and practical passive beamforming design for intelligent reflecting surface aided wireless communications, *IEEE Communications Surveys & Tutorials*, **2022**, *24*(2), 1035-1071.
8. Q. Wu and R. Zhang. Towards smart and reconfigurable environment: Intelligent reflecting surface aided wireless network, *IEEE Communications Magazine*, **2020**, *58*(1), 106-112.
9. Q. Wu and R. Zhang. Beamforming optimization for wireless network aided by intelligent reflecting surface with discrete phase shifts, *IEEE Transactions on Communications*, **2020**, *68*(3), 1838-1851.
10. Y. Song, M. R. A. Khandaker, F. Tariq, and K.-K. Wong. *Truly intelligent reflecting surface-aided secure communication using deep learning,* IEEE 93rd Vehicular Technology Conference, April 2021.

11. L. Dong and H.-M. Wang, Secure MIMO transmission via intelligent reflecting surface, *IEEE Wireless Communication Letters*, **2020**, *9*(6), 787-790.

12. A. Taha, M. Alrabeiah, and A. Alkhateeb. Enabling large intelligent surfaces with compressive sensing and deep learning, *IEEE Access,* **2021**, *9*, 1-19.

13. T. L. Jensen and E. D. Carvalho. *An optimal channel estimation scheme for intelligent reflecting surfaces based on a minimum variance unbiased estimator*, ICASSP 2020-2020 IEEE International Conference on Acoustics, Speech and Signal Processing (ICASSP), 2020.

14. Z. He and X. Yuan. Cascaded channel estimation for large intelligent metasurface assisted massive MIMO, *IEEE Wireless Communication Letters*, **2020**, *9*(2), 210-214.

15. B. Ning, Z. Chen, W. Chen, and Y. Du. *Channel estimation and transmission for intelligent reflecting surface assisted THz communications*, ICC 2020-2020 IEEE International Conference on Communications (ICC), 2020.

16. Y. Han, W. Tang, X. Li, M. Matthaiou and S. Jin. CSI acquisition in RIS-assisted mobile communication systems, *Informatics and Commuter Journal,* **2023**, 1-15.

17. J. Mirza and B. Ali. Channel estimation method and phase shift design for reconfigurable intelligent surface assisted MIMO networks, *IEEE Transactions on Cognitive Communications and Networking,* **2021**, *7*(2), 441-451.

18. S. Xia and Y. Shi. *Intelligent reflecting surface for massive device connectivity: Joint activity detection and channel estimation*, ICASSP 2020-2020 IEEE International Conference on Acoustics, Speech and Signal Processing (ICASSP), 2020.

19. Y. Zniyed, R. Boyer, A. L. de Almeida, and G. Favier. Tensor train representation of MIMO channels using the JIRAFE method, *Signal Processing,* **2020**, *171*.

20. Y. Zniyed, R. Boyer, A. L. F. Almeida, and G. Favier. High-order tensor estimation via trains of coupled third-order CP and Tucker decompositions, *Linear Algebra and Its Applications,* **2020**, *588*, 304-307.

21. Y. Zniyed, R. Boyer, A. L. Almeida, and G. Favier. A TT-based hierarchical framework for decomposing high-order tensors, *SIAM Journal on Scientific Computing*, **2020**, *42*(2), A822-A848.

22. A. L. F. de Almeida, X. Luciani, A. Stegeman, and P. Comon. Confac decomposition approach to blind identification of underdetermined mixtures based on generating function derivatives, *IEEE Transactions on Signal Processing*, **2012**, *60*(11), 5698-5713.

23. A. L. de Almeida, G. Favier, and J. C. Mota. A. L. de Almeida, G. Favier, and J. C. Mota. Space time spreading multiplexing for MIMO wireless communication systems using the PARATUCK-2 tensor model, *Signal Processing*, **2009**, *89*(11), 2103-2116.

24. W. Freitas, G. Favier, and A. L. F. de Almeida. Generalized Khatri-Rao and Kronecker space-time coding for MIMO relay systems with closed-form semi-blind receivers, *Signal Processing*, **2018**, *151*, 19-31.

25. B. Sokal, A. L. de Almeida, and M. Haardt. Semi-blind receivers for MIMO multi-relaying systems via rank-one tensor approximations, *Signal Processing*, **2020**, *166*.

26. D. C. Araujo, A. L. F. de Almeida, J. P. C. L. Da Costa, and R. T. de Sousa. Tensor-based channel estimation for massive MIMO-OFDM systems, *IEEE Access*, **2019**, *7*, 42133-42147.

27. P. R. B. Gomes, A. L. F. de Almeida, J. P. C. L. da Costa, and R. T. de Sousa Jr. Joint DL and UL channel estimation for millimeter wave MIMO systems using tensor modeling, *Wireless Communications and Mobile Computing*, **2019**, 1-13.

28. V. D. Nguyen, K. A. Meraim, N. L. Trung. *Parallelizable PARAFAC decomposition of 3-way tensors*, Proceedings of European Signal Processing Conference (EUSIPCO) IEEE, 2015.

29. T. G. Kolda and B. W. Bader. Tensor decompositions and applications, *SIAM Review*, **2009**, *51*(3), 455-500.

https://doi.org/10.52111/qnjs.2023.17507

30. P. Comon, X. Luciani, and A. L. F. de Almeida. Tensor decompositions, alternating least squares and other tales, *Journal of Chemometrics*, **2009**, *23*(7), 393-405.

31. A. L. F. de Almeida, G. Favier, J. P. C. L. da Costa, and J. C. M. Mota. Overview of tensor decompositions with applications to communications, *Signals and Images: Advances and Results in Speech, Estimation, Compression, Recognition, Filtering, and Processing*, **2016**, *12*, 325-356.

32. A. Y. Kibangou and G. Favier. *Non-iterative solution for PARAFAC with a toeplitz matrix factor*, 2009 17th European Signal Processing Conference, 2009.

33. F. Roemer and M. Haardt. Tensor-based channel estimation and iterative refinements for two-way relaying with multiple antennas and spatial reuse, *IEEE Transactions on Signal Process*, **2010**, *58*(11), 5720-5735.

34. R. Bro. *Multi-way analysis in the food industry: Models, algorithms & applications,* Ph.D. dissertation, University of Amsterdam, 1998.

35. A. Stegeman and N. D. Sidiropoulos. On kruskal's uniqueness condition for the PARAFAC decomposition, *Linear Algebra and Its Applications*, **2007**, *420*(2), 540-552.

36. N. D. Sidiropoulos and R. Bro. On the uniqueness of multilinear decomposition of n-way arrays, *Journal of Chemometrics*, **2000**, *14*(3), 229-239.

37. R. W. Heath, N. Gonzalez-Prelcic, S. Rangan, W. Roh, and A. M. Sayeed. An overview of signal processing techniques for millimeter wave MIMO systems, *IEEE Journal of Selected Topics in Signal Processing*, **2016**, *10*(3), 436-453.

38. B. Li, Z. Zhang, Z. Hu. Channel estimation for reconfigurable intelligent surface-assisted multiuser mmWave MIMO system in the presence of array blockage, *Transactions on Emerging Telecommunications Technologies*, **2021**, *32*.

39. G. T. de Araujo and A. L. F. de Almeida. *PARAFAC-based channel estimation for intelligent reflective surface assisted MIMO system,* IEEE 11th Sensor Array and Multichannel Signal Processing Workshop (SAM), 2020, 1-5.

40. C. You, B. Zheng, and R. Zhang. *Intelligent reflecting surface with discrete phase shifts: Channel estimation and passive beamforming,* ICC 2020-2020 IEEE International Conference on Communications (ICC), 2020.

TẠP CHÍ KHOA HỌC
TRƯỜNG ĐẠI HỌC QUY NHƠN

Các hằng số tương đương của một số chuẩn trong không gian các đường cong Bézier bậc ba N mảnh

Hoàng Văn Đức*

Khoa Toán và Thống kê, Trường Đại học Quy Nhơn, Việt Nam

Ngày nhận bài: 09/06/2023; Ngày sửa bài: 25/09/2023; Ngày nhận đăng: 27/09/2023; Ngày xuất bản: 28/10/2023

TÓM TẮT

Bài báo này nghiên cứu chuẩn của đường cong Bézier N khúc bậc ba và các hằng số tương đương trong không gian $B_{N,3}$ của các đường cong Bézier N khúc bậc ba. Chúng tôi đề xuất các chuẩn $\|\cdot\|_p^{B_3}$ trên không gian B_3 các đường cong Bézier bậc ba và chuẩn $\|\cdot\|_p^{B_{N,3}}$ trên không gian $B_{N,3}$ của các đường cong Bézier N khúc bậc ba. Trong bài báo này chúng tôi bàn về các hằng số tương đương của chuẩn $\|\cdot\|_p^{B_{N,3}}$ và chuẩn L_p trên không gian $B_{N,3}$ các đường cong Bézier N khúc bậc ba. Mỗi đường cong Bézier bậc m có thể được xem như một đường cong Bézier bậc $m+1$. Do đó, chúng tôi cũng nghiên cứu các hằng số tương đương của chuẩn $\|\cdot\|_p^{B_{N,m}}$ và chuẩn $\|\cdot\|_p^{B_{N,m+1}}$ trên không gian các đường cong Bézier N khúc bậc m.

Từ khóa: *Đường cong Bézier bậc ba, hằng số tương đương, chuẩn, khoảng cách.*

**Tác giả liên hệ chính.*
Email: hoangvanduc@qnu.edu.vn

https://doi.org/10.52111/qnjs.2023.17508

QUY NHON UNIVERSITY
JOURNAL OF SCIENCE

Equivalence constants for some norms on the space of N-piece cubic Bézier curves

Hoang Van Duc*

Faculty of Mathematics and Statistics, Quy Nhon University, Vietnam

Received: 09/06/2023; Revised: 25/09/2023; Accepted: 27/09/2023; Published: 28/10/2023

ABSTRACT

This paper is concerned with norms of N-piece cubic Bézier curves and the equivalence relations between some norms on the space $B_{N,3}$ of N-piece cubic Bézier curves. We introduce a norm $\|\cdot\|_p^{B_3}$ on the space B_3 of cubic Bézier curves and a norm $\|\cdot\|_p^{B_{N,3}}$ on the space $B_{N,3}$ of N-piece cubic Bézier curves. This article we deal with the equivalence constants for the norm $\|\cdot\|_p^{B_{N,3}}$ and the L_p norm on the space $B_{N,3}$ of N-piece cubic Bézier curves. An N-piece Bézier curve of degree m can be considered as an N-piece Bézier curve of degree $m+1$. We also study the equivalence constants for the norm $\|\cdot\|_p^{B_{N,m}}$ and the norm $\|\cdot\|_p^{B_{N,m+1}}$ on the space $B_{N,m}$ of N-piece Bézier curves of degree m.
Keywords: *Cubic Bézier curves, equivalence constants, norm, distance.*

1. INTRODUCTION

In 1962, the French engineer Pierre Bézier publicized the Bézier curve which is defined based on Bernstein polynomials. However, the mathematician Paul de Casteljau built Bézier curve by using de Casteljau's algorithm.

Pierre Bézier applied Bézier curves for designing the bodywork of Renault cars. Its importance is due to the fact that, Bézier curves are used in many fields of applications, not only mathematics. For instance, Bézier curves are used in computer graphics, computer-aided design system, robotic, industry, walking, communication, path-planning and aerospace (see[1–8]). Bézier curves are also used to find plane shape optimization which appears in many fields such as environment design, aerospace, structural mechanics, networks, automotive, hydraulic, oceanology and wind engineering (see[9–14]).

Bézier curves are mentioned in many books and articles for instance.[15–17] A continuous curve can be approximated by a Bézier curve. However, when the curve is long and complex, the degree of the Bézier curve is high. As a result, the computation is more difficult. Then, the most common use of Bézier curves is as N-piece cubic Bézier curves. We will focus uniform N-piece cubic Bézier curves.

In this article, we define a norm $\|\cdot\|_p^{B_m}$ on the space B_m of Bézier curves of degree m and a norm $\|\cdot\|_p^{B_{N,m}}$ on the space $B_{N,m}$ of uniform N-piece Bézier curves of degree m. These norms are computed through control points. This article studies the equivalence relations between the norm $\|\cdot\|_p^{B_{N,3}}$ and the L_p norm on the space $B_{N,3}$ of N-piece cubic Bézier curves.

Theorem 1. *For $p \in [1,\infty]$. Let $\beta \in B_{N,3}$, we get*

$$\|\beta\|_{L_p} \leq \|\beta\|_p^{B_{N,3}} \leq 2^{10}\,\|\beta\|_{L_p}.$$

An N-piece Bézier curve of degree m can be considered as an N-piece Bézier curve of degree $m+1$. We also study the equivalence constants for the norm $\|\cdot\|_p^{B_{N,m}}$ and the norm $\|\cdot\|_p^{B_{N,m+1}}$ on the space $B_{N,m}$ of N-piece Bézier curves of degree m.

Theorem 2. *For $p \in [1,\infty]$. Let $\beta \in B_{N,m}$, we get*

$$\frac{1}{2(m+1)}\|\beta\|_p^{B_{N,m}} \leq \|\beta\|_p^{B_{N,m+1}} \leq 2\|\beta\|_p^{B_{N,m}}.$$

2. PRELIMINARIES

For the convenience of reading, we present some definitions and notations that will be used through the article.

Definition 3. ([16] chapter 6, p. 141) Let m be a positive integer and $P_0,\ldots,P_m$ be $m+1$ points in $\mathbb{R}^n$. The *Bézier curve of degree m* with control points $P_0,\ldots,P_m$ is defined by

$$B([P_0,\ldots,P_m],t) := \sum_{i=0}^{m} P_i b_{i,m}(t), \quad t \in [0,1], \qquad (1)$$

*Corresponding author.
Email: hoangvanduc@qnu.edu.vn

https://doi.org/10.52111/qnjs.2023.17508

where $b_{i,m}(t) = \binom{m}{i} t^i (1-t)^{m-i}$ is the Bernstein polynomial.

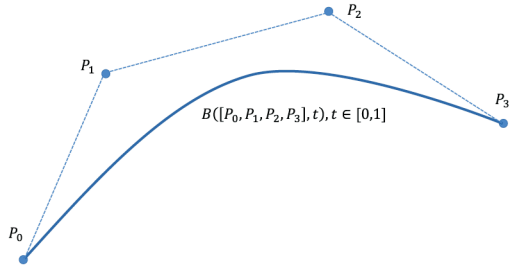

Figure 1. A cubic Bézier curve.

The points P_i are called control points for the Bézier curve of degree m. The polygon formed by connecting the control points with lines, starting with P_0 and finishing with P_m, is called the control polygon. The convex hull of the control polygon contains the Bézier curve.

A uniform N-piece Bézier curve of degree m is a piecewise Bézier curve which has N-pieces, each piece is a Bézier curve of degree m and the point at $t = \frac{j}{N}$, $j = 1,\dots,N-1$, is the connecting point of the pieces. We often drop "uniform". Let us consider the definition of the N-piece Bézier curve of degree m.

Definition 4. [16] Let m, N be positive integers and $P_0,\dots,P_{Nm}$ be $Nm+1$ points in $\mathbb{R}^n$. The *N-piece Bézier curve of degree m* with control points $P_0,\dots,P_{Nm}$ is formed by

$$\begin{aligned}\beta : [0,1] &\to \mathbb{R}^n \\ t &\mapsto \beta(t) = B([P_{jm},\dots,P_{jm+m}], Nt-j) \\ &\text{if } t \in \left[\frac{j}{N}, \frac{j+1}{N}\right].\end{aligned}$$

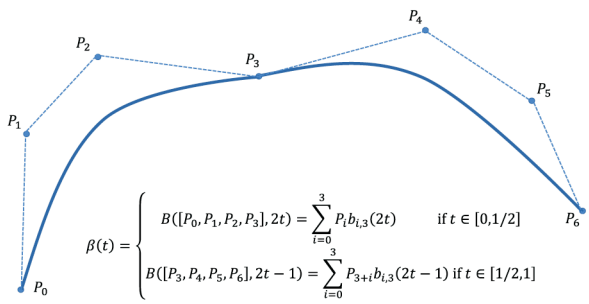

Figure 2. A two-piece cubic Bézier curve.

Notation 5.

- The vector space of Bézier curves of degree m is denoted by the symbol B_m.
- The vector space of N-piece Bézier curves of degree m is denoted by the symbol $B_{N,m}$.
- The set of continuous parametrizations on $[0,1]$ is denoted by the symbol $C^0([0,1],\mathbb{R}^n)$.

We define some norms and distances through control points on the space of Bézier curves of degree m and on the space of N-piece Bézier curves of degree m.

Definition 6. Let $p \in [1,\infty]$. The function $\|\cdot\|_p^{B_m} : B_m \to \mathbb{R}$ is defined by: For any $\beta(t) = \sum_{i=0}^{m} P_i b_{i,m}(t) \in B_m$,

$$\|\beta\|_p^{B_m} := \begin{cases} \left(\sum_{i=0}^{m} \|P_i\|_p^p\right)^{1/p} & \text{if } p \in [1,\infty[\\ \max_{i=0,\dots,m} \{\|P_i\|_\infty\} & \text{if } p = \infty, \end{cases}$$

where $\|\cdot\|_p$ is the p-norm on $\mathbb{R}^n$.

From the properties of the p-norm on $\mathbb{R}^n$ and the Minkowski inequality, it is easily seen that $\|\cdot\|_p^{B_m}$ is a norm on the vector space B_m. Indeed, it is a norm on the space $(\mathbb{R}^n)^{m+1}$ of control polygons. We then have an induced distance on B_m by $d_p^{B_m}(\beta,\gamma) := \|\beta-\gamma\|_p^{B_m}$.

Definition 7. Let $p \in [1,\infty]$. The function $\|\cdot\|_p^{B_{N,m}} : B_{N,m} \to \mathbb{R}$ is defined by: For any $\beta(t) = \beta^{(j)}(Nt-j) = \sum_{i=0}^{m} P_{jm+i} b_{i,m}(Nt-j)$ if $t \in \left[\frac{j}{N}, \frac{j+1}{N}\right]$, $j = 0,\dots,N-1$,

$$\|\beta\|_p^{B_{N,m}} := \begin{cases} \dfrac{1}{N^{1/p}} \left(\sum_{j=0}^{N-1} \left(\|\beta^{(j)}\|_p^{B_m}\right)^p\right)^{1/p} \\ \qquad\qquad \text{if } p \in [1,\infty[\\ \max_{j=0,\dots,N-1} \left\{\|\beta^{(j)}\|_\infty^{B_m}\right\} \text{ if } p = \infty. \end{cases}$$

Using the Minkowski inequality and the properties of the norm $\|\cdot\|_p^{B_m}$ on B_m, it is easy to see that $\|\cdot\|_p^{B_{N,m}}$ is a norm on the vector space $B_{N,m}$. Then we have again an induced distance on $B_{N,m}$ defined by $d_p^{B_{N,m}}(\beta,\gamma) := \|\beta-\gamma\|_p^{B_{N,m}}$.

The norms $\|\cdot\|_p^{B_m}$ and $\|\cdot\|_p^{B_{N,m}}$ can be computed more efficiently than, for instance, the L_p- norm.

3. THE EQUIVALENCE RELATIONS BETWEEN THE NORM $\|\cdot\|_p^{B_{N,3}}$ AND THE L_p NORM ON THE SPACE $B_{N,3}$

Since the space $B_{N,3}$ is a subspace of the space $C^0([0,1],\mathbb{R}^n)$, the norm $\|\cdot\|_{L_p}$ is also a norm on the space $B_{N,3}$ of N-piece cubic Bézier curves. Moreover, N-piece cubic Bézier curves are common and convenient to approximate continuous curves. So, we concentrate on the equivalence relations between the norm $\|\cdot\|_p^{B_{N,3}}$ and the L_p-norm on the space $B_{N,3}$ of N-piece cubic Bézier curves.

For $p \in [1,\infty]$, we first show that the norm $\|\cdot\|_{L_p}$ is weaker than the norm $\|\cdot\|_p^{B_m}$ on the space B_m of Bézier curves of degree m and then show that $\|\cdot\|_{L_p}$ is also weaker than the norm $\|\cdot\|_p^{B_{N,m}}$ on the space $B_{N,m}$ of N-piece Bézier curves of degree m.

Lemma 8. *Let $p \in [1,\infty]$. Then for any $\beta \in B_m$,*

$$\|\beta\|_{L_p} \le \|\beta\|_p^{B_m}.$$

https://doi.org/10.52111/qnjs.2023.17508

Proof. Let $\beta \in B_m$ and assume that

$$\beta(t) = \sum_{i=0}^{m} P_i b_{i,m}(t), \ t \in [0,1].$$

Case $p = 1$. We get

$$\begin{aligned}\|\beta\|_{L_1} &= \int_0^1 \Big\| \sum_{i=0}^{m} P_i b_{i,m}(t) \Big\|_1 dt \\ &\le \sum_{i=0}^{m} \big\|P_i\big\|_1 b_{i,m}(t) \le \sum_{i=0}^{m} \big\|P_i\big\|_1 = \|\beta\|_1^{B_m}.\end{aligned}$$

Case $p \in]1,\infty[$. Using Holder's inequality, we get

$$\begin{aligned}&\sum_{i=0}^{m} \big\|P_i\big\|_p b_{i,m}(t) \\ &\le \Big(\sum_{i=0}^{m} \big\|P_i\big\|_p^p\Big)^{1/p} \Big(\sum_{i=0}^{m} (b_{i,m}(t))^{p/(p-1)}\Big)^{(p-1)/p} \\ &\le \Big(\sum_{i=0}^{m} \big\|P_i\big\|_p^p\Big)^{1/p} \Big(\sum_{i=0}^{m} b_{i,m}(t)\Big)^{(p-1)/p} \\ &= \Big(\sum_{i=0}^{m} \big\|P_i\big\|_p^p\Big)^{1/p}.\end{aligned}$$

Hence

$$\begin{aligned}\|\beta\|_{L_p} &= \Big(\int_0^1 \Big\| \sum_{i=0}^{m} P_i b_{i,m}(t)\Big\|_p^p dt\Big)^{1/p} \\ &\le \Big(\int_0^1 \Big(\sum_{i=0}^{m} \big\|P_i\big\|_p b_{i,m}(t)\Big)^p dt\Big)^{1/p} \\ &\le \Big(\int_0^1 \sum_{i=0}^{m} \big\|P_i\big\|_p^p dt\Big)^{1/p} = \Big(\sum_{i=0}^{m} \big\|P_i\big\|_p^p\Big)^{1/p} \\ &= \|\beta\|_p^{B_m}.\end{aligned}$$

Case $p = \infty$. We get

$$\begin{aligned}\|\beta\|_{L_\infty} &= \Big\| \sum_{i=0}^{m} P_i b_{i,m}(t)\Big\|_{L_\infty} \le \Big(\sum_{i=0}^{m} b_{i,m}(t)\Big) \max_{i=0,\dots,m} \|P_i\|_\infty \\ &= \max_{i=0,\dots,m} \|P_i\|_\infty = \|\beta\|_\infty^{B_m}.\end{aligned}$$

Combining the above cases, we obtain the proof of this lemma. □

Form this estimation, we have the following proposition.

Proposition 9. *Let $p \in [1,\infty]$. Then for any $\beta \in B_{N,m}$,*

$$\|\beta\|_{L_p} \le \|\beta\|_p^{B_{N,m}}.$$

Proof. Let $\beta \in B_{N,m}$ be an N-piece Bézier curve of degree m with control points $P_{jm+i} \in \mathbb{R}^n$, $i = 0,\dots,m$, $j = 0,\dots,N-1$. So

$$\begin{aligned}\beta(t) &= \beta^{(j)}(Nt-j) = \sum_{i=0}^{m} P_{jm+i} b_{i,m}(Nt-j) \\ &\text{if } t \in \Big[\frac{j}{N}, \frac{j+1}{N}\Big], j = 0,\dots,N-1.\end{aligned}$$

Case $p \in [1,\infty)$. We get

$$\begin{aligned}\|\beta\|_{L_p} &= \Big(\int_0^1 \|\beta(t)\|_p^p dt\Big)^{1/p} \\ &= \Big(\sum_{j=0}^{N-1} \int_{\frac{j}{N}}^{\frac{j+1}{N}} \|\beta^{(j)}(Nt-j)\|_p^p dt\Big)^{1/p} \\ &= \frac{1}{N^{1/p}} \Big(\sum_{j=0}^{N-1} \int_0^1 \|\beta^{(j)}(t)\|_p^p dt\Big)^{1/p}.\end{aligned}$$

Using Lemma 8, we obtain

$$\|\beta\|_{L_p} \le \frac{1}{N^{1/p}} \Big(\sum_{j=0}^{N-1} \Big(\|\beta^{(j)}\|_p^{B_m}\Big)^p\Big)^{1/p} = \|\beta\|_p^{B_{N,m}}.$$

Case $p = \infty$. We have

$$\begin{aligned}\|\beta\|_{L_\infty} &= \max_{t\in[0,1]} \|\beta(t)\|_\infty \\ &= \max_{j=0,\dots,N-1} \max_{t\in[\frac{j}{N},\frac{j+1}{N}]} \|\beta^{(j)}(Nt-j)\|_\infty \\ &= \max_{j=0,\dots,N-1} \max_{t\in[0,1]} \|\beta^{(j)}(t)\|_\infty.\end{aligned}$$

Using Lemma 8, we get

$$\|\beta\|_{L_\infty} \le \max_{j=0,\dots,N-1} \|\beta\|_\infty^{B_m} = \|\beta\|_\infty^{B_{N,m}}.$$

Thus, the proof of this proposition is complete. □

Thus, for $p \in [1,\infty]$, we have with respect to the norm $\|\cdot\|_{L_p}$ is weaker than the norm $\|\cdot\|_p^{B_{N,m}}$ on the space $B_{N,m}$ of N-piece Bézier curves of degree m. Since $B_{N,3}$ is a subspace of $B_{N,m}$, this result is useful for the space $B_{N,3}$ of N-piece *cubic* Bézier curves.

In practice, the most common use of Bézier curves is as N-piece cubic Bézier curves. So, we concentrate on the space $B_{N,3}$ of N-piece *cubic* Bézier curves. We will find a constant A such that $\|\cdot\|_p^{B_{N,3}} \le A\|\cdot\|_{L_p}$ on the space $B_{N,3}$ of N-piece *cubic* Bézier curves.

Lemma 10. *Let $p \in [1,\infty[$ and P_0, P_1, P_2, P_3 be four points on $\mathbb{R}^n$, we get*

$$\int_0^1 \Big\| \sum_{i=0}^{3} P_i b_{i,3}(t)\Big\|_p^p dt \ge \frac{1}{2^{10p}} \Big(\sum_{i=0}^{3} \|P_i\|_p^p\Big).$$

Proof. Put

$$M = \max\Big\{\|P_0\|_p, \frac{1}{3}\|P_1\|_p, \frac{1}{3}\|P_2\|_p, \|P_3\|_p\Big\}.$$

https://doi.org/10.52111/qnjs.2023.17508

- Case 1: $M = \|P_0\|_p$.

  We consider the interval $\left[0, \frac{1}{16}\right]$. For any $t \in \left[0, \frac{1}{16}\right]$, we have

$$\|P_0(1-t)^3\|_p \geq \left(1-\frac{1}{16}\right)^3 \|P_0\|_p = \frac{15^3}{16^3}\|P_0\|_p.$$

$$\|P_1 3t(1-t)^2\|_p \leq 3\frac{1}{16}\left(1-\frac{1}{16}\right)^2 \|P_1\|_p \leq 3\|P_0\|_p \frac{3.15^2}{16^3} = \frac{9.15^2}{16^3}\|P_0\|_p$$

$$\|P_2 3t^2(1-t)\|_p \leq 3\left(\frac{1}{16}\right)^2\left(1-\frac{1}{16}\right)\|P_2\|_p \leq 3\|P_0\|_p \frac{3.15}{16^3} = \frac{9.15}{16^3}\|P_0\|_p$$

$$\|P_3 t^3\|_p \leq \frac{1}{16^3}\|P_3\|_p \leq \frac{1}{16^3}\|P_0\|_p.$$

So, for any $t \in \left[0, \frac{1}{16}\right]$, we have

$$\begin{aligned}
&\Big\|\sum_{i=0}^{3} P_i b_{i,3}(t)\Big\|_p \geq \|P_0(1-t)^3\|_p \\
&- \|P_1 3t(1-t)^2\|_p - \|P_2 3t^2(1-t)\|_p - \|P_3 t^3\|_p \\
&\geq \frac{15^3}{16^3}\|P_0\|_p - \frac{9.15^2}{16^3}\|P_0\|_p \\
&- \frac{9.15}{16^3}\|P_0\|_p - \frac{1}{16^3}\|P_0\|_p \\
&= \frac{1214}{4096}\|P_0\|_p.
\end{aligned}$$

Then

$$\begin{aligned}
\int_0^1 \Big\|\sum_{i=0}^{3} P_i b_{i,3}(t)\Big\|_p^p dt &\geq \int_0^{\frac{1}{16}} \Big\|\sum_{i=0}^{3} P_i b_{i,3}(t)\Big\|_p^p dt \\
&\geq \int_0^{\frac{1}{16}} \left(\frac{1214}{4096}\right)^p \|P_0\|_p^p dt \\
&\geq \frac{1}{16}\left(\frac{1214}{4096}\right)^p \frac{1}{2+2.3^p}\Big(\sum_{i=0}^{3}\|P_0\|_p^p\Big) \\
&\geq \frac{1}{2^{10p}}\Big(\sum_{i=0}^{3}\|P_0\|_p^p\Big).
\end{aligned}$$

- Case 2: $M = \frac{1}{3}\|P_1\|_p$.

  We consider the interval $\left[\frac{7}{32}, \frac{9}{32}\right]$. For any $t \in \left[\frac{7}{32}, \frac{9}{32}\right]$, we have

$$\|P_1 3t(1-t)^2\|_p \geq 3.\frac{7}{32}\left(1-\frac{7}{32}\right)^2 \|P_1\|_p = \frac{3.7.25^2}{32^3}\|P_1\|_p,$$

$$\|P_0(1-t)^3\|_p \leq \left(1-\frac{7}{32}\right)^3 \|P_0\|_p \leq \frac{25^3}{32^3}\frac{1}{3}\|P_1\|_p = \frac{25^3}{3.32^3}\|P_1\|_p,$$

$$\|P_2 3t^2(1-t)\|_p \leq 3.\left(\frac{9}{32}\right)^2\left(1-\frac{9}{32}\right)\|P_2\|_p \leq \frac{3.9^2.23}{32^3}\|P_1\|_p,$$

$$\|P_3 t^3\|_p \leq \frac{9^3}{32^3}\|P_3\|_p \leq \frac{1}{3}\|P_1\|_p \frac{9^3}{32^3} = \frac{9^3}{3.32^3}\|P_1\|_p.$$

So, for any $t \in \left[\frac{7}{32}, \frac{9}{32}\right]$, we have

$$\begin{aligned}
&\Big\|\sum_{i=0}^{3} P_i b_{i,3}(t)\Big\|_p \\
&\geq \|P_1 3t(1-t)^2\|_p - \|P_0(1-t)^3\|_p \\
&- \|P_2 3t^2(1-t)\|_p - \|P_3 t^3\|_p \\
&\geq \frac{3.7.25^2}{32^3}\|P_1\|_p - \frac{25^3}{3.32^3}\|P_1\|_p \\
&- \frac{3.9^2.23}{32^3}\|P_1\|_p - \frac{9^3}{3.32^3}\|P_1\|_p \\
&= \frac{6254}{98304}\|P_1\|_p.
\end{aligned}$$

Then

$$\begin{aligned}
\int_0^1 \Big\|\sum_{i=0}^{3} P_i b_{i,3}(t)\Big\|_p^p dt &\geq \int_{\frac{7}{32}}^{\frac{9}{32}} \Big\|\sum_{i=0}^{3} P_i b_{i,3}(t)\Big\|_p^p dt \\
&\geq \int_{\frac{7}{32}}^{\frac{9}{32}} \left(\frac{6254}{98304}\right)^p \|P_1\|_p^p dt \\
&\geq \frac{1}{16}\left(\frac{6254}{98304}\right)^p \frac{1}{2+2.3^{-p}}\Big(\sum_{i=0}^{3}\|P_i\|_p^p\Big) \\
&\geq \frac{1}{2^{10p}}\Big(\sum_{i=0}^{3}\|P_i\|_p^p\Big).
\end{aligned}$$

- Case 3: $M = \frac{1}{3}\|P_2\|_p$. When we substitute $s = 1-t$, this case become Case 2.
- Case 4: $M = \|P_3\|_p$. When we substitute $s = 1-t$, this case become Case 1.

From the above four cases, we have

$$\int_0^1 \Big\| \sum_{i=0}^{3} P_i b_{i,3}(t) \Big\|_p^p dt \geq \frac{1}{2^{10p}} \Big(\sum_{i=0}^{3} \|P_i\|_p^p \Big).$$

□

Lemma 11. *Let P_0, P_1, P_2, P_3 be four points on $\mathbb{R}^n$, we get*

$$\max_{t\in[0,1]} \Big\| \sum_{i=0}^{3} P_i b_{i,3}(t) \Big\|_\infty \geq \frac{13}{96} \max_{i=0,\ldots,3} \|P_i\|_\infty.$$

Proof. Put

$$M = \max \Big\{ \|P_0\|_\infty, \frac{1}{3}\|P_1\|_\infty, \frac{1}{3}\|P_2\|_\infty, \|P_3\|_\infty \Big\}.$$

- Case 1: $M = \|P_0\|_\infty$.
  Since $\sum_{i=0}^{3} P_i b_{i,3}(0) = P_0$, hence

$$\max_{t\in[0,1]} \Big\| \sum_{i=0}^{3} P_i b_{i,3}(t) \Big\|_\infty \geq \|P_0\|_\infty = \max_{i=0,\ldots,3} \|P_i\|_\infty.$$

- Case 2: $M = \frac{1}{3}\|P_1\|_\infty$.
  At $t = \frac{1}{4}$, we get

$$\begin{aligned} \Big\| \sum_{i=0}^{3} P_i b_{i,3}\Big(\frac{1}{4}\Big) \Big\|_\infty &\geq \frac{27}{64}\|P_1\|_\infty - \frac{27}{64}\|P_0\|_\infty - \frac{9}{64}\|P_2\|_\infty - \frac{1}{64}\|P_3\|_\infty \\ &\geq \frac{27}{64}\|P_1\|_\infty - \frac{9}{64}\|P_1\|_\infty - \frac{9}{64}\|P_1\|_\infty - \frac{1}{192}\|P_1\|_\infty \\ &= \frac{13}{96}\|P_1\|_\infty. \end{aligned}$$

  Thus

$$\max_{t\in[0,1]} \Big\| \sum_{i=0}^{3} P_i b_{i,3}(t) \Big\|_\infty \geq \frac{13}{96} \max_{i=0,\ldots,3} \|P_i\|_\infty.$$

- Case 3: $M = \frac{1}{3}\|P_2\|_\infty$. This case is the same to Case 2.
- Case 4: $M = \|P_3\|_\infty$. This case is the same to Case 1.

From the above four cases, we have

$$\max_{t\in[0,1]} \Big\| \sum_{i=0}^{3} P_i b_{i,3}(t) \Big\|_\infty \geq \frac{13}{96} \max_{i=0,\ldots,3} \|P_i\|_\infty.$$

□

Combining the above lemmas, we obtain the following proposition.

Proposition 12. *Let $p \in [1,\infty]$. Then for any $\beta \in B_{N,3}$, we have*

$$\|\beta\|_p^{B_{N,3}} \leq 2^{10} \|\beta\|_{L_p}.$$

Proof. Let $\beta \in B_{N,3}$, assume that

$$\beta(t) = \beta^{(j)}(Nt - j) = \sum_{i=0}^{3} P_{j3+i} b_{i,3}(Nt - j) \quad \text{if } t \in \Big[\frac{j}{N}, \frac{j+1}{N}\Big], j = 0, \ldots, N-1.$$

Case $p \in [1,\infty)$, we have

$$\begin{aligned} \|\beta\|_{L_p} &= \Big(\int_0^1 \|\beta(t)\|_p^p dt \Big)^{1/p} \\ &= \Big(\sum_{j=0}^{N-1} \int_{\frac{j}{N}}^{\frac{j+1}{N}} \Big\| \sum_{i=0}^{3} P_{j3+i} b_{i,3}(Nt-j) \Big\|_p^p dt \Big)^{1/p} \\ &= \frac{1}{N^{1/p}} \Big(\sum_{j=0}^{N-1} \int_0^1 \Big\| \sum_{i=0}^{3} P_{j3+i} b_{i,3}(t) \Big\|_p^p dt \Big)^{1/p}. \end{aligned}$$

Using Lemma 10, we obtain

$$\begin{aligned} \|\beta\|_{L_p} &\geq \frac{1}{N^{1/p}} \Big(\sum_{j=0}^{N-1} \frac{1}{2^{10p}} \Big(\sum_{i=0}^{3} \|P_{j3+i}\|_p^p \Big) \Big)^{1/p} \\ &\geq \frac{1}{2^{10}} \|\beta\|_p^{B_{N,3}}. \end{aligned}$$

Case $p = \infty$, we have

$$\begin{aligned} \|\beta\|_{L_\infty} &= \max_{t\in[0,1]} \|\beta(t)\|_\infty \\ &= \max_{j=0,\ldots,N-1} \max_{t\in[\frac{j}{N},\frac{j+1}{N}]} \Big\| \sum_{i=0}^{3} P_{j3+i} b_{i,3}(Nt-j) \Big\|_\infty \\ &= \max_{j=0,\ldots,N-1} \max_{t\in[0,1]} \Big\| \sum_{i=0}^{3} P_{j3+i} b_{i,3}(t) \Big\|_\infty. \end{aligned}$$

Using Lemma 11, we get

$$\begin{aligned} \|\beta\|_{L_\infty} &\geq \max_{j=0,\ldots,N-1} \frac{13}{96} \max_{i=0,\ldots,3} \|P_{j3+i}\|_\infty \\ &= \frac{13}{96} \|\beta\|_\infty^{B_{N,3}} \geq \frac{1}{2^{10}} \|\beta\|_\infty^{B_{N,3}}. \end{aligned}$$

□

From the above propositions, we obtain the equivalence relations between the norms $\|\cdot\|_p^{B_{N,3}}$ and $\|\cdot\|_{L_p}$ on the space $B_{N,3}$ of N-piece cubic Bézier curve as follows.

Theorem 1. *For $p \in [1,\infty]$. Let $\beta \in B_{N,3}$, we get*

$$\|\beta\|_{L_p} \leq \|\beta\|_p^{B_{N,3}} \leq 2^{10} \|\beta\|_{L_p}.$$

Proof. Using Propositions 9 and 12, we get the proof of this theorem. □

https://doi.org/10.52111/qnjs.2023.17508

The equivalence constants do not depend on the number of pieces in piecewise cubic Bézier curves. From the above theorem, we get the following corollary:

$$d_{L_p}(\beta,\gamma) \le d_p^{B_{N,3}}(\beta,\gamma) \le 2^{10}\, d_{L_p}(\beta,\gamma)$$

for any $\beta,\gamma \in B_{N,3}$.

4. EQUIVALENCE CONSTANTS FOR THE NORMS $\|\cdot\|_p^{B_{N,m+1}}$ AND $\|\cdot\|_p^{B_{N,m}}$ ON $B_{N,m}$

For any Bézier curve of degree m with $m+1$ control points

$$\beta(t) = \sum_{i=0}^{m} P_i b_{i,m}(t),\ \ t \in [0,1],$$

we can choose $m+2$ points $Q_0,\dots,Q_m,Q_{m+1}$ as follows

$$Q_i = \begin{cases} P_0 & \text{if } i=0,\\ \dfrac{i}{m+1}P_{i-1} + \dfrac{m+1-i}{m+1}P_i & \text{if } i=1,\dots,m,\\ P_m & \text{if } i=m+1 \end{cases} \quad (2)$$

such that

$$\beta(t) = \sum_{i=0}^{m} P_i b_{i,m}(t) = \sum_{i=0}^{m+1} Q_i b_{i,m}(t),\ \ \forall t \in [0,1].$$

For simplicity of notation, we admits $P_{-1} = P_{m+1} = O_{\mathbb{R}^n}$. Hence

$$Q_i = \frac{i}{m+1}P_{i-1} + \frac{m+1-i}{m+1}P_i,\ \ \forall i = 0,\dots,m+1.$$

This means that a Bézier curve of degree m is also a Bézier curve of degree $m+1$ and then an N-piece Bézier curve of degree m can be considered as an N-piece Bézier curve of degree m. So, $\|\cdot\|_p^{B_{N,m+1}}$ is also a norm on the space $B_{N,m}$. This section deals with the equivalence relations between the norm $\|\cdot\|_p^{B_{N,m+1}}$ and the norm $\|\cdot\|_p^{B_{N,m}}$ on the space $B_{N,m}$.

We first consider on the space B_m of Bézier curves of degree m.

Lemma 13. *For $p \in [1,\infty]$. Let $\beta \in B_m$, we get*

$$\|\beta\|_p^{B_{m+1}} \le 2\|\beta\|_p^{B_m}.$$

Proof. Let $\beta \in B_m$, assume that

$$\begin{aligned}\beta(t) =& B([P_0,\dots,P_m],t) = \sum_{i=0}^{m} P_i b_{i,m}(t),\\ =& B([Q_0,\dots,Q_{m+1}],t) = \sum_{i=0}^{m+1} Q_i b_{i,m+1}(t),\\ & \forall t \in [0,1],\end{aligned}$$

where $P_i \in \mathbb{R}^n$, $Q_i \in \mathbb{R}^n$ and

$$Q_i = \frac{i}{m+1}P_{i-1} + \frac{m+1-i}{m+1}P_i,\ \ \forall i = 0,\dots,m+1.$$

Case $p \in [1,\infty)$, we have

$$\begin{aligned}\|\beta\|_p^{B_{m+1}} =& \left(\sum_{i=0}^{m+1} \|Q_i\|_p^p\right)^{1/p}\\ =& \left(\sum_{i=0}^{m+1} \left\|\frac{i}{m+1}P_{i-1} + \frac{m+1-i}{m+1}P_i\right\|_p^p\right)^{1/p}.\end{aligned}$$

From Minkowski's inequality, we obtain

$$\begin{aligned}\|\beta\|_p^{B_{m+1}} \le& \left(\sum_{i=0}^{m+1} \left\|\frac{i}{m+1}P_{i-1}\right\|_p^p\right)^{1/p}\\ &+ \left(\sum_{i=0}^{m+1} \left\|\frac{m+1-i}{m+1}P_i\right\|_p^p\right)^{1/p}\\ \le& \left(\sum_{i=0}^{m} \|P_i\|_p^p\right)^{1/p} + \left(\sum_{i=0}^{m} \|P_i\|_p^p\right)^{1/p}\\ =& 2\|\beta\|_p^{B_m}.\end{aligned}$$

Case $p = \infty$, we have

$$\begin{aligned}\|\beta\|_\infty^{B_{m+1}} =& \max_{i=0,\dots,m+1} \|Q_i\|_\infty\\ =& \max_{i=0,\dots,m+1} \left\|\frac{i}{m+1}P_{i-1} + \frac{m+1-i}{m+1}P_i\right\|_\infty\\ \le& \max_{i=0,\dots,m+1} \left\|\frac{i}{m+1}P_{i-1}\right\|_\infty\\ &+ \max_{i=0,\dots,m+1} \left\|\frac{m+1-i}{m+1}P_i\right\|_\infty\\ \le& 2\max_{i=0,\dots,m} \|P_i\|_\infty = 2\|\beta\|_\infty^{B_m}.\end{aligned}$$

□

Then we estimate an upper bound on the space $B_{N,m}$ of N-piece Bézier curves of degree m.

Proposition 14. *For $p \in [1,\infty]$. Let $\beta \in B_{N,m}$, we get*

$$\|\beta\|_p^{B_{N,m+1}} \le 2\|\beta\|_p^{B_{N,m}}.$$

Proof. For any $\beta \in B_{N,m}$,

$$\begin{aligned}\beta(t) =& \beta^{(j)}(Nt-j) = \sum_{i=0}^{m} P_{jm+i} b_{i,m}(Nt-j)\\ & \text{if } t \in \left[\frac{j}{N}, \frac{j+1}{N}\right], j = 1,\dots,N-1.\end{aligned}$$

Since a Bézier curve of degree m is also a Bézier curve of degree $m+1$, an N-piece Bézier curve of degree m is also an N-piece Bézier curve of degree $m+1$. We consider two cases:

Case $p \in [1,\infty]$. Applying Lemma 13, we obtain

$$\begin{aligned}\|\beta\|_p^{B_{N,m+1}} =& \frac{1}{N^{1/p}}\left(\sum_{j=0}^{N-1} \left(\|\beta^{(j)}\|_p^{B_{m+1}}\right)^p\right)^{1/p}\\ \le& \frac{1}{N^{1/p}}\left(\sum_{j=0}^{N-1} \left(2\|\beta^{(j)}\|_p^{B_m}\right)^p\right)^{1/p}\\ =& 2\|\beta\|_p^{B_{N,m}}.\end{aligned}$$

https://doi.org/10.52111/qnjs.2023.17508

Case $p=\infty$. From Lemma 13, we obtain

$$\begin{aligned}\|\beta\|_{\infty}^{B_{N,m+1}} &= \max_{j=0,\dots,N-1}\|\beta^{(j)}\|_{\infty}^{B_{m+1}}\\ &\le \max_{j=0,\dots,N-1}2\|\beta^{(j)}\|_{\infty}^{B_m}=2\|\beta\|_{\infty}^{B_{N,m}}.\end{aligned}$$

□

Consider $p\in[1,\infty[$. We use the parity of m to evaluate a lower bound for the norm $\|\cdot\|_p^{B_{m+1}}$ with respect to the norm $\|\cdot\|_p^{B_m}$ on the space B_m. From this estimation, we find equivalence constants on the space $B_{N,m}$ of N-piece Bézier curves of degree m.

Lemma 15. *Let $p\in[1,\infty[$. The inequality*

$$\frac{1}{2(m+1)}\|\beta\|_p^{B_m}\le\|\beta\|_p^{B_{m+1}}$$

holds for all $\beta\in B_m$.

Proof. Let $\beta\in B_m$, assume that

$$\begin{aligned}\beta(t)=&B([P_0,\dots,P_m],t)=\sum_{i=0}^{m}P_ib_{i,m}(t),\\ =&B([Q_0,\dots,Q_{m+1}],t)=\sum_{i=0}^{m+1}Q_ib_{i,m+1}(t),\\ &\forall t\in[0,1],\end{aligned}$$

where $P_i\in\mathbb{R}^n$, $Q_i\in\mathbb{R}^n$ and

$$Q_i=\frac{i}{m+1}P_{i-1}+\frac{m+1-i}{m+1}P_i,\ \ \forall i=0,\dots,m+1.$$

We consider 2 cases.

- Case 1: m is an odd number. We have

$$\begin{aligned}\|\beta\|_p^{B_{m+1}}&=\left(\sum_{i=0}^{m+1}\|Q_i\|_p^p\right)^{1/p}\\ &\ge\left(\sum_{i=0}^{(m+1)/2}\left\|\frac{i}{m+1}P_{i-1}+\frac{m+1-i}{m+1}P_i\right\|_p^p\right)^{1/p}.\end{aligned}$$

Using the Minkowski inequality, we obtain

$$\begin{aligned}\|\beta\|_p^{B_{m+1}}\ge&\left(\sum_{i=0}^{(m+1)/2}\left\|\frac{m+1-i}{m+1}P_i\right\|_p^p\right)^{1/p}\\ &-\left(\sum_{i=0}^{(m+1)/2}\left\|\frac{i}{m+1}P_{i-1}\right\|_p^p\right)^{1/p}\\ \ge&\left(\sum_{i=0}^{\frac{m+1}{2}-1}\frac{m+1-i}{m+1}\|P_i\|_p^p\right)^{1/p}\\ &-\left(\sum_{i=0}^{\frac{m+1}{2}-1}\frac{i+1}{m+1}\|P_i\|_p^p\right)^{1/p}\\ \ge&\left(\sum_{i=0}^{\frac{m+1}{2}-1}\frac{m+3}{2(m+1)}\|P_i\|_p^p\right)^{1/p}\\ &-\left(\sum_{i=0}^{\frac{m+1}{2}-1}\frac{m+1}{2(m+1)}\|P_i\|_p^p\right)^{1/p}\\ \ge&\frac{1}{m+1}\left(\sum_{i=0}^{\frac{m+1}{2}-1}\|P_i\|_p^p\right)^{1/p}.\end{aligned}$$

Furthermore, we have

$$\begin{aligned}\|\beta\|_p^{B_{m+1}}&=\left(\sum_{i=0}^{m+1}\|Q_i\|_p^p\right)^{1/p}\\ &\ge\left(\sum_{i=\frac{m+1}{2}+1}^{m+1}\left\|\frac{i}{m+1}P_{i-1}+\frac{m+1-i}{m+1}P_i\right\|_p^p\right)^{1/p}.\end{aligned}$$

From the Minkowski inequality, we get

$$\begin{aligned}\|\beta\|_p^{B_{m+1}}\ge&\left(\sum_{i=\frac{m+1}{2}+1}^{m+1}\left\|\frac{i}{m+1}P_{i-1}\right\|_p^p\right)^{1/p}\\ &-\left(\sum_{i=\frac{m+1}{2}+1}^{m+1}\left\|\frac{m+1-i}{m+1}P_i\right\|_p^p\right)^{1/p}\\ \ge&\left(\sum_{i=\frac{m+1}{2}}^{m}\frac{i+1}{m+1}\|P_i\|_p^p\right)^{1/p}\\ &-\left(\sum_{i=\frac{m+1}{2}}^{m}\frac{m+1-i}{m+1}\|P_i\|_p^p\right)^{1/p}\\ \ge&\left(\sum_{i=\frac{m+1}{2}}^{m}\frac{m+3}{2(m+1)}\|P_i\|_p^p\right)^{1/p}\\ &-\left(\sum_{i=\frac{m+1}{2}}^{m}\frac{m+1}{2(m+1)}\|P_i\|_p^p\right)^{1/p}\\ =&\frac{1}{m+1}\left(\sum_{i=\frac{m+1}{2}}^{m}\|P_i\|_p^p\right)^{1/p}.\end{aligned}$$

Then

$$\begin{aligned}2\|\beta\|_p^{B_{m+1}}\ge&\frac{1}{m+1}\left(\sum_{i=0}^{\frac{m+1}{2}-1}\|P_i\|_p^p\right)^{1/p}\\ &+\frac{1}{m+1}\left(\sum_{i=\frac{m+1}{2}}^{m}\|P_i\|_p^p\right)^{1/p}\\ \ge&\frac{1}{m+1}\left(\sum_{i=0}^{m}\|P_i\|_p^p\right)^{1/p}\\ =&\frac{1}{m+1}\|\beta\|_p^{B_m}.\end{aligned}$$

- Case 2: m is an even number. We have

$$\begin{aligned}\|\beta\|_p^{B_{m+1}}&=\left(\sum_{i=0}^{m+1}\|Q_i\|_p^p\right)^{1/p}\\ &\ge\left(\sum_{i=0}^{m/2}\left\|\frac{i}{m+1}P_{i-1}+\frac{m+1-i}{m+1}P_i\right\|_p^p\right)^{1/p}.\end{aligned}$$

https://doi.org/10.52111/qnjs.2023.17508

Applying Minkowski's inequality, we have

$$\begin{aligned}\|\beta\|_p^{B_{m+1}} \geq & \left(\sum_{i=0}^{m/2}\left\|\frac{m+1-i}{m+1}P_i\right\|_p^p\right)^{1/p} \\ & -\left(\sum_{i=0}^{m/2}\left\|\frac{i}{m+1}P_{i-1}\right\|_p^p\right)^{1/p} \\ = & \left(\sum_{i=0}^{m/2}\frac{m+2}{2(m+1)}\|P_i\|_p^p\right)^{1/p} \\ & -\left(\sum_{i=0}^{\frac{m}{2}-1}\frac{m}{2(m+1)}\|P_i\|_p^p\right)^{1/p} \\ \geq & \left(\sum_{i=0}^{m/2}\frac{m+2}{2(m+1)}\|P_i\|_p^p\right)^{1/p} \\ & -\left(\sum_{i=0}^{m/2}\frac{m}{2(m+1)}\|P_i\|_p^p\right)^{1/p} \\ = & \frac{1}{m+1}\left(\sum_{i=0}^{m/2}\|P_i\|_p^p\right)^{1/p}.\end{aligned}$$

Furthermore, we have

$$\begin{aligned}\|\beta\|_p^{B_{m+1}} &= \left(\sum_{i=0}^{m+1}\|Q_i\|_p^p\right)^{1/p} \\ &\geq \left(\sum_{i=\frac{m}{2}+1}^{m+1}\left\|\frac{i}{m+1}P_{i-1}+\frac{m+1-i}{m+1}P_i\right\|_p^p\right)^{1/p}.\end{aligned}$$

From the Minkowski inequality, we have

$$\begin{aligned}\|\beta\|_p^{B_{m+1}} \geq & \left(\sum_{i=\frac{m}{2}+1}^{m+1}\left\|\frac{i}{m+1}P_{i-1}\right\|_p^p\right)^{1/p} \\ & -\left(\sum_{i=\frac{m}{2}+1}^{m+1}\left\|\frac{m+1-i}{m+1}P_i\right\|_p^p\right)^{1/p} \\ \geq & \left(\sum_{i=m/2}^{m}\frac{m+2}{2(m+1)}\|P_i\|_p^p\right)^{1/p} \\ & -\left(\sum_{i=\frac{m}{2}+1}^{m}\frac{m}{2(m+1)}\|P_i\|_p^p\right)^{1/p} \\ \geq & \left(\sum_{i=\frac{m}{2}+1}^{m}\frac{m+2}{2(m+1)}\|P_i\|_p^p\right)^{1/p} \\ & -\left(\sum_{i=\frac{m}{2}+1}^{m}\frac{m}{2(m+1)}\|P_i\|_p^p\right)^{1/p} \\ = & \frac{1}{m+1}\left(\sum_{i=\frac{m}{2}+1}^{m}\|P_i\|_p^p\right)^{1/p}.\end{aligned}$$

Then

$$\begin{aligned}2\|\beta\|_p^{B_{m+1}} &\geq \frac{1}{m+1}\left(\sum_{i=0}^{m/2}\|P_i\|_p^p\right)^{1/p} \\ &+\frac{1}{m+1}\left(\sum_{i=\frac{m}{2}+1}^{m}\|P_i\|_p^p\right)^{1/p} \\ &\geq \frac{1}{m+1}\left(\sum_{i=0}^{m}\|P_i\|_p^p\right)^{1/p} = \frac{1}{m+1}\beta\|_p^{B_m}.\end{aligned}$$

Combining the above results, we obtain

$$\|\beta\|_1^{B_{D+1}} \geq \frac{1}{2(m+1)}\|\beta\|_1^{B_m}.$$

□

We now estimate on the space B_m of Bézier curve of degree m.

Lemma 16. *Let $\beta \in B_m$, we get*

$$\frac{1}{m+1}\|\beta\|_\infty^{B_m} \leq \|\beta\|_\infty^{B_{m+1}}.$$

Proof. Let $\beta \in B_m$, assume that

$$\begin{aligned}\beta(t) =& B([P_0,\ldots,P_m],t) = \sum_{i=0}^{m}P_i b_{i,m}(t), \\ =& B([Q_0,\ldots,Q_{m+1}],t) = \sum_{i=0}^{m+1}Q_i b_{i,m+1}(t), \\ & \forall t \in [0,1],\end{aligned}$$

where $P_i \in \mathbb{R}^n$, $Q_i \in \mathbb{R}^n$ and

$$Q_i = \frac{i}{m+1}P_{i-1} + \frac{m+1-i}{m+1}P_i, \ \forall i = 0,\ldots,m+1.$$

We assume that $\|\beta\|_\infty^{B_m} = \|P_{i_0}\|_\infty$.

- If $0 \leq i_0 < \dfrac{m+1}{2}$.

$$\begin{aligned}\|\beta\|_\infty^{B_{m+1}} &= \max_{i=0,\ldots,m+1}\{\|Q_i\|_\infty\} \\ &\geq \left\|\frac{i_0}{m+1}P_{i_0-1}+\frac{m+1-i_0}{m+1}P_{i_0}\right\|_\infty \\ &\geq \frac{m+1-i}{m+1}\|P_{i_0}\|_\infty - \frac{i_0}{m+1}\|P_{i_0-1}\|_\infty \\ &= \frac{m+1-2i_0}{m+1}\|P_{i_0}\|_\infty \\ &\geq \frac{1}{m+1}\|P_{i_0}\|_\infty = \frac{1}{m+1}\|\beta\|_\infty^{B_m}.\end{aligned}$$

https://doi.org/10.52111/qnjs.2023.17508

- If $i_0 = \dfrac{m+1}{2}$. (This case requires that m is an odd number.)

$$\begin{aligned}
\|\beta\|_\infty^{B_{m+1}} &= \max_{i=0,\dots,m+1}\{\|Q_i\|_\infty\}\\
&\geq \left\| \frac{i_0+1}{m+1}P_{i_0} + \frac{m+1-(i_0+1)}{m+1}P_{i_0+1}\right\|_\infty\\
&\geq \frac{i_0+1}{m+1}\|P_{i_0}\|_\infty - \frac{m-i_0}{m+1}\|P_{i_0+1}\|_\infty\\
&= \frac{2i_0+1-m}{m+1}\|P_{i_0}\|_\infty\\
&\geq \frac{1}{m+1}\|P_{i_0}\|_\infty = \frac{1}{m+1}\|\beta\|_\infty^{B_m}.
\end{aligned}$$

- If $i_0 > \dfrac{m+1}{2}$.

$$\begin{aligned}
\|\beta\|_\infty^{B_{m+1}} &= \max_{i=0,\dots,m+1}\{\|Q_i\|_\infty\}\\
&\geq \left\| \frac{i_0+1}{m+1}P_{i_0} + \frac{m+1-(i_0+1)}{m+1}P_{i_0+1}\right\|_\infty\\
&\geq \frac{i_0+1}{m+1}\|P_{i_0}\|_\infty - \frac{m-i_0}{m+1}\|P_{i_0+1}\|_\infty\\
&= \frac{2i_0+1-m}{m+1}\|P_{i_0}\|_\infty\\
&\geq \frac{1}{m+1}\|P_{i_0}\|_\infty = \frac{1}{m+1}\|\beta\|_\infty^{B_m}.
\end{aligned}$$

Combining the above results, we obtain

$$\|\beta\|_\infty^{B_{m+1}} \geq \frac{1}{m+1}\|\beta\|_\infty^{B_m}.$$

□

We then consider on the space $B_{N,m}$ of N-piece Bézier curves of degree m.

Proposition 17. *Let $p \in [1,\infty]$. The inequality*

$$\frac{1}{2(m+1)}\|\beta\|_p^{B_{N,m}} \leq \|\beta\|_p^{B_{N,m+1}}$$

holds for any $\beta \in B_{N,m}$.

Proof. Let $\beta \in B_{N,m}$, assume that

$$\begin{aligned}
\beta(t) =& \beta^{(j)}(Nt-j) = \sum_{i=0}^{m} P_{jm+i}b_{i,m}(Nt-j)\\
&\text{if } t \in \left[\frac{j}{N}, \frac{j+1}{N}\right], j = 1,\dots,N-1.
\end{aligned}$$

Because a Bézier curve of degree m is also a Bézier curve of degree $m+1$, an N-piece Bézier curve of degree m is also an N-piece Bézier curve of degree $m+1$. We consider two cases: Case $p \in [1,\infty)$. From Lemma 15, we get

$$\begin{aligned}
\|\beta\|_p^{B_{N,m+1}} =& \frac{1}{N^{1/p}}\left(\sum_{j=0}^{N-1}\left(\|\beta^{(j)}\|_p^{B_{m+1}}\right)^p\right)^{1/p}\\
\geq& \frac{1}{N^{1/p}}\left(\sum_{j=0}^{N-1}\left(\frac{1}{2(m+1)}\|\beta^{(j)}\|_p^{B_m}\right)^p\right)^{1/p}\\
=& \frac{1}{2(m+1)}\|\beta\|_p^{B_{N,m}}.
\end{aligned}$$

Case $p = \infty$. From Lemma 16, we get

$$\begin{aligned}
\|\beta\|_\infty^{B_{N,m+1}} &= \max_{j=0,\dots,N-1}\|\beta^{(j)}\|_\infty^{B_{m+1}}\\
&\geq \max_{j=0,\dots,N-1}\frac{1}{m+1}\|\beta^{(j)}\|_\infty^{B_m}\\
&= \frac{1}{m+1}\|\beta\|_\infty^{B_{N,m}}.
\end{aligned}$$

Thus, the proof of this proposition is complete. □

From the above result, we obtain the following theorem.

Theorem 2. *For $p \in [1,\infty]$. Let $\beta \in B_{N,m}$, we get*

$$\frac{1}{2(m+1)}\|\beta\|_p^{B_{N,m}} \leq \|\beta\|_p^{B_{N,m+1}} \leq 2\|\beta\|_p^{B_{N,m}}.$$

Proof. Using Propositions 14 and 17, we get the proof of this theorem. □

Thus, we have the following corollary

$$\begin{aligned}
\frac{1}{2(m+1)}d_p^{B_{N,m}}(\beta,\gamma) \leq& d_p^{B_{N,m+1}}(\beta,\gamma)\\
\leq& 2d_p^{B_{N,m}}(\beta,\gamma),
\end{aligned}$$

for any $\beta,\gamma \in B^{N,m}$.

5. CONCLUSION

This article introduces a norm $\|\cdot\|_p^{B_{N,3}}$ of piecewise cubic Bézier curves which is defined by control points. This norm is convenient to compute. We also show the equivalence constants for the norm $\|\cdot\|_p^{B_{N,3}}$ and the norm L_p. These equivalence constants do not depend on the number of pieces. Thus, we can use the norm $\|\cdot\|_p^{B_{N,3}}$ to consider the convergence for sequences of piecewise cubic Bézier curves. This result is important for using piecewise cubic Bézier curves to find optimal trajectories.

Acknowledgment

This research is conducted within the framework of science and technology projects at institutional level of Quy Nhon University under the project code T2022.745.01.

REFERENCES

1. J. E. McIntyre. *Guidance, flight mechanics and trajectory optimization*, National Aeronautics and Space Administration, Washington, D.C., 1968.

2. F. Bullo, J. Cortés, S. Martínez. *Distributed control of robotic networks*, Princeton University Press, Princeton, New Jersey, 2009.

3. M. Farber. *Invitation to topological robotics*, European Mathematical Society (EMS), Zürich, 2008.

4. J. V. Neumann. *Collected works. Vol. VI: Theory of games, astrophysics, hydrodynamics and meteorology*, The Macmillan Co., New York, 1963.

5. K. J. Worsley. Boundary corrections for the expected Euler characteristic of excursion sets of random fields, with an application to astrophysics, *Advances in Applied Probability*, **1995**, *27*, 943–959.

6. M. Farber. Topological complexity of motion planning, *Discrete & Computational Geometry. An International Journal of Mathematics and Computer Science*, **2003**, *29*, 211–221.

7. M. Farber, S. Tabachnikov, S. Yuzvinsky. Topological robotics: motion planning in projective spaces, *International Mathematics Research Notices*, **2003**, *34*, 1853–1870.

8. R. M. Murray, S. S. Sastry. Nonholonomic motion planning: steering using sinusoids, *Institute of Electrical and Electronics Engineers Transactions on Automatic Control*, **1993**, *38*(5), 700–716.

9. J. Sokolowski, J.-P. Zolésio. *Introduction to shape optimization*, Springer-Verlag, Berlin, 1992.

10. J. Haslinger, R. A. E. Mäkinen. *Introduction to shape optimization*, Society for Industrial and Applied Mathematics (SIAM), Philadelphia, Pennsylvania, 2003.

11. G. Allaire. *Shape optimization by the homogenization method*, Springer-Verlag, New York, 2002.

12. B. Mohammadi, O. Pironneau. *Applied shape optimization for fluids*, 2nd edition, Oxford University Press, Oxford, 2010.

13. F. de Gournay, G. Allaire, F. Jouve. Shape and topology optimization of the robust compliance via the level set method, *ESAIM. Control, Optimisation and Calculus of Variations*, **2008**, *14*(1), 43–70.

14. D. Bucur, G. Buttazzo. *Variational methods in some shape optimization problems*, Scuola Normale Superiore, Pisa, 2002.

15. J. Gallier. *Curves and surfaces in geometric modeling*, Morgan Kaufmann, San Francisco, California, 2000.

16. D. Marsh. *Applied geometry for computer graphics and CAD*, 2nd edition, Springer-Verlag London, London, 2005.

17. T. W. Sederberg. Applications to computer aided geometric design, *American Mathematical Society*, **1998**, *53*, 67–89.

https://doi.org/10.52111/qnjs.2023.17508

TẠP CHÍ KHOA HỌC
TRƯỜNG ĐẠI HỌC QUY NHƠN

Cấu trúc và tính chất quang của vật liệu zirconium(oxy)nitride tổng hợp từ hạt nano zirconium dioxide

Nguyễn Thị Minh Uyên[1], Lê Trần Phương Thảo[1], Đặng Bùi Nhật Lê[2], Lê Thị Mỹ Nhi[3], Phạm Quỳnh Nhi[3], Lê Thị Bích Tuyền[3], Văn Thị Thùy Trang[1], Lê Thị Ngọc Loan[1,*]

[1]Khoa Khoa học Tự nhiên, Trường Đại học Quy Nhơn, Việt Nam
[2]Khoa Khoa học và kỹ thuật vật liệu, Trường Đại học Phenikaa, Việt Nam
[3]Khoa Sư phạm, Trường Đại học Quy Nhơn, Việt Nam

Ngày nhận bài: 16/08/2023; Ngày sửa bài: 06/10/2023; Ngày nhận đăng: 13/10/2023; Ngày xuất bản: 28/10/2023

TÓM TẮT

Trong những năm gần đây, việc sử dụng thiết bị thu nhiệt năng mặt trời đang ngày càng gia tăng vì đây là một phương pháp trực tiếp và hiệu quả để biến năng lượng mặt trời thành các nguồn năng lượng có thể sử dụng được. Trong xu hướng này, các nghiên cứu tập trung vào việc phát triển cấu trúc nano của các nitride kim loại chuyển tiếp và oxynitride kim loại, nhằm tối đa hóa khả năng thu năng lượng từ mặt trời. Trong nghiên cứu này, vật liệu zirconium(oxy)nitride (Zr(O)N) đã được tổng hợp thành công bằng cách xử lý ZrO_2 trong môi trường khí NH_3 ở nhiệt độ cao nhằm ứng dụng trong quá trình chuyển đổi năng lượng quang nhiệt. Để xác định đặc điểm cấu trúc tinh thể, hình thái và tính chất của các vật liệu này, các kỹ thuật phân tích như nhiễu xạ tia X (XRD), kính hiển vi điện tử quét (SEM) và phân tích phổ phản xạ khuếch tán tử ngoại khả kiến (UV-Vis DRS) đã được sử dụng. Các kết quả cho thấy rằng pha tinh thể zirconium(oxy)nitride bắt đầu hình thành ở nhiệt độ 1150 ^oC. Các vật liệu Zr(O)N đã tổng hợp thể hiện khả năng hấp thụ năng lượng mặt trời và tạo ra nhiệt một cách hiệu quả. Các kết quả này cho thấy Zr(O)N có thể được tổng hợp bằng phương pháp đơn giản và có tiềm năng lớn trong các ứng dụng chuyển hóa năng lượng quang - nhiệt.

Từ khóa: *Hạt nano ZrO_2, ZrN, Zr(O)N, chuyển hóa năng lượng quang nhiệt.*

**Tác giả liên hệ chính.*
Email: lethingocloan@qnu.edu.vn

https://doi.org/10.52111/qnjs.2023.17509

QUY NHON UNIVERSITY
JOURNAL OF SCIENCE

Structural and optical characterization of zirconium(oxy)nitride synthesized from zirconium dioxide nanoparticles

Nguyen Thi Minh Uyen[1], Le Tran Phuong Thao[1], Dang Bui Nhat Le[2], Le Thi My Nhi[3], Pham Quynh Nhi[3], Le Thi Bich Tuyen[3], Van Thi Thuy Trang[1], Le Thi Ngoc Loan[1,*]

[1]Faculty of Natural Sciences, Quy Nhon University, Vietnam
[2]Faculty of Materials Science and Engineering, Phenikaa University, Vietnam
[3]Faculty of Pedagogy, Quy Nhon University, Vietnam

Received: 16/08/2023; Revised: 06/10/2023; Accepted: 13/10/2023; Published: 28/10/2023

ABSTRACT

In recent years, there has been a growing focus on solar thermal collectors as they offer a direct and efficient means of converting solar energy into usable forms. In line with this, significant attention has been directed towards advancing transition metal nitride and metal oxynitride nanostructures for solar-thermal collectors to maximize solar energy harvesting. In this study, we have successfully synthesized zirconium(oxy)nitride (Zr(O)N) materials for photothermal energy conversion. The process involved treating ZrO_2 in NH_3 at high temperatures, resulting in the creation of nanoparticles with promising properties. To characterize the materials, we conducted thorough investigations using X-ray diffraction (XRD), scanning electron microscopy (SEM), and ultraviolet-visible diffuse reflectance spectroscopy (UV-Vis DRS). The findings indicate that the Zr(O)N crystalline phase initiates its formation at 1150 °C. The Zr(O)N materials possess a robust capacity for absorbing solar energy and efficiently producing heat. Furthermore, these outcomes highlight the feasibility of synthesizing Zr(O)N through a straightforward approach, underscoring their significant potential for applications in photothermal conversion.

Keywords: *ZrO_2 nanoparticles, ZrN, Zr(O)N, photothermal energy conversion.*

1. INTRODUCTION

In recent times, there has been a notable increase in the exploration of group IVB transition-metal nitrides, as opposed to noble metals like Au and Ag, to broaden the scope of plasmonic applications and deepen our understanding of light-matter interactions.[1,2] This shift has the potential to revolutionize core technologies in fields such as telecommunications, computing, efficient solar harvesting, solid-state lighting, photochemistry, photo- and bio-sensing, diagnostics, and therapeutics.[3,4] Among these materials, titanium nitride (TiN) has garnered significant interest. However, zirconium nitride (ZrN) holds particular importance due to its distinct physical properties, including excellent anti-corrosion characteristics and a high melting point.[5] Importantly, ZrN exhibits a zero crossover wavelength within the visible spectrum, similar to Au, which grants them plasmonic properties in the visible and near-infrared regions.[3] This

**Corresponding author.*
Email: lethingocloan@qnu.edu.vn

https://doi.org/10.52111/qnjs.2023.17509

feature enhances their ability to absorb sunlight and convert it into heat, making them highly suitable for solar light harvesting applications.[6]

Numerous techniques can be employed for the synthesis of ZrN, such as high-energy ball milling of Zr elemental powders in a nitrogen gas environment at room temperature,[7] the magnesium thermal reduction process,[8] a nonthermal plasma reactor,[9] the initiation of exothermal reactions through microwave radiation,[10] and the utilization of metalorganic chemical vapor deposition method.[11,12] Among these approaches, the reduction-nitridation of zirconium oxide (ZrO_2) is frequently employed for the synthesis of zirconium nitride. This method involves the direct nitriding of ZrO_2 using ammonia gas at elevated temperatures.[12-14]

Zirconium Nitride (ZrN) possesses distinctive properties, including a high melting point (2952 ^oC) and single crystal hardness (22.7±1.7 GPa), strong covalent Zr-N bonding and excellent chemical resistance, and stability, making it highly suitable for applications as coatings and protective layers.[15-17] Recently, ZrN has garnered attention as an excellent material for electrodes in energy storage and conversion,[18] owing to its exceptional electrical conductivity, mobility, and impressive electrochemical performance.[4,19,20] Moreover, ZrN has emerged as a promising alternative plasmonic material, finding diverse applications in solar cells,[21] solar light harvesting,[22] and solar to heat energy conversion.[23,24] Its unique properties make it a valuable candidate in these solar-related technologies. Furthermore, zirconium oxynitride, similar to zirconium nitride, has piqued special interest as a material for solar-thermal collectors. This interest is due to its remarkable solar absorptance and thermal stability.[9,24,25] Thus, both ZrN and zirconium oxynitride exhibit great potential in advancing various applications related to energy conversion and utilization.

In this study, a straightforward approach was introduced to produce zirconium(oxy)nitride nanoparticles through the reduction-nitridation process of zirconium oxide nanoparticles (ZrO_2 NPs) in NH_3 gas at elevated temperatures. SEM images illustrated that average particles increased during nitridation process. Notably, the results revealed the formation of cubic ZrN phase at 1150 °C, and the materials exhibited strong and broad absorption spanning from the visible to near-infrared region (~300 – 2000 nm). Furthermore, the potential of the synthesized nanoparticles in solar-thermal energy conversion was also assessed.

2. EXPERIMENTAL

2.1. Chemicals

The raw materials used in this study including zirconium dioxide (ZrO_2, 99.95%), zirconium nitride (ZrN, 99.9%), ammonia and nitrogen gas (NH_3, H_2, > 99.9%) were supplied from Aladdin Reagent Co., Ltd., China.

2.2. NH_3 treatment of ZrO_2 nano particles

Initially, 8 mg of ZrO_2 powder was carefully placed into a ceramic boat, which was then positioned at the center of a quartz-tube furnace using a customized setup. This setup allowed for precise control of temperature, pressure, and gas flow during the experiment. One end of the quartz tube was connected to the gas inlet, with N_2 and NH_3 gases available. The other end was connected to a mechanical vacuum pump. To begin the process, the quartz tube was evacuated to achieve a vacuum level of 10^{-3} mbar. Subsequently, the furnace was pre-heated to 300 °C. To eliminate any contaminants, the tube was purged multiple times with N_2 gas. Once prepared, the temperature in the furnace was raised either to 1050 or 1150 °C, both at a ramping rate of 5 °C min^{-1}. After the desired temperature was stabilized, pure ammonia gas was continuously introduced into the furnace at a flow rate of 400 sccm for a duration of

1.5 hours. Following this, the furnace was gradually cooled down to 100 °C in an NH_3 environment and further to room temperature in N_2 before unloading the sample.

2.3. Material characterization

The crystalline structure of the obtained samples was studied by powder X-ray diffraction (XRD) employing an X-ray diffractometer (Brucker Phaser, D2) using Cu Kα irradiation (λ = 0.154 nm). The surface morphology of the synthesized materials was characterized by scanning electron microscopy (SEM) using a HITACHI S-4800 microscope. UV-Vis absorption spectra were measured using a Shimadzu 2600 UV-visible spectrometer.

2.4. Photothermal materials study

For each experimental run, 0.8g of PVP (Polyvinylpyrrolidone) and 9.5 mL of DMF (N,N-Dimethylformamide) were combined in a 100 mL glass beaker and stirred for a period of 4 hours. Subsequently, 0.01g of ZrO_2 1150 nanoparticles was added to the mixture and dispersed with sonication for 10 minutes. The resulting ZrO_2 1150 nanoparticle suspension was then used to create thin layers on glass slides (2 cm x 2 cm) through the spin-coating method, spinning at 1500 rpm for 60 seconds.

To evaluate the solar-thermal energy conversion performance of the prepared samples, a custom-made closed metal chamber made of steel was utilized. The metal chamber was insulated with fiber glass material to minimize heat loss. The prepared samples were placed at the center of this chamber and exposed to sunlight irradiation. The temperature of the ZrO_2 1150 layer was monitored using a K-type temperature probe. Additionally, temperature measurements inside the chamber and the ambient air outside were recorded using mercury temperature meters. The photon flux of sunlight was measured using a luminous flux meter from China. Throughout the experiments, data was recorded at 10-minute intervals to analyze the performance of the samples.

3. RESULTS AND DISCUSSION

The XRD patterns of the ZrO_2 NPs before and after the NH_3 treatment at 1050 and 1150 °C (sample ZrO_2 1050 and ZrO_2 1150) are presented in Figure 1. In the case of ZrO_2 nanoparticles (referred to as ZrO_2 TM), all observed diffraction peaks corresponding to monoclinic (m) and tetragonal (t) crystal structure phases were accurately matched with standard data of ZrO_2 (PDF Card - 00-036-0420 and PDF Card - 00-042-1164, respectively).[26,27] This result also indicates high purity of ZrO_2 TM (red trace).

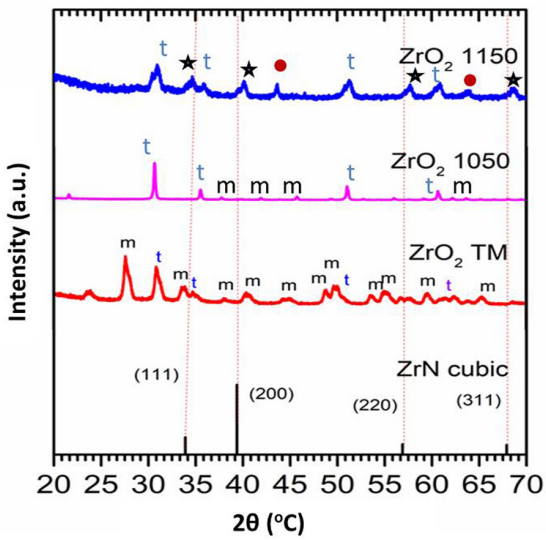

Figure 1. XRD diffraction patterns of ZrO_2 precusor and ZrO_2 after annealing in NH_3 at 1050 and 1150 °C.

Upon NH_3 treatment of ZrO_2 at 1050 °C, the peaks related to the monoclinic (m) phase of ZrO_2 nearly vanish, while most of those corresponding to the tetragonal ZrO_2 remain, e.g., at 31.3°, 36.3°, 52.3° and 62.1° (pink trace).[28,29] Furthermore, at the higher temperature of 1150 °C, the treatment results in the appearance of new peaks at 33.9°, 39.4°, 56.9°, and 67.9° (black stars), corresponding to diffraction planes of the (111), (200), (220), and (311) atomic planes of the face-centered cubic (FCC) structure of ZrN (PDF Card - 00-031-1493).[16,30] There are two peaks at 43.1° and 63.2° (red dots) which can be attributed to the insulating-metallic phase transition (ZrO_xN_y).[29]

https://doi.org/10.52111/qnjs.2023.17509

Interestingly, annealing ZrO_2 in NH_3 transforms the mixture of monoclinic and tetragonal crystal structure phases into the single phase of t-ZrO_2 and initiates a new phase of ZrN.

Figure 2 displays scanning electron microscopy (SEM) images of a representative sample, along with the particle size distribution, which was measured and determined using Digital Micrograph.

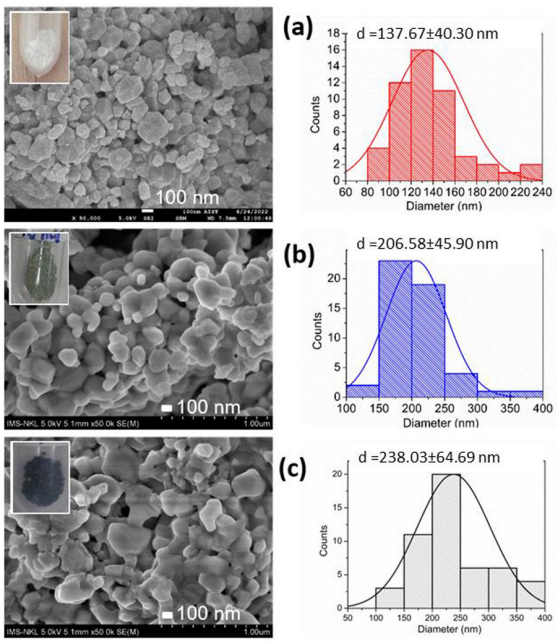

Figure 2. SEM images and the particle size distribution of (a) ZrO_2 TM, as well as ZrO_2 after being treated in NH_3 at different temperatures: (b) 1050 °C, and (c) 1150 °C. The color of the powders is also illustrated in the respective insets.

The SEM images present the shapes and sizes of ZrO_2 TM nanoparticles (Figure 2a) and the same nanoparticles after annealing in ammonia at 1050 °C (Fig. 2b) and 1150 °C (Figure 2c). In Figure 2a, ZrO_2 TM exhibits a wide variation in particle sizes, with an average diameter of approximately 137.67 ± 40.30 nm, represented by the top red distribution curve. After treatment at 1050 °C, the average diameter increases significantly to 206.58 ± 45.90 nm, a nearly 15% increment, as shown by the middle blue distribution. Subsequently, the particle size further grows by about 17% after treatment NH_3 at 1150 °C, resulting in an average diameter of about 238.03 ± 64.69 nm, as illustrated in the bottom black curve. The growth of particle sizes is due to higher reaction temperature. In addition, the substantial differences in size between the ZrO_2 1050 and ZrO_2 1150 samples, approximately 22% and 27%, respectively, can be attributed to the significant variability in the size of the ZrO_2 TM particles, estimated to be around 29%.

The findings reveal that NH_3 treatment at temperatures ranging from 1050 to 1150 °C does not significantly impact the surface morphology of the nanoparticles. However, it does induce remarkable changes in both particle size and the appearance of the powder color. These color variations are clearly visible in the optical images within the SEM images, showcasing a gradual shift from white (ZrO_2 TM) to dark gray (ZrO_2 1050) and ultimately black (ZrO_2 1150), which is the typical color of ZrN powder. This color transformation aligns with the light absorption characteristics observed in the following UV-Vis absorption spectra.

To investigate the optical properties of the composites, UV-vis diffuse reflectance spectral analysis was conducted on ZrO_2 powder, as well as the ZrO_2 samples treated in NH_3 at 1050 and 1150 °C. The results obtained from the analysis are presented in Figure 3.

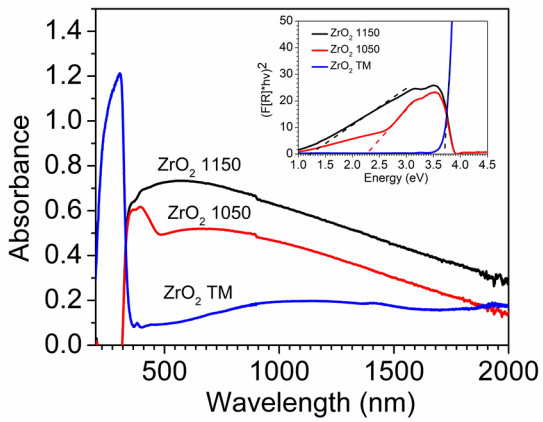

Figure 3. UV-Vis absorption spectra of the representative samples and the corresponding band gap calculations using the Kubelka-Munk method as indicated in the inset.

The UV-Vis absorption spectrum ZrO_2 TM shows a sharp and prominent absorption band with maximum at around 277 nm (4.48 eV in photon energy) which can arise due to the transition between valence band to conduction band.[28,31] However, this absorption peak for the ZrO_2 nanostructure in the UV-region is at lower energy as compared to the previous report on the optical band gap for bulk ZrO_2 (5.0 eV).[32] This indicates that there is still contribution from extrinsic states towards the absorption in this region. Apart from the strong absorption peak, a broad and weak absorption from visible to near infrared exists. The weak absorption in the visible and near IR region is expected to arise from transitions involving extrinsic states such as surface trap states or defect states or impurities.[32] The direct band gap energy can be determined by Kubelka-Munk method, about 3.7 eV, as indicated by the blue trace in the inset of Figure 3.

When comparing with pure ZrO_2, the absorption spectrum of ZrO_2 1050 reveals distinct characteristics. It displays a pronounced absorption peak at 391 nm with an energy gap (E_g) of approximately 2.3 eV, as depicted in the red trace within the inset. Additionally, there is a broad and potent absorption band spanning from the visible to the near-infrared spectrum. The initial absorption can be attributed to the band gap of zirconium oxynitride,[28,33,34] while the broad absorption is the result of a continuous depopulation of the d-band and the creation of an energy gap between the valence band and the Fermi level.[35]

Upon increasing the annealing temperature to 1150 °C, a phase transition to ZrN commences from the outer layer of ZrO_2 1150 particles, as evidenced by the XRD pattern. This transformation yields a significantly intensified and broadened absorption spectrum over a wide range, extending from the ultraviolet to the near-infrared region. Several factors contribute to this phenomenon, including the plasmonic behavior arising from the metallic content of ZrN/Zr_2ON_2,[9,36] the presence of oxygen/zirconium vacancies or interstitials[32,37] and a diverse distribution of particle sizes, as observed in Figure 2. Notably, the broad plasmon resonance spectrum featuring a central peak around 530 nm and the heightened light absorption within the visible-near infrared range at elevated temperatures hold immense promise for applications in solar light harvesting.

Figure 4 illustrates temperature measurements conducted within a metallic enclosure and on glass coated with ZrO_2 1150 nanoparticles. The temperature of the ZrO_2 1150-coated glass is depicted as the red trace, the air temperature within the chamber is represented by the black trace, and the photon flux is displayed as the blue trace (transmitted through a chamber window glass with over 90% light transmission). In Figure 4a, temperature measurements taken outdoors in an environment with an ambient air temperature of 26 °C are displayed for both inside the chamber and the glass film coated with ZrO_2 1150 nanoparticles, all under sunlight illumination.

The outcomes reveal a proportional increase in the temperature of the ZrO_2 1150-coated glass with rising photon flux. After a continuous 60-minute exposure to sunlight, the glass coated with ZrO_2 1150 nanoparticles reaches a peak temperature of 60 °C, presenting a temperature differential (ΔT) of approximately 15 °C above the air temperature within the enclosed metal box (around 45 °C). These initial findings strongly suggest the potential of zirconium oxynitride as a viable material for applications involving photothermal energy conversion.

https://doi.org/10.52111/qnjs.2023.17509

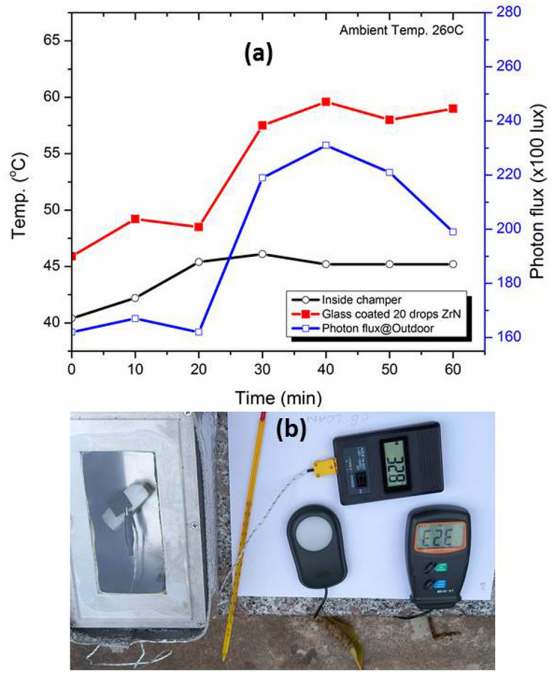

Figure 4. Temperature arising from ZrO_2 1150 material under sunlight exposure: the temperature of the ZrO_2 1150-coated glass is depicted as the red trace, the air temperature within the chamber is represented by the black trace, and the photon flux is displayed as the blue trace (transmitted through a chamber window glass with over 90% light transmission).

4. CONCLUSION

In brief, we have illustrated a straightforward method for producing zirconium(oxy)nitride nanoparticles. These particles display robust and extensive light absorption across a wide spectrum of solar wavelengths, encompassing the UV-vis to infrared range. We evaluated their ability for photothermal energy conversion by employing a metal chamber setup, where ZrO_2 1150 nanoparticles -coated glass were tested. The results indicated a significant heat generation, surpassing the surrounding temperature by approximately 30%. This experimentation underscores the promising prospects of utilizing zirconium(oxy)nitride for enhancing solar-to-heat conversion performance.

Acknowledgements

This work is financially supported by the Ministry of Education and Training of Vietnam under the grant number B2022-DQN-04.

REFERENCES

1. A. Lalisse, G. Tessier, J. Plain, and G. Baffou. Plasmonic efficiencies of nanoparticles made of metal nitrides (TiN, ZrN) compared with gold, *Scientific Reports*, **2016**, *6*, 1-10.
2. G. V. Naik, V. M. Shalaev, and A. Boltasseva. Alternative plasmonic materials: Beyond gold and silver, *Advanced Materials*, **2013**, *25*(24), 3264-3294.
3. P. Patsalas. Zirconium nitride : A viable candidate for photonics and plasmonics?, *Thin Solid Films*, **2019**, *688*, 137438.
4. B. J. Tan, Y. Xiao, F. S. Galasso, and S. L. Suib. Thermodynamic analysis and synthesis of zirconium nitride by thermal nitridation of sol-gel zirconium oxide, *Chemistry of Materials,* **1994**, *7*, 918-926.
5. U. Guler, V. M. Shalaev, and A. Boltasseva. Nanoparticle plasmonics: going practical with transition metal nitrides, *Materials Today*, **2015**, *18*(4), 1-11.
6. M. S. El-Eskandarany and A. H. Ashour. Mechanically induced gas-solid reaction for the synthesis of nanocrystalline ZrN powders and their subsequent consolidations, *Journal of Alloys and Compounds*, **2000**, *313*(1), 224-234.
7. Z. Wu, Z. Chen, L. Wang, L. Fang, T. Zhou, T. Mei, C. Zhang, Q. Li. Solid-state synthesis of zirconium nitride and hafnium nitride powders, *Journal of the Ceramic Society of Japan*, **2021**, *129*(3), 200-203.
8. S. Exarhos, A. Alvarez-Barragan, E. Aytan, A. A. Balandin, and L. Mangolini. Plasmonic core-shell zirconium nitride-silicon oxynitride nanoparticles, *ACS Energy Letters*, **2018**, *3*(10), 2349-2356.
9. R. A. Shishkin and E. S. Maiorova. Microwave vs autoclave synthesis of nanodisperse ZrN powder, *Glass and Ceramics*, **2017**, *74*(3), 123-125.
10. M. Banerjee, S. Kim, K. Xu, D. Barreca. Fabrication of ZrO_2 and ZrN films by metalorganic chemical vapor deposition employing new Zr precursors, *Crystal Growth & Design*, **2012**, *12*(10), 5079-5089.

11. A. S. Chernyavskii. Synthesis of ceramics based on titanium, zirconium, and hafnium nitrides, *Inorganic Materials*, **2019**, *55*(13), 1303-1327.

12. B. Fu and L. Gao. Synthesis of nanocrystalline zirconium nitride powders by reduction-nitridation of zirconium oxide, *Journal of the American Ceramic Society*, **2004**, *87*(4), 696-698.

13. B. J. Tan, Y. Xiao, F. S. Galasso, and S. L. Suib. Thermodynamic analysis and synthesis of zirconium nitride by thermal nitridation of sol-gel zirconium oxide, *Chemistry of Materials*, **1994**, *6*(7), 918–926.

14. S. K. Kim and V. V. Le. Surface & coatings technology cathodic arc plasma deposition of nano-multilayered ZrN/AlSiN thin films, *Surface and Coatings Technology*, **2011**, *206*(6), 1507–1510.

15. Z. Lei, Q. Zhang, X. Zhu, D. Ma, F. Ma, Z. Song, Y. Q. Fu. Corrosion performance of ZrN/ZrO_2 multilayer coatings deposited on 304 stainless steel using multi-arc ion plating, *Applied Surface Science*, **2018**, *431*, 170-176.

16. Y. Lu, Z. Yuan, H. Shen, X. Huai, and Z. Huang. High-temperature phase relations of ZrN–ZrO_2–Y_2O_3 ternary system, *Journal of Advanced Ceramics*, **2018**, *7*(4), 388-391.

17. T. Boldoo, J. Ham, E. Kim, and H. Cho. Review of the photothermal energy conversion performance of nanofluids, their applications, and recent advances, *Energies*, **2020**, *13*(21), 5748.

18. Y. Zhong, X. H. Xia, F. Shi, J. Y. Zhan, J. P. Tu, and H. J. Fan. Transition metal carbides and nitrides in energy storage and conversion, *Advanced Science*, **2016**, *3*(5), 1500286.

19. R. W. Harrison and W. E. Lee. Processing and properties of ZrC, ZrN and ZrCN ceramics: a review, *Advances in Applied Ceramics*, **2016**, *115*(5), 294-307.

20. N. Saiprasad, A. Boretti, L. Rosa. and S. Castelletto. Novel plasmonic materials to improve thin film solar cells efficiency, *Conference: Proc. SPIE 9668, Micro+Nano Materials, Devices, and Systems,* **2015**, 966847.

21. G. Baffou, F. Cichos, and R. Quidant. Applications and challenges of thermoplasmonics, *Nature Materials*, **2020**, *19* (9), 946-958.

22. L. T. T. Lieu, N. T. Lam, N. H. Hue, N. V. Nghia, N. M. Vuong, H. N. Hieu, N. V. Thang, L. V. Le, N. V. Huong, P.-C. Lin, A. Yadav, I. Madarevic, E. Janssens, H. V. Bui, and L. T. N. Loan. Titanium nitride nanodonuts synthesized from natural ilmenite ore as a novel and efficient thermoplasmonic material, *Nanomaterials*, **2021**, *11*(1), 76-87.

23. K. Xu, M. Du, L. Hao, J. Mi, Q. Yu, and S. Li. A Review of high-temperature selective absorbing coatings for solar thermal applications, *Journal of Materiomics*, **2020**, *6*(1), 167-182.

24. K. Ibrahim, H. Taha, M. M. Rahman, H. Kabir, and Z. T. Jiang. Solar selective performance of metal nitride/oxynitride based magnetron sputtered thin film coatings: A comprehensive review, *Journal of Optics (United Kingdom)*, **2018**, *20*(3), 033001.

25. P. R. Rauta, P. Manivasakan, V. Rajendran, B. B. Sahu, B. K. Panda, and P. Mohapatra. Phase transformation of ZrO_2 nanoparticles produced from zircon, *Phase Transitions*, **2012**, *85*(1), 13–26.

26. D. Manoharan, A. Loganathan, V. Kurapati, and V. J. Nesamony. Ultrasonics sonochemistry unique sharp photoluminescence of size-controlled sonochemically synthesized zirconia nanoparticles, *Ultrasonics Sonochemistry*, **2015**, *23*, 174–184.

27. J. C. Garcia, L. M. Scolfaro, A. T. Lino, V. N. Freire, and G. A. Farias. Structural , electronic, and optical properties of ZrO_2 from ab initio calculations, *Journal of Applied Physics*, **2006**, *100*, 104103.

28. P. Carvalho, J. M. Chappé, L. Cunha, S. Lanceros-Mendez, P. Alpuim, F. Vaz, E. Alves, C. Rousselot, J. P. Espinos, A. R. González-Elipe. Influence of the chemical and electronic structure on the electrical behavior of zirconium oxynitride films, *Journal of Applied Physics*, **2008**, *103*, 10.

29. W. Yin and Q. Wang. Feasibility of biological applications for zirconium nitride

https://doi.org/10.52111/qnjs.2023.17509

powders synthesized by gas – solid elemental combination method, *Journal of Nanoscience and Nanotechnology*, **2019**, *19*, 3319-3325.

30. L. Kumari, G. H. Du, W. Z. Li, R. S. Vennila, S. K. Saxena, and D. Z. Wang. Synthesis, microstructure and optical characterization of zirconium oxide nanostructures, *Ceramics International*, **2009**, *35*(6), 2401-2408.

31. A. Emeline, G. V. Kataeva, A. S. Litke, A. V. Rudakova, V. K. Ryabchuk, and N. Serpone. Spectroscopic and photoluminescence studies of a wide band gap insulating material: Powdered and colloidal ZrO_2 sols, *Langmuir*, **1998**, *14*(18), 5011-5022.

32. D. I. Bazhanov, A. A. Knizhnik, A. A. Safonov, A. A. Bagatur'yants, M. W. Stoker and A. A. Korkin. Structure and electronic properties of zirconium and hafnium nitrides and oxynitrides, *Journal of Applied Physics*, **2005**, *97*(4), 044108.

33. T. D. Boyko, A. Zerr, and A. Moewes. Tuning the electronic band gap of oxygen-bearing cubic zirconium nitride, *ACS Applied Electronic Materials*, **2021**, *3*, 4768-4773.

34. P. Carvalho, J. Borges, M. S. Rodrigues, N. P. Barradas, E. Alves, J. P. Espinós, A. R. González-Elipe, L. Cunha, L. Marques, M. I. Vasilevskiy, F. Vaz. Optical properties of zirconium oxynitride films: The effect of composition, electronic and crystalline structures, *Applied Surface Science*, **2015**, *358*, 660-669.

35. Q. Guo, T. Wang, Y. Ren, Y. Ran, C. Gao, H. Lu, Z. Jiang, and Z. Wang. Plasmonic properties of nonstoichiometric zirconium nitride, oxynitride thin films, and their bilayer structures, *Physical Review Materials*, **2021**, *5*(6), 65201.

36. L. Kumari, W. Z. Li, J. M. Xu, R. M. Leblanc, D. Z. Wang, Yi Li, Haizhong Guo, and Jiandi Zhang. Controlled hydrothermal synthesis of zirconium oxide nanostructures and their optical properties, *Crystal Growth & Design*, **2009**, *9*(9), 3874-3880.

37. S. Exarhos, A. A. Barragan, E. Aytan, A. A. Balandin, and L. Mangolini. Plasmonic core-shell zirconium nitride – silicon oxynitride nanoparticles, *ACS Energy Letters*, **2018**, *3*(10), 2349-2356.

TẠP CHÍ KHOA HỌC
TRƯỜNG ĐẠI HỌC QUY NHƠN

Hiểu rõ hơn về khoáng sản: Chương trình phân loại khoáng sản nâng cao tích hợp AI giải thích được và mô hình ngôn ngữ lớn

Nguyễn Trương Thành Hưng[1], Trương Thị Cẩm Mai[2,*]

[1]Phòng thí nghiệm Analytics Everywhere, Trường Đại học New Brunswick, Canada
[2]Khoa Khoa học tự nhiên, Trường Đại học Quy Nhơn, Việt Nam

Ngày nhận bài: 29/08/2023; Ngày sửa bài: 24/10/2023; Ngày nhận đăng: 27/10/2023; Ngày xuất bản: 28/10/2023

TÓM TẮT

Khoáng sản, với thành phần hóa học phức tạp và cấu trúc tinh thể, đóng một vai trò then chốt trong nhiều quá trình hóa học, ứng dụng, và nghiên cứu. Truyền thống, việc phân loại chúng được thực hiện thông qua các kỹ thuật quan sát và hóa học. Tuy nhiên, với việc tăng số lượng mẫu, các phương pháp này thường mất nhiều thời gian. Những tiến bộ gần đây trong Trí tuệ nhân tạo (AI) và Học sâu (DL) hứa hẹn những cải tiến đột phá về tốc độ và độ chính xác của việc phân loại khoáng sản. Tuy nhiên, các mô hình DL, mặc dù chính xác, thường hoạt động như những "hộp đen", làm cho quyết định của chúng không tường minh. Để giải quyết điều này, nghiên cứu của chúng tôi giới thiệu một khung chương trình dựa trên AI cho việc phân loại khoáng sản, kết hợp các mô hình tiên tiến với AI Giải thích được (XAI) và mô hình AI sinh ngôn ngữ lớn (LLMs) như GPT-4. Chương trình này không chỉ phân loại một số lượng lớn các khoáng sản mà còn giải thích lý do phía sau mỗi lựa chọn phân loại. Thông qua sự kết hợp của mô hình Swin Transformer V2 cho việc nhận dạng khoáng sản, GradCAM cho tính minh bạch của mô hình, và GPT-4 để truy xuất thông tin khoáng sản chi tiết, chương trình cung cấp sự kết hợp cân đối giữa hiệu suất, khả năng giải thích và thông tin hướng tới người dùng. Chương trình có thể được truy cập công khai, nhấn mạnh tiềm năng của AI trong việc cách mạng hóa việc phân loại khoáng sản trong khi vẫn đáp ứng nhu cầu về sự rõ ràng, minh bạch và giáo dục người dùng. Đường dẫn truy cập công khai tại *https://huggingface.co/spaces/minatosnow/mineral_framework.*

Từ khóa: *Phân loại khoáng sản, AI giải thích được, mô hình AI sinh ngôn ngữ lớn.*

**Tác giả liên hệ chính.*
Email: truongcammai@qnu.edu.vn

QUY NHON UNIVERSITY
JOURNAL OF SCIENCE

Understanding minerals better: Advancing mineral classification framework through explainable AI and large language model integration

Truong Thanh Hung Nguyen[1], Thi Cam Mai Truong[2,*]

[1]Analytics Everywhere Lab, University of New Brunswick, Canada
[2]Faculty of Natural Sciences, Quy Nhon University, Vietnam

Received: 29/08/2023; Revised: 24/10/2023; Accepted: 27/10/2023; Published: 28/10/2023

ABSTRACT

Minerals, with their intricate chemical compositions and crystalline structures, play a pivotal role in diverse chemical processes, applications, and research. Traditionally, their classification was achieved through observational and chemical techniques. However, with increasing sample sizes, these methods often proved time-consuming. Recent advances in Artificial Intelligence (AI) and Deep Learning (DL) promise transformative improvements in the speed and accuracy of mineral classification. However, DL models, for all their precision, often operate as "black boxes", making their decision-making opaque. To address this, our study introduces an innovative AI-powered framework for mineral classification, integrating state-of-the-art models with Explainable AI (XAI) and generative AI large language models (LLMs) like GPT-4. This framework not only categorizes a wide-ranging number of minerals but also elucidates the reasoning behind each classification. Through a combination of Swin Transformer V2 models for mineral identification, GradCAM for model transparency, and GPT-4 for detailed mineral information retrieval, the framework offers a balanced blend of performance, interpretability, and user-centric information. Available for public access, this system underscores the potential of AI to revolutionize mineral classification while staying attuned to the demands of clarity, transparency, and user education. The framework can be publicly accessed via *https://huggingface.co/spaces/minatosnow/mineral_framework.*

Keywords: *Mineral classification, explainable AI, generative AI large language models.*

1. INTRODUCTION

Minerals are naturally occurring inorganic substances with a specific chemical composition and crystalline structure.[1] Mineral classification is the systematic categorization of minerals based on their physical and chemical properties.[2,3] This classification provides detailed insights into the chemical composition and structure of minerals. By categorizing minerals, chemists can predict their behavior, reactivity, and stability.[4] This understanding is fundamental for various chemical processes, including synthesis, analysis, and industrial applications. Mineral classification is not only an academic exercise but also a vital practice in the chemical field. It underpins various industrial processes, medical applications, environmental protection, and research endeavors. Its importance continues to grow with the increasing complexity and specialization of chemical products and

**Corresponding authors.*
Email: truongcammai@qnu.edu.vn

https://doi.org/10.52111/qnjs.2023.17510

processes, making it an indispensable aspect of modern chemistry.[2,3,5]

Traditionally, mineral classification has been carried out through a combination of physical observation and chemical analysis.[6] Regarding the physical properties, minerals are often classified based on their hardness, luster, color, streak, and specific gravity. The Mohs scale, for example, is used to classify minerals based on hardness.[7,8] Minerals can be grouped into classes based on their primary anionic species, such as silicates, carbonates, and sulfates.[9,10] Chemical tests, such as flame tests and wet chemical analysis, are used to identify the presence of specific elements or compounds.[6,11] X-ray diffraction and other microscopic techniques are also employed to analyze the crystalline structure of minerals, further categorizing them into specific groups.[12–14] Additionally, another approach is to use polarizing microscopes to study the optical properties of minerals, such as birefringence and pleochroism, which can be essential for classification.[15–17]

However, conventional methods might be labor-intensive and time-consuming, particularly when dealing with a large number of samples. With the advent of Artificial Intelligence (AI) and Deep Learning (DL), the field of mineral classification has witnessed a significant transformation.[18–20] The application of DL techniques to mineral classification on images has opened new avenues for accurate and automated classification. DL models can easily scale to handle vast datasets, providing rapid classification without compromising accuracy.

Nevertheless, DL models, particularly complex neural networks (NNs), are often referred to as "black boxes" due to their lack of transparency in how they arrive at a particular decision.[21–24] While these models can achieve high accuracy, understanding the specific reasoning behind their decisions can be elusive. This lack of transparency poses significant challenges, particularly in understanding the rationale behind specific classifications and in ensuring trust and compliance with regulatory standards. Consequently, there is a growing imperative for the integration of Explainable AI (XAI) methods, which aim to unravel the intricate workings of DL models, providing insights into their decision-making processes.[25,26] Besides that, recent works in generative AI large language models (LLMs) have shown promising results in generating human-like text that can be leveraged to provide more information and facts about the model's decisions.[27]

Hence, in this paper we propose an AI-assisted mineral classification framework leveraging several state-of-the-art models in a multi-class classification task integrated with XAI techniques and generative AI LLMs. This integration not only enhances the interpretability of mineral classification but also provides clear and plausible insights into the decision-making process for the end-users. Our proposed framework is tailored to meet the specific needs of the chemical field, ensuring that the classifications are both scientifically robust and readily interpretable. Through our framework, we aim to address the critical challenge of transparency in AI-driven mineral classification, offering a solution that balances performance with interpretability, and understandability, tailored to the unique requirements of the chemical domain. The framework can be publicly accessed via *https://huggingface.co/spaces/minatosnow/mineral_framework*.

2. RELATED WORK

2.1. Deep learning in mineral classification

DL has emerged as a powerful tool in the field of mineral classification, leveraging the ability to learn complex patterns and relationships directly from data, which has been greatly facilitated by the availability of large datasets, powerful computing resources, and the development of sophisticated algorithms.[18–20]

Convolutional Neural Networks (CNNs)[28] are deeply structured feedforward NNs and one

of the representative algorithms of DL, which can be applied to automatically extract optical features of minerals for mineral identification or accelerate the microphase classification. A hybrid approach combining mineral photo image features extracted by CNN EfficientNet-b4 and mineral hardness features to identify minerals.[7] U-Net model is utilized to effectively and automatically extract deep feature information of ore minerals, realizing intelligent recognition and classification under the microscope.[29] ResNet-18 and ResNet-50 models is proposed for DL-based intelligent mineral recognition, enhancing data with image flipping and scale transformation.[30–32]

However, challenges related to interpretability and data dependence remain, where the generated models are complex and difficult to interpret and good accuracy is only guaranteed when the amount of data is large enough, limiting the application in scenarios with limited data, calling for further research and innovation in the field.[20,33]

2.2. Swin transformer – hierarchical vision transformer using shifted windows

Given the aim of our research to classify images according to their corresponding mineral specimen, we undertake this endeavor within the paradigm of image classification-a canonical yet persistently demanding task within the domain of computer vision (CV). For this purpose, we have chosen to utilize a leading-edge model known as the Swin Transformer. The Swin Transformer is a hierarchical vision transformer characterized by its use of shifted windows to compute its representations.[34] This model has been meticulously crafted to navigate the inherent challenges of transposing transformers from linguistic contexts to visual ones. These challenges encompass the vast disparities in scale among visual entities and the inherent high resolution of pixels in images, which stand in stark contrast to the relative simplicity of words within a textual context. The deployment of a shifted windowing scheme serves a dual purpose: it enhances computational efficiency by restricting self-attention computations to discrete, non-overlapping local windows, and concurrently, it facilitates cross-window connections. The hierarchical nature of this architecture bestows upon it the versatility to operate across multiple scales, all while maintaining linear computational complexity in relation to image size. Such attributes render the Swin Transformer a suitable candidate for an array of vision tasks, spanning from image classification to object detection and semantic segmentation.[34] These qualities make Swin Transformer compatible with a broad range of vision tasks, including image classification, object detection, and semantic segmentation.[35]

Furthermore, Swin Transformer V2 represents a sophisticated evolution of the original Swin Transformer model, with an emphasis on augmenting both its capacity and resolution.[36] The associated paper addresses three predominant challenges encountered during the training and application of expansive vision models: training instability, discrepancies in resolution between the stages of pre-training and fine-tuning, and an acute dependence on labeled data. To rectify these issues, the authors propose three primary strategies: 1) The combination of a residual-post-norm approach with cosine attention to bolster training stability; 2) The introduction of a log-spaced continuous position bias method, facilitating the seamless transference of models pre-trained on low-resolution images to downstream tasks necessitating high-resolution inputs; and 3) The deployment of a self-supervised pre-training technique named SimMIM, which mitigates the requirement for vast repositories of labeled images. Leveraging these strategies, the researchers were successful in training a Swin Transformer V2 model comprising a staggering 3 billion parameters, marking its

https://doi.org/10.52111/qnjs.2023.17510

position as one of the most voluminous dense vision models presently available. Impressively, this model has established new benchmarks in performance across four cardinal vision tasks: ImageNet-V2 image classification, COCO object detection, ADE20K semantic segmentation, and Kinetics-400 video action classification.[36,37]

2.3. Explainable AI

XAI is a field of research that aims to make the decisions and predictions of AI systems more transparent and interpretable to humans. There are several approaches to achieving this goal, including gradient-based, perturbation-based, and Class Activation Mapping (CAM)-based methods.

Gradient-based methods, such as LRP,[38] use gradient signals to assign the burden of the decision on the input features. These techniques can be evaluated for their robustness and the role that adversarial robustness plays in having meaningful explanations.

Perturbation-based methods investigate properties of deep neural networks (DNNs) by perturbing the input of a model. For example, part of the input image can be occluded with a mask or a word in a sentence can be replaced with its synonym, and the changes in the output of the model can be observed. Some notable perturbation-based methods are LIME,[23] RISE, D-RISE,[39] D-CLOSE.

CAM-based methods, such as CAM,[40] GradCAM,[41] GradCAM++, SeCAM,[24,42] ScoreCAM,[43] are visual explanation techniques that use class activation maps to highlight the regions of an input image that are most relevant to the model's prediction.

In this work, we employ GradCAM[41] for model debugging and to make CNN-based models more transparent to end-users, primarily in visual tasks like image classification. By visualizing the important regions in an image as a high-resolution heatmaps, developers and end-users can better understand if a model is focusing on the correct patterns or perhaps getting misled by noise or other irrelevant features. GradCAM offers easily interpretable visualizations that align well with human intuition.[44]

2.4. Generative AI with large language models

In the arena of AI, generative AI LLMs have garnered significant attention. Such models, underpinned by extensive datasets, possess the aptitude to synthesize text that is strikingly analogous to human-authored content. One of the most distinguished models in this domain is the Generative Pre-trained Transformer (GPT), a brainchild of OpenAI.[45] GPT has seen several iterations, with the latest being GPT-4.[46] In parallel, Llama 2 has emerged as a notable LLM, a product of collaborative efforts between Meta and Microsoft. This model stands out due to its

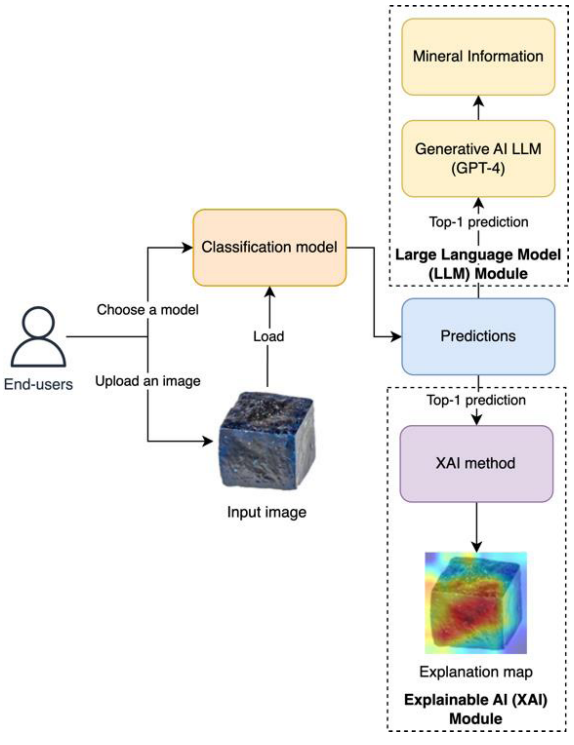

Figure 1. The flowchart representation of the proposed mineral classification framework. After the classification model receives the input image loaded by end-users, the top-1 prediction is fed into the XAI method to deliver the explanation map, and into the generative AI LLM to give information and facts about the classified mineral.

training on a contemporaneous and more eclectic dataset. Claude 2, heralded by Anthropic, is another LLM worth mentioning, boasting enhanced performance, safety, harmlessness and an aptitude for generating more extensive responses. Additionally, the BLOOM, an exemplar of open science and accessibility, was conceived by the BigScience team at Hugging Face. Specifically designed to elaborate on textual prompts, BLOOM capitalizes on industrial-grade computational capacities to produce coherent text across 46 languages and 13 programming languages, rivaling the fidelity of human-generated content.

These expansive LLMs exemplify the forefront of advancements in their uncanny capacity to emulate human text generation. Their implications are manifold, particularly within domains such as natural language processing (NLP) and machine learning (ML). Consequently, they remain at the epicenter of fervent academic inquiry and technological progression.[27,47]

3. PROPOSED FRAMEWORK

In this work, we introduce an innovative framework for mineral classification augmented by Swin Transformer V2 models. This framework seamlessly integrates XAI techniques with LLMs with the overarching aim of enhancing the interpretability and understandability of the generated models. A comprehensive illustration of the structural composition of our mineral classification framework is provided in Figure 1. Moreover, to offer a tangible glimpse into its real-world implementation, the user interface (UI) of our proposed framework is depicted in Figure 2.

The ensuing sections meticulously detail each phase of our methodology-ranging from data preparation and model training to the nuanced intricacies of integrating XAI and LLMs into our framework.

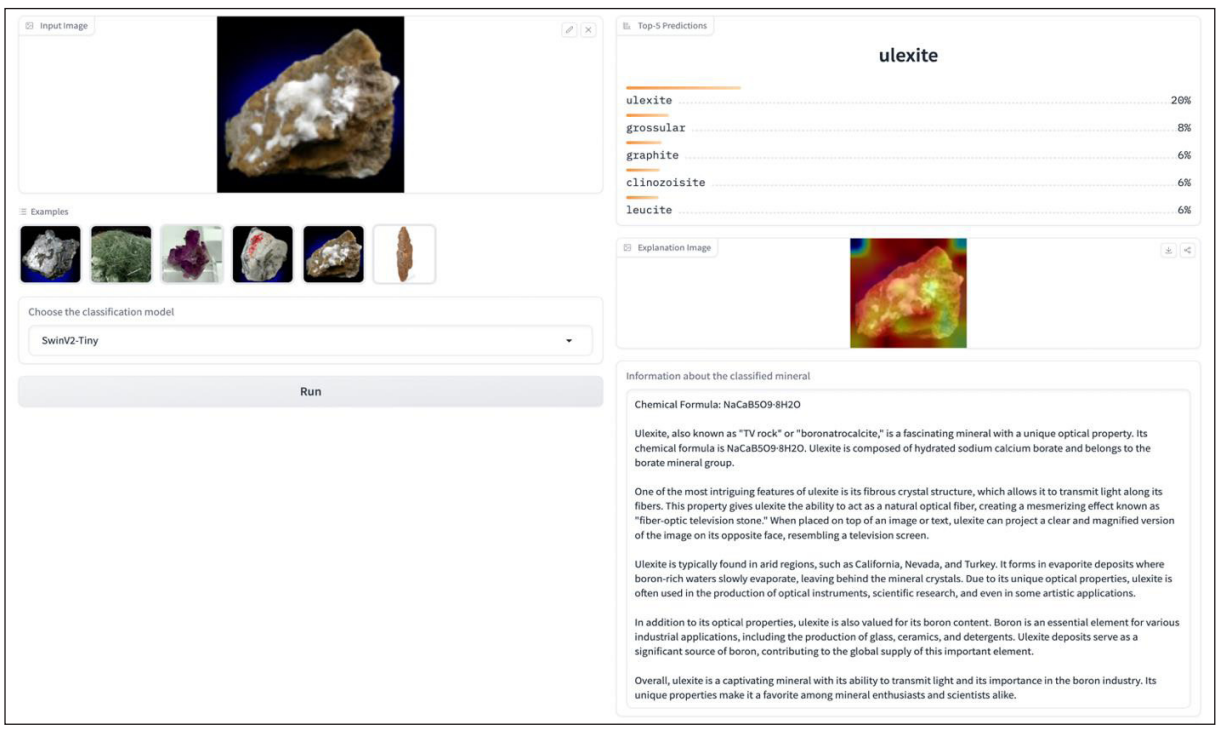

Figure 2. The mineral classification framework user interface (UI) deployed on the Huggingface platform with Gradio UI. The framework requires end-users to upload a mineral image and choose a classification model (the default model is set as SwinV2-Tiny) on the left panel. On the right panel, the top-5 predictions from models, explanation map of XAI methods on the model's prediction, and information retrieval about the top-1 classified mineral from GPT-4 are delivered.

https://doi.org/10.52111/qnjs.2023.17510

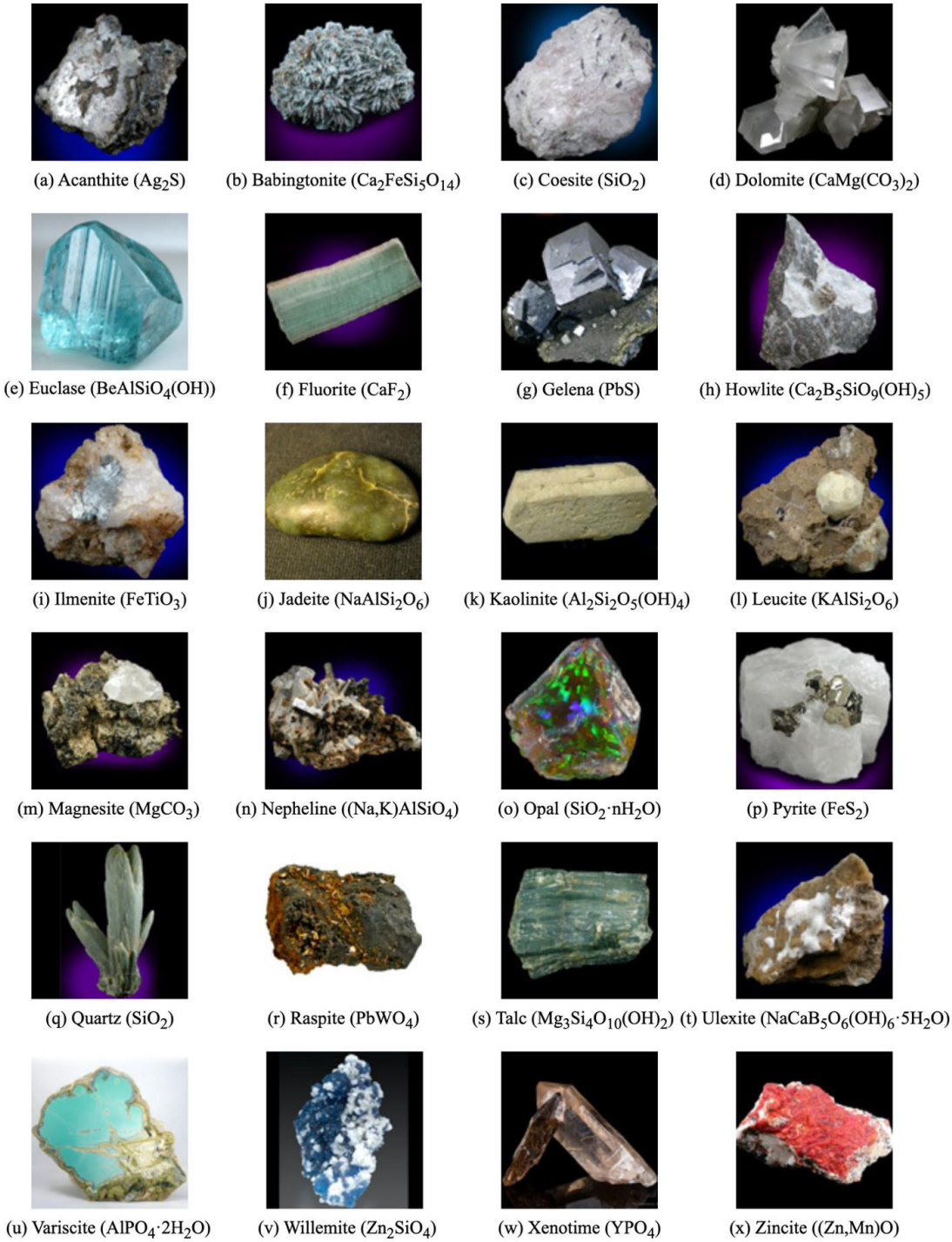

Figure 3. Samples of mineral specimens in the mineral dataset. Each mineral is shown in their name and formula.

3.1. Data preparation

Initiating with data acquisition, we embarked on a web-crawling exercise, amassing a rich dataset of mineral images, each meticulously annotated with their respective labels. The dataset contains around 4,000 images of 282 different minerals, each with labels. The dimensions of these images stand at 110 × 110 pixels. The labeling schema is comprehensive, encapsulating various attributes such as the mineral name, associated crystal system, chemical groupings, rock typologies, and fracture characteristics. For the purpose of model training and evaluation, the dataset was stratified into training and test sets, adhering to an 80% to 20% split ratio.

Given the inherent challenges posed by a limited number of images per mineral specimen (averaging about 14 images for each mineral type) and the relatively diminutive image dimensions, we employed a series of data augmentation strategies. Techniques such as Random Resized Crop and Random Horizontal Flip were judiciously applied to the training dataset to diversify and enhance its content.

3.2. Model training

Within the mineral classification framework, we incorporated three variants of the Swin Transformer V2 model, differentiated by their size: the Tiny-sized model (SwinV2-T), the Small-sized model (SwinV2-S), and the Base-sized model (SwinV2-B). Each of these models has undergone preliminary training on the ImageNet-1k dataset at a resolution of 256 × 256 pixels.[48] Recognizing the intricacies of a multiclass classification task, we elected the cross-entropy (CE) as our loss function, with the top-1 accuracy metric serving as the cornerstone of our evaluation process.

The training set, derived from our curated dataset, was harnessed to fine-tune these models. An advanced image preprocessing tool, the Vision Transformer (ViT), was deployed to ensure uniform normalization of images, thus harmonizing their resolution to align with the models' specifications. All associated hyperparameters pertinent to the fine-tuning process are systematically delineated in Table 1.

Table 1. The defined hyperparameters for finetuning the Swin Transformer V2 models.

Hyperparameter	Value
learning_rate	5e-5
warmup_ratio	0.1
gradient_accumulation_steps	4
batch_size	32

Subsequent to the fine-tuning phase, a rigorous evaluation was conducted to assess the performance of each model variant, employing the test set as the benchmark.

3.3. XAI integration

In this section, we leverage XAI to enhance the interpretability and transparency of Swin Transformer V2 models. We utilize GradCAM as the XAI method.[41] Given an input image, the forward pass computes activations at the chosen layer. The gradients of the class score concerning this layer's activations are then computed. These gradients are globally average-pooled to produce weights. Finally, a weighted combination of forward activation maps produces the GradCAM heatmap.

$$L_{GradCAM} = ReLU(\sum_{k} \alpha_k^c A^k)$$

where:

- $L_{GradCAM}$ is the explanation map for class c.
- α_k^c are the global-average-pooled gradients.
- A^k represents the forward activation maps for the chosen layer.
- $ReLU$ ensures that only positive influences on the class prediction are visualized.

3.4. Information retrieval with GPT-4

Given the multitude of mineral specimens that can be identified and categorized by our models, we recognized the imperative to supplement the raw classification with pertinent information. To this end, we employ the capabilities of GPT-4. This strategic integration is underpinned by the objective of furnishing end-users-who may lack prior familiarity with the specific mineral depicted in the image-with comprehensive and contextually relevant insights.

Upon obtaining the results from our primary classification model, we extract the top-most prediction, which is then utilized as an input for GPT-4. This methodology enables the provision of comprehensive and contextual data to the end-user. Notably, we have configured GPT-4 to emulate the expertise of a mineralogist, thereby ensuring that the generated information is not only informative but is also presented in a manner that is both engaging and cogent. It is worth emphasizing that vague or generic

https://doi.org/10.52111/qnjs.2023.17510

explanations are deliberately avoided, thereby enhancing the utility and reliability of the provided details.

To further bolster the authenticity and veracity of the information retrieved, we have imparted explicit instructions to GPT-4, directing it to rely solely on information from reputable sources. Among the preferred repositories are Wikipedia, an encyclopedia recognized for its vast and up-to-date content; The Mineral and Gemstone Kingdom, known for its exhaustive listings and detailed mineralogical insights; and the Mineral Resources Database, a repository hailed for its accuracy and comprehensive coverage. By anchoring our information retrieval process in such esteemed sources, we aspire to ensure that the knowledge disseminated to the users is both trustworthy and of the highest academic caliber.

4. RESULTS

In this section, we systematically present the empirical results and observations gleaned from the evaluations of the Swin Transformer V2 models. Initially, we will provide a quantitative assessment of the models based on the test set, followed by an exploration of the visual explanations in the form of saliency maps.

4.1. Quantitative assessment of model performances

We subject three distinct models - SwinV2-T, SwinV2-S, and SwinV2-B - to rigorous evaluation, both on training and test sets. As depicted in Figure 4, all three models demonstrate comparable CE loss on the training set. Notably, SwinV2-B emerges as the earliest to converge, trailed by SwinV2-S and SwinV2-T. Furthermore, SwinV2-B boasts the lowest CE loss among the trio.

However, a contrasting pattern emerges upon examining their performance on the test set, as shown in Figure 5. SwinV2-S achieves the lowest CE loss. Nevertheless, all three models showcase an analogous behavior; their CE losses manifest a steady uptick after the initial 1,000 training steps. This tendency suggests a pronounced overfitting to the training data and limited generalization to unseen datasets. This observation is further corroborated by accuracy metrics on the test set, with the most compact model, SwinV2-T, outperforming its counterparts.

In contemporary AI research, the efficiency of models, especially concerning GPU power consumption measured in Watts (W), has emerged as a crucial criterion. Lower power usage signifies a reduced carbon footprint, advancing the cause of sustainable and eco-friendly AI modeling. As one would anticipate, SwinV2-T, with its parsimonious parameterization, consumes the least power, trailed by SwinV2-S and then SwinV2-B, as evident from Figure 6.

Given the above empirical observations, factoring in both performance and efficiency, we advocate SwinV2-T as the primary model recommendation within our framework. However, we offer users the flexibility to leverage other models as per their requirements.

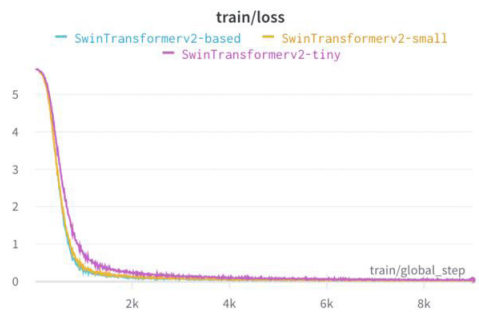

(a) The loss of three models on the training set

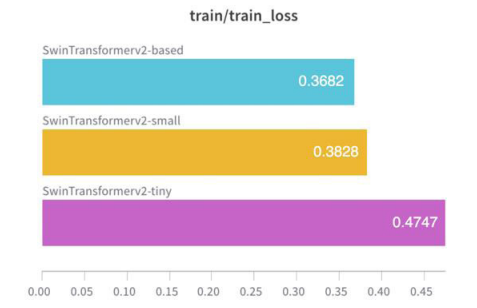

(b) The average loss of three models on the training set

Figure 4. The (a) loss and (b) average loss of three classification models, namely SwinV2-T (pink), SwinV2-S (yellow), and SwinV2-B (blue), on the training set during the training phase.

4.2. In-depth qualitative analysis of classification explanations

This section provides a meticulous qualitative dissection of the explanations underlying the classification decisions made by our selected model.

Figure 7 demarcates two distinct classification cases associated with the SwinV2-T model: an instance of accurate classification and a contrasting case of misclassification.

In scenarios where the classification proves accurate, the model's top-1 prediction perfectly resonates with the ground truth, illustrated by the case of the mineral Boleite. A closer examination reveals that the model, in its discernment, emphasizes specific features of the mineral. Specifically, it pays particular attention to the frontal facade of the mineral, which seems to be a key determinant in its accurate classification.

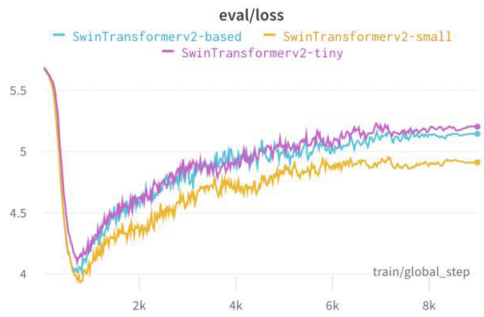

(a) The loss of three models on the test set

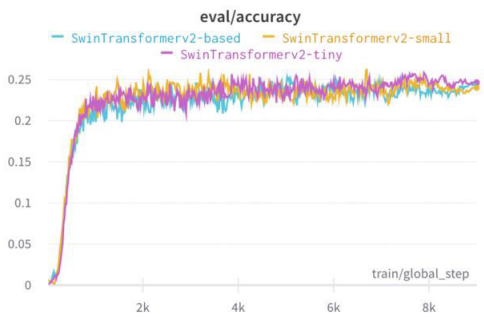

(b) The accuracy of three models on the test set

Figure 5. The (a) loss and (b) accuracy of three models, namely SwinV2-T (pink), SwinV2-S (yellow), and SwinV2-B (blue) on the test set during the training phase.

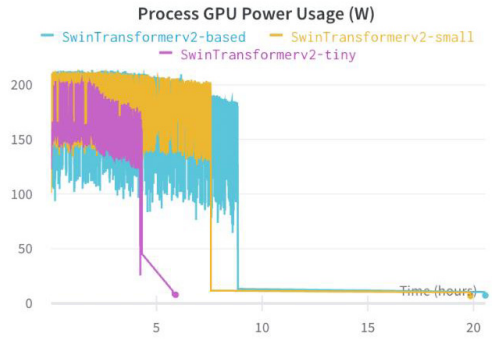

Figure 6. The process GPU power usage (in Watt) of three models, namely SwinV2-T (pink), SwinV2-S (yellow), and SwinV2-B (blue) during the training phase.

However, in instances where the classification goes awry, the model's decision-making intricacies become all the more fascinating. Taking the case where the model erroneously identifies an image as Monazite, with the second-highest probability assigned to Xenotime, the GradCAM explanation offers invaluable insights. The model seems to be unduly influenced by the image's background and specific sections of the Xenotime that are color-matched with training samples of Monazite. Such idiosyncrasies in model behavior, illuminated by XAI techniques, accentuate the need for interpretability. It ensures that even when the model falters, its decision-making rationale remains transparent, allowing users to comprehend and, potentially, correct or circumvent such pitfalls.

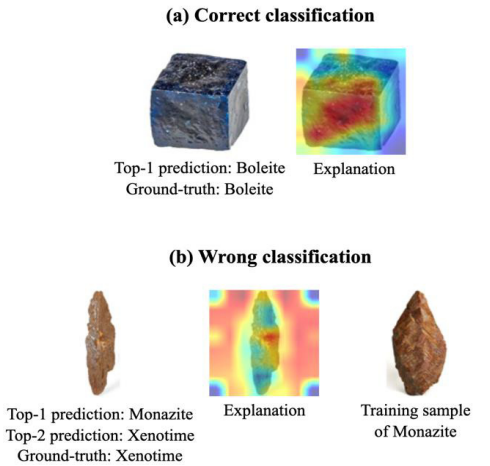

Figure 7. Examples of XAI-driven explanations for (a) an accurate classification and (b) an instance of misclassification as determined by SwinV2-T. Notably, the latter also integrates a training exemplar of the misclassified mineral, offering users an added layer of context.

https://doi.org/10.52111/qnjs.2023.17510

4.3. Comprehensive insights through information retrieval

Table 2. Information retrieval with GPT-4 on classified minerals. As being instructed to deliver only facts from credible sources, the GPT-4 can deliver human-like information to end-users.

Mineral: Monazite **GPT-4:** Monazite is a rare-earth phosphate mineral with the chemical formula (Ce,La,Nd,Th)PO_4. It is typically reddish-brown in color and has a resinous to vitreous luster. Monazite is an important source of rare-earth elements, which are used in various high-tech applications including electronics, magnets, and catalysts. It is also known for its radioactive properties, containing thorium and uranium. Due to its scarcity and economic value, monazite is often mined for its rare-earth content.
Mineral: Acanthite **GPT-4:** Acanthite is a silver sulfide mineral with the chemical formula Ag_2S. It is an important ore of silver and is commonly found in hydrothermal veins and low-temperature deposits. Acanthite is known for its metallic luster and dark gray to black color. It has a high density and is relatively soft. Acanthite is often associated with other silver minerals such as native silver and argentite. It is widely used in the production of silver metal and jewelry.

Building upon the top-1 classification of our mineral classification framework, GPT-4 acts as a sophisticated intermediary, extracting and presenting informative details about the identified minerals, such as Monazite and Acanthite, as shown in Table 2. Leveraging its vast training data, which encapsulates extensive knowledge on diverse mineral specimens, GPT-4 ensures that the information procured is not just accurate but is also curated to cater to users with varied levels of prior knowledge.

Furthermore, by incorporating safety protocols that ensure information retrieval solely from reputable sources, such as Wikipedia, The Mineral and Gemstone Kingdom, and the Mineral Resources Database, we guarantee the veracity and reliability of the procured data. Thus, users not only receive a rich tapestry of mineralogical information but also the assurance of its credibility. In essence, the synergy between our classification framework and GPT-4 creates an enriched user experience, fostering a more profound understanding and appreciation of the minerals.

5. CONCLUSION AND FUTURE WORK

Throughout this work, we have presented an AI-driven mineral classification framework characterized by its high interpretability and informative capabilities. This framework, bolstered by advanced XAI techniques and LLM, is strategically designed to cater to a wide audience, including those with limited or no prior expertise in mineralogy or AI. The incorporation of XAI proves invaluable, particularly in instances of incorrect model decisions, facilitating a more transparent and comprehensible insight into the model's reasoning. Such transparency is crucial in bolstering user trust and understanding, enabling them to more confidently engage with the system. Our future works revolve around broadening the scope of our dataset by integrating data from diverse and robust sources. This not only promises to enhance the model's precision but also its efficiency. Additionally, we aim to delve deeper into the human-centric aspect of our system. Specifically, we intend to orchestrate comprehensive human evaluations that will scrutinize both the plausibility and the faithfulness of explanations and information generated by XAI techniques and LLMs. Such evaluations will serve as a litmus test, assessing the real-world applicability and impact of our framework on its intended users.

REFERENCES

1. P. Patnaik. *Handbook of inorganic chemicals*, McGraw-Hill, New York, 2003.
2. S. T. Ishikawa, V. C. Gulick. An automated mineral classifier using Raman spectra, *Computers & Geosciences*, **2013**, *54*, 259-268.

3. A. S. Povarennykh. *Crystal chemical classification of minerals*, Springer, 2014.

4. C. Owen, D. Pirie, G. Draper. *Earth Lab: Exploring the Earth Sciences,* Cengage Learning, 2010.

5. C. Klein, B. Dutrow. *Manual of mineral science,* John Wiley & Sons, 2007.

6. R. L. Shriner, C. K. Hermann, T. C. Morrill, D. Y. Curtin, R. C. Fuson. *The systematic identification of organic compounds,* John Wiley & Sons, 2003.

7. X. Zeng, Y. Xiao, X. Ji, G. Wang. Mineral identification based on deep learning that combines image and Mohs hardness, *Minerals*, **2021**, *11*(5), 506.

8. M. E. Broz, R. F. Cook, D. L. Whitney. Microhardness, toughness, and modulus of Mohs scale minerals, *American Mineralogist*, **2006**, *91*, 135-142.

9. S. S. Lam, D. Fortin, B. Davis, T. Beveridge. Mineralization of bacterial surfaces, *Chemical Geology*, **1996**, *132*, 171-181.

10. I. V. Veksler, A. M. Dorfman, P. Dulski, V. S. Kamenetsky, L. V. Danyushesky, T. Jeffries, D. B. Dingwell. Partitioning of elements between silicate melt and immiscible fluoride, chloride, carbonate, phosphate and sulfate melts, with implications to the origin of natrocarbonatite, *Geochimica et Cosmochimica Acta*, **2012**, *79*(2), 20-40.

11. V. Apte. *Flammability Testing of Materials Used in Construction, Transport, and Mining*, Woodhead Publishing, 2021.

12. A. Ali, Y. W. Chiang, R. M. Santos. X-ray diffraction techniques for mineral characterization: A review for engineers of the fundamentals, applications, and research directions, *Minerals*, **2022**, *12*(2), 205.

13. G. W. Brindley. Identification of clay minerals by X-ray diffraction analysis, *Clays and Clay Minerals*, **1952**, *1*, 119-129.

14. J. Srodon, V. A. Drits, D. K. McCarty, J. C. Hsieh, D. D. Eberl. Quantitative X-ray diffraction analysis of clay-bearing rocks from random preparations, *Clays and Clay Minerals*, **2001**, *49*(6), 514-528.

15. S. Aligholi, R. Khajavi, M. Razmara. Automated mineral identification algorithm using optical properties of crystals, *Computers & Geosciences*, **2015**, *85*, 175–183.

16. C. D. Gribble. *Optical mineralogy: principles and practice,* Springer Science & Business Media, 2012.

17. C. Gribble. *A practical introduction to optical mineralogy,* Springer Science & Business Media, 2012.

18. A. G. Flores, S. Ilyas, G. W. Heyes, H. Kim. A critical review of artificial intelligence in mineral concentration, *Minerals Engineering*, **2022**, *189*, 107884.

19. H. P. Borges, M. S. de Aguiar. *Mineral classification using machine learning and images of microscopic rock thin section,* Advances in Soft Computing: 18th Mexican International Conference on Artificial Intelligence, MICAI 2019, Xalapa, Mexico, October 27-November 2, 2019, Proceedings 18, 2019, 63-76.

20. T. Long, Z. Zhou, G. Hancke, Y. Bai, Q. Gao. A review of artificial intelligence technologies in mineral identification: classification and visualization, *Journal of Sensor and Actuator Networks*, **2022**, *11*(3), 50.

21. H. T. T. Nguyen, H. Q. Cao, K. V. T. Nguyen, N. D. K. Pham. *Evaluation of explainable artificial intelligence: Shap, lime, and cam,* Proceedings of the FPT AI Conference, 2021, 1–6.

22. E. Tjoa, C. Guan. A survey on explainable artificial intelligence (xai): Toward medical xai, *IEEE Transactions on Neural Networks and Learning Systems*, **2020**, *32*, 4793–4813.

23. M. T. Ribeiro, S. Singh, C. Guestrin. *"Why should I trust you?" Explaining the predictions of any classifier,* Proceedings of the 22nd ACM SIGKDD international conference on knowledge discovery and data mining, 2016, 1135-1144.

24. A. Chattopadhay, A. Sarkar, P. Howlader, V. N. Balasubramanian. *Grad-cam++: Generalized gradient-based visual explanations for deep convolutional networks,* 2018 IEEE winter conference on applications of computer vision (WACV), 2018, 839-847.

https://doi.org/10.52111/qnjs.2023.17510

25. D. Gunning, M. Stefik, J. Choi, T. Miller, S. Stumpf, G.-Z. Yang. XAI-Explainable artificial intelligence, *Science Robotics*, **2019**, *4*(37), eaay7120.

26. F. Xu, H. Uszkoreit, Y. Du, W. Fan, D. Zhao, J. Zhu. *Explainable AI: A brief survey on history, research areas, approaches and challenges*, Natural Language Processing and Chinese Computing: 8th CCF International Conference, NLPCC 2019, Dunhuang, China, October 9-14, 2019, Proceedings, Part II 8, 2019, 563-574.

27. B. Min, H. Ross, E. Sulem, A. P. B. Veyseh, T. H. Nguyen, O. Sainz, E. Agirre, I. Heinz, D. Roth. Recent advances in natural language processing via large pre-trained language models: A survey, *ACM Computing Surveys*, **2021**.

28. Y. Lecun, Y. Bengio. *Convolutional networks for images, speech, and time-series,* The handbook of brain theory and neural networks, 1995, *3361*.

29. X. S. Teng, Z. Y. Zhang. Artificial intelligence identification of ore minerals under microscope based on deep learning algorithm, *Acta Petrologica Sinica*, **2018**, *34*, 3244-3252.

30. P. Theerthagiri, A. U. Ruby, B. Chaithanya, R. R. Patil, S. Jain. D-Resnet: deep residual neural network for exploration, identification, and classification of beach sand minerals, *Multimedia Tools and Applications*, **2023**, 1-25.

31. G. Yanjun, Z. Zhe, L. Hexun, L. Xiaohui, C. Danqiu, Z. Jiaqi, W. Junqi. The mineral intelligence identification method based on deep learning algorithms, *Earth Science Frontiers*, **2020**, *27*(5), 39-47.

32. W. Ren, M. Zhang, S. Zhang, J. Qiao, J. Huang. *Identifying rock thin section based on convolutional neural networks*, Proceedings of the 2019 9th International Workshop on Computer Science and Engineering (WCSE 2019), Hong Kong, China, 2019, 15-17.

33. T. Miller, D. Cembrowska-Lech, A. Kisiel, P. Kozlovska, A. Krzemińska, S. Mosiundz, A. Kutsevych, K. Lewita, M. Jawor. Applied statistics and machine learning in earth sciences: choosing the right approach for modern scientific research, *Collection of Scientific Papers*, **2023**, 244–249.

34. Z. Liu, Y. Lin, Y. Cao, H. Hu, Y. Wei, Z. Zhang, S. Lin, B. Guo. *Swin transformer: Hierarchical vision transformer using shifted windows*, Proceedings of the IEEE/CVF international conference on computer vision, 2021, 10012-10022.

35. D. Luo, W. Zeng, J. Chen, W. Tang. Deep learning for automatic image segmentation in stomatology and its clinical application, *Frontiers in Medical Technology*, **2021**, *3*, 767836.

36. Z. Liu, H. Hu, Y. Lin, A. Yao, Z. Xie, Y. Wei, J. Ning, Y. Cao, Z. Zhang, L. Dong, F. Wei, B. Guo. *Swin transformer v2: Scaling up capacity and resolution,* Proceedings of the IEEE/CVF conference on computer vision and pattern recognition, 2022, 12009-12019.

37. J. Kang, S. Tariq, H. Oh, S. S. Woo. A survey of deep learning-based object detection methods and datasets for overhead imagery, *IEEE Access*, **2022**, *10*, 20118-20134.

38. A. Binder, G. Montavon, S. Lapuschkin, K. -R. Müller, W. Samek. *Layer-wise relevance propagation for neural networks with local renormalization layers*, Artificial Neural Networks and Machine Learning–ICANN 2016: 25th International Conference on Artificial Neural Networks, Barcelona, Spain, September 6-9, 2016, Proceedings, Part II 25, 2016, 63-71.

39. V. Petsiuk, R. Jain, V. Manjunatha, V. I. Morariu, A. Mehra, V. Ordonez, K. Saenko. *Black-box explanation of object detectors via saliency maps,* Proceedings of the IEEE/CVF Conference on Computer Vision and Pattern Recognition, 2021, 11443-11452.

40. B. Zhou, A. Khosla, A. Lapedriza, A. Oliva, A. Torralba. *Learning deep features for discriminative localization,* 2016 IEEE Conference on Computer Vision and Pattern Recognition (CVPR), 2016, 2921-2929.

41. R. R. Selvaraju, M. Cogswell, A. Das, R. Vedantam, D. Parikh, D. Batra. *Grad-cam: Visual explanations from deep networks via gradient-based localization,* Proceedings of the IEEE International conference on computer vision, 2017, 618-626.

42. P. X. Nguyen, H. Q. Cao, K. V. Nguyen, H. Nguyen, T. Yairi. SeCAM: Tightly accelerate the image explanation via region-based segmentation, *IEICE Transactions on Information and Systems*, **2022**, *105*, 1401-1417.

43. H. Wang, Z. Wang, M. Du, F. Yang, Z. Zang, S. Ding, P. Mardziel, X. Hu. *Score-CAM: Score-weighted visual explanations for convolutional neural networks,* Proceedings of the IEEE/CVF conference on computer vision and pattern Recognition Workshops, 2020, 24-25.

44. T. T. H. Nguyen, V. B. Truong, V. T. K. Nguyen, Q. H. Cao, Q. K. Nguyen. *Towards Trust of Explainable AI in Thyroid Nodule Diagnosis Check for updates,* Artificial Intelligence for Personalized Medicine: Promoting Healthy Living and Longevity, 2023, *1106,* 11.

45. T. Brown, B. Mann, N. Ryder, M. Subbiah, J. D. Kaplan, P. Dhariwal, A. Neelakantan, P. Shyam, G. Sastry, A. Askell, S. Agarwal, A. H. Voss, G. Krueger, T. Henighan, R. Child, A. Ramesh, D. M. Ziegler, J. Wu, C. Winter, C. Hesse, M. Chen, E. Sigler, M. Litwin, S. Gray, B. Chess, Jack Clark, C. Berner, S. McCandlish, A. Radford, I. Sutskever, D. Amodei. Language models are few-shot learners, *Advances in Neural Information Processing Systems*, **2020**, *33*, 1877–1901.

46. OpenAI. GPT-4 Technical Report, 2023.

47. H. Huang, O. Zheng, D. Wang, J. Yin, Z. Wang, S. Ding, H. Yin, C. Xu, R. Yang, Q. Zheng, others. ChatGPT for shaping the future of dentistry: the potential of multi-modal large language model, *International Journal of Oral Science*, **2023**, *15*, 29.

48. J. Deng, W. Dong, R. Socher, L. J. Li, K. Li, L. F. Fei. *Imagenet: A large-scale hierarchical image database,* 2009 IEEE conference on computer vision and pattern recognition, 2009, 248–255.

TẠP CHÍ KHOA HỌC
TRƯỜNG ĐẠI HỌC QUY NHƠN
TẬP 17, SỐ 5, THÁNG 10 - 2023
ISSN: 1859-0357 E-ISSN: 2815-6242

MỤC LỤC